

FROM BLOCK COPOLYMERS TO FUNCTIONAL NANOSTRUCTURED MATERIALS

Zur Erlangung des akademischen Grades einer
DOKTORIN DER NATURWISSENSCHAFTEN
(Dr. rer. nat)

der KIT-Fakultät für Chemie und Biowissenschaften
des Karlsruher Instituts für Technologie (KIT)

genehmigte
DISSERTATION

von

Divya Varadharajan

aus

Chennai, Indien

KIT-Dekan: Prof. Dr. Reinhard Fischer

Referent: Dr. Guillaume Delaittre

Korreferent: Prof. Dr. Patrick Théato

Tag der mündlichen Prüfung: 18.07.2018

Die vorliegende Arbeit wurde im Zeitraum von Januar 2015 bis Juli 2018 unter Anleitung von Dr. Guillaume Delaittre und Prof. Dr. Christopher Barner-Kowollik am Karlsruher Institut für Technologie - Universitätsbereich angefertigt.

Hiermit bestätige ich wahrheitsgemäß, dass ich die vorliegende Arbeit im Rahmen der Betreuung durch Dr. Guillaume Delaittre und Prof. Dr. Christopher Barner-Kowollik selbstständig verfasst und keine anderen Quellen und Hilfsmittel als die angegebenen verwendet habe. Wörtlich oder inhaltlich übernommene Stellen sind als solche kenntlich gemacht und die Satzung des Karlsruher Instituts für Technologie (KIT) zur Sicherung guter wissenschaftlicher Praxis wurde beachtet. Des Weiteren erkläre ich, dass ich mich derzeit in keinem weiteren laufenden Promotionsverfahren befinde und keine vorausgegangenen Promotionsversuche unternommen habe.

Karlsruhe, den 04.06.2018

Divya Varadharajan

ABSTRACT

Block copolymer (BCP) self-assembly is a powerful tool for fabricating nanostructured materials featuring domains in the sub-50 nm regime. Introducing surface reactivity into such nanomaterials would make them extremely attractive for specific applications in the areas of controlled immobilization, nanopatterning, and micro-/nanoarray fabrication.

This dissertation presents an original strategy for the preparation of reactive nanostructured materials possessing nanodomains of ≤ 20 nm using functional BCPs. For this, libraries of functional BCPs were first prepared by a post-polymerization modification (PPM) approach. A poly(methyl methacrylate-*stat*-pentafluorophenyl methacrylate)-*block*-poly(styrene-*stat*-pentafluorostyrene) (P(MMA-*r*-PFPMA)-*b*-P(S-*r*-PFS)) precursor BCP was synthesized by reversible addition-fragmentation chain-transfer (RAFT) polymerization. Subsequently, bifunctional PMMA-*b*-PS BCPs were generated by PPM of PFPMA and PFS with functional amines and thiols, respectively. Orthogonality between *para*-fluoro-thiol substitution reaction (PFTR) and amidation was established in the process, while revealing a new reactivity of PFPMA towards thiols.

Subsequently, preparation of nanostructured nanoparticles and membranes is targeted using the self-assembly of functional BCPs. ‘Patchy’ nanoparticles were prepared by self-organized precipitation of chloro, azido and pentafluorophenyl (PFP) functionalized polystyrene-*block*-polyisoprene (PS-*b*-PI) BCPs. The presence of pendant and lateral functional groups in the BCP, as well as the nanoparticle preparation conditions influenced the formation of nanoparticles, leading to morphologies such as dots, onion-like, and stacked lamellae. Model thiols could be patterned selectively on the PS domains in the stacked lamellae nanoparticles demonstrating the potential of such reactive nanoparticles for precise immobilization. Further, a strategy to generate nanoporous membranes using the self-assembly of an amphiphilic BCP containing a PFP-based cleavable junction has been developed. Optimum PFTR conditions to synthesize the amphiphilic BCP containing PS and a water-soluble segment are highlighted. Lastly, functional copolymers containing novel photoacid and photobase generators were synthesized to trigger pH changes upon light irradiation to uncover the underlying influence of pH on inflammation.

ZUSAMMENFASSUNG

Selbstassemblierung von Blockcopolymeren (BCPs) stellt ein mächtiges Werkzeug in der Herstellung nanostrukturierter Materialien mit Domänen unter 50 nm dar. Die Bestückung derartiger Materialien mit reaktiven Oberflächenelementen macht sie hochattraktiv für die Bereiche kontrollierter Immobilisierung, Nanostrukturierung und Fabrikation von Mikro-/Nanoarrays.

Die vorliegende Dissertation präsentiert eine neuartige Strategie zur Darstellung reaktiver nanostrukturierter Materialien mit Nanodomänen in einer Größenordnung von weniger als 20 nm unter Verwendung funktionalisierter Blockcopolymerer. Zu diesem Zweck wurden Bibliotheken bifunktionaler BCPs, basierend auf poly(Methylmethacrylat-*stat*-Pentafluorophenylmethacrylat)-*block*-(Polystyrol-*stat*-Pentafluorostyrol) (P(MMA-*r*-PFPMA)-*b*-P(S-*r*-PFS)) mittels Postpolymerisationsmodifikation hergestellt. Die BCPs wurden mithilfe reversibler Additions-Fragmentierungs Polymerisation (RAFT) synthetisiert. Funktionalisierung erfolgte durch Modifikation der PFPMA-Einheiten mit Aminen und PFS-Einheiten mit Thiolen. Im Zuge dessen wurde die Orthogonalität zwischen der *para*-Fluoro-Thiol Reaktion (PFTR) und der Amidierung von PFP-Aktivestern etabliert, sowie ein weiterer Reaktionsweg zwischen PFPMA und Thiolen aufgedeckt.

Die Darstellung nanostrukturierter Nanopartikel und Membranen wurde durch Selbstassemblierung funktioneller BCPs in Angriff genommen. Gemusterte Nanopartikel wurden mittels selbstorganisierender Fällung von Chloro-, Azido- und PFP-funktionalen PS-*b*-PI BCPs hergestellt. Die Gegenwart funktionaler lateraler und Seitengruppen im BCP, sowie die genutzten Herstellungsbedingungen beeinflussten die Ausbildung gepunkteter, zwiebelartiger oder gestapelt lamellarer Morphologien. Modellthiole konnten selektiv auf den PS Domänen gestapelt lamellarer Nanopartikel immobilisiert werden, was das außerordentliche Potential solcher Nanopartikel für selektive Modifikationen demonstriert. Des Weiteren wurde eine Strategie entwickelt, um nanoporöse Membranen unter Ausnutzung der Selbstassemblierung amphiphiler BCPs mit spaltbarer PFP-basierter Verknüpfung zu gewinnen. Darüber hinaus wurden ideale PFTR Bedingungen zur Darstellung amphiphiler BCPs aus PS und wasserlöslichen Einheiten aufgezeigt. Zuletzt

wurden funktionelle Copolymere mit neuartigen Photosäure- und Photobasegeneratoren synthetisiert, mithilfe derer der grundlegende Einfluss von pH-Wert auf Entzündungsreaktionen anhand bestrahlungsgesteuerter pH-Sprünge untersucht werden kann.

TABLE OF CONTENTS

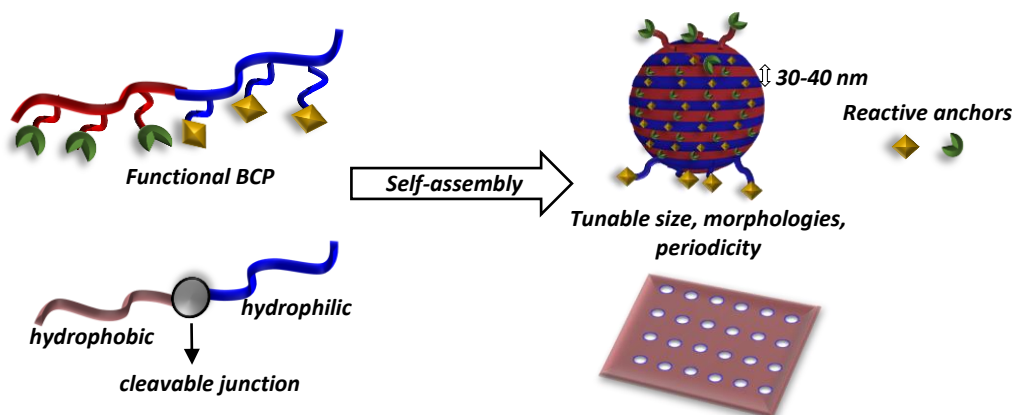
Abstract.....	i
Zusammenfassung.....	iii
Table of contents.....	v
1. Introduction.....	1
2. Theoretical Background.....	5
2.1 BLOCK COPOLYMERS (BCPs).....	5
2.2 FREE RADICAL POLYMERIZATION (FRP).....	6
2.3 REVERSIBLE-DEACTIVATION RADICAL POLYMERIZATION (RDRP).....	8
2.3.1 Nitroxide-Mediated Polymerization (NMP).....	9
2.3.2 Atom-Transfer Radical Polymerization (ATRP).....	10
2.3.3 Reversible Addition-Fragmentation Chain-Transfer Polymerization (RAFT).....	11
2.4 POST-POLYMERIZATION MODIFICATION (PPM).....	14
2.4.1 Activated Ester-Amine Substitution.....	15
2.4.2 Para-Fluoro –Thiol Substitution Reaction (PFTR).....	18
2.5 PHASE SEPARATION AND SELF-ASSEMBLY OF BCPS IN BULK.....	20
2.5.1 Thermodynamic explanation of microphase separation.....	21
2.5.2 Effect of BCP composition on microphase separation.....	25
2.5.3 Effect of molar mass and dispersity on microphase separation.....	26
2.5.4 Microphase separation in BCP/Homopolymer blends.....	28
2.6 SELF-ASSEMBLY OF BCPS IN SOLUTION.....	29
2.6.1 BCP self-assembly under confinement.....	30
2.7 APPLICATIONS OF BCP SELF-ASSEMBLY.....	40
2.7.1 Nanoporous membranes.....	40
2.7.2 Multicompartment nanoparticles.....	42
2.8 ANALYTICAL METHODS FOR NANOSTRUCTURED NANOPARTICLES.....	46
2.8.1 Transmission Electron Microscopy (TEM).....	46
2.8.2 Scanning Transmission Electron Microscopy (STEM).....	49
2.8.3 Stimulated Emission Depletion Microscopy (STED).....	51

3. Synthesis of Functional Block Copolymers.....	55
3.1 INTRODUCTION.....	55
3.2 STRATEGY	56
3.3 RESULTS AND DISCUSSION.....	57
3.3.1 Synthesis of PFP-functionalized BCPs.....	57
3.3.2 Functional BCP library: Establishing orthogonal reactions between two distinct PFP-derivatives	60
3.3.3 Proof of Concept: Reactivity of F-atoms of PFPMA towards nucleophilic thiol substitution.....	69
3.4 CONCLUSION.....	72
4. Fabrication of Functional Nanostructured Materials	75
4.1 INTRODUCTION.....	75
4.2 AIMS AND METHODS.....	76
4.3 RESULTS AND DISCUSSION.....	78
4.3.1 Selection of the BCP system.....	78
4.3.2 Preparation of surface reactive nanostructured nanoparticles	79
4.3.3 Preparation of porous membranes	99
4.4 CONCLUSION.....	107
5. Photoreactive Polymers as Inflammation Probes	111
5.1 INTRODUCTION.....	111
5.2 STRATEGY	114
5.3 RESULTS AND DISCUSSION.....	115
5.3.1 Synthesis of the photobase generator (PBG)	115
5.3.2 Synthesis of P(OEGMA-r-PBG) copolymer CP1.....	118
5.3.3 Photolysis study of P(OEGMA-r-PBG) CP1.....	120
5.3.4 Synthesis of the photoacid generator (PAG)	125
5.3.5 Synthesis of P(OEGMA-r-PAG) copolymer CP2	126
5.3.6 Photolysis study of P(OEGMA-r-PAG) CP2	127
5.4 CONCLUSION.....	129
6. Summary and Outlook	131

7. Materials and Methods.....	135
7.1 MATERIALS	135
7.2 CHARACTERIZATION	136
7.2.1 Characterization of the polymers	136
7.2.2 Characterization of the nanoparticles and nanodiscs	138
8. Synthetic Protocols	139
8.1 SYNTHETIC PROTOCOLS PERTAINING TO CHAPTER 3	139
8.2 SYNTHETIC PROTOCOLS PERTAINING TO CHAPTER 4	145
8.3 SYNTHETIC PROTOCOLS PERTAINING TO CHAPTER 5	154
References	161
Appendix.....	175
List of Abbreviations	211
List of Figures	215
List of Schemes.....	219
List of Tables	221
Acknowledgements.....	223
List of Publications	225

1. INTRODUCTION

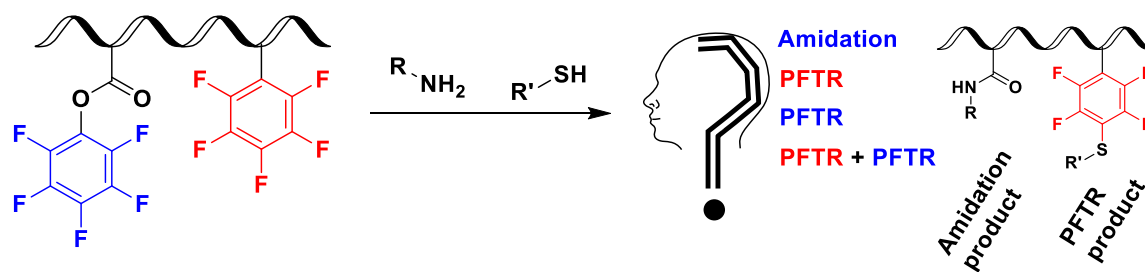
The future of nanotechnology and device miniaturization lies in the development of high resolution nanopatterns for applications in the field of nanolithography, selective separation membranes, and substrates for precise nanopatterning. Currently, certain top-down approaches such as dip-pen lithography (DPN)¹ and electron-beam lithography² are extensively used to achieve chemical patterning in the sub-50 nm range, but come with limitations such as high instrumentation and production costs. In this respect, block copolymers (BCPs) are a fascinating class of soft materials that have the ability to self-assemble forming ordered phase-separated nanostructures with feature sizes as small as 5 nm.³ Capitalizing on the capabilities of BCPs, the central concept of the current work revolves around fabrication of functional nanostructured materials using BCPs for patterned surface immobilization. The key to obtain materials with defined morphologies and periodicities lies in understanding the principles of BCP self-organization with respect to both their synthetic and physicochemical properties. In view of this, reversible-deactivation radical polymerization (RDRP) techniques provide access to numerous chemical as well as architectural diversities that are important handles to tune the morphology of phase segregation.



Scheme 1.1. Strategy employed in this thesis for the fabrication of functional nanomaterials for patterned immobilization using BCPs.

Following this, the presented work can broadly be divided in two parts: (i) modular synthetic approach towards the synthesis of functional homo- and block copolymers, and (ii)

fabrication of functional nanostructured materials such as ‘patchy’ nanoparticles and porous membranes using functional BCPs. The strategy used to achieve the aforementioned goals in this thesis is represented in Scheme 1.1. This strategy is unique as BCPs already known to phase separate are equipped with small amounts of reactive functional groups, thereby retaining the properties of the backbone polymer. We envisage that the self-assembly of such functional BCPs will lead to nanopatterned surfaces that possess chemically heterogeneous reactive domains. These ordered functional anchors can further be used for immobilization of (bio)molecules in close proximity.



Scheme 1.2. Orthogonality problem addressed to obtain functional BCPs

To achieve this, a large part of this thesis deals with the synthesis of libraries of functional BCPs based on poly(methyl methacrylate)-*block*-polystyrene (PMMA-*b*-PS) and polystyrene-*block*-polyisoprene (PS-*b*-PI). Different reversible deactivation radical polymerization (RDRP) techniques have been employed to obtain the precursor BCPs. Further, either a simple well-known post-polymerization modification (PPM) approach for the PMMA-*b*-PS system, or direct copolymerization with functional comonomers for PS-*b*-PI were employed to incorporate functional handles. For the PPM approach, two main chemistries, namely *para*-fluoro–thiol substitution reaction (PFTR) and activated ester-amine reaction (amidation) were exploited (Scheme 1.2). Within this framework, the synthetic challenges to obtain well-defined functional BCP precursors possessing versatile functional anchors for further modification has been addressed.

The second section of this thesis focusses on the self-organization of the functional BCPs to obtain different nanostructured particles. A detailed study to understand the influence of various parameters such as the nature of the functional groups and the method of preparation of the nanoparticles has been conducted. This allowed for general conclusions to be

drawn regarding their influence on the morphologies of phase separation in the nanoparticles. Such functional nanostructured nanoparticles can be used for precise chemical patterning with molecules of interest in an orthogonal fashion on the same substrate. Apart from nanoparticles, nanoporous membranes derived from BCPs are desirable materials for selective separation owing to their tunable pore sizes and the possibility of selective functionalization. In this direction, a BCP possessing a cleavable junction between the two blocks to create pores has been introduced. This method is highly versatile as the choice of monomers for the BCPs, their molar masses as well as incorporation of functional anchors can be tailored to obtain the desired functional porous membrane.

Finally, novel photoreactive polymers have been developed to use them as tools to study the pH change that occurs during inflammation. A novel near-IR cleavable photoacid and photobase generator (PAG and PBG, respectively) has been designed to firstly be incorporated into polymeric scaffolds that act as carriers. Furthermore, their ability to undergo photolysis and in turn release or catch protons has been studied. Such functional polymers can be modified further for use in targeted delivery to sites of inflammation to better understand of the underlying mechanism of inflammation.

2. THEORETICAL BACKGROUND

The theory behind all the concepts, methods, and instrumentations used in this thesis is dealt with in this chapter. Firstly, an introduction into the synthetic strategies employed for the synthesis of functional copolymers and block copolymers (BCPs) are described, drawing a comparison between free radical polymerization (FRP) and reversible-deactivation radical polymerization (RDRP) techniques. In the next section, post-polymerization modification (PPM) as a versatile and robust technique to obtain a library of functional BCPs is outlined. Further, the theory of microphase separation of BCPs both in bulk and in solution, laying focus on the latter, is detailed. Lastly, important analytical methods used for analyzing nanostructured nanoparticles are explained.

2.1 Block Copolymers (BCPs)

Block copolymers are a specific class of copolymers, in which chemically distinct monomer units are grouped together and covalently attached to each other at junction points along the polymer chain. Figure 2.1 shows some of the BCP architectures, which can be categorized into linear, branched (graft and star BCPs), and cyclic architectures. The advancement in several polymer synthetic strategies such as reversible-deactivation radical polymerization (RDRP), along with simple and robust post-polymerization modification (PPM) techniques has allowed for the synthesis of precise BCPs with tailored architectures. One of the ubiquitous features of BCPs is their ability to undergo microphase separation to form a wide range of nanoscale ordered structures. Due to this fascinating feature, BCPs have been a popular topic of interest for several decades. Apart from this, BCPs are being extensively used for fabricating advanced materials such as thermoplastic elastomers, porous materials, nanostructured nanoparticles, etc. As the synthesis of defined BCPs and their phase separation behavior contributes a large part of this thesis, the following sections in this chapter describe the various methods used for BCP synthesis followed by a detailed discussion about BCP phase separation and their applications.

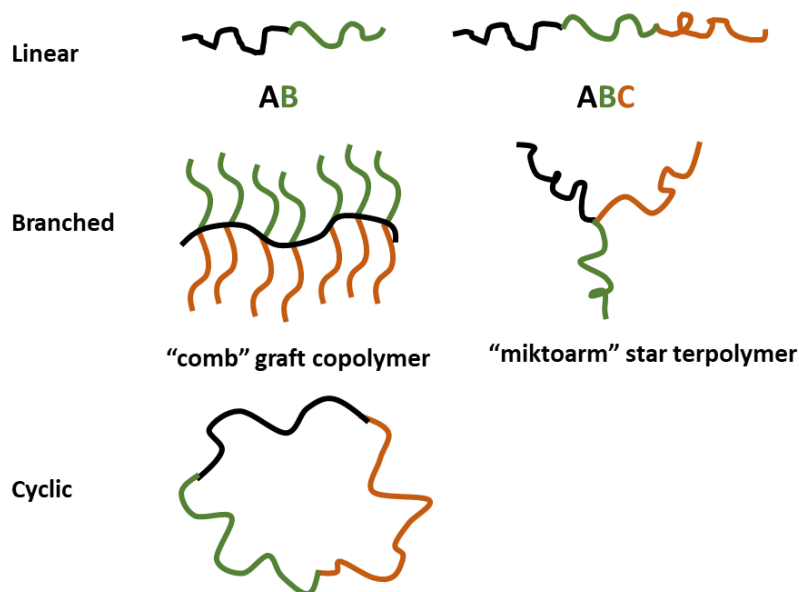


Figure 2.1. Classification of different BCP architectures, where A, B, and C represent a distinct monomer.

2.2 Free Radical Polymerization (FRP)

The use of radical polymerization (RP) in industry⁴ to produce commercial polymers originates from several unique characteristics that differentiate it from other polymerization processes like step-growth and ionic polymerizations. Conventional FRP has certain advantages over other polymerization processes as it does not require rigorous process conditions and can be used for the (co)polymerization of several vinyl monomers. It is much less sensitive to the effects of impurities and more tolerant to functional groups. The mechanism of FRP consists of three fundamental steps - *initiation*, *propagation*, and *termination*:

Initiation: This step involves two processes, namely, the decomposition of the initiator to produce free radicals and the addition of a monomer to the primary radical $R\cdot$ to yield the chain radical, which is called the initiation. Among other methods, the radicals are commonly produced either by thermal or photochemical decomposition of organic peroxides or azo/diazo compounds. The efficiency of the radicals to initiate chains can be estimated by comparing the number of initiators decomposed to that of the polymer chains formed as follows:

$$R_i = d[M \bullet]/dt = 2 f k_d [I]$$

where only a fraction f of the initiator initiates the polymerization. Consequently, the rate of initiation is proportional to the initiator concentration $[I]$ and its efficiency f , as well as k_d is the rate constant for initiation.

Propagation: During this step, the growth of polymer chains occurs by successive addition of the monomers. In general, it is assumed that the radical reactivity is independent of the chain length of the growing polymers, which means, all the propagation steps have the same rate constant. Therefore, the rate of polymerization equals the monomer consumption in the propagation step. Since both the monomer M and the growing polymer chain $M \bullet$ are involved in propagation, the rate constant k_p is proportional to both and described as below:

$$R_p = -d[M]/dt = k_p [M] [M \bullet]$$

Termination: Termination occurs when pairs of radicals react with each other and annihilate their activities. This can occur via combination or disproportionation. In the former case, two growing polymer chains combine to form a single, non-reactive polymer chain, while in the latter case a hydrogen is transferred from one radical to another resulting in two polymer chains, one with a saturated chain end and another with an unsaturated chain end. Both types of termination are combined into one rate equation as:

$$R_t = -d[M \bullet]/dt = 2 k_t [M \bullet]^2$$

Although FRP is ranked among the most important polymerization techniques for industrial production of polymers, it bears limitations such as poor control over some of the key elements of the process that do not allow for the formation of well-defined polymers, with control over their molar masses, dispersities, chain architecture, composition, as well as site specific functionality. “Living” polymerization on the other hand provides such control,⁵ leading to unique opportunities in material design. The development of functional polymers with well-defined structures opens the door to improving the properties of materials currently available and developing new materials that precisely meet the targeted properties.

2.3 Reversible-Deactivation Radical Polymerization (RDRP)

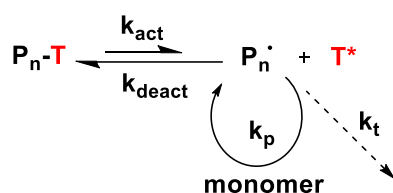
Radical polymerization (RP) is still extensively used for the industrial production of polymers, but classical RP does not allow for the synthesis of polymers with designer architectures or with predetermined narrow molar mass distributions. This situation started to change dramatically in 1982 with the seminal work of Otsu,^{6,7} who then proposed a reversible deactivation of the growing chains as one of the first existing theories in the field of RP. Since then, a plethora of such controlled radical polymerization (CRP) techniques, or now referred to as RDRP, are available. The underlying concept is that the growing polymer chains are regularly reverting to a dormant form and the overall period of chain growth of an individual propagating chain is now extended to a few hours from ~ 1 sec in conventional RPs. At any given instant, only a small fraction of chains are growing, but as long as the interconversion between the active and dormant species is faster than the propagation, all chains grow at the same rate. Nonetheless, it is important to note that even in such a polymerization where chain termination and irreversible chain transfers are reduced to a very low level, they are not completely absent.

The extension of the lifetime of the propagating species relies on establishing a dynamic equilibrium between a low concentration of active propagating chains and a predominant amount of dormant chains that are incapable of propagation or termination. This renders the polymerization “controlled”.^{8,9} Therefore, an ideal RDRP should exhibit the following: (i) a linear evolution of $\ln((1/1-\text{conversion}))$ with time which would account for a constant radical propagation concentration, (ii) a linear increase of the molar mass (M_n) with monomer conversion, (iii) low dispersities, (iv) a quantitative α and ω end functionalization, and (v) the possibility to further grow the polymer chain on addition of additional monomers finally enabling the synthesis of BCPs.¹⁰

Although several RDRP techniques are now established, this chapter deals with the three most prominent ones, nitroxide-mediated polymerization (NMP), atom-transfer radical polymerization (ATRP) and reversible addition-fragmentation chain-transfer polymerization (RAFT).

2.3.1 Nitroxide-Mediated Polymerization (NMP)

NMP is historically the first, and perhaps the easiest of the three RDRP techniques. It is a process where the dynamic equilibrium (described in the previous section) and hence, a control over the polymerization is achieved by persistent radical effect (PRE).¹¹ It is based on a thermally controlled reversible termination mechanism between the growing propagating macroradical and a nitroxide, which acts as the controlling agent, to generate a macroalkoxyamine as the predominant species. This dormant functionality then generates back the propagating species and the nitroxide by a simple homolytic cleavage. When the latter is chosen wisely, the activation-deactivation equilibrium is established (Scheme 2.1)



Scheme 2.1. Activation-deactivation equilibrium in NMP. The thermal dissociation of dormant species (k_{act}) ensures a low concentration of radicals.

Consequently, two types of initiating systems exist: (i) *bimolecular system* where a classical thermal initiator like 2,2'-azobisisobutyronitrile (AIBN) and a separate stable free nitroxide like 2,2,6,6-tetramethylpiperidinyl-1-oxy (TEMPO) is used,¹² and (ii) *one component system* where unimolecular initiator alkoxyamine is used.¹²⁻¹⁴ The bimolecular system bears an advantage that conventional RP processes can be used with only addition of the nitroxide species, but the activation-deactivation equilibrium is now shifted towards the dormant species due to an excess of the free nitroxide and thereby decreasing the polymerization rate. Yet another problem of the bimolecular system is that the radical initiator has an efficiency (f , described earlier) less than 1, and an exponentially decaying decomposition. These problems are circumvented using a unimolecular initiating system due to its structure, where a 1:1 ratio of the initiating radical and nitroxide is released after dissociation, which is rather fast compared to the former system. Among the several nitroxides/alkoxyamines commonly used (Figure 2.2), MAMA-SG1,¹⁵ also known as Blocbuilder™, has been used as the alkoxyamine for the synthesis of BCPs discussed in

Chapter 4. This MAMA-SG1 has a high dissociation rate coefficient and, in addition, contains a carboxylic acid group, which could be further transformed offering numerous possibilities to produce complex macroarchitectures.

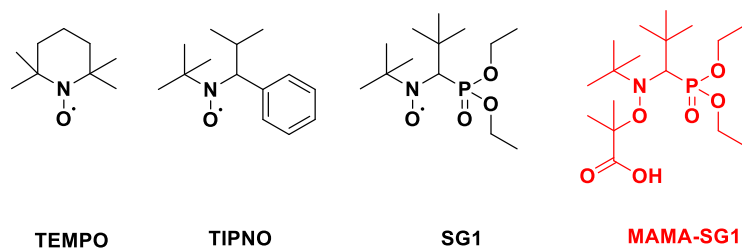


Figure 2.2. Structure of various nitroxides for a bimolecular system (black) and of an alkoxyamine for a unimolecular system (red) used as controlling agents in NMP.

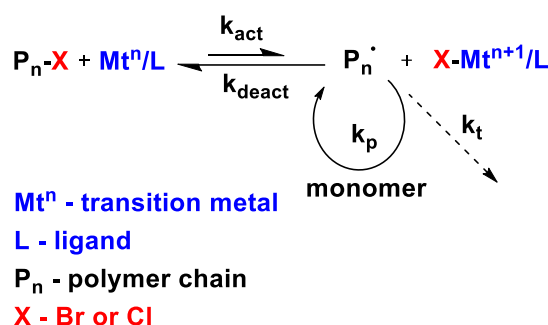
Despite all the intensive research carried out in the last 30 years in academia and industry, several issues limit the exploitation of NMP for commercial use. Some of these issues are the slow polymerization rates, insufficient availability of commercial NMP controlling agents, low molar masses ($< 150 \text{ kg mol}^{-1}$), and restriction in usage of a wide variety of monomers, although some progress has been made recently.

2.3.2 Atom-Transfer Radical Polymerization (ATRP)

ATRP is arguably the most extensively used RDRP techniques used for building complex polymer architectures with high degree of precision. It was first independently reported by Matyjaszewski,¹⁶ Sawamoto,¹⁷ and Percec.¹⁸ It can be run with a large range of monomers (with the exception of acids) using relatively accessible initiators in a range of temperatures from 0 °C and above.

ATRP is based on an electron transfer process, where, the (pseudo)halogen is transferred between a dormant species (an alkyl halide or macromolecular species, R-X or P_n-X) and a transition metal complex in the lower oxidation state (Mtⁿ/L, activators). This in turn results in the formation of propagating radicals (P_n•).¹⁹ The metal complex in a higher oxidation state (Mtⁿ⁺¹/L, deactivators) is coordinated to a ligand (Scheme 2.2). The deactivator then reacts with the propagating radical in a reverse reaction to form the dormant species and the activator again. Consequently, in ATRP, which is controlled by the equilibrium

between the propagating radicals and dormant species, the equilibrium is strongly shifted towards the latter ($k_{\text{act}} \ll k_{\text{deact}}$).²⁰



Scheme 2.2. ATRP equilibrium showing transition metal activation (k_{act}) of a dormant species with a radically transferable atom.

Among several transition metals such as Ru, Fe, Mo, Os, Cu is the most commonly used as the metal in the redox-active transition metal complexes $\text{Cu}^{\text{I}}/\text{L}$ and $\text{X-Cu}^{\text{II}}/\text{L}$. The choice of this metal-ligand complex²¹ has a strong influence on the activation-deactivation constant (K_{ATRP}) in addition to temperature,^{22,23} pressure^{24,25} and solvent²⁶ (K_{ATRP} is directly proportional to the solvent polarity). For example, the ideal catalyst for ATRP of less reactive monomers or used at lower concentration should have a large value for K_{ATRP} i.e., large k_{act} . Further, k_{act} increases with temperature and activation energy is higher for less reactive R-X and Cu-ligand complexes.²² A study on the effect of pressure showed negative value of activation for ATRP making it more feasible at higher pressures.²⁴

Overall, ATRP is a versatile method for the synthesis of several functional (co)polymers and BCPs with precise control over their molar mass, dispersity, chain end functionality and fidelity. Nonetheless, a prerequisite for precise synthesis of such polymers is an accurate understanding of the mechanism through detailed structure-activity correlations and effects of several parameters such as temperature, solvent, pressure, etc.

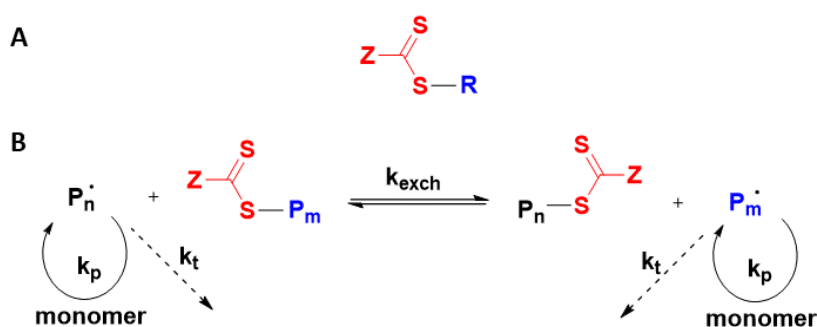
2.3.3 Reversible Addition-Fragmentation Chain-Transfer Polymerization (RAFT)

Since the first report of RAFT polymerization in 1998,^{27,28} it has grown to be one of the most useful techniques to prepare complex polymers. Recently, it has gained popularity over NMP and ATRP owing to its wide tolerance to functional monomers compared to

2. THEORETICAL BACKGROUND

NMP and ATRP, while having an easy experimental set-up compared to that of ATRP. Its attraction lies in the fact that it is a degenerative transfer system where there is ideally no change in the overall number of radicals during the activation-deactivation process, unlike that of NMP and ATRP.

A schematic representation of a typical RAFT is depicted in Scheme 2.3 A. In the RAFT mechanism, following the activation step (forming radical species from the radical initiator), the radical species adds to the RAFT agent (chain-transfer agent, CTA) to enter an equilibrium between the active and the dormant species (Scheme 2.3 B). The basis of RAFT mechanism seen from the chain transfer step are degenerate as they involve a reversible transfer of the chain end group (typically a thiocarbonylthio group, $Z-C(=S)S-R$) between the dormant chain (macroCTA) and the propagating radicals.



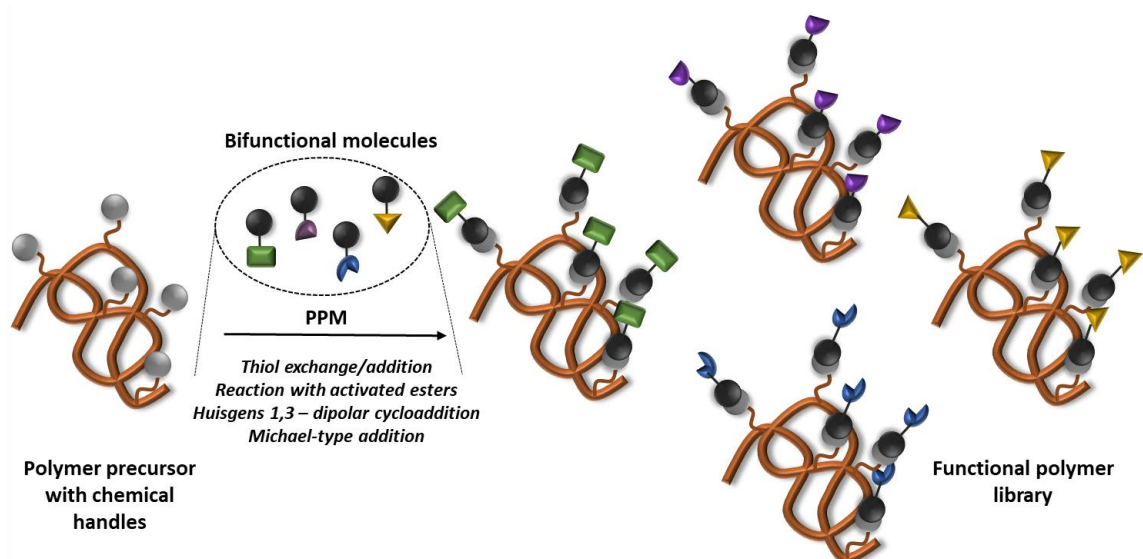
Scheme 2.3. (A) General structure of a RAFT agent. (B) Equilibrium between the active and dormant species in a RAFT process.

The overall RAFT process consists of the monomer insertion between the R (α chain end) and the Z (ω chain end) groups of the CTA. It is important to note that unlike in the other RDRP systems, the radical initiator is a key requirement in RAFT as it allows for the tuning of the system with respect to the polymerization rate and the number of fraction of living chains under well-chosen polymerization conditions. Although bimolecular termination directly corresponds to the number of radicals, such an event in a RAFT process does not lead to the loss of “livingness” of a chain end, but the number of chains bearing the thiocarbonylthio end group remains independent of the extent of termination.

responsible for the reactivity of the C=S towards radical addition, the R group affects the RAFT process through radical addition to the CTA, subsequent fragmentation (requires to be a good leaving group) and finally propagation. In summary, for an optimal RAFT system, one requires a high rate of radical generation and/or a solvent-induced acceleration. Additionally, a higher polymerization rate allows for shorter polymerization times or lower initiator amounts in order to reach higher conversions.^{31–36}

2.4 Post-Polymerization Modification (PPM)

As discussed in Section 2.3, RDRP has paved the path for the synthesis of a wide array of polymers with targeted molar masses, narrow molar mass distributions, with a rich variety in functionality and defined architectures like BCPs, gradient and graft copolymers, and stars. With this, RDRP has brought tremendous focus to the synthesis of BCPs, which due to the covalent attachment of two (or more) distinct segments gives rise to a variety of intriguing properties and applications. Consequently, there has been a huge demand for the synthesis of libraries of BCPs bearing several discrete functionalities. Post-polymerization modification (PPM) is a robust technique based on the homo- or copolymerization of monomers bearing chemoselective handles that do not polymerize themselves, but can quantitatively be converted to a broad range of functional handles in a subsequent step (Scheme 2.4). The viability of such a method arises from the excellent conversions that are achievable under mild conditions, the functional group tolerance as well as the orthogonality of the PPM reactions.³⁷



Scheme 2.4. Synthesis of functional polymer libraries by post-polymerization modification.

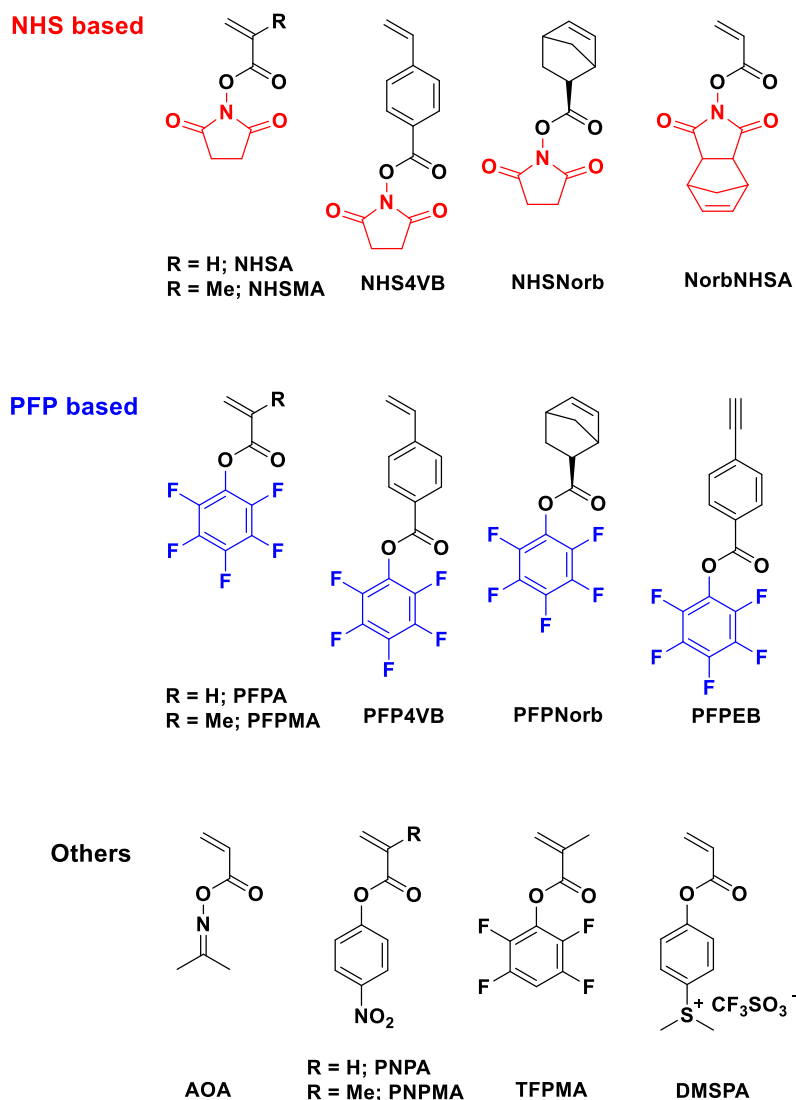
Subsequently, the emergence of RDRP gave rise to the discovery and/or revival of various chemoselective coupling reactions as well as substitution reactions such as azide – alkyne cycloaddition (AAC),^{37,38} thiol-addition,^{39–42} Michael-type addition,^{43,44} nucleophilic active ester-amine exchange,^{45–51} Huisgen 1,3- dipolar cycloaddition^{37,52–56} etc. Together, RDRP and PPM have expanded the platform for the exploitation of their combined use to obtain various functional polymers. In particular, activated ester-amine conjugation chemistry for the preparation of functional polymers has been used during the course of this thesis, taking advantage of the wide availability of natural and synthetic amines. In addition, owing to the biological, clinical, environmental relevance, and the ability of thiols to undergo various reactions,³⁹ a particular type of thiol-substitution reaction, *para*-fluoro thiol substitution reaction (PFTR) was exploited. Consequently, these two PPM tools have been discussed in the following two sections in detail.

2.4.1 Activated Ester-Amine Substitution

The synthesis as well as the PPM of polymers containing activated esters was pioneered by Ferruti⁴⁷ and Ringsdorf⁴⁶ in the 1970s. Active esters are classical reactive groups and yet remain one of the most reactive groups for PPM because their reaction with amines proceeds at room temperature to 100% conversion leading to the corresponding amides.

2. THEORETICAL BACKGROUND

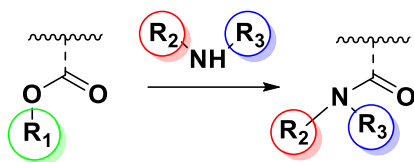
Scheme 2.5 represents a selection of useful active ester monomers that are used for the synthesis of functional polymers.



Scheme 2.5. Collection of a few activated-ester monomers. *N*-hydroxy succinimide acrylate (NHSA), and *N*-hydroxy succinimide methacrylate (NHSMA),^{45–48,57–60} *N*-succinimidyl 4-vinylbenzoate (NHS4VB),^{48,61,62} *N*-hydroxysuccinimidyl 5-norbornene-2-carboxylate (NHSNorb),^{63–66} endo-*N*-hydroxy-5-norbornene-2,3-dicarboxyimide acrylate (NorbNHSA),⁶⁷ pentafluorophenyl acrylate (PFP) and pentafluorophenyl methacrylate (PFPMA),⁶⁸ pentafluorophenyl 4-vinylbenzoate (PFP4VB),^{50,69,70} pentafluorophenyl 5-norbornene-2-carboxylate (PFPNorb),⁷¹ pentafluorophenyl 4-ethynylbenzoate (PFPEB),⁷² acetonoxime acrylate (AOA),^{73,74} *p*-nitrophenyl acrylate (PNPA), *p*-nitrophenyl methacrylate (PNPMA),^{75,76} 2,3,5,6-tetrafluorophenyl methacrylate (TFPMA)⁷⁷ and 4-acryloxyphenyldimethylsulfonium triflate (DMSPA).⁷⁸

In general, amines are reacted with the polymers containing activated ester comonomers owing to their good nucleophilicity compared to alcohols, for example, providing selectivity without the need for protecting groups. The polymerization of the above mentioned activated ester monomers gives rise to functional polymer precursors which can then be modified further by PPM by reaction with amines (Scheme 2.6).

Among the NHS based monomers, NHSA and NHSMA are most commonly used to prepare side chain NHS ester based polymers. The drawbacks of such a polymer system would be the limited solubility of the polymers in solvents like DMF and DMSO and unexpected side chain reactions taking place during the aminolysis step.⁷⁹ The solubility problem can be solved by copolymerization with other monomers or a better alternative to combat both problems would be replacing the NHS ester with other activating groups, such as pentafluorophenyl (PFP) ester groups as shown by Theato and co-workers.^{49,71}



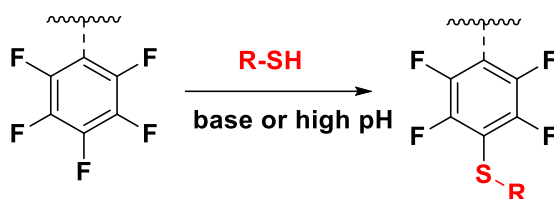
Scheme 2.6. PPM by activated ester-amine chemistry.

Consequently, after NHS ester monomers, PFP ester monomers are next most exploited monomers that can be homo- or copolymerized by various RDRP techniques. Generally, PFP ester (co)polymers are more reactive to amines compared to their NHS ester analogues, and their acrylates are more reactive than the respective methacrylates.⁸⁰ Apart from showing reactivity to a range of amines,^{50,80} some PFP ester monomers like PFPMA also help in the improvement of the physical properties of a polymer, for example, the glass transition temperature of methyl methacrylate (MMA) by copolymerizing it with PFPMA.⁸¹ Barz and Zentel described the synthesis of water-soluble, biologically relevant hydroxypropyl methacrylamide (HPMA) based (co)polymers by the PPM of PFPMA with 2-hydroxypropyl amine.⁸²⁻⁸⁴ Another interesting property of PFPMA based copolymer was recently reported in our group regarding the reactivity of its fluorine atoms towards thiols in a substitution reaction, while retaining its reactivity towards amines as an activated ester in certain cases.⁸⁵ Unequivocally, it can be said that PFP ester based homo- and copolymers

are extremely useful for PPM to obtain new novel functional polymers, and especially worthwhile as they are often fully orthogonal to other click chemistries (like PFTR), making them extremely powerful synthetic handles.

2.4.2 *Para*-Fluoro –Thiol Substitution Reaction (PFTR)

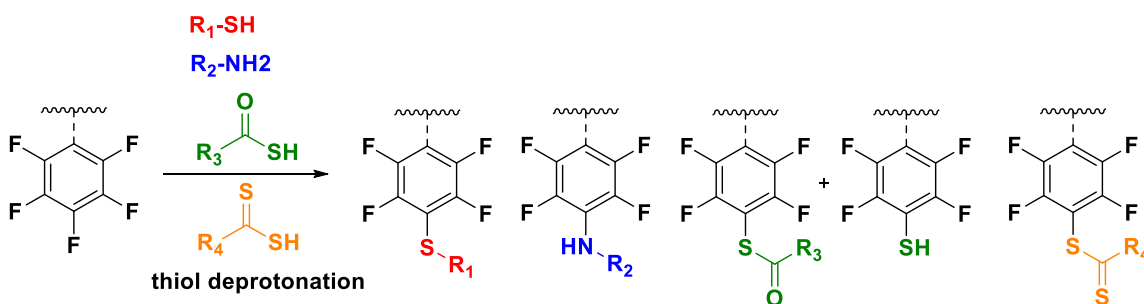
Thiols are an important class of synthetic reagents due to their large commercial and synthetic availability, biological relevance as well as their ability to undergo several thiol-X ligations. The three most widely studied reactions of thiols are radical thiol-ene, and thiol-yne additions, as well as Michael addition.^{42,86–90} Recently, another thiol-based ligation has gained popularity, namely, the *para*-fluoro –thiol substitution reaction (PFTR), wherein the *para* fluorine atom of a pentafluorophenyl (PFP) moiety undergoes nucleophilic substitution by thiols (Scheme 2.7).



Scheme 2.7. Schematic representation of PFTR on PFP-based moieties.

PFP moieties are particularly interesting as the aromatic ring is stable during (radical) polymerizations, and undergoes PFTR exclusively in the *para* position under mild conditions due to its large activation from its *ortho* and *meta* fluorine neighbours.^{91,92} It is important to note that this reactivity holds true for aliphatically connected PFP groups, like pentafluorobenzyl derivatives, but differs for PFP esters.⁹³ Combining two such PFP based molecules, namely 2,3,4,5,6 pentafluorostyrene (PFS) and pentafluorophenyl methacrylate (PFPMA) incorporated as comonomers in a BCP, we recently reported the feasibility of performing amidation using amines on PFPMA and PFTR on PFS in an orthogonal fashion. Interestingly, as a first report, we could identify the reaction of *para* and *meta* fluorine of PFPMA (an activated ester with a carbonyl connection to PFP) towards PFTR even faster than PFS (aliphatic connection to PFP).⁸⁵

In the field of polymer chemistry, although polyPFS homo- and copolymers have been extensively exploited as handles for PFTR, polyPFS homopolymer is largely insoluble in most polar solvents⁹⁴ limiting its versatility. Addressing this concern, Roth and co-workers reported the synthesis of several PFP-based methacrylic monomers that were polymerized by RAFT polymerization and further subjected to PFTR with a variety of thiols.³⁹ Nonetheless, as PFS-based homo- and copolymers still remain largely useful to conduct mechanistic investigations of the underlying processes, our group also demonstrated the orthogonality of PFTR with thiol-ene type addition, where the former requires a nucleophile while the latter follows a radical mechanism.⁹⁵ Although it is seen that all PFTRs are carried out with the polymers in organic solvents like DMF, we recently achieved the PFTR in aqueous media, wherein high pH was used for thiol deprotonation unlike in a classical PFTR where a base is used for the same purpose.⁹⁶ Lastly, with respect to the reactivity of *para* fluorine of PFP containing polymers towards *para* fluoro substitution reactions, apart from thiols, it can also undergo substitutions with other nucleophiles such as amines, alcohols, and carbonylthiolates (Scheme 2.8).⁹⁷



Scheme 2.8. General overview of the *para*-fluoro substitution reactions of PFP based homo- or copolymers with various nucleophiles.

Finally, PFTR is a highly versatile modular ligation owing to high yields, modularity, chemoselectivity, formation of stable products and large scale purification in most cases. As a result of this, it has found applications in various fields. For example, it has been used to form cross-linked polymers,⁹⁸ in porphyrin chemistry,⁹⁹ and for side-chain functionalization of cyclic polymers to form hyperbranched polymers.¹⁰⁰ It was also used for the synthesis of glycopolymers^{101–104} because the formation of *S*-glycosidic bond after PFTR is

stable towards enzymatic cleavage and to perform surface reactions.¹⁰⁵ Broadly, PFTR is used in the polymer chemistry to create novel polymers with improved properties.^{39,106–109}

2.5 Phase Separation and Self-Assembly of BCPs in Bulk

Self-assembly is the spontaneous arrangement of building blocks into larger structures that may have defined symmetry, long range order and complex architectures. For several applications such as photonics,¹¹⁰ and lab-on-a-chip technology in biosciences,^{111,112} etc., traditional lithographic techniques (*top-down approach*) are being extensively used in spite of the highly expensive mass production. Shrinking this patterning (from a few microns) with added chemical specificity down to sub 100 nm regime can be made possible with a *bottom-up approach*. This approach utilises the unique properties of different molecules to self-assemble and lead to complex structures, such as patterned surfaces with domains in the sub 100 nm range. Bottom-up fabrication method is considered superior to the top-down approach as it is typically more cost-effective and does not lay a limitation on the resolution that can be obtained.^{113,114} In this respect, BCPs are gaining popularity as their self-assembly into ordered, micro-phase separated nanoscale morphologies offers high spatial resolution.^{115,116} In order to get more complex functional systems for real world applications, both strategies could be integrated (Figure 2.4).¹¹⁷ Therefore, it is important to understand the theory behind BCP microphase separation.

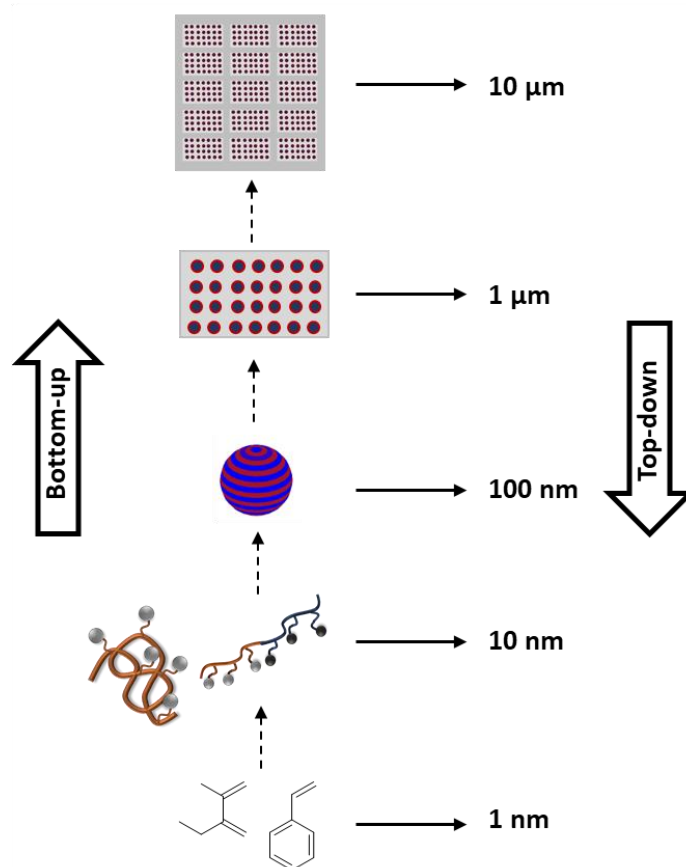


Figure 2.4. Various structure hierarchies from BCP systems.

2.5.1 Thermodynamic explanation of microphase separation

BCP consists of at least two chemically distinct polymer chains that are covalently linked at junction points. To understand the microphase-separation theory (MST), a simple diblock copolymer (diBCP) in its molten state was considered and the thermodynamic description was developed by Leibler in 1980.¹¹⁸ Considering such a system, only two relevant quantities are needed for the characterization of phase equilibria: (i) composition of the BCP (f) that describes the volume fractions of each block, (ii) the product χN , where, N = the degree of polymerization, and χ = the Flory-Huggins interaction parameter. Two important assumptions in addition are that all the chains in the diBCP system have the same N and that the BCP is monodispersed.

2. THEORETICAL BACKGROUND

In an A-B type BCP, the two species A and B reach an equilibrium density profile ρ_A and ρ_B which minimizes the free energy of the system. The energy of interaction of the different species is described in equation 2.1 as:

$$\alpha \rho_A \rho_B \equiv kT \chi \rho_A \rho_B \quad (2.1)$$

where α is the effective interaction parameter that is related to the energy of interactions between A-A (ϵ_{AA}), B-B (ϵ_{BB}) and A-B (ϵ_{AB}) as in equation 2.2.

$$\alpha = \epsilon_{AB} - \frac{1}{2} (\epsilon_{AA} + \epsilon_{BB}) \quad (2.2)$$

The two factors f and N are regulated through the polymerization stoichiometry and affect the translational and configurational entropy, while the magnitude of (the largely enthalpic) χ is determined by the selection of A-B monomer pairs and has a temperature dependence given by:

$$\chi = \frac{\alpha}{T} + \beta \quad (2.3)$$

where α and β are constants depending on the architectural constraints and composition of the BCP. On increasing the energy parameter χ (i.e., by lowering the temperature), a tendency to decrease the contact between A and B is seen in order to lower the contribution of the interaction energy parameter to the free energy (equation 2.1 and 2.3). But, this decreases the entropy of the system and thereby there is an increase in the free energy.^{119,120} Consequently, microphase separation in BCPs relies on the fact that the chemically distinct polymer chains induce thermodynamic incompatibility, which implies an unfavourable mixing enthalpy in combination with a small mixing entropy.

On the one hand, for $\chi = 0$ or positive, but sufficiently small, the entropy effects are dominantly favoring mixing, which means that the system exhibits an isotropic phase with the polymer chains A and B interpenetrating – such a phase is called the *disordered phase*. On the other hand, when the system is cooled or is made up of long chains such that χN is larger than a critical value, the enthalpic term (in equation 2.1) dominates and the BCP exhibits microphase separation or *order-disorder transition* (ODT). This implies that the thermal average of ρ_A ($\langle \rho_A \rangle$) and ρ_B ($\langle \rho_B \rangle$) are not uniform, which in turn means that there

are domains that are rich in phase A and others that are rich in phase B. Therefore, at all points, the product ρ_{APB} is low and hence the enthalpic term. A phase of the system in which a microdomain structure occurs is an ordered phase or a mesophase, and depending on the composition of the BCP (f), on the interaction parameter (χ) and temperature (T), several different mesophases can be observed (Figure 2.5). As polystyrene-*block*-polyisoprene (PS-*b*-PI) has been used during the course of the work in this thesis (Chapter 4), an experimental phase diagram of this system is represented in Figure 2.5 as reported by Bates and co-workers.¹²¹ It can be seen that the resemblance to the theoretical phase diagram is rather high.³

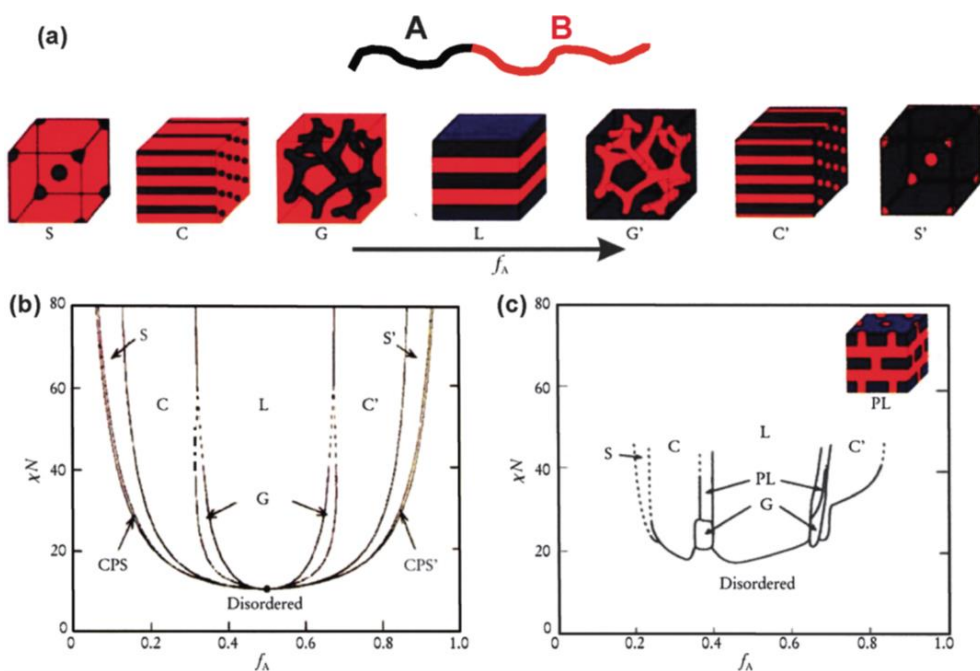


Figure 2.5. (a) Equilibrium morphologies of AB diblock copolymer (BCP) in bulk, where S and S' = bcc (body-centered-cubic spheres), C and C' = hcp (hexagonally packed cylinders), G and G' = bcc (bicontinuous gyroids), and L = lamellae. (b) Theoretical phase diagram predicted by self-consistent field theory (SCFT), based on the volume fraction (f) of the two blocks and χN where χ is the Flory-Huggins interaction parameter and N is the overall degree of polymerization, and CPS and CPS' = closely packed spheres. (c) Experimental phase diagram of polystyrene-*block*-polyisoprene (PS-*b*-PI), where f_A is the volume fraction of PI and PL is the perforated lamellae phase. Reprinted with permission from reference 121 from The Royal Society of Chemistry.

2.5.1.1 Explanation of the phase diagram

The phase diagram is separated into several regions (as seen in Figure 2.5) which is characterized by the relative stability of the microstructures and the dependency of the sizes of the microstructures (periodicity or domain sizes, L_0), on the overall molar mass of the polymer. Most BCPs exhibit ordered microdomain structures at lower temperatures but with increasing temperature the incompatibility of the components decreases. At a critical temperature, the order-to-disorder temperature (T_{ODT}), BCPs become ordered.^{118,119} The T_{ODT} depends on f , N , χ and the conformational symmetry of each block. For $\chi N \ll 1$, a BCP melt is disordered and the A-B interactions are sufficiently low. This regime is called the *weak segregation limit* (WSL). The BCPs showing this behavior are characterized by a widened interface and approaching this regime, thermotropic order-order transitions (OOT) are predicted. As $\chi N > 10$, nearly pure A and B domains are formed and this regime is the *strong segregation limit* (SSL). In this regime, the thermotropic OOT are not expected. The interaction energy associated with the A-B contacts is localized in the interfacial regions; the system minimizes the total area of such an interface by decreasing the energetically unfavorable contacts. To combine the above two segregation limits, the self-consistent mean field theory (SCFT) was developed.³

Between $\chi N = 10.5$ and 12.5 (WSL), L_0 is proportional to $N^{0.5}$. In the intermediate region, when $\chi N = 12.5$ to 95 , L_0 is proportional to $N^{0.72}$ and above this in the SSL, L_0 is proportional to $N^{0.67}$. Although the WSL area gives the smallest feature sizes or domain sizes, the thermodynamic driving force is small and there is a possibility of formation of disordered regions. On the other hand, the SSL could also be problematic in the use of such materials because the thermodynamic driving force for microphase separation is very strong and achieving equilibrium might require annealing techniques. In the region of the phase diagram where balance of intermolecular forces results in microphase separation as seen in Figure 2.5, when $f_A = f_B = 0.5$, lamellae (L) structures are formed. As f_A increases to 0.6 - 0.7 , a bicontinuous gyroid (bcg) phase of cubic symmetry is formed. It is important to note here that this phase has a narrow stable composition range, particularly in the SSL and intermediate segregation limits. At higher f_A values, a composition range exists where hcp arrangement is seen, where block B cylinders are in a matrix of A. Finally, block B adopts bcc spheres arrangement. As the gyroid structure is structurally complex to obtain and has

a narrow stability range, it has been less studied. It is nevertheless of interest for particular applications as it consists of two interpenetrating continuous networks of A and B. On the contrary, lamellar, hcp and bcc are extensively studied, and of those, lamellar structure is widely used for nanopatterning and material development as discussed later in this chapter.

2.5.2 Effect of BCP composition on microphase separation

One of the most important factors determining the phase separation morphology in BCPs is their composition. It is understood that the shape of the polymer/polymer interface varies with the chain lengths of both components of the BCP. As microphase separation occurs, the two blocks A and B of an AB BCP separate from each other to lower the interfacial energy. The degree of stretching depends on the volume fraction of one of the blocks with respect to the other. In the case of an AB symmetrical BCP (where the volume fractions of both blocks are equal), the AB interface is flat as seen in Figure 2.6 a. With increase in volume fraction of one of the components f relative to the other (i.e., f_A) and as the BCP starts becoming compositionally asymmetric, it is more likely to observe a curved interface because the A chains have to stretch significantly for the formation of a planar interface (Figure 2.6 b). In such a case, the conformational entropy loss of A is too high. Hence, 'A' chains expand along the direction that is parallel to the interface to gain the conformational entropy under a condition where the segment densities of A and B must be kept constant and must be the same as that of the bulk densities of the homopolymers. As a result of this, the interface becomes convex towards B (Figure 2.6 c). The effect of curvature becomes more pronounced as the composition of the BCP becomes more asymmetric and therefore, the morphological variations for a two-component BCP system is as shown in Figure 2.5 a.

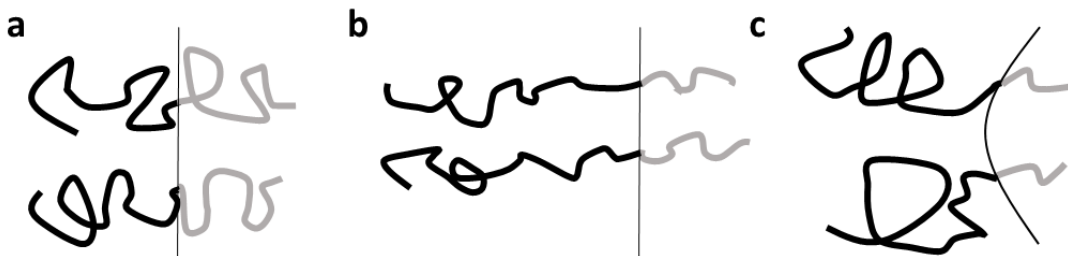


Figure 2.6. Schematic representation of chain conformations at the microphase separated state: a) flat interface from compositionally symmetric AB BCP system, b) an unstable flat interface when $f_A \gg f$, and c) a stable curved interface when $f_A \gg f_B$. The black line in all morphologies represents a part of the interface between the two blocks A and B of an AB BCP.

2.5.3 Effect of molar mass and dispersity on microphase separation

A wide variety of microstructure develops in BCP systems upon microphase separation (MS) as discussed previously. MS is a result of two effects that compete: (i) dissimilar blocks prefer to segregate due to their chemical incompatibility, and (ii) the spatial extent of phase separation is limited by the fact that the two incompatible segments are covalently bound. As a compromise of both these effects, periodic microstructures are observed. The scale at which this phase segregation occurs is directly related to the length of the polymer chains: the periodicity (L_0) or domain diameters smaller than 50 nm can be obtained.¹²² In general, L_0 is directly proportional to the molar mass,^{123,124} i.e., to obtain larger periodicity, the overall molar mass of the BCP must be increased. In BCP melts, the segregation effects are strong: when $0.3 < f < 0.7$, χN is of the order 10-15. For many monomer pairs, χ is approximately 0.1, so the microphase separation does not occur for chains where $N < 100$.¹¹⁸ Taking into consideration the formation of a simple microphase separated lamellae structures, where $f_A = f_B = 0.5$, the value of χN was simplified by Farrell *et al.* and determined as follows: for microphase separation to occur, χN should be greater than 10.4 arising from equation 2.4. Their simple approach is very similar to the more complex theories first developed by Leibler using SCFT.¹²⁵

$$1.19 (\chi_{AB} N)^{1/3} = (\chi_{AB} N) / 4 \quad (2.4)$$

Most BCPs are nowadays prepared by RDRP techniques. The resulting polymer architectures are not monodisperse. In view of this, it must be noted that the dispersities of the polymer has an effect on the periodicity.¹²⁶ This was demonstrated experimentally by Lynd *et al.* for two polymer systems poly(ethylene-*alt*-propylene)-*b*-poly(DL-lactide) (PL) and PS-*b*-PI. Typically, it was observed that increasing dispersities decreased $(\chi N)_{\text{ODT}}$ except when the dispersity is increased in a block comprising the majority of the diblock copolymer, wherein $(\chi N)_{\text{ODT}}$ then increased with the dispersity value.¹²⁶

2.5.4 Microphase separation in BCP/Homopolymer blends

A diBCP A-block-B at appropriate conditions undergoes microphase separation to form microdomain structures. Addition of a homopolymer hA or hB which is chemically equivalent or similar to one of the two blocks significantly influences the equilibrium structure.¹²⁷⁻¹²⁹ Such diBCP/hA or diBCP/hB blends exhibit both macro- and microphase separation structures. Certain parameters influence the phase separation behaviour: (i) the BCP composition [$f_A = N_A/(N_A + N_B)$, where N_A and N_B are the degrees of polymerizations of the two components A and B]; (ii) the concentration of the homopolymer ϕ_A and $\phi_B = V_{hA}$ or hB/V ; (iii) The ratio of N in the diBCP to $N_{h,A}$ or $N_{h,B}$ in the homopolymer (iv) the homopolymer molecular weight; and (v) temperature. When $N/N_h \ll 1$, macrophase separation is observed in addition to microphase separation ($N/N_h \geq 1$).

Let us consider a mixture of AB diBCP and homopolymer (hB) when $N_h \gg N$. In the strong segregation limit (SSL) long homopolymers must separate from the diBCP since an insertion of hB significantly increases the elastic energy of the block elongation.¹³⁰ In this case, the hB contribution (F_h) is as shown in equation 2.5.

$$F_h = \frac{\phi}{N_h} \ln \frac{1}{\phi} \quad (2.5)$$

The free energy is then calculated as:¹³¹

$$F_{ord} = \frac{1-\phi}{N} \sqrt[3]{\chi N} W(f, \phi) + F_h \quad (2.6)$$

where, F_{ord} is the free energy in SSL and W is the geometric factor which depends on the type of the ordered structure. Consequently, the period of the structure is given by:

$$R = \alpha N^{2/3} \chi^{1/6} W_2(f, \phi) \quad (2.7)$$

Various theories prove that bicontinuous phases are stable in the region $f = 0.56$ to 0.68 of the BCP compositions and homopolymer volume fractions between 0.18 to 1 .¹³² Likhtman *et al.* on the other hand predict that the bicontinuous phases are rather stable for homopolymer fractions of 0.33 to 0.4 .¹³⁰ They also prove that long homopolymer chains added to

the minority block of the BCP can induce morphological transformation from lamellar to bicontinuous structure or lamellar to cylindrical or cylindrical to spherical.

In a particular example PS-*b*-PI/PS or PI blend system,¹³¹ Floudas *et al.* arrived at the following conclusions: (i) only microphase separation takes place when < 25% PS or PI homopolymer is added to PS-*b*-PI, (ii) addition of the majority component of the BCP decreases the T_{ODT} (order-to-disorder transition temperature) due to the increase in the free energy of the ordered diBCP and a decrease in the disordered free energy, (iii) addition of the minority component of the BCP can decrease ($N > N_h$) or increase ($N < N_h$) the T_{ODT} , where the latter is a result of the decrease of the ordered diblock free energy on addition of the homopolymer, (iv) drastic changes occur in the periodicity and the formation of non-equilibrium structures with the addition of minority phase. Therefore, the compatibility between the two blocks of a BCP can be controlled by the addition of a small amount of homopolymer.

2.6 Self-Assembly of BCPs in Solution

As discussed previously, BCP self-assemblies are observed due to the energetic incompatibility of the two blocks as the covalent bond linking them prevents macrophasic separation. From BCP phase separation in melt to its phase separation in solution, the introduction of solvent increases the level of complexity for the self-assembly of BCPs in solution. For example, the self-assembly of A-B diBCP in a good solvent/non-solvent mixture involves six χ parameters, namely χ_{AB} , χ_{AG} , χ_{AN} , χ_{BN} , χ_{BG} , and χ_{GN} , where G represents the good solvent for both blocks and N the nonsolvent. The complexity increases with increasing number of components in the BCP solution.

The self-assembly of BCPs in aqueous media has largely been studied where water is used as the selective solvent for the formation of a wide variety of materials. Depending on the solubility of the blocks in water, the BCPs can be classified as amphiphilic,^{133,134} double hydrophilic¹³⁵ and double hydrophobic systems.¹³⁶ The self-assembly of extensively studied amphiphilic BCP systems are based on polystyrene-*block*-polyacrylic acid (PS-*b*-PAA), PS-*block*-polyethylene oxide (PS-*b*-PEO) and PS-*block*-polyvinylpyridine (PS-*b*-

PVP).^{137,138} Various morphologies such as spherical micelles, rods, bicontinuous structures, lamellae, vesicles, large compound micelles and vesicles (LCMs, LCVs), tubules, “onions”, or “eggshells” that are either thermodynamically induced or kinetically controlled can be obtained during the microphase separation of such asymmetric amphiphilic BCPs. Likewise, the phase separation behavior of double-hydrophilic BCPs in dilute or concentrated aqueous solutions have been studied leading to different morphologies.^{139,140} In these cases it was observed that even a small difference in hydrophilicity of the blocks resulted in the formation of various morphologies. Although both types of BCPs can lead to a plethora of morphologies and applications in various fields, the third variety of BCP containing two hydrophobic components is also widely studied. Chapter 4 further deals with the BCP phase separation of double hydrophobic BCP systems.

2.6.1 BCP self-assembly under confinement

BCPs can self-assemble in bulk, solution, and in thin films.^{3,119,141} As described in the previous section, microphase separation structures in bulk can be influenced by the volume fraction of both blocks and their incompatibility, among other parameters, to obtain various morphologies.^{3,119} This symmetry can be broken using confinement in one (1D), two (2D), and three dimensions (3D) in order to obtain novel morphologies and phase alignments not accessible in the bulk (Figure 2.7 a). Confinement in 1D in the form of thin films confined between two planar surfaces^{142,143} is one of the most widely studied system. In such a situation, the film thickness and the interfacial interactions act as the boundary conditions for confinement.^{144–146} 2D confinement has also been investigated theoretically^{147–149} and experimentally.^{150,151} Examples include the inner part of electrospun fibres¹⁵² and nanoimprinted trenches.¹⁵³

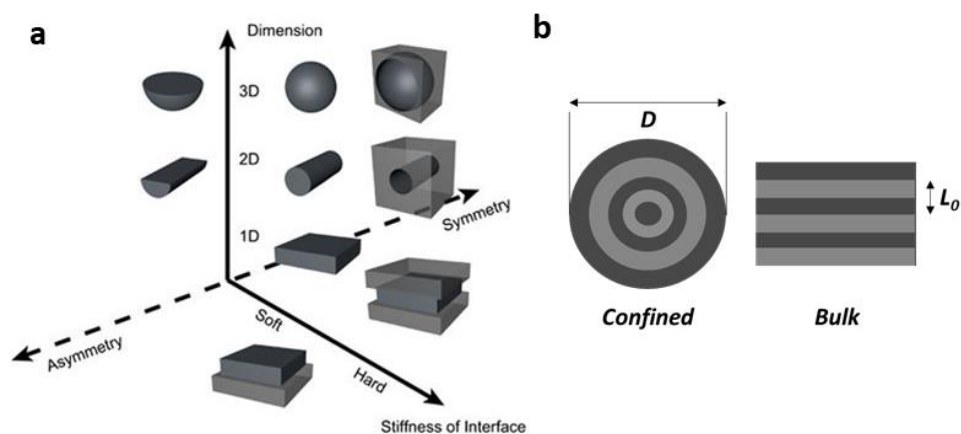


Figure 2.7. a) BCP self-assembly under 1D, 2D (fibers), and 3D confinement (particles) and their symmetry and interface stiffness. b) Comparing the definition of periodicity (L_0) of a phase separated structure (e.g., lamellae) in the bulk state and size D corresponding to the confinement space. Reprinted with permission from reference 154.

A few examples of 3D confinement spaces include spheres,^{155–157} inverted spheres,^{158,159} and more recently, hemispheres.^{160,161} 3D spherical confinement can be formed by several processes, for example, self-organised precipitation (SORP)¹⁶² to obtain different morphologies like onion-like, concentric cylinders among others.^{155,163–165} In this method, nano- or microparticles are prepared by the evaporation of the good solvent in which the BCP is initially dissolved from a mixture of good and non- solvents containing different *kinetically trapped morphologies*.^{155,162,166,167} To obtain the *thermodynamically favored morphology*, the sample can further be annealed by temperature¹⁶⁸ or by solvent.¹⁶⁹

2.6.1.1 Shape and size in 3D confinement systems

Spherical (spherical and ellipsoidal) and polyhedral (tetrahedron, cubic, etc.) are examples of 3D confinement as shown in Figure 2.8. In any confinement system, it is crucial to understand the size of the confinement. The periodicity of the domains in a phase separated structure is described as L_0 in the bulk phase, while the size of the confinement spaces in 3D is defined as D . To be able to assess the strength of confinement, D/L_0 is used as a tool for determination of the strength of the polymer frustration.¹⁷⁰ This is because the size of the confinement is normalized by the periodicity of the domains in the phase separated structure. In other words, a small value of D/L_0 indicates a strong frustration of the polymer

chains and *vice-versa*. The size of the phase separated structures in BCPs is solely thermodynamically driven as the polymer chains are covalently bound.¹⁷¹

The degree of confinement is weak if the value of D/L_0 is greater than 3 or 4, while it is strong when D is approximately equal to L .^{155,172} In the weak confinement as the size of the confinement space D is much larger than the periodicity of the original phase separated structure in the bulk phase, the morphologies are rather similar to that of the bulk state. Whereas, in the strong confinement, deviations in the phase separated structure from that of the bulk state are observed.

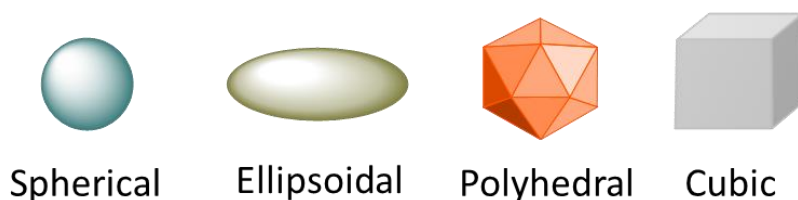


Figure 2.8. Selection of possible shapes for 3D confinement of BCPs.

2.6.1.2 Understanding the Interface in 3D confinement

In a system where the polymer chains are confined in a 3D environment, the interface such as air, solvent, or resin plays an important role in the phase separation behaviour of the polymer leading to different morphologies. If one considers a BCP made up of two polymeric chains A and B confined within a 3D matrix M, the interaction energy ϵ can change depending on the interaction between one of the components A or B and M (Figure 2.9). Chi *et al* have demonstrated various phase separated structures obtained using SCFT simply by varying the interaction energy.¹⁷³

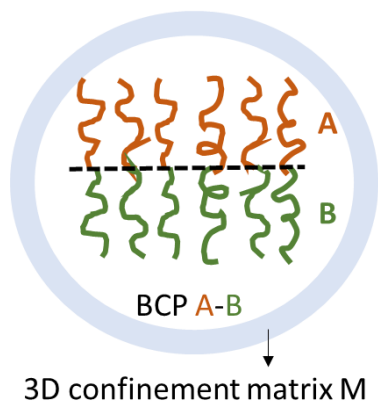


Figure 2.9. Interaction between the polymer chains A and B of a diBCP A-*b*-B and the matrix in a 3D confinement space.

If the BCPs are confined within hard matrices, the confinement size and the interface between the BCP and matrix are clearly defined. This concept was first demonstrated by Arsenault *et al.* using colloidal crystals and inverse opals.¹⁷⁴ Unlike hard matrices that cannot be deformed, polymers can also be confined within “soft” matrices that can be deformed and provide higher mobility for the polymer chains within the confinement. This also means that the shape of the interface may change between that of the polymer chains and the matrix in order to reduce the free energy. When the polymers are confined in “soft” matrices such as liquid or air, the interactions between the interface and the polymer chains can be controlled leading to various phase-separated structures. Therefore, by tuning the interface, different morphologies of phase separation of a BCP can be observed.

2.6.1.3 Fabrication of 3D confinement spaces for BCPs

Polymer nanoparticles produce 3D confinement spaces. Some of the methods to prepare polymer nanoparticles are aerosol,¹⁷⁵ emulsion and mini emulsion polymerization,^{176,177} solvent evaporation from emulsion droplets that contain polymer solutions,¹⁷⁸ and precipitation.¹⁶² Among them, as an example, using emulsification of BCP, droplets rich in polystyrene-*block*-poly(4-vinylpyridine) (PS-*b*-P4VP) BCPs were produced when a solution of this polymer in chloroform was added to water where the resulting particles were stabilized by a surfactant (Figure 2.10 a).¹⁷⁹ The resulting BCP nanoparticles showed axially stacked lamellae internal structures as seen in Figure 2.10 b.

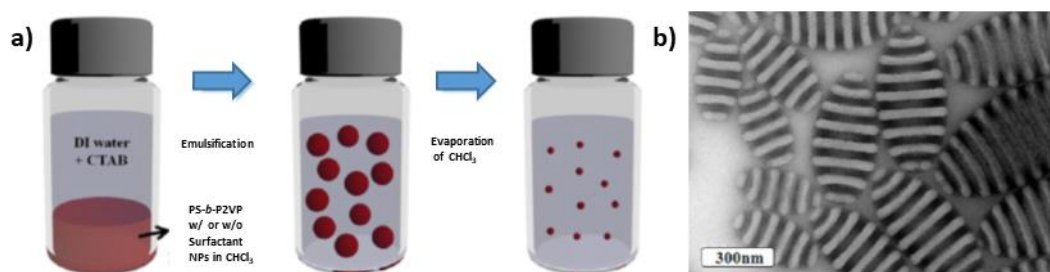


Figure 2.10. BCPs in 3D confinement. a) Schematic representation of preparation of PS-*b*-P4VP BCP colloidal particles. b) Transmission electron microscopy (TEM) image of BCP nanoparticles containing axially stacked PS and P4VP domains. Reprinted with permission from *J. Am. Chem. Soc.*, 2013, **135**, 6649–6657. © 2013 American Chemical Society.

Precipitation is yet another technique with which BCP particles can be prepared. In precipitation, the polymer is dissolved in a solvent and poured into a large excess of a poor solvent that is miscible with the good solvent by vigorously stirring the solution. By changing the stirring speed and the temperature of the poor solvent, polymer particles of the order of ten to hundreds of nanometers can be obtained. Nonetheless, preparing hydrophobic BCP nanoparticles has not been easy. In this respect, self-organised precipitation (SORP) is a versatile precipitation method wherein the BCP is dissolved in a good solvent for both blocks and a non-solvent is added dropwise into it followed by the evaporation of the good solvent.¹⁸⁰ Here, by changing the polymer concentration in the good solvent, the mixing ratio of good and poor solvent and the evaporation speed of the good solvent, polymer particles ranging from tens of nanometers to micrometers can be obtained. Nanoparticles of hydrophobic BCPs can be prepared in hydrophilic solvents as the interface between a hydrophilic solvent such as water and a hydrophobic BCP is stabilized by the absorption of oxonium ions on the hydrophobic surface.¹⁸¹ In general, precipitation is advantageous for the preparation of BCP particles as it does not require the use of surfactants for the stabilization of the particles. Using the aforementioned fabrication techniques, nanoparticles of BCPs with internally phase-separated nanostructures can be prepared.

Apart from the above mentioned methods, nanoparticles can also be prepared by electrohydrodynamic (EHD) co-jetting.¹⁸² Using this technique, different morphologies of phase-separation in the nanoparticles can be obtained by varying the properties of the polymer

solution, as well as EHD parameters that include the electric potential and the flow rate. This technique has been shown to be useful to prepare nano- and microparticles containing more than two compartments and several unique architectures.¹⁸³ Such multicompartment particles possess dissimilar materials in each compartment and combine orthogonal properties in the same particle allowing for precise surface modification to create surface patterns. Multicompartment particles with a combination of tailored physical and chemical properties for different applications is further discussed in Section 2.7.2.

2.6.1.4 Morphologies of BCPs in nanoparticles (3D spherical confinement)

As discussed in Section 2.6.1.1, 3D confinement may be weak or strong depending on the values of D/L_0 . The boundary between both confinements occurs at approximately $D/L_0 \approx 4$. The value of D/L_0 is important to determine the morphologies of phase-separated structures in the weak confinement regime too. Manners and co-workers demonstrated the presence of different morphologies of polystyrene-*block*-polybutadiene (PS-*b*-PB) copolymers with PS encapsulated in the 3D confinement. The particles were prepared by the emulsion method using pluronic (PEO-*b*-polypropylene oxide-*b*-PEO) as a surfactant. Although the microphase-separated structures are perforated lamellae in the bulk state, the TEM images inside the particles showed blends of particles with various sizes and different orientation of the frustrated phases proving the effect of D/L_0 on the morphologies.¹⁷⁴ As experimental methods can become difficult to observe complex morphologies, computer simulations (Monte Carlo) have also been performed to obtain predicted self-assembled morphologies of a symmetrical diBCP confined in spheres (Figure 2.11).¹⁷⁰

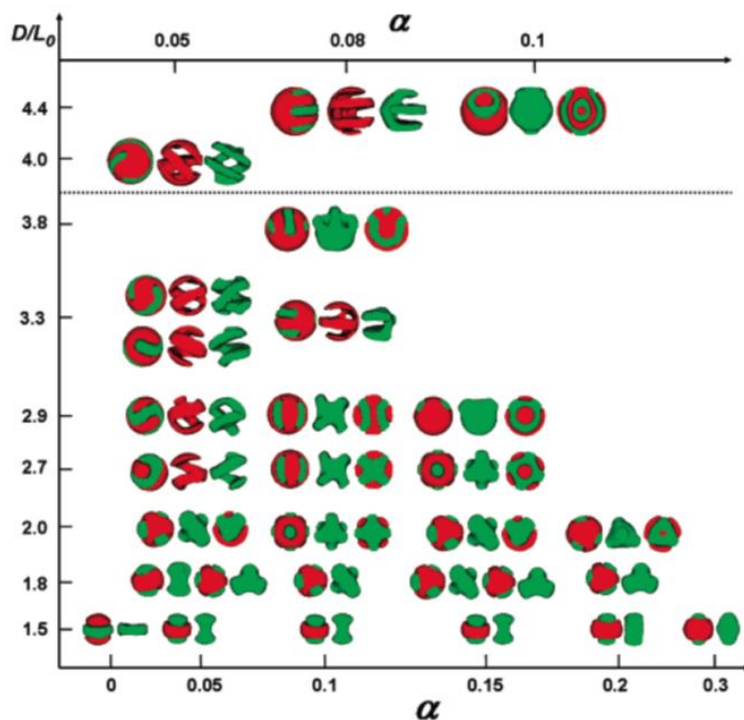


Figure 2.11. Self-assembled morphologies for symmetric diblock copolymers confined in spherical pores as functions of the ratio D/L_0 and α , where for each concentric-spherical lamellar morphology, only a cross-section view is given and the boundary of the concentric spherical lamellae is given with two identical structures at each D/L_0 value. In each Figure, the morphologies are corresponding to the lower α coordinate for $D/L_0 < 3.8$, and corresponding to the upper R coordinate for $D/L_0 > 3.8$. Red parts represent the component “A” of the BCP while the green that of component “B”. Reprinted with permission from reference *Macromolecules*, 2007, **40**, 9133–9142. © 2007 American Chemical Society.

The above simulation was performed for a symmetrical diBCP of the type A_6B_6 , where the number of monomers in a polymer chain $N_A = N_B = 6$, volume fraction of each of the blocks $f_A = f_B = 0.5$, total monomer concentration at 85% and this model forms lamellae structures in bulk with $L_0 = 9.33$. α represents the surface preference of component “A” of the model BCP. It is clear that a variety of morphologies can be obtained depending on the value of D/L_0 and α . One characteristic feature observed at the intermediate α values shown is that embedded structures where A segments form specific features on the surface and B segments form struts embedded in the A-segment are common for pores where $D/L_0 \leq 2.7$. Another trend can be observed at $D/L_0 \approx 2.3$ -2.5, the shape of the strut changes with increase in α . Finally, it can also be seen that at intermediate α values (≈ 0.05), single and

double helical structures are obtained when $D/L_0 \approx 2.5-3.3$ and 4.0 and $D/L_0 \approx 2.7-3.3$, respectively.

From an experimental point of view, when nanoparticles of BCPs like PS-*b*-PI are prepared by SORP, one observes striking changes in the internal morphologies in the strong confinement region compared to that in the bulk.

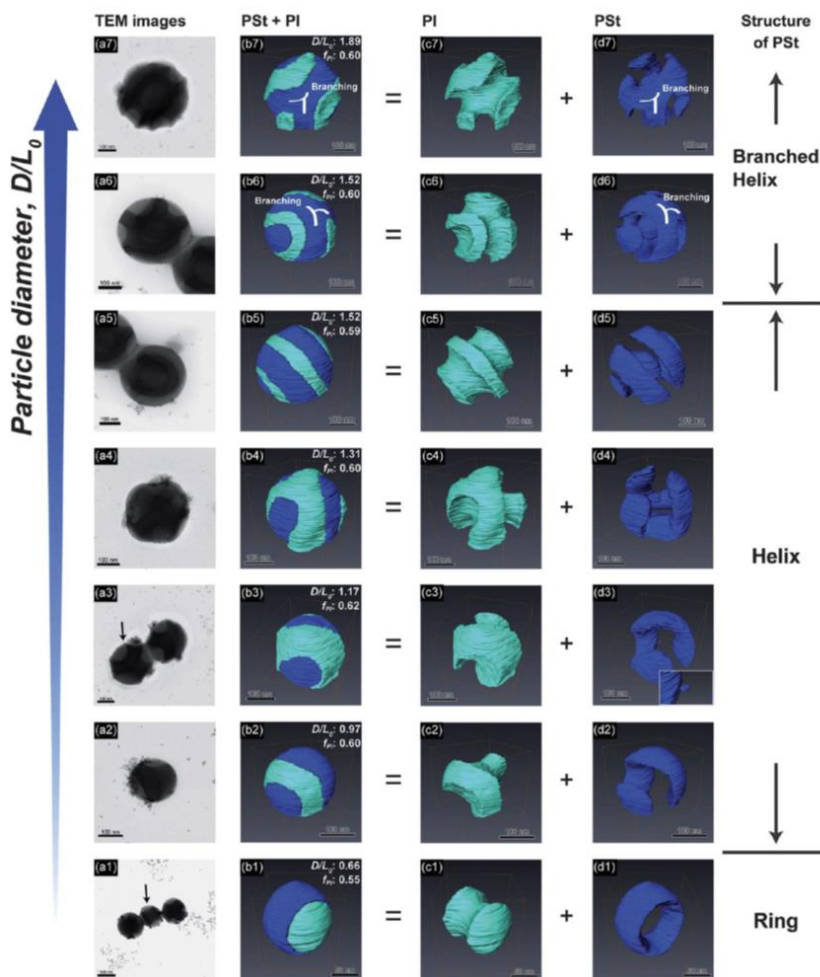


Figure 2.12. (a1-a7) TEM images of PS-*b*-PI BCP nanoparticles where the dark regions represent PI and the bright regions that of PS. (b1-b7) Reconstructed 3D images of the nanoparticles represented in a1-a7, where the PS and PI phases are shown in blue and green, respectively. (c1-c7) PI and (d1-d7) PS phases shown separately. Reprinted with permission from reference 156 from The Royal Society of Chemistry.

Figure 2.12 shows the microphase-separated structures of PS-*b*-PI nanoparticles prepared by SORP and their 3D reconstruction by transmission electron microtomography

(TEMT),¹⁵⁶ which is a powerful method for observing static and dynamic phase transitions.¹⁸⁵ From the TEMT, it can be seen that D/L_0 influences the morphologies of the internal phase-separated structures in the nanoparticles. Based on the PS phases represented in Figure 2.12 (d1-d7), the microphase-separated structures can be classified into ring ($D/L_0 = 0.66$), helix ($0.97 < D/L_0 < 1.52$) or branched helix ($1.52 < D/L_0 < 1.89$). With increase in D/L_0 , the helix in the PS phase twists more intricately in the surface regions as seen in Figure 2.12 d4 and d5. But, for $D/L_0 > 1.17$, spherical PS domains can be seen with their size increases with increasing particle diameters.

In summary, the interfacial energy between the polymer chains of the BCP and the interface plays an important role in determining the microphase-separated structures in nanoparticles. This can be seen as a function of the surface structures of the nanoparticles. There can be two different scenarios: (i) the interaction of one of the blocks of the BCP is higher than the other with the interface in case of which the microdomains of that block cover the particle surface, and (ii) when both blocks of the BCP interact equally with the interface, the particle surface encompasses both blocks on the surface as discussed above. Morphologies of BCPs in bulk and in confined spaces can therefore differ. In the bulk, the morphologies are a consequence of the volume fraction of both blocks of a BCP (f) and their interaction parameter χ . On the contrary, in confined environments, the interfaces between the confinement matrix and the polymer chains tend to bend the morphologies observed in bulk.

2.6.1.5 Effect of molar mass of BCPs on the microphase-separated structures in nanoparticles

As discussed previously, the internal phase-separated structures of BCPs in 3D confinement are influenced by the volume fraction of both blocks and their interaction with the interface. In addition to this, the molar mass of the BCP also has an influence on the phase-separated structures in nanoparticles (3D spherical confinement). In the strong confinement region, the microphase separation in bulk differs from that in solution. For example, a hydrophobic diBCP that shows lamellae structures in films, microphase separates to form unidirectionally stacked lamellae and onion structures in nanoparticles.^{166,186} Higuchi *et al.* studied the influence of molar mass of hydrophobic PS-*b*-PI BCPs on the internal phase

separation structures formed in nanoparticles as a function of their D/L_0 ratio and measured the same by scanning transmission electron microscopy (STEM) to observe the internal phase-separated structures.¹⁵⁵ The nanoparticles were prepared by SORP using PS-*b*-PI BCPs of various molecular weights ranging from 30,000 to 1.5 million g mol^{-1} (Figure 2.13 a).

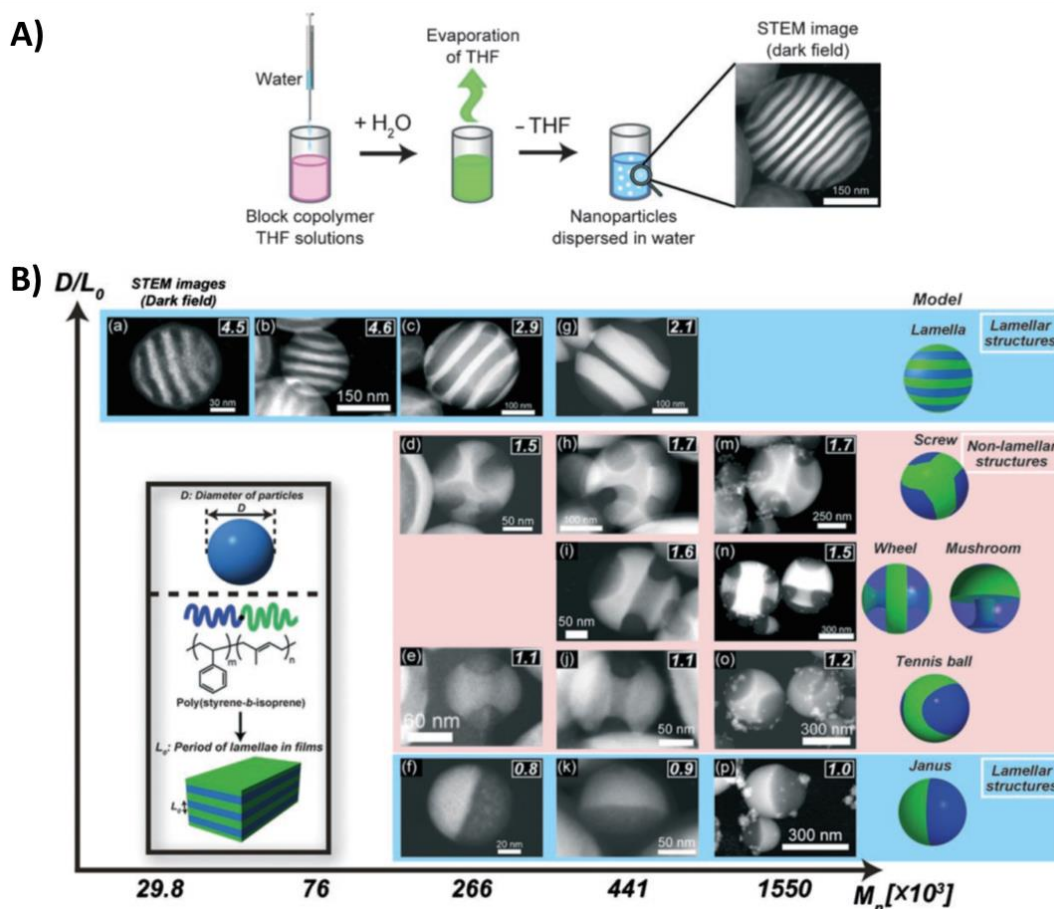


Figure 2.13. A) Preparation of PS-*b*-PI BCP nanoparticles by self-organized precipitation (SORP). B) STEM images of various phase separation morphologies in PS-*b*-PI BCP nanoparticles as a function of molar mass and D/L_0 ratio, where D is the particle diameter and L_0 corresponds to the period of lamellae structures in thin films. In figure b), (a), (b), (c-f), (g-k) and (m-p) show the internal phase-separated structures of PS-*b*-PI₃₀, PS-*b*-PI₇₆, PS-*b*-PI₂₆₆, PS-*b*-PI₄₁₂ and PS-*b*-PI₁₅₅₀ respectively. In each of the cases from (a-p), the D/L_0 ratio is represented in the top right corner of each TEM image. © Wiley-VCH Verlag GmbH & Co. KGaA. Reproduced with permission.

The nanoparticles exhibited various internal structures such as Janus-, tennis ball-, mushroom-, screw- and wheel-like in spite of their films only forming lamellae structures in all

cases (Figure 2.13b). Compared to the simulation results obtained in a 3D confinement system, few observations were reported: (i) when $D/L_0 > 2.0$, unidirectionally stacked lamellae structures were formed in the nanoparticles, (ii) when $1 < D/L_0 < 2$, non-lamellae structures were observed such as screw like ($D/L_0 = 1.7$), mushroom- and wheel-like ($D/L_0 = 1.5$), tennis ball-like ($D/L_0 = 1.1-1.2$), Janus-type ($D/L_0 < 1.0$). Therefore, different morphologies of phase separation as a function of D/L_0 are seen for BCPs confined in nanoparticles by varying the molar mass of the BCPs.

2.7 Applications of BCP Self-Assembly

Most of the desirable properties of BCPs arise from their ability to undergo microphase separation to form well-defined nanostructures with various morphologies, sizes and tunable functionality and sizes. This has been a tremendous driving force for the extensive amount of research done on BCP phase separation to use them for various applications, for instance in the form of BCP porous membranes¹⁸⁷ and multicompartiment or nanostructured nanoparticles.¹⁸⁸

2.7.1 Nanoporous membranes

Membrane technology has already been well established, for example in the reverse osmosis (RO) system for water purification, but BCPs have not been much used for membrane applications than that of homopolymers. One of the biggest advantages of using BCPs for porous membrane preparation is the versatility in the control of pore morphology, being able to attain narrow pore size distribution and high porosity. With these unique features, nanoporous materials find applications largely in the field of energy conversion and storage,¹⁸⁹ biomimetic channels,¹⁹⁰ antifouling coatings,¹⁹¹ as well as water purification systems.¹⁹² In general, two methods can be used to generate pores in BCP membranes: (i) casting a BCP film followed by selective block sacrifice, and (ii) self-assembly and non-solvent-induced phase separation (SNIPS).¹⁸⁷ SNIPS is more promising for industrial production of porous membranes as it a fast and scalable process. Nevertheless, cleaving the junction between a BCP and selectively solubilizing the minor phase or degrading its backbone is extremely useful for the mechanistic studies of pore formation. Utilizing this concept, a pioneer work was published by Lee *et al.*, where they prepared a BCP film containing isoprene and generated pores by exposing it to ozone, while the other block was cross-

linked.^{193,194} More recently, Theato and co-workers described the preparation of functionalized nanoporous films and fibres from BCPs linked by a photocleavable molecule, and in addition featuring activated esters for further modification.¹⁹⁵ Herein, PEO-*b*-PPFPMA BCP films and fibers were prepared with *ortho*-nitrobenzyl as the photo-cleavable junction which was cleaved by UV light (Figure 2.14).

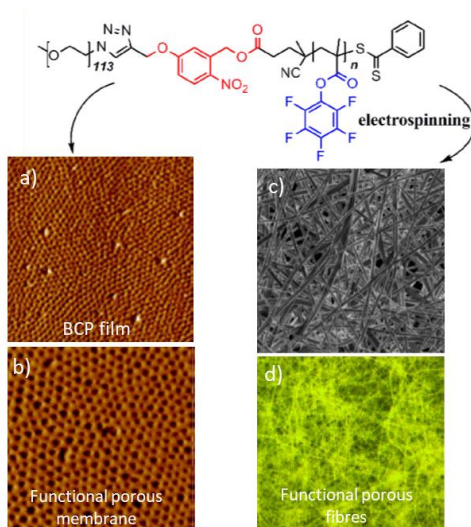


Figure 2.14. PEO-*b*-PPFPMA BCP with *ortho*-nitrobenzyl (ONB) photocleavable junction (in red). a) and b) AFM phase image of the BCP thin film and functional porous BCP thin film after UV induced cleavage of linker and treatment with amine, respectively. c) and d) SEM image of electrospun BCP fibers and confocal microscopy image of functional porous fibers after functionalization with a green dye, respectively. Scale: 2 $\mu\text{m} \times 2 \mu\text{m}$ (a), 1 $\mu\text{m} \times 1 \mu\text{m}$ (b), 10 μm (c), and 100 μm (d). Reprinted with permission from reference *Macromolecules*, 2013, **46**, 5195–5201. © 2013 American Chemical Society

BCP nanoporous membranes also find applications in the field of biology and in medicine for drug delivery. Yang *et al.* demonstrated the tremendous potential for BCP nanoporous membranes for controlled drug release.¹⁹⁶ They developed a new drug delivery device for controlled protein drug delivery. For this, the nanoporous membranes with controllable pore sizes were prepared using polystyrene-*block*-poly(methyl methacrylate) (PS-*b*-PMMA) BCP with $f_{\text{PS}}:f_{\text{PMMA}} = 0.75:0.25$ that gave rise to cylindrical microdomains. To obtain the pores, the PMMA domains were etched by immersing the film into acetic acid and controlled protein drug delivery tests were successful with bovine serum albumin (BSA) for up to 2 months using the nanoporous BCP membrane containing cylindrical nanochannels (Figure 2.15).

Therefore, using functional linkers at junction points cleavable by different methods can be an interesting strategy to generate pores in films. Such an example of preparing porous membranes using BCPs containing an active-ester junction has been described in Chapter 4.

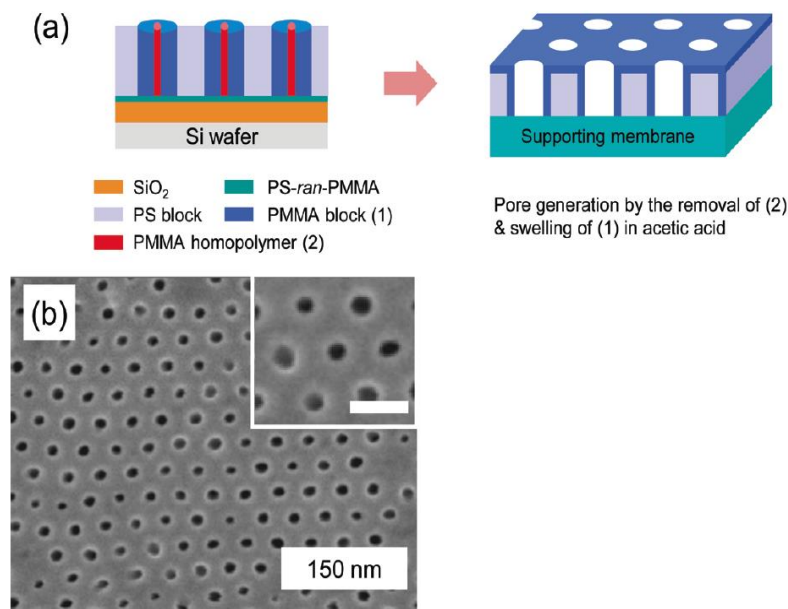


Figure 2.15. (a) Schematics for the preparation of block copolymer membrane with cylindrical nanochannels. (b) Field-emission scanning electron microscopy (FE-SEM) images of the top surface exhibiting cylindrical pores. Scale bar in the inset corresponds to 30 nm. Reprinted with permission from reference *ACS Nano*, 2010, **4**, 3817–3822. © 2010 American Chemical Society

2.7.2 Multicompartment nanoparticles

Self-assembly of BCPs using selective solvents is a powerful and versatile method to create nanoparticles with defined size, surface morphology/internal structures and functionality. BCP design directly influences the morphology of phase-separation in the nanoparticle (volume fractions of each block), size of the nanoparticle (overall molar mass) as well as the incorporation of functional moieties as chemical anchors. There are several examples in literature where amphiphilic BCPs and their blends are used for the preparation of micellar nanoparticles with tunable surface chemistry and physical behaviour directed at various applications.^{197–200} On the other hand, amphiphilic BCPs or hydrophobic BCPs and their blends can also be used for the preparation of multicompartment particles, i.e.,

“patchy” particles with small domains (sub 100 or 50 nm range) and have accessible functional groups making them useful for small molecule or biomolecule conjugation. Such materials can be fabricated in different ways: (i) EHD co-jetting of polymer solutions to obtain particles with multiple compartments or patches, where functional moieties as comonomers in the polymer may be introduced, or (ii) BCP or BCP blends self-assembly in solution to obtain much smaller domains in sub 50 nm range. In the latter case, one may introduce functional comonomers for further attachment of molecules of interest and also induce morphological transformations from within the nanoparticle, to supramolecular transformations leading to new architectures. Some examples in the respective fields have been stated below.

Rahmani *et al.* demonstrated the fabrication of several micropatterned particles displaying orthogonal functionalities.¹⁸³ Functional polylactide derivatives were subjected to EHD co-jetting leading to compartmentalized fibres which were then sliced into microdiscs. Further, using orthogonal chemistries, different biomolecules such as biotin-streptavidin conjugate and BSA were immobilized precisely on the patches (Figure 2.16).

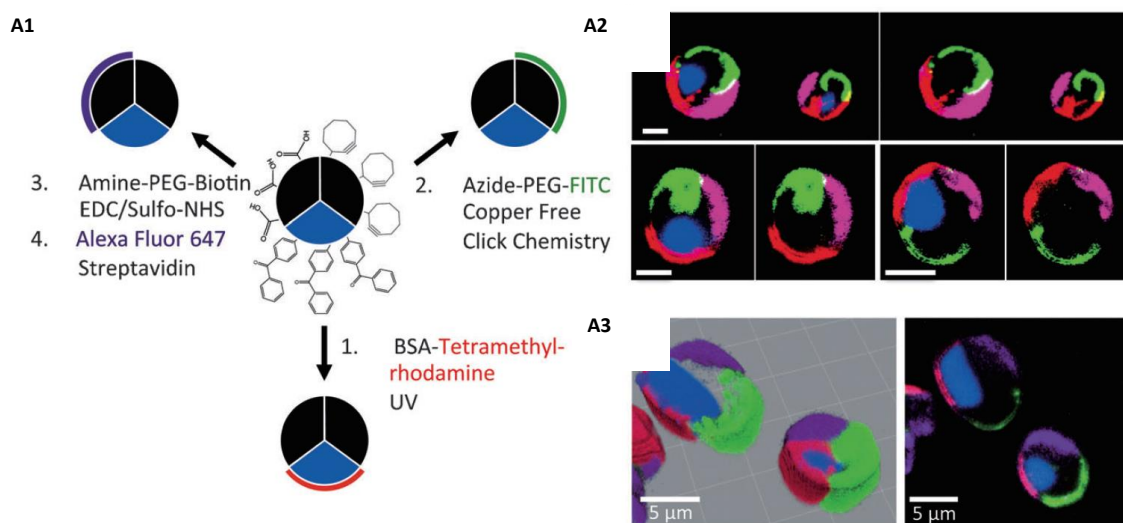


Figure 2.16. A1) Three-patch particle decorated with alkyne, carboxylic acid and benzophenone functional groups and their utilization for attachment of biomolecules. A2) Confocal images of the microparticles after functionalization. A3) 3D volume rendered image of the confocal microscope images shown in A2. Scale bars represent 5 μm. © Wiley-VCH Verlag GmbH & Co. KGaA. Reproduced with permission.

2. THEORETICAL BACKGROUND

As this technique does not allow for the fabrication of functional nanoparticles with sub 100 nm patches, BCP self-assembly is extensively used for this purpose. Several reports of BCPs such as PS-*b*-PI have been shown to self-assemble in solution to form nanoparticles with surface nanostructures.^{201–203} In an interesting report by Higuchi *et al.*, PS-*b*-PI BCPs were prepared by SORP at different temperatures to form disordered, unidirectional stacked lamellae and onion-like phase-separated structures in nanoparticles.¹⁶⁸ Further, on thermal annealing, disorder-order and order-order transformation in phase separation morphology was induced (Figure 2.17).

Further, BCPs and their blends can also be used for the fabrication of nanoparticles with ordered phase-separated structures in the sub 50 nm regime and further be supramolecularly transformed into other materials (e.g., stacked-lamellae structured nanoparticles into nanodiscs,¹⁶⁷ onion-like structures into nanorings,²⁰⁴ and hexagonal cylinders into nanowires).²⁰⁴ BCP blends have also been used to obtain nanoparticles with different morphologies of phase separation,^{167,205,206} and more recently, some functional analogues for precise patterned immobilization.²⁰⁷

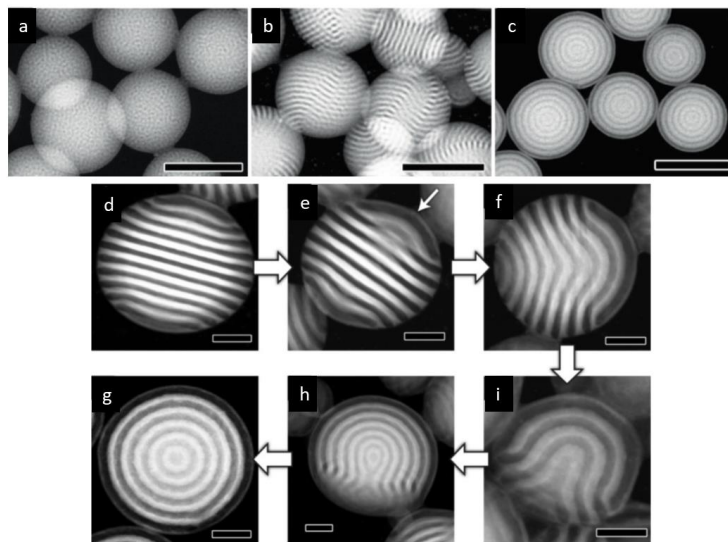


Figure 2.17. a-c) STEM images (dark field) of PS-*b*-PI₃₀ nanoparticles prepared at different temperatures showing spheres, stacked-lamellae and onion-like internal structures, respectively. Scale bars represent 300 nm. d-i) STEM images of transformation of stacked lamellae structured nanoparticles shown in ‘b’ (d-h) to finally obtain onion-like structures in nanoparticles (g). Scale bars represent 100 nm. © Wiley-VCH Verlag GmbH & Co. KGaA. Reproduced with permission.

Schmidt *et al.* demonstrated the fabrication of functional striped ellipsoidal nanoparticles for spatially controlled functionalization using a new synthetic platform.²⁰⁷ This was achieved by blending PS-*block*-poly(2-vinylpyridine) (PS-*b*-P2VP) with functional PS or P2VP copolymers. The nanoparticles were prepared by an emulsification strategy and desired properties were imparted by changing the nature of the functional PS or P2VP copolymers used for blending. (Figure 2.18). Up to date, although several BCP thin films as platforms for precise patterning have been developed, not many examples of BCP (functional) self-assembly in solution leading to nanoparticles with patterned surface structures have been reported. Owing to the great potential for improvement and its suitability for practical applications, Chapter 4 deals with the preparation of reactive “patchy” nanoparticles.

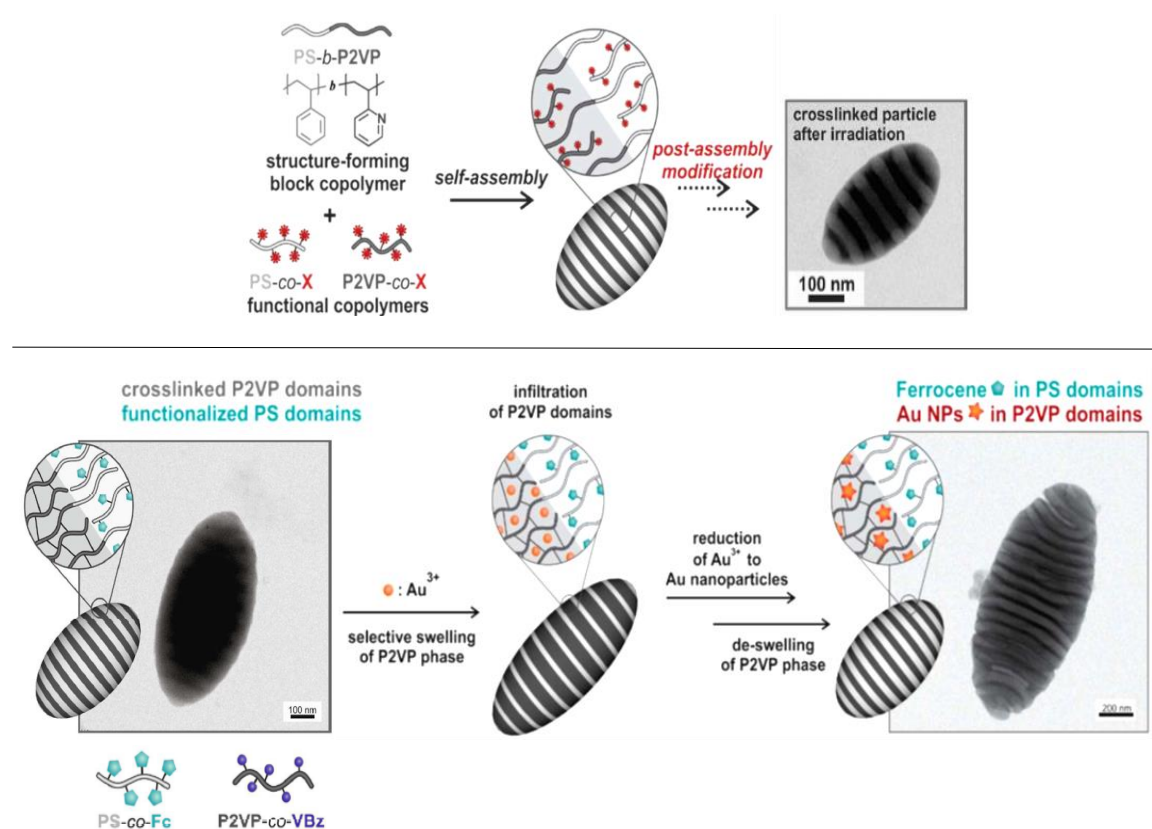


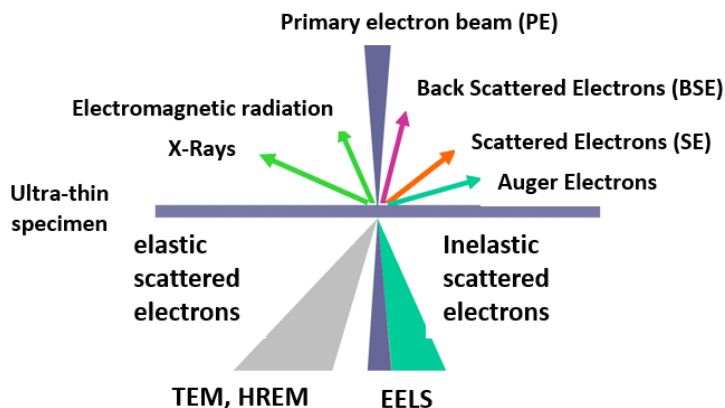
Figure 2.18. (Top) Schematic representation of the developed platform approach for spatially controlled functionalization of striped ellipsoidal particles. (Bottom) Multifunctional ellipsoidal striped nanoparticles via *non-covalent post-assembly* modification. Synthetic route describing the introduction of gold nanoparticles into the P2VP domains and TEM dark field images of the respective BCP blended nanoparticles. Reprinted with permission from reference 207 from The Royal Society of Chemistry.

2.8 Analytical Methods for Nanostructured Nanoparticles

2.8.1 Transmission Electron Microscopy (TEM)

2.8.1.1 Basic principle

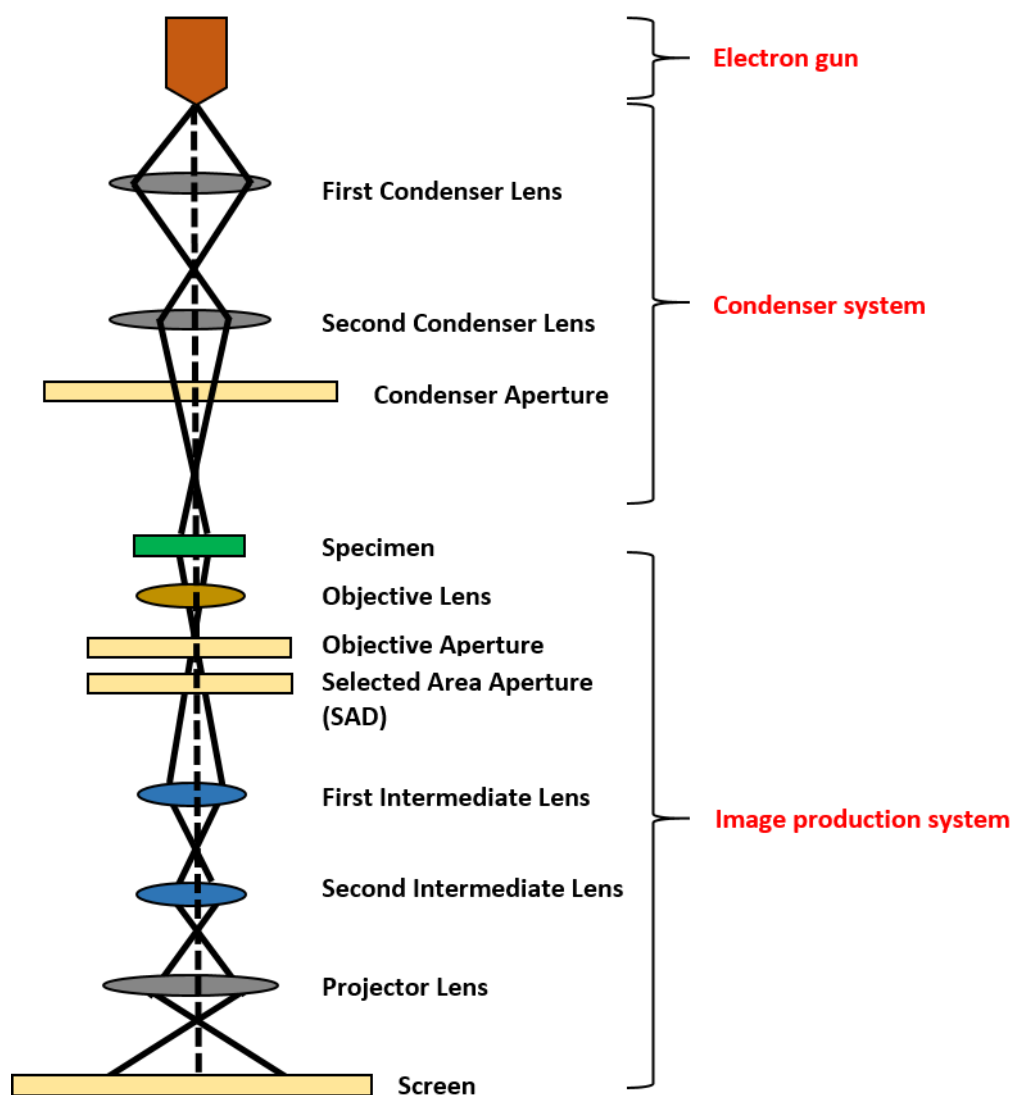
TEM using high energy monochromatic beam of electrons accelerated at voltages up to 300 kV i.e., nearly to the speed of light. The electron beam behaves like a wave with wavelengths shorter than light waves by a million fold. The electron beam is transmitted through an ultra-thin specimen, interacting with the specimen as it passes through. When the highly energetic primary electron beam interacts with the specimen, electrons can scatter or backscatter elastically or inelastically, produce many interactions, or give rise to different signals like X-rays, Auger electrons, or electromagnetic radiation (Scheme 2.9). Some of them are relevant to TEM. An image is formed from the interaction between the electrons and the specimen, the image is then magnified and focused on to an imaging device, such as a fluorescent screen, a layer of photographic film, or to be detected by a sensor such as a CCD camera.²⁰⁸



Scheme 2.9. Probable interactions between the primary electron beam and a specimen.

2.8.1.2 Instrumentation

The instrumentation of a TEM can be classified into three major sections: (i) electron gun, (ii) condenser system, and (iii) image production. A ray diagram showing all three sections is shown in Scheme 2.10.



Scheme 2.10. Schematic representation of the three components (electron gun, condenser system and image production system) in a TEM.

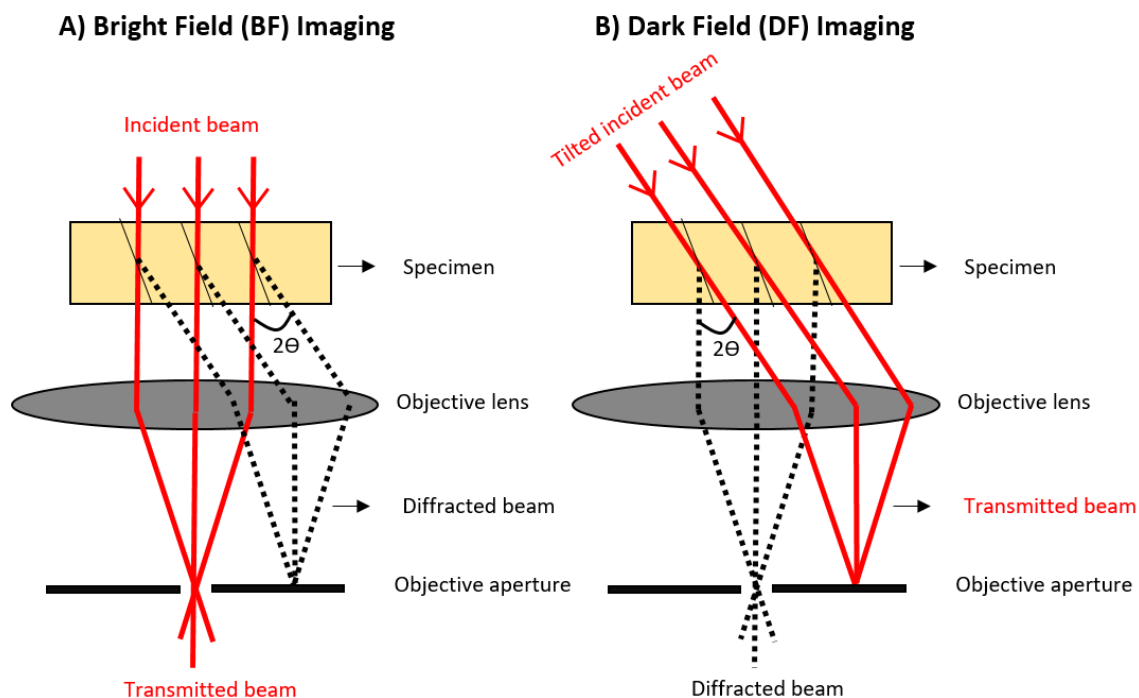
Electron gun: The electron gun is responsible for firing the electrons towards the specimen. There are several types of electron guns, but a heated tungsten filament is most commonly used to create the primary electron beam. The electrons are then drawn toward an anode at one end of the electron gun, where a hole allows the passage of the electrons towards the specimen.

Condenser system: After the electrons leave the electron gun, they enter the condenser system. This system consists of one or two electromagnetic lenses that are made up of coils

2. THEORETICAL BACKGROUND

of wires. The first condenser lens determines the “spot size” of the electron beam and the second lens changes the size of this spot on the sample. The magnetic field created by the lenses focuses and constricts the electrons into a thin beam. The condenser aperture is a thin disk or a metal strip with a small circular aperture that restricts the electron beams and filters the unwanted scattered electrons before image formation.

Image production: The electrons from the condenser system enters the image production system after it passes through the specimen. Depending on the type of interaction of the electron beam and the specimen, transmitted beam, diffracted beam, and inelastically scattered electrons are generated. The *objective aperture* enhances contrast by blocking the high-angle scattered electrons. Depending on the position of the objective aperture, two different types of TEM images, bright field (BF) and dark field (DF) images can be obtained (Scheme 2.11). The *projector lens* then expands the focused electron beam of interest onto a fluorescent or phosphorescent screen to create an image. The phosphor screen is usually made up of fine zinc sulfide for direct observation by the user.



Scheme 2.11. Ray diagram illustrating the image formation in the BF (A) and DF (B) mode.

2.8.1.3 Resolution of a TEM

Resolution in TEM is given by the following equation:

$$d = \frac{0.753}{\alpha \sqrt{V}}$$

where d is the resolution in nm; α is the half aperture angle and V is the accelerating voltage in volts. For example, when the electron beam is accelerated at 100 KV, the resolution of the TEM is 0.24 nm. The resolution improves with higher accelerating voltages.

2.8.1.4 Advantages and disadvantages of TEM

TEM has certain advantages such as real and diffraction pattern information can be obtained from a sample region; chemical information via energy dispersive X-ray spectroscopy (EDX) and high resolution imaging is possible; and several phase contrast images can be obtained. On the other hand, TEM requires special sample preparation; high vacuum is a requirement; non-conducting samples require gold or carbon coating and it implies high capital and running costs.

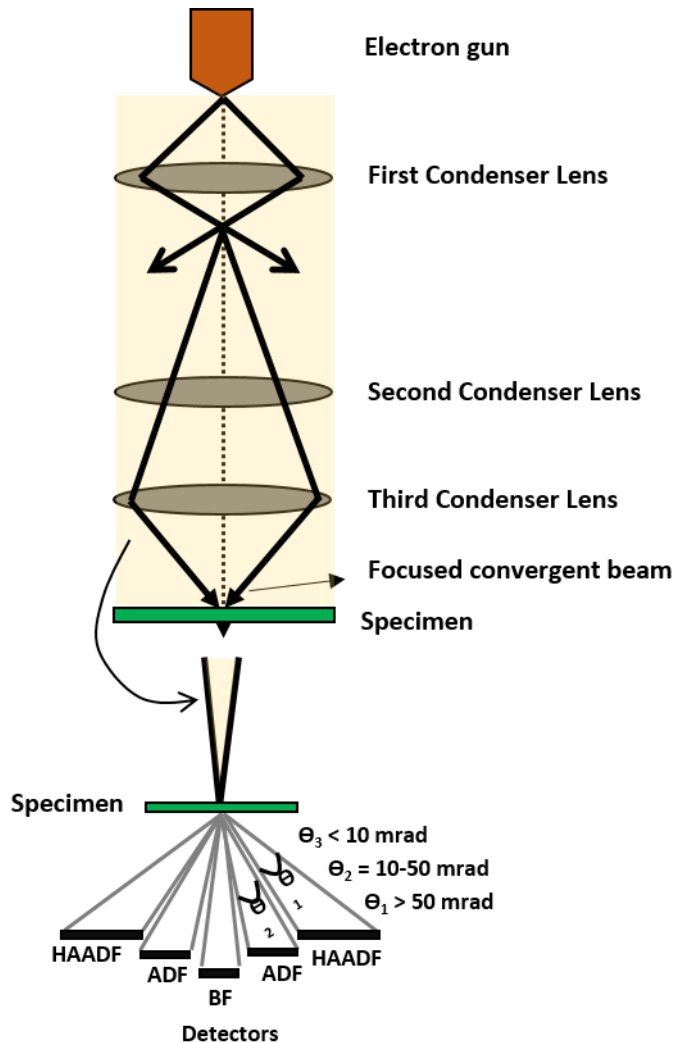
2.8.2 Scanning Transmission Electron Microscopy (STEM)

2.8.2.1 Basic principle

A schematic representation of the optical configuration of STEM is shown in Scheme 2.12.²⁰⁹ A series of lenses focus an electron beam to form a precise probe that is incident upon an ultra-thin sample. The final focusing lens is the *objective lens* while the other pre-lenses are the *condenser lenses*. The lens system on the whole provides enough demagnification of the spot-sized electron source to form an atomic scale probing on the sample. The objective lens provides the final and the largest demagnification step. An *objective aperture* restricts the numerical aperture down to a size where any kind of aberration in the optical system can be lowered to avoid blurring of the sample. Finally, scan coils are arranged to scan the probe over the sample and a variety of scattered beams are obtained that can be plotted as a function of the probe position to obtain a magnified image of the sample. The most commonly collected ones are: (i) transmitted electrons, where the electrons leave

2. THEORETICAL BACKGROUND

the sample at low angles with respect to the optical axis (BF mode), (ii) transmitted electrons that leave the sample at high angles compared to the optical axis (annular dark field (ADF) mode), (iii) X-rays generated from any electron excitation in the sample (EDX), and (iv) transmitted electrons that have lost energy by transmitting through the sample. These electrons can be plotted as a function of their energy loss to obtain an electron energy loss spectrum, known as EELS.

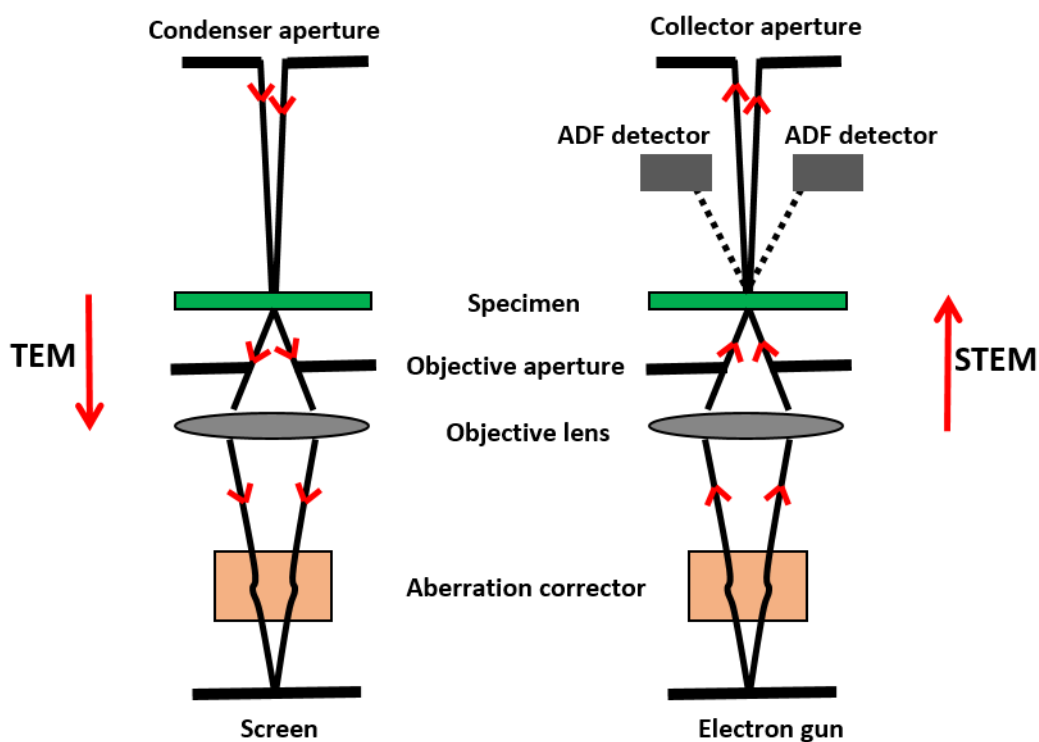


Scheme 2.12. A general schematic representation of the optical configuration of a STEM.

2.8.2.2 STEM vs TEM

An important concept concerning STEM is the “principle of reciprocity”. According to this principle, the STEM imaging optics (before the sample) are equivalent to the TEM imaging

optics (after the sample) (Scheme 2.13). Likewise, the role of the detector plane in STEM can be compared to the illumination setup in the TEM. For example, for a BF image, in TEM, the sample is illuminated with a coherent electron beam, and post-specimen optics are responsible for obtaining a highly magnified image of the transmitted electron beam from the sample. On the other hand, in the case of STEM, the highly demagnified imaging optics of the source on the sample is scanned over the specimen. The transmission from the specimen interaction is then calculated with respect to the position of the probe. This principle is the key to understanding that the image contrast in case of TEM and STEM will have the same form.



Scheme 2.13. A schematic diagram showing the equivalence between bright-field STEM and conventional TEM (CTEM) using the principle of reciprocity.

2.8.3 Stimulated Emission Depletion Microscopy (STED)

2.8.3.1 Basic principle²¹⁰

Stimulated emission depletion microscopy is a variant of high resolution fluorescence microscopy technique. It differs from other confocal microscopies as it overcomes diffraction

2. THEORETICAL BACKGROUND

limits. A schematic representation of the STED microscope as well as the difference in energy diagram compared to that of a confocal microscope are shown in Figure 2.19. STED uses pairs of synchronised laser pulses, where the first pulse is used to excite the fluorescence dye and an ordinary diffraction limited focus is obtained. The second pulse, known as the depletion pulse, is red-shifted in frequency to the emission spectrum of the dye. The depletion pulses are spatially arranged in the shape of a doughnut such that only the fluorescence from the molecules at the periphery of it are quenched via stimulated emission. The depletion laser intensity remains zero at the centre of the doughnut where the fluorescence from the molecule remains unaffected and is detected by single-photon sensitive detectors.

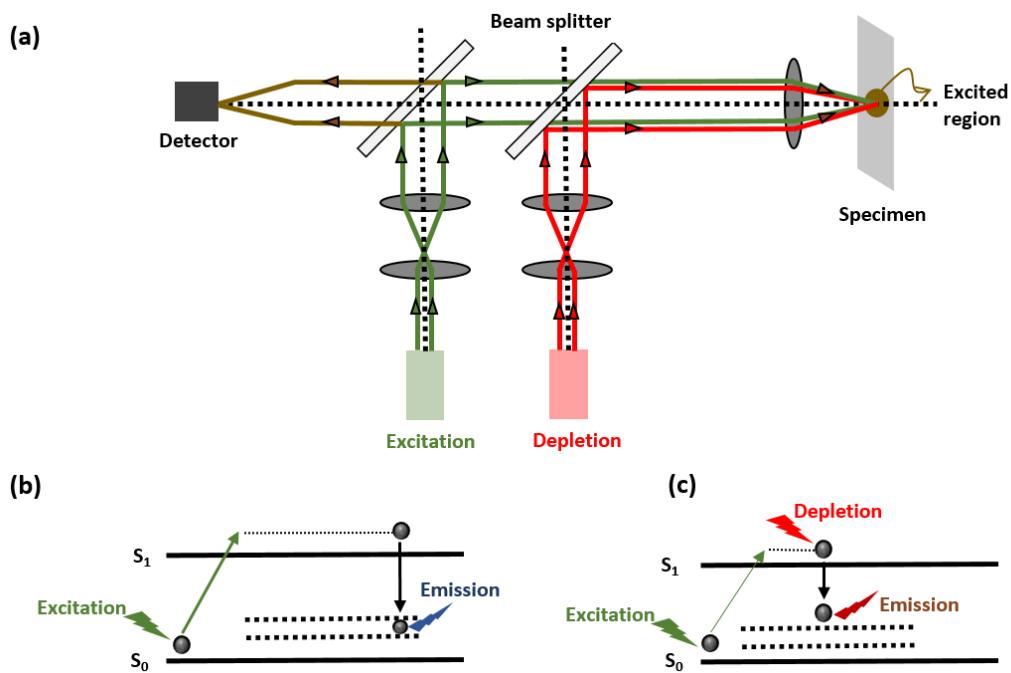


Figure 2.19. The STED concept. (a) Schematic representation of a STED microscope. Energy diagram comparisons between fluorescence and depletion in confocal (b) and STED microscopies (c).

2.8.3.2 Resolution

The resolution of STED microscopy is given by:²¹¹

$$d = \frac{\lambda}{2 NA + (\sqrt{1 + I/I_S})}$$

Where d is the resolution in nm, λ is the wavelength of light in nm, NA is the numerical aperture of the objective lens, I is the maximum intensity of the STED beam and I_S is the saturation intensity characteristic to the dye used. If the STED laser intensity is higher than a certain threshold, all the spontaneous emission is dominated by the stimulated emission which leads to the complete suppression of the fluorescence, called depletion.

3. SYNTHESIS OF FUNCTIONAL BLOCK COPOLYMERS

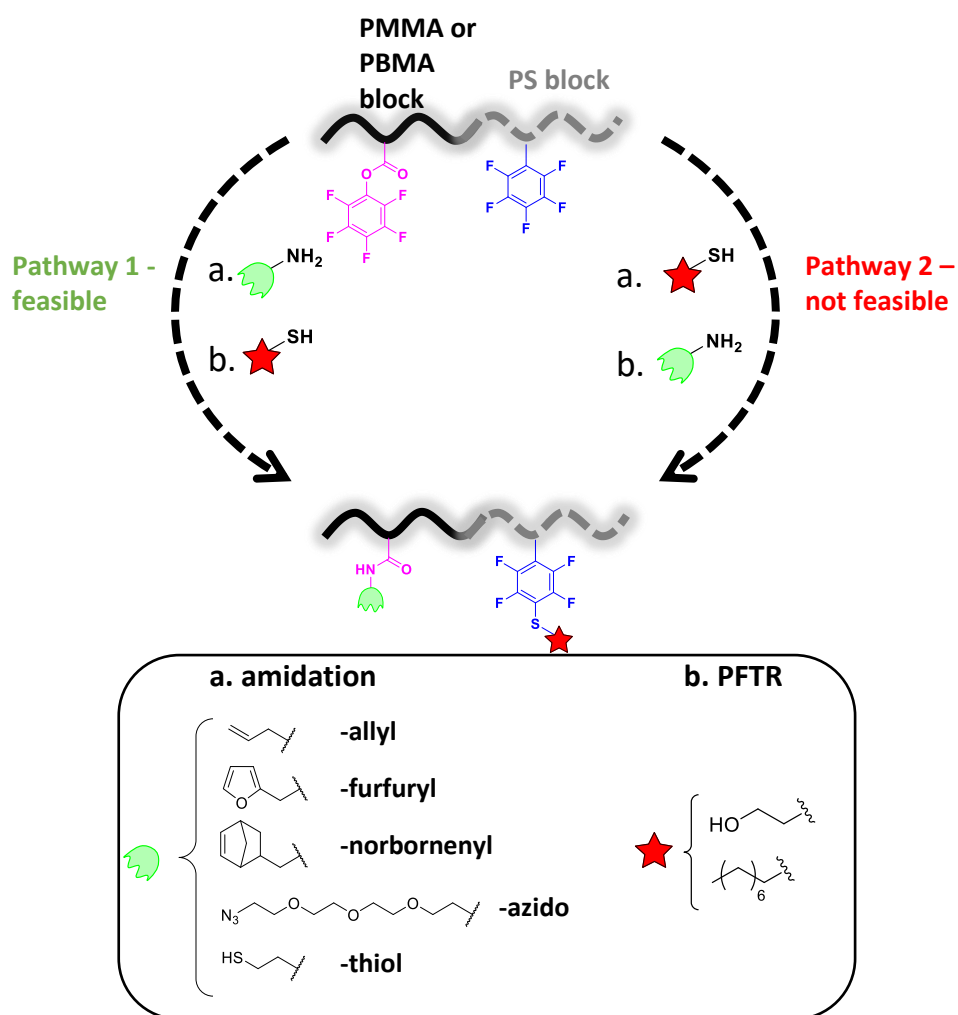
3.1 Introduction

The availability of RDRP techniques as discussed Section 2.3 allows for the facile synthesis of functional BCPs, but is limited depending on the complexity and polymerizing ability of the functional comonomers. Advantageously, post-polymerization modification (PPM) is a technique using which functional BCPs can be synthesized by simple chemical modifications of well-defined precursor BCP. On the one hand, it is possible to synthesize a new BCP from a precursor BCP that finally differs in its physical and chemical properties. For example, water-soluble polymers can be synthesized by PPM of a well-defined activated ester-containing polymer precursor (hydrophobic) with amines in a simple reaction under mild conditions.²¹² On the other hand, it is widely used to obtain functional BCPs with tunable functionality, where certain properties of the backbone such as degree of polymerization, amount of functional comonomer, architecture, and fractions of the blocks are retained while only altering the nature of their functionality. In the past few years, several coupling reactions such as radical thiol-ene and thiol-yne additions, Michael addition,³⁷ thiol-disulfide exchange, azide-alkyne cycloaddition, Diels-Alder, and activated ester/amine exchange^{213,214} have been popular in this regime. Another important aspect is the feasibility and compatibility of the functional comonomer for copolymerization with another monomer by RDRP techniques. Considering the feasibility of polymerization and robustness of their PPM reactions, pentafluorophenyl (PFP) based esters are emerging as popular synthetic handles for PPM owing to their ability to readily undergo nucleophilic substitution reactions with the abundant pool of commercially available amines.^{49,50,71} The PFP group is capable of undergoing yet another “click” type of reaction known as *para*-fluoro–thiol substitution reaction (PFTR). Taking advantage of versatility of the PFP moiety, this chapter describes the synthesis of PFP-functionalized BCP precursors, and their

Parts of this chapter and the associated experimental section (Section 8.1 and Appendix A) are adapted or reproduced from reference 85 and 235: D. Varadharajan, G. Delaittre, *Polym. Chem.*, 2016, **7**, 7488-7499. © The Royal Society of Chemistry; H. Turgut, D. Varadharajan, Nico Dingenouts, G. Delaittre, *Macromol. Rapid Comm.*, 2018, marc.201800231, *accepted*. © WILEY-VCH Verlag GmbH & Co. KGaA, Weinheim

PPM to obtain a variety of functional BCPs. A simple technique such as PPM was sought after to be able to generate a library of functional BCPs, to then be able to screen them for the preparation of functional nanostructured nanoparticles (discussed in Chapter 4).

3.2 Strategy



Scheme 3.1. Schematic representation of the strategy used (amidation + PFTR) to create dual reactive PMMA-*b*-PS and PnBMA-*b*-PS BCP precursors.

A BCP containing relatively well-established segments, poly(methyl methacrylate-*stat*-pentafluorophenyl methacrylate)-*b*-poly(styrene-*stat*-pentafluorostyrene) (P(MMA-*r*-PFPMA)-*b*-P(*S-r*-PFS)) was used to establish a suitable platform for facile generation of functional BCP libraries. PFPMA and PFS were chosen because: (i) of the high reactivity

of PFPMA with amines, (ii) among the others, *carbon*-linked PFP derivative (PFS) is the most employed for thiol-halo^{215,216} reactions^{217,218} and, (iii) PFS structurally resembles styrene and hence is a compatible comonomer for the PS block.

In general, two steps were performed: (i) a functional BCP precursor based on P(MMA-*r*-PFPMA)-*b*-P(S-*r*-PFS) was synthesized by RAFT polymerization, and (ii) PPM following two pathways, i.e., active-ester-amine reaction or amidation followed by PFTR (*Pathway 1*), or PFTR followed by amidation (*Pathway 2*). This was helpful to understand the reactivities of PFS and PFPMA towards thiols and amines, respectively. A general schematic representation of the strategy is represented in Scheme 3.1. Certain important parameters such as reaction time (10-60 min), nature of the base used for PFTR (trimethylamine (TEA) or 1,8-diazabicyclo[5.4.0]-undec-7-ene (DBU)), and temperature (room temperature (RT) and 50 °C) were investigated to formulate an ideal route towards functional BCP synthesis. The optimum conditions were further used to obtain reactive BCP precursors based on poly(*n*-butyl methacrylate-*r*-pentafluorophenyl methacrylate)-*b*-poly(styrene-*r*-pentafluorostyrene) (P(nBMA-*r*-PFPMA)-*b*-P(S-*r*-PFS)).

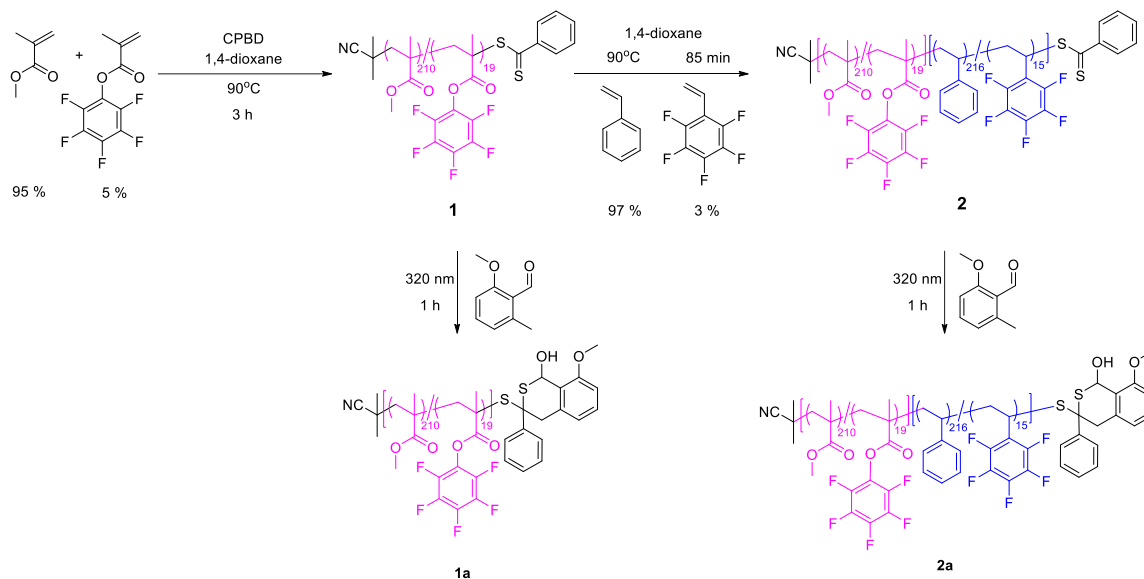
3.3 Results and Discussion

3.3.1 Synthesis of PFP-functionalized BCPs

Firstly, a well-defined BCP precursor (P(MMA-*r*-PFPMA)-*b*-P(S-*r*-PFS), **2**) was synthesized by RAFT polymerization, where the functional monomers PFPMA and PFS were statistically incorporated in the PMMA and PS block, respectively (Scheme 3.2). Two factors were considered for the synthesis of the BCPs: (i) final molar mass of approximately 50000 g mol⁻¹ was targeted to ensure the microphase separation of the BCP in bulk to ultimately obtain nanostructured nanoparticles, and (ii) equivalent volume fractions of both block were maintained to obtain specific morphologies (discussed in Chapter 4). The overall molar mass was calculated using the ¹H NMR spectrum, and the formation of the BCP was confirmed by size-exclusion chromatography (SEC) (Figure 3.1 A and C, respectively). The molar mass of P(MMA-*r*-PFPMA) macroRAFT agent **1** was first determined by SEC, which was then used to calculate the molar mass of the final BCP **2** using the ¹H NMR spectrum ($M_{n,NMR} = 51600 \text{ g mol}^{-1}$; $M_{n,SEC} = 46500 \text{ g mol}^{-1}$; $D = 1.25$). Due to the

3. SYNTHESIS OF FUNCTIONAL BLOCK COPOLYMERS

absence of any distinct protons corresponding to the functional comonomers PFPMA and PFS after polymerization, their presence was qualitatively confirmed by ^{19}F NMR spectroscopy (Figure 3.1 B).



Scheme 3.2. Synthetic route towards the synthesis of P(MMA-*r*-PFPMA)-*b*-P(S-*r*-PFS) and the capping of the RAFT end group.

The amount of functional group incorporated in both blocks was kept below 10 mol% to not alter the properties of the backbone of the BCP. This is important to study their phase separation behavior as discussed in the next chapter. Keeping this in mind, an initial feed of 5 mol% of PFPMA and 3 mol% of PFS was employed. But, as both PFPMA and PFS polymerize faster than their respective monomers MMA and styrene, 8% of PFPMA and 7 mol% of PFS were finally incorporated in BCP **2** (the calculations for the exact incorporation of the functional monomers have been elaborated in Section 8.3 using Figure A1-A, B, and D (Appendix A) .

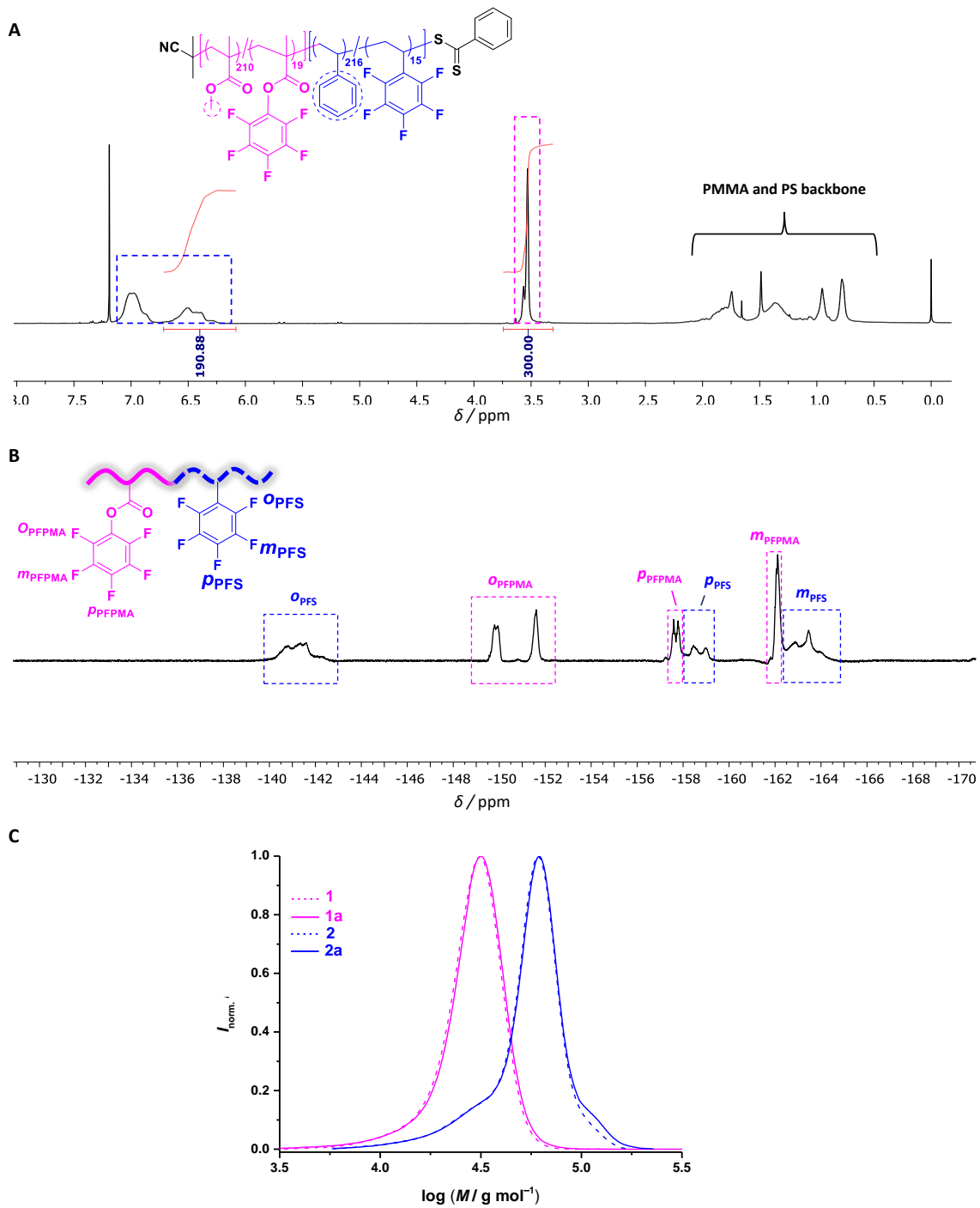


Figure 3.1. A) ^1H NMR spectrum of BCP **2** showing the integrals used for calculating the overall molar mass. B) ^{19}F NMR spectrum of BCP **2a**. C) SEC traces of macroRAFT agent **1**, polymer **1a**, and BCPs **2** and **2a**. Adapted from reference 85 from The Royal Society of Chemistry.

Having obtained the BCP precursor, the dithiobenzoate RAFT end group was “capped” as it is susceptible to aminolysis, readily leading to the formation of thiols.²¹⁹ This could lead to the formation of disulfide bridges or cross-linking as a consequence of PFTR. The end group capping was performed using 2-methoxy-6-methylbenzaldehyde in a photo-triggered Diels-Alder cycloaddition reaction to form the deactivated counter part of BCP **2**, i.e. BCP **2a** (Scheme 3.2). Similarly, the end-group in polymer **1** was also capped to form polymer **1a** which was later used for mechanistic investigations. The conventional method of radical combination using AIBN²²⁰ was avoided due to its unreliable reproducibility. The end-group capping was characterized by UV-Vis spectrometry by the disappearance of the characteristic absorption band of the RAFT end group at 310 nm (Figure 3.2). Furthermore, the SEC traces before and after the photocapping remain unchanged (Figure 3.1 C).

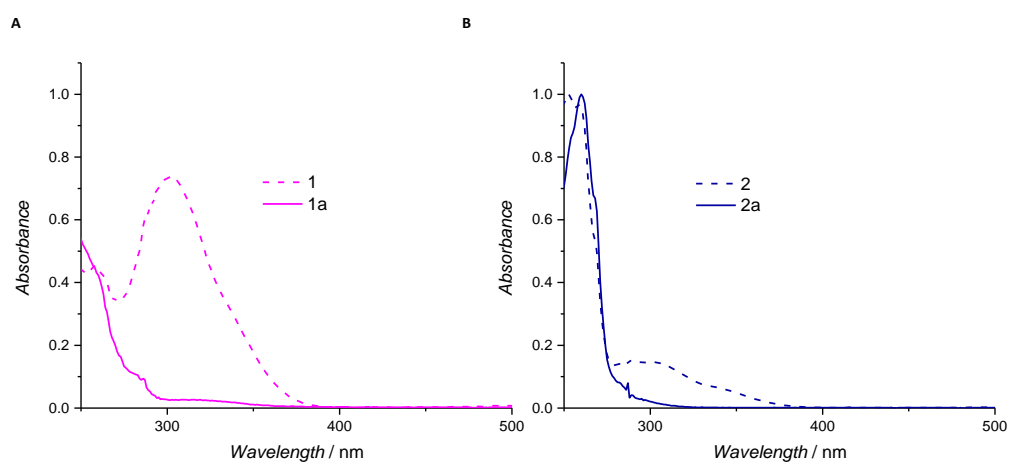


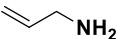
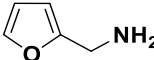
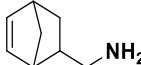
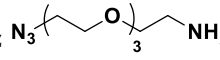
Figure 3.2. UV-Vis spectra of **1** and **2** before (pink and blue dashed line, respectively) and after (pink and blue solid line, **1a** and **2a** respectively) end group capping with 2-methoxy-6-methylbenzaldehyde. Adapted from reference 85 from The Royal Society of Chemistry.

3.3.2 Functional BCP library: Establishing orthogonal reactions between two distinct PFP-derivatives

In this study, the conditions to perform amidation (on PFPMA) and PFTR (on PFS) in an orthogonal fashion on a single BCP **2a** bearing both the PFP moieties was optimized. (Scheme 3.1). Two routes, *Pathway 1*, and *Pathway 2*, as mentioned earlier are possible to achieve the same. If both pathways emerge successful, the scope for synthesizing large

libraries of functional BCPs using various combinations of amines and thiols can be achieved. For instance, one could incorporate a single amine alongside a pool of thiols using *Pathway 1*, while *Pathway 2* could serve for the opposite. Hence, both pathways were investigated in detail leading to certain fundamental observations.

Table 3.1. Characteristics of the BCPs obtained through modification of **2a** using *Pathway 1* with different amines and octanethiol (OT) as a model thiol.

Amine		2a _{amine}				2a _{amine→OT}			
Name	Structure	x_{amine}	$M_{n,\text{NMR}}$ (g mol ⁻¹)	$M_{n,\text{SEC}}$ (g mol ⁻¹)	D	x_{OT}	$M_{n,\text{NMR}}$ (g mol ⁻¹)	$M_{n,\text{SEC}}$ (g mol ⁻¹)	D
allyl		0.93	52500	49500	1.18	0.97	52500	48000	1.24
fur		0.95	52500	47000	1.22	0.99	51500	45000	1.23
nor		0.89	53000	47500	1.22	0.99	52000	47000	1.21
az		0.88	53000	46000	1.23	0.96	55000	46000	1.24

x_{amine} = calculated grafted amine content/calculated original PFPMA content

x_{OT} = calculated grafted octanethiol content/calculated original PFS content

Investigation of Pathway 1: Chronologically, *Pathway 1* was first investigated. Several amines bearing a second reactive group on the other end of the molecule were reacted with the PFPMA units by amidation, followed by PFTR using octanethiol (OT) as a model thiol (Table 3.1). Amines possessing a second reactive group were specifically chosen to enable the synthesis of yet another sub-library, after a second round of functionalization of this new moiety. The second reactive groups in the amines are alkenyl moieties such as allyl and norbornyl (nor) that undergo several ene-reactions or cycloadditions, furanyl (fur) involved in Diels-Alder cycloadditions, and azide (az) for 1,3-dipolar cycloadditions (refer to Table 3.1). Nevertheless, this secondary functionalization is not dealt with in this thesis as we aim at uncovering the basic reactivities of PFP-derivatives with amines and thiols. Following this, amidation was performed with the amines stated above under standard conditions (50 eq. with respect to PFPMA units) in the presence of triethylamine (TEA, 5 eq.

3. SYNTHESIS OF FUNCTIONAL BLOCK COPOLYMERS

with respect to PFPMA units) at 50 °C. Firstly, allylamine was used and quantitative transformation of the PFPMA units was confirmed by the presence of the respective amine peaks in the ^1H NMR spectrum (Figure 3.3 A, pink) as well as the disappearance of the fluorine peaks of PFPMA in ^{19}F NMR spectrum (Figure 3.3 B, pink).

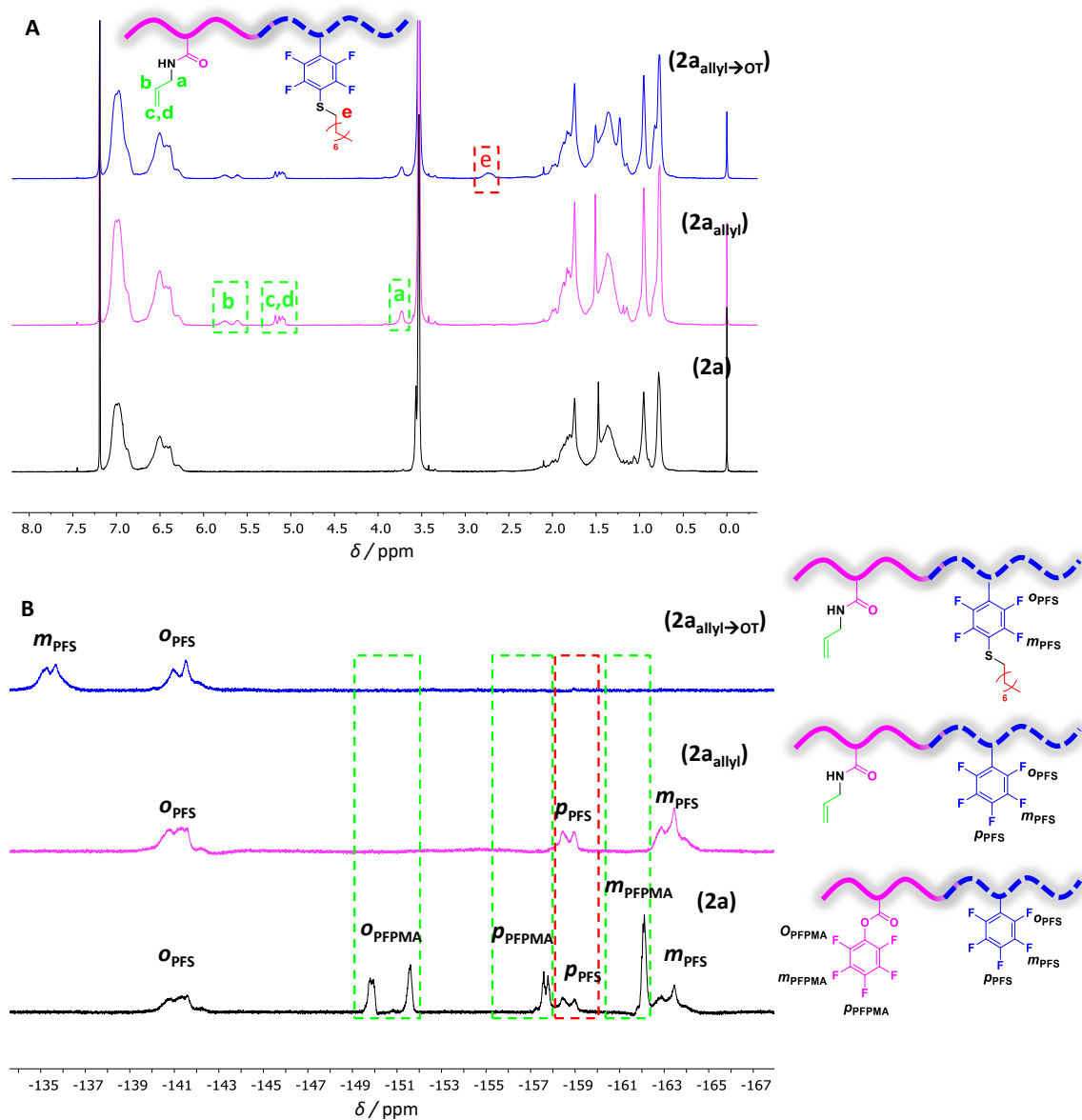


Figure 3.3. ^1H (A) and ^{19}F (B) NMR spectra of BCPs **2a** (black), **2a_{allyl}** (pink), and **2a_{allyl}→OT** (blue). Reprinted with permission from reference 85 from The Royal Society of Chemistry.

The purified amide product $2a_{\text{allyl}}$ was then subjected to PFTR with OT to obtain $2a_{\text{allyl} \rightarrow \text{OT}}$ confirmed by reviewing the ^{19}F NMR spectrum (Figure 3.3 B, blue), where the original *para*-PFS peak disappeared and a shift of the *meta*-PFS is clearly seen as a consequence of the disappearance of *para*-PFS peak. This was also confirmed by the presence of a peak at 2.6 ppm in the ^1H NMR (Figure 3.3 A, blue) that corresponds to the $\alpha\text{-CH}_2$ protons of OT. 7.4 mol% of allylamine and 6.8 mol% of OT was calculated to be incorporated into the BCP after amidation and PFTR. This suggests that amidation proceeded to 93% with a possibility of partial hydrolysis and a near-quantitative conversion of the PFS units. Near-integral overlapping SEC traces of $2a$, $2a_{\text{allyl}}$, and $2a_{\text{allyl} \rightarrow \text{OT}}$ evidences that the overall polymer architecture remained intact after being subjected to *Pathway 1* (Figure 3.4). Similar experiments were conducted using all other amines (see Table 3.1) and the results were similar to that of *Pathway 1*, leading to a small library of dual functional BCPs (for NMR spectra, refer to Appendix A, Figure A2, Figure A3, Figure A4, and the respective SEC traces are plotted in Appendix A, Figure A5, Figure A6, and Figure A7).

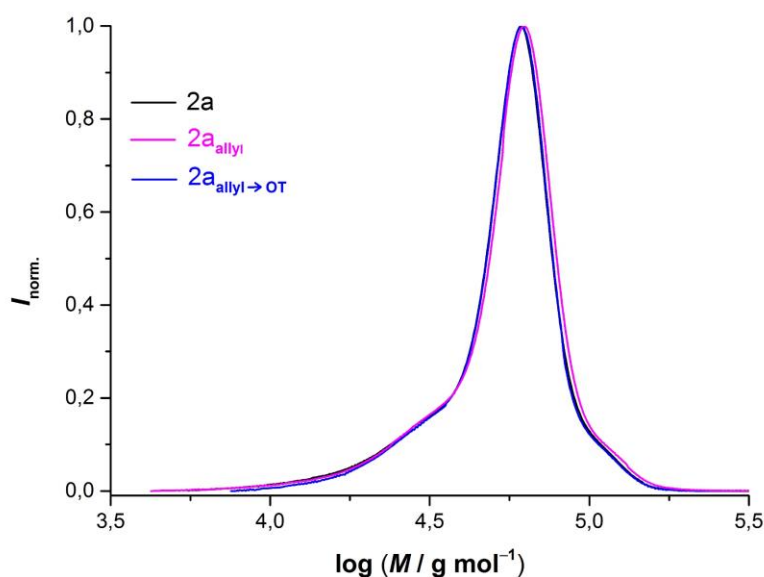


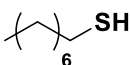
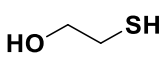
Figure 3.4. SEC traces of BCPs $2a$ (black), $2a_{\text{allyl}}$ (pink) and $2a_{\text{allyl} \rightarrow \text{OT}}$ (blue). Reprinted with permission from reference 85 from The Royal Society of Chemistry.

Investigation of Pathway 2: After *Pathway 1* was established to be a suitable and an efficient route towards dual functional BCPs, *Pathway 2* was investigated. PFTR was first

3. SYNTHESIS OF FUNCTIONAL BLOCK COPOLYMERS

performed on the PFS units using standard conditions (5 eq. of thiol and 1 eq. of DBU per unit of PFS). Contrary to what we expected, the PFPMA units did not remain unreacted to the PFTR conditions. To the best of our knowledge, this behaviour of PFPMA has not been explored. Therefore, to get a better understanding of the events of happenings, two aspects were considered: (i) the activity of fluorine atoms of PFPMA towards PFTR, and (ii) its effect in turn towards the reactivity of substituted PFPMA with amines. To address this, a study was conducted exploring different reaction conditions, such as time (10-60 min), effect of bases that catalyse the PFTR reaction (TEA and DBU) and the type of thiol (OT and mercaptoethanol) (Table 3.2).

Table 3.2. Activity of the fluorine atoms of PFPMA and PFS towards thiols at different reaction times.

Entry	Thiol	Time (min)	PFPMA			PFS
			<i>para</i>	<i>Mono-meta</i>	<i>Bi-meta</i>	<i>para</i>
1		10	✓	✓	✗	✓*
2		30	✓	✓	✗	✓*
3		60	H	✓	✓	✓
4		10	✓	✓	✓*	✓*
5		30	✓	✓	✓*	✓*
6		60	H	✓	✓	✓

*Partial substitution; H = PFPMA hydrolysed

Effect of reaction time on PFTR: First, the effect of reaction time on PFTR was studied using both OT and mercaptoethanol. BCP **2a** was subjected to PFTR for 10, 30, and 60 minutes using OT, until 100% conversion on the PFS units was achieved. ^{19}F NMR spectra of the purified polymer after every time point were measured to precisely follow the progress of the reaction (Figure 3.5). After just 10 minutes, PFPMA underwent 100% nucleophilic substitution with the thiol in the *para* position, as seen by the disappearance of the *para*-F peak of PFPMA and appearance of the shifted *meta*-F peak at -133.6 ppm. But, the PFS units at this point remained almost unreacted as seen by the appearance of only a small shifted *meta*-F peak of PFS at -136 ppm. This already proves that PFPMA is more reactive towards PFTR than PFS under the same given conditions.

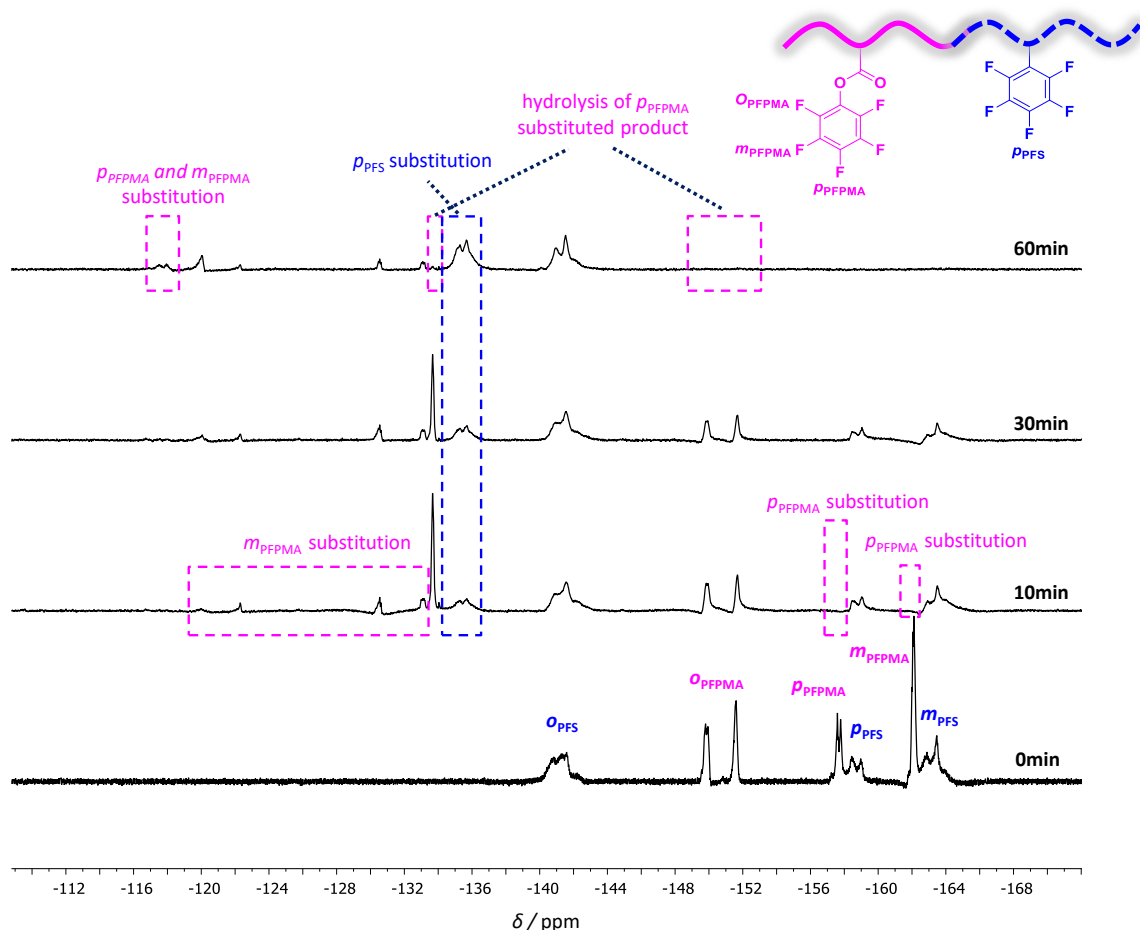


Figure 3.5. ^{19}F NMR of BCP **2a** at various time intervals using standard PFTR conditions at RT. Reprinted with permission from reference 85 from The Royal Society of Chemistry.

Furthermore, appearance of new peaks in the region of -134 and -110 ppm suggests that PFPMA also possesses other reactive fluorine atoms. To decipher the probable reactivity of *meta*- and/or the *ortho*-F atoms towards thiols, one has to understand the reactivity of pentafluorobenzenes (PFB). The orientation of substitution in PFB derivatives is directly correlated to the maximum number of activating fluorines. The *para* isomer was found to be the major substitution product of such PFB derivatives based solely on the effects of fluorine, such as in PFTR.²²¹ After 30 minutes, PFS undergoes PFTR slowly and, at the same time the other fluorine atoms of PFPMA still undergo nucleophilic substitution by the thiols. After 60 minutes when the PFTR is achieved to 100% completion in PFS, the overall large decrease in the *F*-atom peaks of PFPMA suggests that they are almost completely hydrolyzed. Yet, the presence of peaks in the region of -134 to -110 ppm indicate

3. SYNTHESIS OF FUNCTIONAL BLOCK COPOLYMERS

that the *meta*-F PFPMA substituted products remain stable towards hydrolysis. From these time-dependent experiments, it can be ascertained that the *para*-F atoms of PFPMA react faster with thiols than that of the *para*-F of PFS, while the reactivity of *meta*-F of PFPMA may be faster or comparable to the reactivity of *para*-F of PFS towards thiols. Similar time-dependent experiments using mercaptoethanol instead of OT was carried out and similar results were obtained (see Appendix A, Figure A8). In order to clearly recognize the order of substitution of fluorine atoms of PFPMA with thiols, an independent study was conducted (discussed in Section 3.3.3) using polymer **1a** without the interference of PFS.

Table 3.3. Activity of PFPMA and PFS fluorine atoms towards thiols varying certain parameters: base, temperature and reaction times.

Entry	Base (eq./PFS)	Thiol (eq./PFS)	Temp (°C)	Time (min)	PFPMA			PFS
					<i>para</i>	<i>Mono-meta</i>	<i>Bi-meta</i>	<i>para</i>
1	DBU (2)	OT (10)	RT	10	H	✓	✓	✓
2	TEA (5)	OT (50)	50	1440	✓	✓	✗	✗
3	TEA (2)	OT (10)	RT	240	✓	✗	✗	✗

H = hydrolysis

Effect of base and temperature on PFTR: In an attempt to reach 100% conversion on PFS during PFTR on BCP **2a**, the quantities of the thiol and DBU were doubled compared to the standard conditions (now 10 eq. and 2 eq. per unit of PFS, respectively, Table 3.3 Entry 1). Under these conditions, PFS undergoes 100% conversion, but the *para*-F substituted PFPMA units at the same time are completely hydrolyzed (Figure 3.6, Entry 1). In order to control the reaction, TEA, also known to catalyze PFTR under certain conditions, was used to probe the reactivity of PFPMA and PFS towards thiols using similar reaction conditions to that of amidation (50 °C, 24 h, 5 eq. TEA and 50 eq. OT per unit of PFPMA, Table 3.3, Entry 2). Surprisingly, under these conditions, the *para*- and *meta*-F of PFPMA undergo complete substitution by OT, but all remaining fluorine atoms of PFPMA and PFS as well as the substituted PFPMA units remain intact (Figure 3.6, Entry 2). To rule out the possibility of PFPMA units being unstable to higher temperatures (50 °C) and long reaction times in the presence of a base, milder conditions were employed to perform the same

reaction (Table 3.3, Entry 3). Under these mild conditions, PFTR could exclusively be achieved on PFPMA leaving PFS and *meta*- and *ortho*-F of PFPMA unaffected (Figure 3.6, Entry 3). From these observations, it is clear that PFS does not undergo PFTR at all in the presence of PFPMA using a mild base like TEA, and under standard conditions, possesses less or similar reactivity to thiols than the *para*- and *meta*-F of PFPMA.

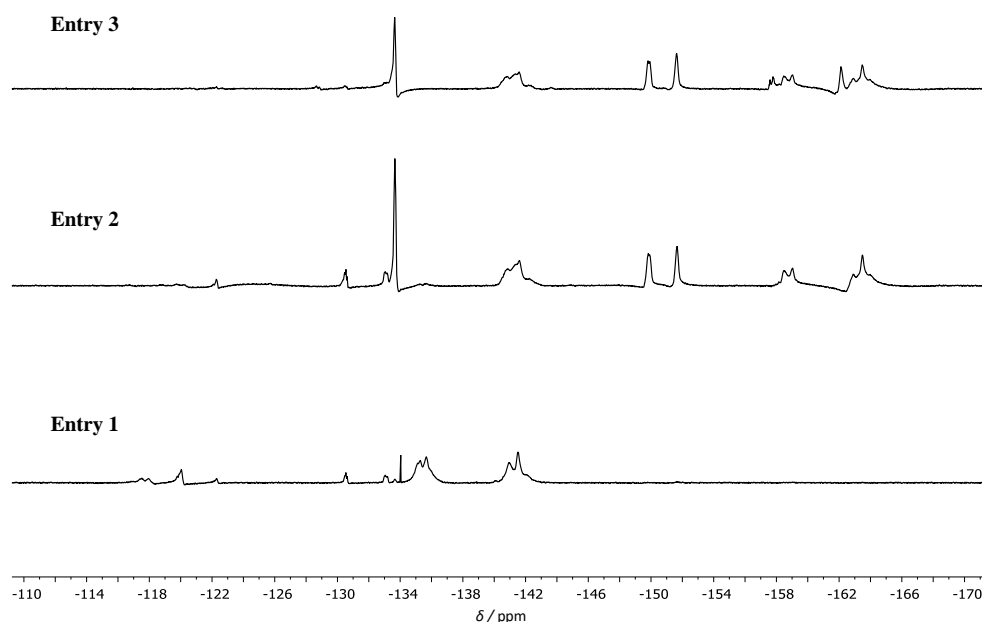


Figure 3.6. ^{19}F NMR spectra of the BCPs obtained after PFTR of BCP **2a** with OT under different conditions of base, temperature, and reaction times, corresponding to the entries in Table 3.3. Reprinted with permission from reference 85 from The Royal Society of Chemistry.

After understanding the reactivities of PFPMA and PFS on **2a** towards thiols, the next step of *Pathway 2*, i.e., amidation was conducted. As an example, the product of the reaction of PFTR on **2a** with TEA (Table 3.3, Entry 2) was subjected to amidation with furfurylamine (Figure 3.7 A). It can be seen that the starting BCP of this reaction (**3**) possesses a 100% *para*-substituted PFPMA and a percentage of partially *meta*-substituted product (Figure 3.7 B). When **3** is reacted with furfurylamine (using standard amidation conditions), only the *para*-substituted PFPMA undergoes amidation, while the *meta*-substituted species remains as it is clearly seen by the disappearance of m'_{PFPMA} and o_{PFPMA} peaks and unchanged peak pattern between -133 and -118 ppm, respectively (Figure 3.7 B, top).

3. SYNTHESIS OF FUNCTIONAL BLOCK COPOLYMERS

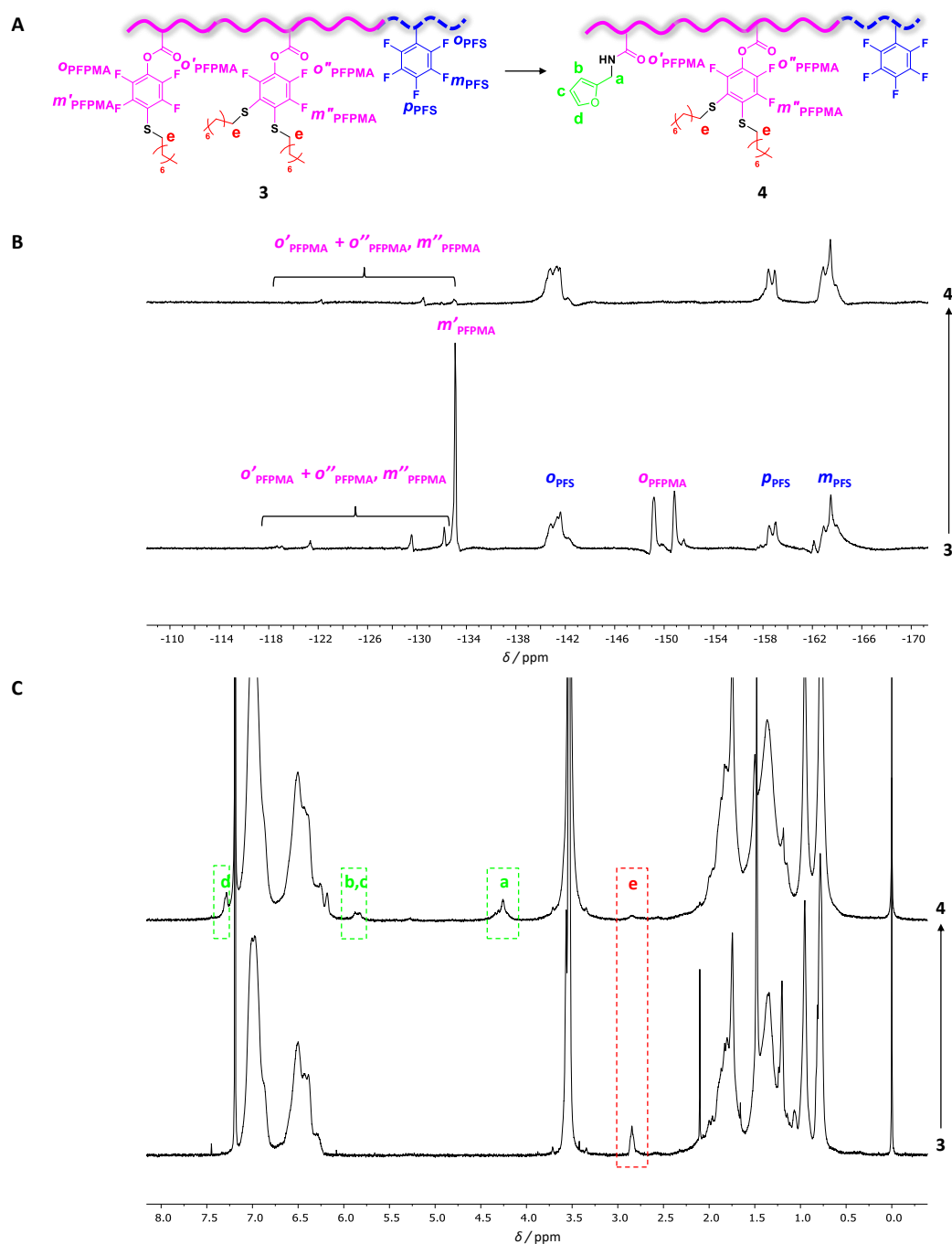


Figure 3.7. (A) Underlying reaction scheme for the amidation of **3**. ^{19}F (B) and ^1H (C) spectra of **3** (bottom) and **4** (top). Reprinted with permission from reference 85 from The Royal Society of Chemistry.

Unfortunately, due to low peak intensities of the fluorine peaks of *meta*-substituted PFPMA as well as an unclear baseline, this observation cannot be quantitatively determined. Yet, it can be unambiguously stated that under all of the above investigated conditions for a BCP

system as **2a** containing two distinct PFP units, 100% PFTR on PFS is not feasible until PFPMA undergoes complete substitution by the thiol first and the *para*-substituted product is hydrolyzed further.

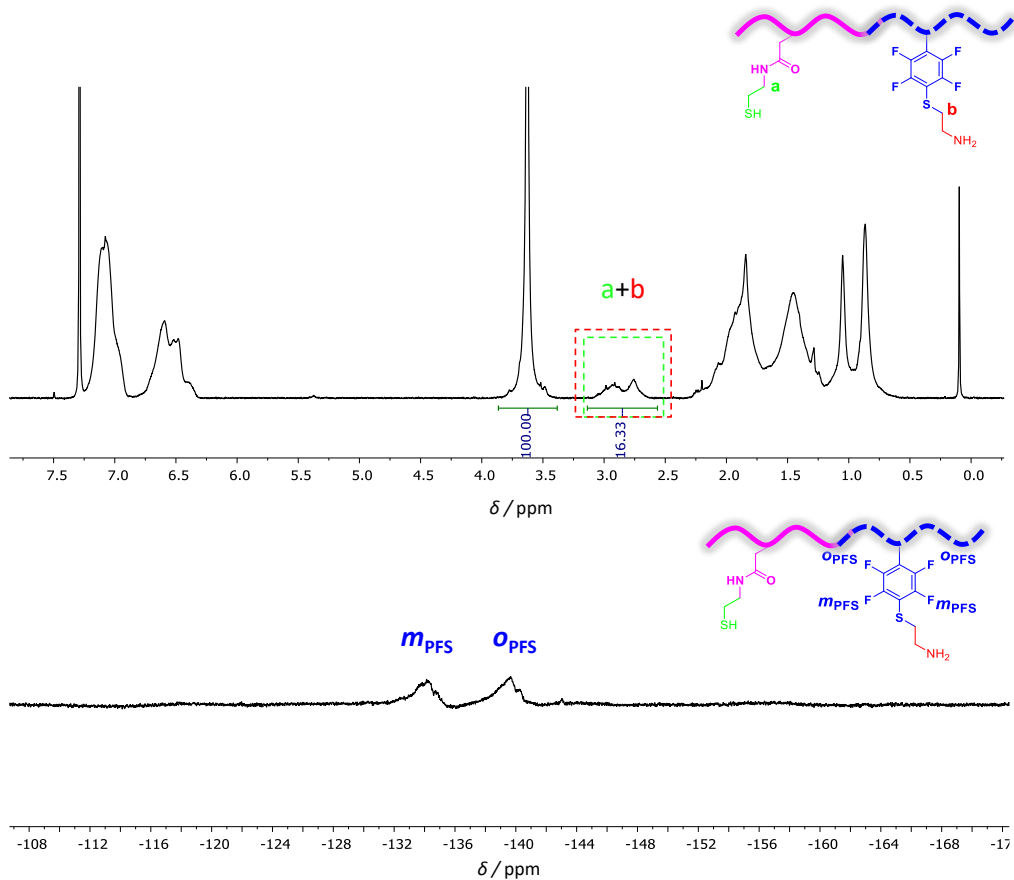


Figure 3.8. ^1H (top) and ^{19}F (bottom) spectra after one-pot orthogonal dual functionalization of **2a** with aminoethanethiol. Adapted from reference 85 from The Royal Society of Chemistry.

3.3.3 Proof of Concept: Reactivity of F-atoms of PFPMA towards nucleophilic thiol substitution

To provide a more detailed information about the reactivity of fluorine atoms of PFPMA with thiols without the effects of PFS, if any, polymer **1a** was used that is devoid of PFS units. Again, both OT and mercaptoethanol were used as model thiol for PFTR with polymer **1a**. It is apparent from Figure 3.9 that unlike PFS, the *meta* and *ortho* fluorine atoms of PFPMA are also reactive towards nucleophilic thiol substitution. One of the factors that

3. SYNTHESIS OF FUNCTIONAL BLOCK COPOLYMERS

governs the order of substitution of the fluorine atoms is the quantity of thiol. When 1 eq. of thiol per PFPMA unit is used, only the *para*-F undergoes nucleophilic substitution as seen from the presence of intact *ortho*-F and shifted *meta*-F of PFPMA as well as the integral value of α -CH₂ of OT at 3.6 ppm in the ¹H NMR (Figure 3.10). But, when the thiol concentration is increased to 5 eq. per unit of PFPMA, multiple substitutions corresponding to the *meta* or *ortho* substitutions are visible (Figure 3.9). When the same reaction was performed with mercaptoethanol as the thiol, similar results were observed (refer to Appendix A, Figure A9).

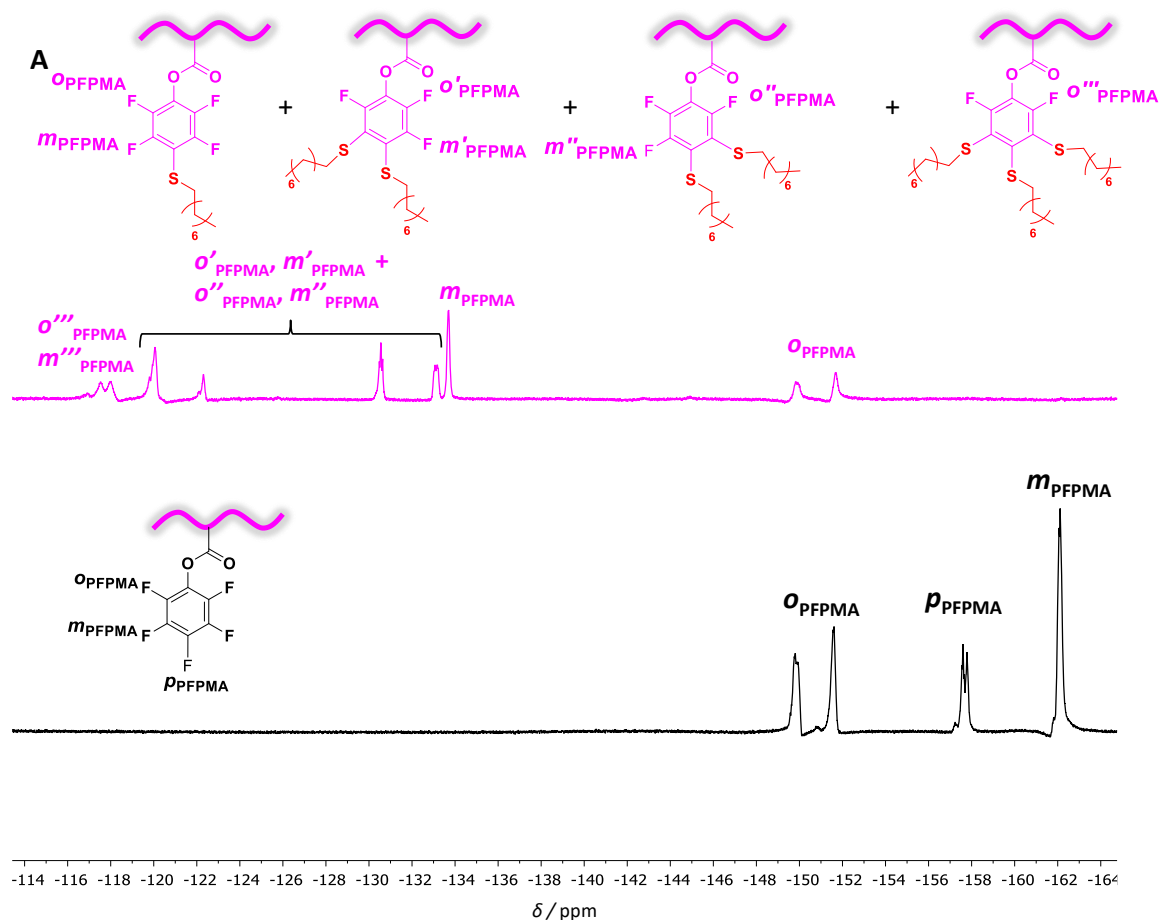


Figure 3.9. ¹⁹F NMR spectra of **1a** before (black) and after (pink) reaction with OT under standard PFTR conditions. Reprinted with permission from reference 85 from The Royal Society of Chemistry.

To be able to come to a conclusion regarding reactivities of the fluorine atoms, certain aspects must be taken into account: nature of the nucleophile, steric effects, and polarity of

the solvent. From literature, it is known that powerful electron donating groups, such as thiols increase the proportion of *meta* substitutions.²²¹ This holds true as long as steric effects do not interfere in the conjugation of π -electrons on the substituent with the aromatic ring.^{221,222} In our case, as the PFB derivative is a PFP ester that is attacked by OT first in the *para* position, further *meta* substitution is more plausible compared to *ortho* substitutions. Nevertheless, the mechanism of a thiol substitution in the *ortho* position of PFB derivatives has a complex mechanism that is incompletely understood.²²²

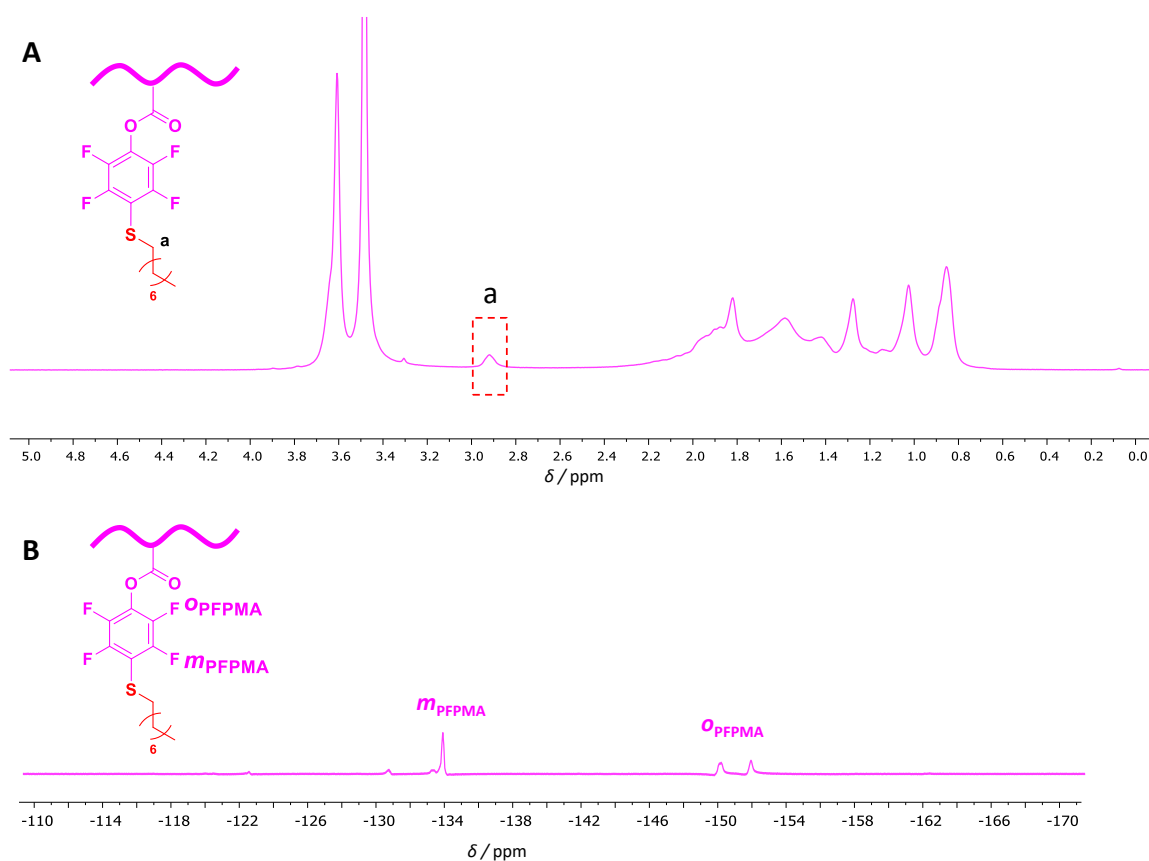


Figure 3.10. ^{19}F (B) and ^1H (A) NMR spectra after the reaction of polymer **1a** with 1 eq. of OT leading only to *para*-F substitution during nucleophilic thiol substitution reaction. Reprinted with permission from reference 85 from The Royal Society of Chemistry.

The polarity of the solvent used also has an effect on the orientation of substitution of the fluorine atoms in a nucleophilic thiol substitution reaction. It affects the interactions between the substituent R in case of $\text{C}_6\text{F}_5\text{R}$ and the thiol (the incoming nucleophile), wherein the *ortho* substitutions are significant when there is a strong bond formation in the non-polar solvent. But, in the current study, we utilize DMF for all reactions and this should

bring about the opposite effect. Therefore, under all the conditions utilized in our study, the order of substitutions of the fluorine atoms of PFPMA follow the order *para*, *meta* (mono), *meta* (di), and no reactivity of *ortho* fluorine atoms. Nevertheless, the mechanism of the order of substitution remains unclear at this point.

Finally, extending the concept, another precursor BCP P(nBMA-*r*-PFPMA)-*b*-P(S-*r*-PFS) (**5**) was synthesized by RAFT polymerization and using similar strategy as for BCP **2**, the RAFT end group was capped with 2-methoxy-6-methylbenzaldehyde to obtain BCP **5a** (Scheme 3.2). The characteristics of BCP **5a** are (calculated using similar procedure as for BCP **2a**): $M_{n,NMR} = 55300 \text{ g mol}^{-1}$; $M_{n,SEC} = 54100 \text{ g mol}^{-1}$; $D = 1.18$; $f_{PS};f_{PI} = 0.51:0.49$; % PFPMA and PFS incorporated = 6.8 mol% and 6 mol%, respectively. The ^1H , ^{19}F NMR spectra of **5a**, and the size-exclusion chromatograms (**5** and **5a**) are represented in Appendix A, Figure A10. Followed by this, using *Pathway 1*, **5a** was subjected to amidation using allylamine (^1H and ^{19}F NMR spectra: Appendix A, Figure A11 A, and Figure A12 A, respectively), furfurylamine (^1H and ^{19}F NMR spectra: Appendix A, Figure A11 B, and Figure A12 B, respectively), and norbornene methylamine (^1H and ^{19}F NMR spectra: Appendix A, Figure A11 C, and Figure A12 C, respectively). The presence of the respective ^1H peaks of the amines in each case, and the disappearance of the F-peaks belonging to the PFPMA moiety confirmed the successful amidation reactions.

3.4 Conclusion

Two bifunctional diblock copolymers P(MMA-*r*-PFPMA)-*b*-P(S-*r*-PFS) and P(nBMA-*r*-PFPMA)-*b*-P(S-*r*-PFS) containing PFPMA and PFS in the PMMA or PnBMA and PS blocks, respectively were synthesized by RAFT polymerization. Precise control was achieved over their molar masses ($\approx 50000 \text{ g mol}^{-1}$), dispersity and the functional group incorporation (PFPMA $\approx 8\%$ and PFS $\approx 5\%$). The end group stabilized P(MMA-*r*-PFPMA)-*b*-P(S-*r*-PFS) based BCP was used for preliminary investigations to understand the reactivity of PFPMA and PFS towards amines and thiols by amidation and PFTR, respectively. To prove the versatility of amidation and PFTR, four different amines (allylamine, furfurylamine, norbornene methylamine, and azido-PEG-amine), two thiols (octanethiol and mercaptoethanol) and a dual reactive aminoethanethiol were employed. Using *Pathway 1* (amidation on PFPMA followed by PFTR on PFS units), a small library of

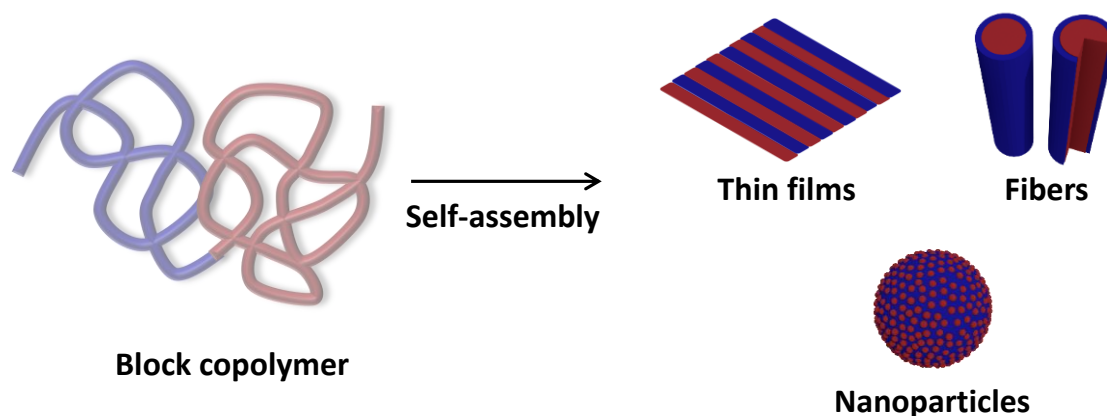
reactive functional BCPs was successfully obtained with a combination of all amines and thiols investigated. Subsequently, using *Pathway 2* (PFTR followed by amidation), the same could not be achieved owing to the reactivity of the fluorine atoms of PFPMA towards thiols. Under the standard PFTR conditions, PFPMA units were more susceptible to substitution by thiols compared to that of PFS. Furthermore, not only was PFPMA susceptible to PFTR, but also underwent substitution by thiols in its *meta*-F position. Due to the competing nature of PFPMA and PFS towards thiols, different parameters such as the reaction time, nature of the base and the stoichiometry of the thiol used were tuned to control the order of substitution. In any case, when both PFPMA and PFS units are present, 100% conversion of PFS towards PFTR could not be achieved without affecting the PFPMA units. But, when equimolar stoichiometry of the thiol and the PFPMA units were used in a mild basic condition (such as TEA), exclusive *para*-substituted PFPMA product was obtained that remains reactive towards amines in an amidation reaction. But, *meta*-substituted PFPMA moieties render them inactive towards amidation. The inertness of the *ortho*-F atom and the order of reactivity of all fluorine atoms of PFPMA towards thiol substitution was confirmed on subjecting the homopolymer P(MMA-*r*-PFPMA) in the absence of PFS units to both the thiols. In conclusion, the order of substitution of the fluorine atoms of two pentafluorophenyl groups towards thiol substitution reaction under the same conditions follows the order: *para* PFPMA > (mono) *meta* PFPMA > (di) *meta* PFPMA > *para* PFS.

Therefore, *Pathway 1* can be employed for the straightforward synthesis of a library of dual reactive BCPs using robust post-polymerization modification methods. This strategy can be widened for use with several BCP precursors, and a variety of interesting functional amines and thiols. On the contrary, although *Pathway 2* is not suitable in this context, certain interesting findings, such as the exclusive *para*-fluoro thiol substitution of PFPMA units, can be exploited for other applications. Taking advantage of this chemistry, we envisaged its use to design an amine-cleavable linker for the preparation of porous membranes (discussed in Chapter 4).

4. FABRICATION OF FUNCTIONAL NANOSTRUCTURED MATERIALS

4.1 Introduction

In the last several decades, intense research efforts have been dedicated towards understanding and bridging the structural gap between structures found in nature and simpler man-made micro- and nanomaterials. Towards this, significant development has been made in the bottom-up approach based on block copolymers (BCPs) with remarkable progress in their bulk self-assembly to obtain arbitrary nanostructures with smaller domain sizes. BCPs can be confined in 1 dimension (1D) as thin films, in 2D as electrospun fibers as well as in 3D in the form of nanoparticles (Scheme 4.1). The formation of thin films has been most exploited among the others, while 2D confinement has been investigated theoretically, and experimentally to a lesser extent.



Scheme 4.1. Self-assembly of block copolymers into thin films, fibers, and nanoparticles, i.e., 1D, 2D, and 3D confinement, respectively.

Parts of this chapter and the associated experimental section (Section 8.1 and Appendix B) are adapted or reproduced from reference 239: D. Varadharajan, H. Turgut, J. Lahann, H. Yabu, G. Delaittre, *Adv. Funct. Mater.*, 2018, adfm.201800846, *in press*. © WILEY-VCH Verlag GmbH & Co. KGaA. Parts of Section 4.3.3. were executed by Stefan Frech.

Furthermore, recent studies have indicated that the self-assembly of BCPs in solution is a viable technique to produce complex nanostructured nanoparticles with domain sizes in the sub-50 nm range.^{223–225} In the process of internal phase separation of BCPs in 3D confinement (i.e., spheres/particles), different morphologies can be obtained, *e.g.*, Janus,^{226–201} lamellae,^{167,179,224,227,228} cylinder,¹⁶⁵ or dot patterns.^{164,229,230} The multicompartment-based bulk, as well as chemical surface heterogeneities lead to the designation of such internally structured nanoparticles as “patchy”. Although Janus nanoparticles are the most common, whose main peculiarity lies in their interfacial properties, high-order internal structuration may be useful for mimicking natural phenomena or for interacting in a more efficient way with biological systems. For example, they could be used for the controlled docking of specific complementary enzymes on defined patches leading to enhanced cascade reactions due to their spatial proximity.²³¹

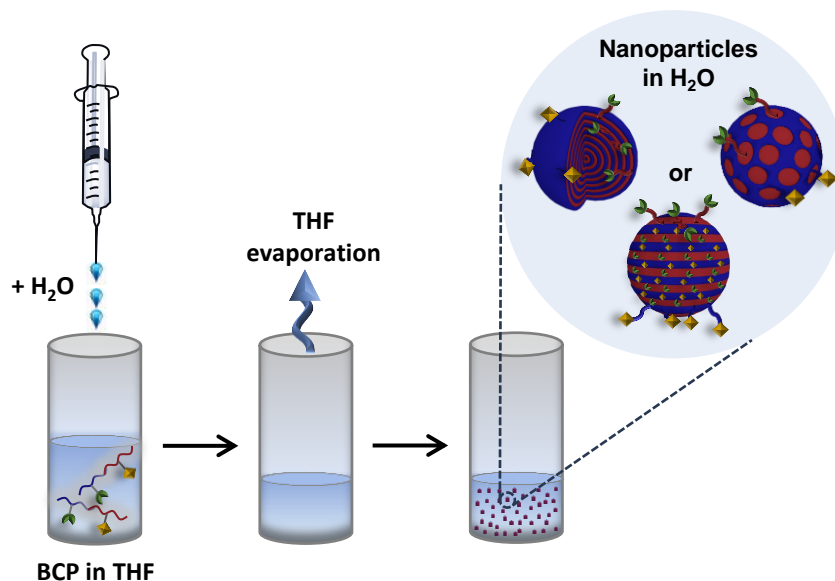
Although such patchy nanoparticles have been in existence, the currently available synthetic BCP nanoparticles that bear high spatial and structural control are by-and-large restricted to polymers^{155,167,232} and blends²⁰⁶ that are devoid of functionality. Among the few examples of functional patchy nanoparticles, Robb *et al.* describe the use of nanoparticles from post-modified poly(allyl glycidyl ether)-*b*-polylactide as modular delivery vehicles.¹⁹⁷ Recently, Hirai *et al.* reported the preparation of virus-like particles using an asymmetric polystyrene-*b*-poly(*t*-butyl acrylate) BCP²³³ and Schmidt *et al.* that of reactive ellipsoidal striped nanoparticles from polystyrene-*b*-poly(2-vinylpyridine) BCP blended with analogous functional homopolymers.²⁰⁷

Hence, a large part of this chapter describes the preparation of patchy nanoparticles using BCPs that would ultimately possess precisely patterned functional anchors at their surfaces. The last section of this chapter outlines the synthetic versatility and capability of BCPs for fabricating porous membranes.

4.2 Aims and Methods

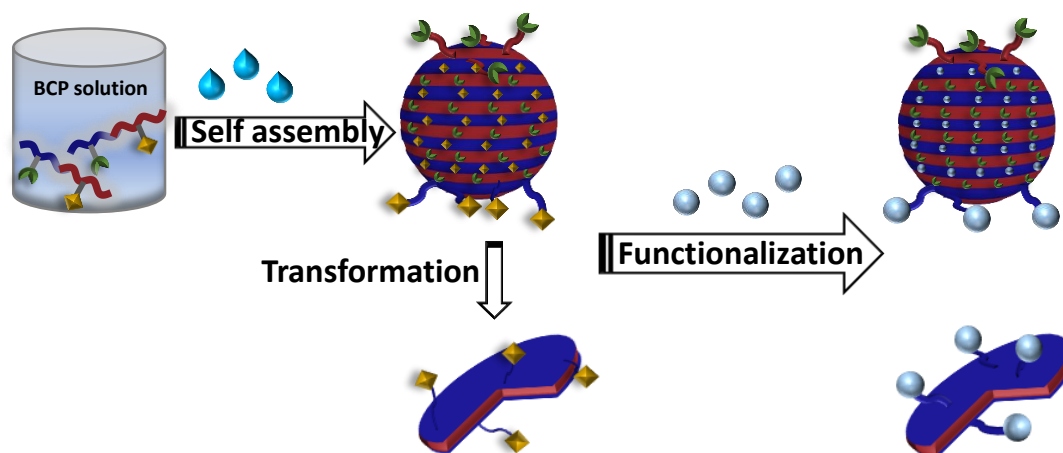
Here, considering the great potential of functional patchy BCP nanoparticles, we aimed at studying the evolution and control of phase separation morphologies of different functional BCPs during the process of nanoparticle formation by a simple nanoprecipitation method

termed as self-organized precipitation (SORP, (Scheme 4.2)).¹⁸⁰ Firstly, the two BCPs based on P(MMA-*r*-PFPMA)-*b*-P(S-*r*-PFS) and P(nBMA-*r*-PFPMA)-*b*-P(S-*r*-PFS) discussed in Chapter 3 were used for the preparation of nanoparticles and their internal phase separation structures was observed. Next, another small library of structurally identical polystyrene-*b*-polyisoprene (PS-*b*-PI), which differ only by the nature of a small fraction of functional groups introduced in the PS segment, were studied.



Scheme 4.2. Schematic representation of self-organized precipitation (SORP) utilized for the preparation of patchy nanoparticles.

For the PS-*b*-PI BCP system, various aspects that affect the morphology of phase separation were taken into consideration: (i) the synthetic strategy used to synthesize the polymer, (ii) the mole fraction and nature of the functional groups incorporated and (iii) conditions used for the preparation of nanoparticles to acquire tailored morphologies and sizes (solvent, concentration, blending). Further, focus has been laid on obtaining striped nanoparticles that have domains in the 15–30 nm range, which could potentially be used as immobilization platforms for chemical patterning, or for (bio)molecules (Scheme 4.3). Finally, the accessibility of surface reactive groups for domain-specific decoration, as well as the generation of surface-reactive anisotropic daughter nanoparticles, i.e., nanodiscs, by selective immobilization and selective elimination (SISE) of the patchy nanoparticles has been demonstrated (Scheme 4.3).



Scheme 4.3. Overall scheme representing the preparation of patchy nanoparticles from functional block copolymers (BCPs), the supramolecular transformation of the striped particles into nanodiscs, and their surface functionalization.

4.3 Results and Discussion

4.3.1 Selection of the BCP system

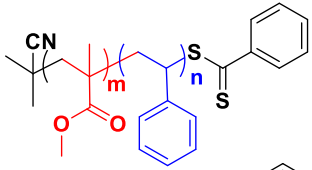
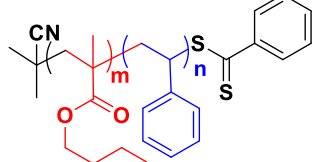
To enable the fabrication of nanoparticles with surface structuration, three hydrophobic functional BCP systems based on (i) PMMA-*b*-PS, (ii) PnBMA-*b*-PS, and (iii) PS-*b*-PI were tested. For a BCP in the melt, equal volume fractions of the blocks lead to lamellar phase separation in the solid state.³ Therefore, the volume fractions of each block of the BCPs was kept close to 0.5 because we finally aim at obtaining unidirectional stacked lamellae internal structuration. The targeted molar masses of the BCPs were *ca.* 50 kg mol⁻¹ to enable the formation of domains in the sub-50 nm range, which is relevant for biomimetic applications as discussed in Section 4.1. For immobilization, different functional groups were incorporated for each of the BCP systems: (i) for the PMMA-*b*-PS and PnBMA-*b*-PS BCPs, their functional analogues described in Chapter 3 were intended to be used, and (ii) a small set of functional PS-*b*-PI BCPs possessing halide, azide, and pentafluorophenylalkyl moieties in the PS block was used. The amount of functional groups in each of the blocks for all the BCP systems were kept low (< 10 mol%) so as to impart functionality, while likely not perturbing the phase separation behaviour of the original BCP scaffold. This is based on observations in our group of a similar set of BCPs, which

revealed that in the solid state these BCPs lead to lamellar morphologies with only minor changes in the interlamellae distance.^{234,235}

4.3.2 Preparation of surface reactive nanostructured nanoparticles

Nanoparticles were prepared by SORP as shown in Scheme 4.2. It involves the use of a good solvent to molecularly dissolve the block copolymer. Then, a miscible non-solvent of both blocks is added (usually water), leading to the formation of nanoparticles. Within these nanoparticles in 3D confinement, the block copolymer eventually is in the solid state after evaporation of the good solvent, and the two blocks phase-separate. Note that in this technique, both segments are excluded of the continuous phase (*i.e.*, water), as opposed to classic nanoprecipitation of amphiphilic diblock copolymers. In our case, tetrahydrofuran (THF) was used as the good solvent owing to its suitability to dissolve both BCP segments in all the investigated systems, its miscibility with water, and its volatility. For potential applications, we targeted an average particle size of approximately 150–300 nm as it usually offers a good compromise between high surface area and good processability (*e.g.*, separation by centrifugation). This size range also permits the coexistence of several repeating patterns with a period of ca. 30–50 nm within the same particle. The particle sizes were tuned by varying the concentration of the polymer solution and the mixing ratio of good solvent to non-solvent.

2.8.3.3 PMMA-*b*-PS and PnBMA-*b*-PS block copolymer systems

		$f_{(PS)}$	$M_{n,NMR}$ (g mol ⁻¹)	\mathcal{D}
PMMA- <i>b</i> -PS		0.55	42500	1.25
PnBMA- <i>b</i> -PS		0.52	46000	1.19

Scheme 4.4. Structure and characteristics of the PMMA-*b*-PS and PnBMA-*b*-PS block copolymers synthesized and utilized for the current study. f_{PS} is the volume fraction of the PS block. $M_{n,NMR}$ is the number-average molar mass determined by a combination of SEC and NMR. \mathcal{D} is the dispersity value determined by SEC.

Keeping the above parameters in mind, nanoparticles were first prepared using PMMA-*b*-PS block copolymer (Scheme 4.4). This BCP was chosen as it is relatively easy to synthesize (refer to Chapter 3) and is hydrophobic making it a good candidate for the preparation of nanoparticles in THF/water mixture. The non-functional analogue was initially used in an attempt to understand the process of phase separation of such BCPs leading to different internal structures. Subsequently, nanoparticles were prepared using different concentrations of the BCPs (5, 1, and 0.1 mg mL⁻¹ in THF) by SORP using a THF/water mixture of 1:1 (Figure 4.1 A-C). At any given polymer concentration, nanoparticles of sizes between 150-400 nm were obtained which is in the desirable range. But, it is clear that no surface structuration is visible at the surface implying the presence of only one of the blocks of the BCP at the interface. To understand this type of phase separation behavior, it is important to understand the role of solubility parameters (SPs) of the respective blocks that influences the morphology of phase separation.²⁰⁵ SP describes the affinity of a particular segment of a polymer towards water during the formation on nanoparticles, *i.e.*, their rate of precipitation on addition of water during SORP. Motoyoshi *et al.* described the dependence of SP on the phase separation structures in blends of PI with various homopolymers.²⁰⁵ Accordingly, in comparison to the solubility parameter of water (47.9 MPa^{1/2}), that of PI, PS, and

PMMA are 16.5, 18.6, and 19.3 MPa^{1/2}, respectively. Thus, a blend of PI and PMMA homopolymers is reported to form core-shell particles due to the higher SP of PMMA. In our case, although the SPs of PS and PMMA are similar, we hypothesize that the relatively high SP of PMMA makes it preferential at the surface owing to the method of nanoparticle preparation that involves water. As this renders the PMMA-*b*-PS BCP system incapable of forming nanoparticles with both segments (PS and PMMA) at the surface of the nanoparticle, the functional analogues of this BCP (discussed in Chapter 3) were not further tested.

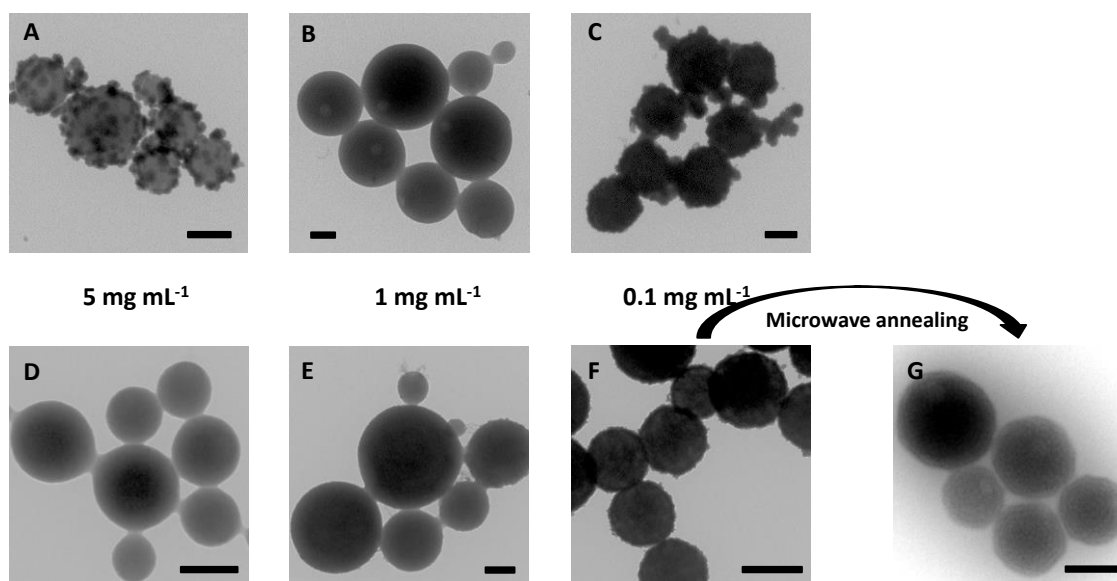


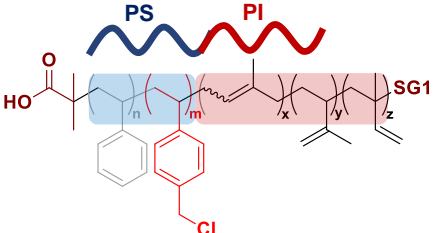
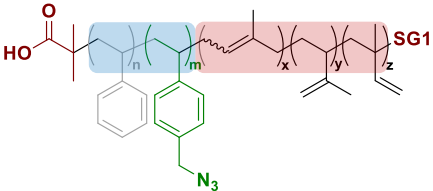
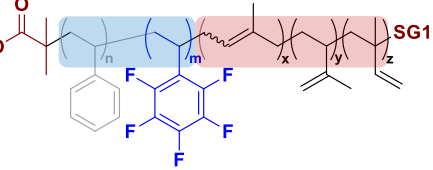
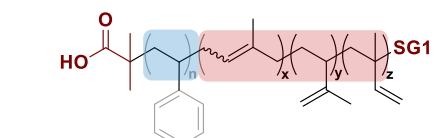
Figure 4.1. Transmission electron microscope (TEM) images of PMMA-*b*-PS (A-C) and PnBMA-*b*-PS (D-G) nanoparticles prepared by SORP with polymer concentrations of 5 mg mL⁻¹ (A,D), 1 mg mL⁻¹ (B,E) and 0.1 mg mL⁻¹ (C,F) in THF with THF/water ratio of 1:1. (G) TEM image of the microwave annealed nanoparticles shown in (F). Scale bars represent 200 nm.

Consequently, another BCP system PnBMA-*b*-PS was employed considering the lower SP PnBMA segment (18.0 MPa^{1/2}). Owing to the SPs of PI and PnBMA, blends of PI and PnBMA have been reported to form Janus particles instead of core-shell particles as in the case of PI/PMMA blends.²⁰⁵ Therefore, as for PMMA-*b*-PS, SORP was used to prepare nanoparticles from PnBMA-*b*-PS using different polymer concentrations (5, 1, and 0.1 mg mL⁻¹) in THF and a THF/water ratio of 1:1 (Figure 4.1 D-F). Contrary to our expectation, it can be seen that under all conditions, the PnBMA segment prefers to remain at the surface of the nanoparticle forming core-shell nanoparticles. As several efforts have been made to

tune the morphologies obtained on BCP phase separation by the use of external fields,^{236,237} we attempted to transform the core-shell nanoparticles (Figure 4.1 F) to be able to bring both PS and PnBMA segments at the surface of the nanoparticles. Among several annealing methods used for this purpose, for the first time Higuchi *et al.* reported the use of microwave annealing to transform the random structures in PS-*b*-PI nanoparticles to thermodynamically stable structures within minutes.²³⁸ As microwave annealing can lead to the acceleration of phase separation in BCPs both at the surface and the interior of the nanoparticle, we applied microwave annealing conditions to the PnBMA-*b*-PS nanoparticles (seen in Figure 4.1 F) to obtain nanoparticles as seen in Figure 4.1 G. Obviously, a transformation in the internal structures to onion-like structures is visible. Unfortunately, even after 15 minutes of subjecting the particles to microwave annealing, no further transformation to stacked-lamellae structures was observed. Although this BCP system shows more potential towards obtaining the desired stacked lamellae structured nanoparticles, it was not investigated further. But, in order to understand the influence of several parameters that affect the formation of different internal structures during BCP self-assembly, and ultimately obtain the desired surface reactive nanostructured nanoparticles (or patchy nanoparticles), a simpler well-established PS-*b*-PI BCP was evaluated as elaborated next.

2.8.3.4 PS-*b*-PI block copolymer system

The PS-*b*-PI BCP scaffold was chosen for two reasons. First and foremost, this is the first system which has been shown to yield nanoparticles with internal nanostructuring by SORP.¹⁸⁰

		$m/(n+m)$	f_{PS}	$M_{n,NMR}$	\mathcal{D}
P1		0.06	0.47	48.9	1.32
P2		0.06	0.47	48.8	1.35
P3		0.04	0.50	47.3	1.32
P4		-	0.48	43.0	1.35

Scheme 4.5. Structure and characteristics of the PS-*b*-PI block copolymers synthesized and utilized for the current study. f_{PS} is the volume fraction of the PS block. $M_{n,NMR}$ is the number-average molar mass determined by a combination of SEC and NMR. \mathcal{D} is the dispersity value determined by SEC. The ternary molar ratio of isomeric isoprene units $x:y:z$ is typically equal to 0.80:0.13:0.07.

Secondly, we recently optimized SG1 nitroxide-mediated polymerization (NMP) as a straightforward route for the synthesis of functional PS-*b*-PI with reasonable dispersity.²³⁴ Therefore, a small set of PS-*b*-PI block copolymers was developed that includes halide (**P1**), azide (**P2**), and pentafluorophenylalkyl (**P3**) moieties in the PS block (Scheme 4.5). The selected functional comonomers were chosen such that they structurally closely resemble the PS backbone, yet introduce sufficient reactivity at the surface of the nanoparticles for precise molecular immobilization.

2.8.3.5 Evolution of hydrodynamic diameters of BCP nanoparticles

Followed by the synthesis of the functional PS-*b*-PI BCPs, nanoparticles were prepared by a simple nanoprecipitation method called SORP. As mentioned above, tetrahydrofuran (THF) was used as the good solvent owing to its suitability to dissolve both PS and PI segments, its miscibility with water, and its volatility. The incorporation of a small amount of functional monomer in the PS block of **P1–3** did not change the overall solubility in THF. However, the concentration of the polymer solution and the mixing ratio of good solvent to non-solvent exerted an influence on particle size (see below). As mentioned in Section 4.3.2, we targeted particle sizes of approximately 150-300 nm.

In general, the process of formation of nanoparticles is based on the principle of nucleation, where the BCPs are first dissolved in a good solvent and an increase in the amount of non-solvent causes the compact folding of polymer chains into small nuclei.¹⁶² The particle sizes are further governed by the concentration of the polymer solution and the solubility of both blocks of the BCP in the THF/water mixture. During the formation of nanoparticles, THF was slowly allowed to evaporate, and that in turn decreased the solubility of the hydrophobic BCPs **P1–3**. As it is already known that the hydrodynamic diameters of non-functional PS-*b*-PI influences the internal phase-separated structures of the nanoparticles,^{155,166} we conducted a brief study focusing on the size dependence of nanoparticles made of functional BCPs **P1–3**. Different preparation conditions were evaluated for each BCP (see Table 4.1): two initial polymer concentrations in THF (0.1 and 1.0 mg mL⁻¹) and three THF:water ratios (1:3, 1:1, and 3:1 vol/vol). In each of the cases, the particles sizes were measured both by DLS and by TEM (using statistical analysis). Refer to Figure B1, Figure B2, and Figure B3 in Appendix B for a comparison of the size distribution of the nanoparticles obtained from BCPs **P1**, **P2**, and **P3**, respectively by DLS (intensity- and number-based), and TEM.

Table 4.1. Summary of different conditions used to prepare the functional nanoparticles and their Z-average hydrodynamic diameter as measured by DLS (D_h (DLS)) and particle sizes obtained from TEM by statistical analysis (D (TEM)).

Polymer	Polymer conc. mg mL ⁻¹	Entry	% THF	D_h (DLS) nm	PDI (DLS)	D (TEM) nm	PDI (TEM)
P1	1	1	25	150	0.232	417	0.452
		2	50	223	0.219	362	0.317
		3	75	234	0.173	436	0.427
	0.1	4	25	183	0.080	170	0.099
		5	50	168	0.214	210	0.057
		6	75	256	0.102	237	0.040
P2	1	7	25	203	0.175	390	0.302
		8	50	1676	0.667	1066	0.082
		9	75	2885	0.764	1360	0.077
	0.1	10	25	350	0.309	217	0.126
		11	50	1074	0.429	1125	0.073
		12	75	2968	0.803	2010	0.129
P3	1	13	25	227	0.106	199	0.148
		14	50	293	0.120	147	0.045
		15	75	207	0.054	200	0.066
	0.1	16	25	136	0.022	125	0.034
		17	50	359	0.110	295	0.017
		18	75	187	0.019	215	0.037

Four main trends were witnessed (Figure 4.2): (i) Firstly, all nanoparticles prepared with a THF-to-water content of 1:3 vol/vol were within the same hydrodynamic diameter regime, with most of them in the 150–250 nm range, irrespective of the polymer concentration (see Figure 1 at 25 vol% THF and Table 4.1, Entries 1, 4, 7, 10, 13, and 16), (ii) Within the range of tested conditions, the polymer concentration did not have a marked impact on the hydrodynamic diameters, (iii) The hydrodynamic diameters for nanoparticles prepared from BCPs with chloromethylphenyl (**P1**) and pentafluorophenyl (**P3**) functionalities were rather insensitive to preparation conditions, and (iv) BCP **P2**, with azidomethylphenyl functionality, behaved very differently from the **P1** and **P3** during nanoprecipitation. Indeed, while nanoparticles prepared from the former ones remained within the same size

domain under all studied conditions, nanoparticles prepared with **P2** underwent a significant size increase with increasing THF content to actually reach micrometer range at THF:water ratios of 1:1 and 3:1 vol/vol.

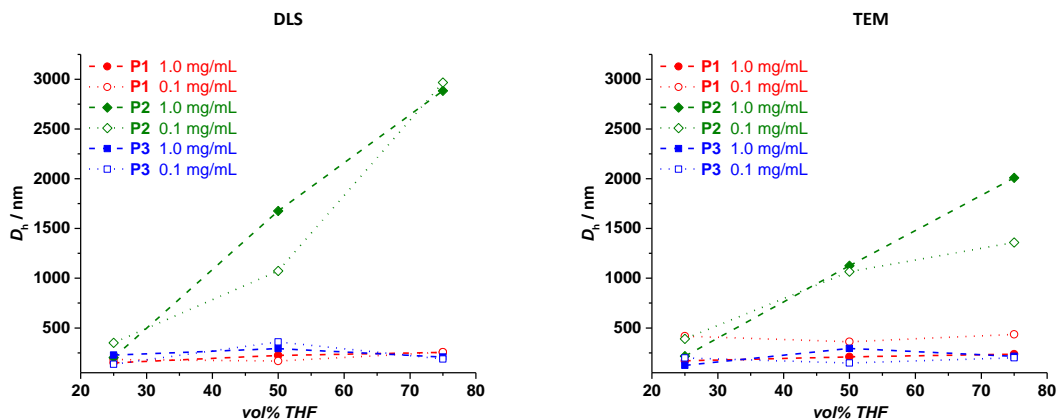


Figure 4.2. Evolution of the intensity-average hydrodynamic diameters obtained by DLS (DLS) and particle sizes from TEM statistical analysis (TEM) of nanoparticles during SORP with increasing THF content (25, 50, 75%) prepared from BCPs **P1–3** at different polymer concentrations (0.1 and 1 mg mL^{-1}). Reproduced from reference 239.

The particle size distribution obtained by TEM by statistical analysis (100 TEM images with approximately 100 particles each were taken, Appendix B, Figure B1, Figure B3 (histogram)) was within the range obtained by DLS (intensity-based, Figure B1, Figure B3 (black dotted line)) for BCPs **P1** and **P3**. Deviations were seen in the case of **P2** (Appendix B, Figure B2). But, as expected, the diameters obtained from DLS follow the order $D_{\text{intensity}} > D_{\text{number}}$ in most cases for BCPs **P1–P3** (see Appendix B, Figure B1, Figure B2, and Figure B3, black dotted line vs black solid line). Additionally, the hydrodynamic diameters from DLS (intensity mean) were almost always higher than those obtained by statistical analysis of TEM images (refer to Appendix B, Figure B1, Figure B2, and Figure B3, black dotted line vs histogram). Nevertheless, the overall trend of evolution of hydrodynamic diameters obtained from DLS and TEM was similar, as clearly visualized in Figure 4.2.

The nature of the functional comonomers may explain such a behavior. Since the particles are formed via a nucleation and growth process during THF evaporation,¹⁶² an increasing THF content, *i.e.*, an extended evaporation time of THF, should lead to larger particles. On the contrary, when a low THF content is used during nanoprecipitation, that is a large

amount of non-solvent, the polymer chains should quickly collapse, thereby creating a large number of nuclei and consequently smaller particles. This was for instance the case of **P3**, which possesses the most hydrophobic type of functional moiety (pentafluorophenylalkyl). However, **P2** possesses rather polar azide moieties (dipoles), which may retard chain collapse by having a relatively higher affinity towards both water and THF. Hence, only a small number of nuclei are formed and the particles grow to a larger size as THF evaporates. In any case, it was possible to obtain nanoparticles within the desired size range for all functional PS-*b*-PI polymers. Next, the internal phase separation of the nanoparticles, and their related surface patterns we aimed at obtaining for precise immobilization was studied.

2.8.3.6 Study of the morphologies of internally phase-separated BCP nanoparticles

The internal phase separation structures were observed for BCPs **P1-3** as well as two non-functional PS-*b*-PI analogues (**P4**, synthesized by NMP, and **P5**, commercial, synthesized by anionic polymerization). They were observed using TEM or scanning TEM (STEM) after reacting the nanoparticles with an aqueous solution of osmium tetroxide (OsO₄). OsO₄ was used to chemically crosslink the double bonds present in the PI block and its corresponding phases in a selective manner. The presence of Os in the PI-containing domains also leads to contrast in electron microscopy. In the present study, all classic transmission electron microscopy (TEM) pictures were acquired in bright field (BF) mode, while STEM images were obtained in dark field (DF) mode. Therefore, in the TEM images, dark and bright regions represent the PI and PS blocks, respectively, and vice versa in STEM images.

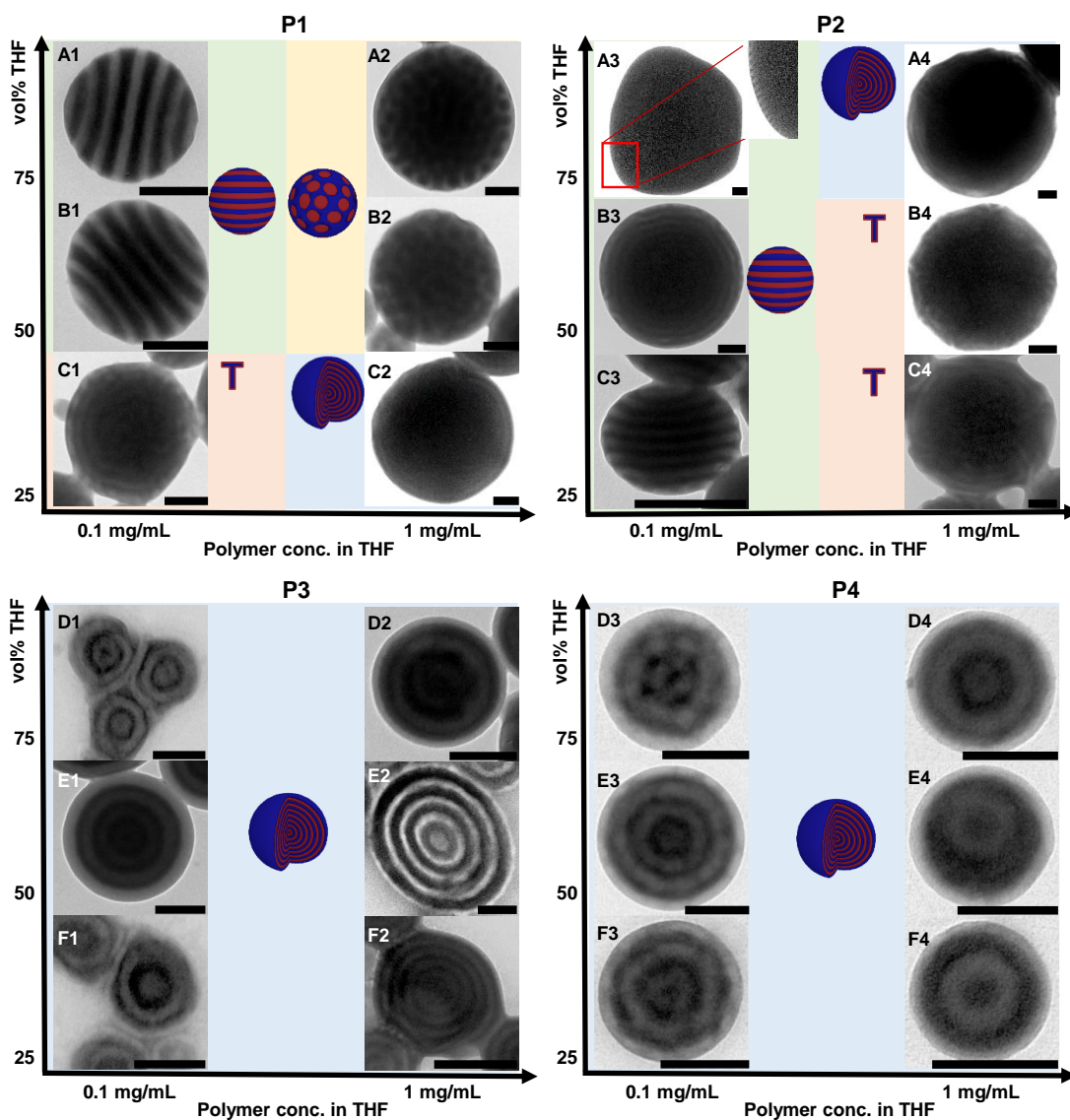


Figure 4.3. Bright field transmission electron microscopy images for nanoparticles obtained by SORP with BCPs **P1–4** in various conditions. E2 is a cross-sectional image of a nanoparticle. The dark regions represent the PI domains. All scale bars represent 100 nm. The blue and red domains in the schematic representations refer to the PS and PI blocks, respectively. “T” stands for transformation structures or disordered structures. Lower magnification TEM images for BCPs **P1–3** displaying larger population of nanoparticles for each sample can be found in Figure B4, Figure B5, and Figure B6 respectively. Reproduced from reference 239.

At 0.1 mg mL^{-1} (Figure 4.3, columns (A–F)1 and (A–F)3), all nanoparticles internally phase separated to form stacked lamellae structures (*i.e.*, striped particles), onion-like par-

ticles, or intermediate morphologies termed “T” as they correspond to states of transformation between two well-defined structures. An increase in concentration to 1 mg mL⁻¹ led to clear onion-like structures in a majority of cases, *e.g.*, for all **P3** and **P4** nanoparticles (Figure 4.3, (D–F)2 and (D–F)4), as well as “T” structures between onion-like and stacked lamellae (Figure 4.3, B4 and C4). In addition, internal spherical morphologies were also observed (Figure 4.3, A2 and B2).

2.8.3.7 Understanding the morphologies of phase-separation in the nanoparticles

The morphology of phase separation is governed by the Flory-Huggins interaction parameter (χ) between the two blocks, the SPs of the respective blocks, the volume fractions of the polymer segments (f), as well as the effect of 3D confinement of the polymeric chains at the nanoscale.^{155,170,240} As the SPs of both polystyrene (PS) and polyisoprene (PI) are similar,²⁰⁵ their precipitation rates should be similar upon addition of water during SORP. This is therefore expected to result in simultaneous precipitation of both segments, leading to morphologies containing both PS and PI at the surface, at least under certain conditions of concentration, temperature, and good solvent/non-solvent ratio. This was the case for PS-*b*-PI BCPs which are devoid of functional moieties able to alter SPs.¹⁵⁵ Clearly, with the currently considered BCPs **P1–3**, chloromethyl, azidomethyl, and PFP substituents played an important role since they led to different morphologies in identical conditions, as seen in Figure 4.3. A previous study by Li *et al.* described the effect of selective solvent that swells specific polymer domains and alters the effective volume fraction ratio and curvature between polymer segments, thereby inducing morphological changes.¹⁶⁹ It can be postulated that the presence of the functional groups do induce a modification of the swelling behavior of the PS phase with THF. Based on the pseudo phase diagram represented in Figure 4.3, the concentration of polymer as well as the amount of THF significantly affected the morphologies. Various defined morphologies finally leading to stacked lamellae were only observed at the lower polymer concentration of 0.1 mg mL⁻¹.

Additionally, varying the amount of THF had an effect on the internal phase separation only in the case of **P1** and **P2**, while **P3** remained unperturbed. However, **P3** did not form stacked lamellae structures under any of the conditions tested. Due to the hydrophobic nature of PFS, **P3** precipitates as soon as water is added (see above), while the presence of

more polar chloro and azido groups in **P1** and **P2**, respectively, possibly induces slower precipitation, enhancing the formation of stacked lamellae structured nanoparticles. As **P1** lies between **P2** and **P3** with respect to the hydrophilicity of the comonomer, such higher ordered structures form at 50 and 75% THF (Figure 4.3 A1 and B1), while they already appear at 25% THF for **P2** (Figure 4.3 C3).

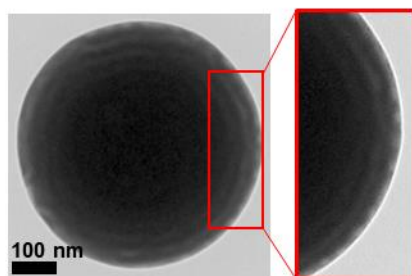


Figure 4.4. An enlarged view of Figure 4.3 B3 showing the outermost layer of the nanoparticles obtained from **P2** at 0.1 mg mL^{-1} and 50 vol% of THF. Reproduced from reference 239.

Apart from these observed phenomena, **P2** showed distinct deviations from other polymers. Although at a concentration of 0.1 mg mL^{-1} with 25% THF (Figure 4.3, C3) **P2** formed clear stacked lamellae structured nanoparticles, such behavior became less apparent at 50 and 75% (Figure 4.3, B3 and A3). The internal structure of these increasingly larger particles was not lamellar. But, a closer look at the surface of these nanoparticles revealed the presence of both P(S-*co*-AMS) and PI blocks (see Figure 4.3, A3 inset, as well as Figure 4.4 for an enlarged view), allowing their surface structure to qualify as lamellae. There are clear interfacial effects, which are in analogy with those observed for sufficiently thick block copolymer films in which atmosphere-film and film-substrate interactions lead to differing phase organizations in the bulk and at the interfaces. In a nutshell, the final morphologies are certainly the result of a complex interaction between relative swelling by THF, interfacial interactions with the continuously evolving THF/water mixture, concentration effects, global chain and individual segment collapse kinetics, among others.

Interestingly, a constant observation was that in all cases where onion-like structures are encountered (Figure 4.3, C2, A4, and rows D–F), the outermost layer always consisted of PS, as distinguished by the light region. Strikingly, this observation contradicts the fact that

the lower interfacial surface tension between PI and water (55.8 mN/m) compared to that of PS and water (58 mN/m) would lead to formation of nanoparticles with PI as the outermost layer.^{168,241} The current observation was indeed the reverse of previously reported SORP results for PS-*b*-PI BCPs. Such a reversal in the interfacial behavior came from the presence of the carboxylic acid end group attached to the extremity of the PS block, which originates from the NMP initiator employed for the synthesis (see Section 8.2). This highly polar moiety drives the formation of onion-like phase separated structures pulling the PS block towards the interface with the polar liquid phase. This hypothesis was confirmed by comparing the internal structure of nanoparticles produced by nanoprecipitation with the NMP-made PS-*b*-PI **P4** without any functional comonomer unit, to those obtained in the same conditions with a commercial PS-*b*-PI BCP (**P5**), which was synthesized by anionic polymerization bearing no functional end or pendant group. As expected, in the latter case (**P5**), onion-like structures were observed with PI as the outermost layer, as represented by the dark regions in Figure 4.5 and as opposed to Figure 4.3 (E3–4).

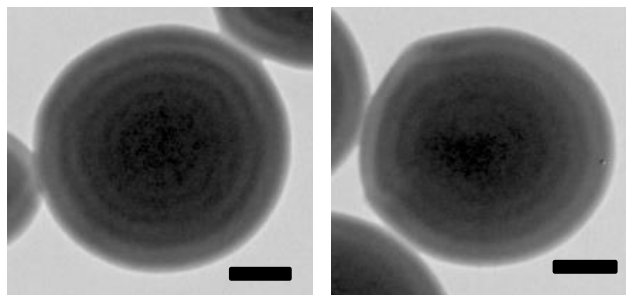


Figure 4.5. Bright field TEM images for nanoparticles obtained by SORP with commercial BCP **P5**, at 50 vol% THF and a polymer concentration of 0.1 mg mL⁻¹ (left) or 1 mg mL⁻¹ (right). Dark regions represent PI domains due to osmium staining. Scale bars represent 100 nm. Reproduced from reference 239.

In conclusion, it was possible to produce the targeted striped nanoparticles in the range of 150–300 nm with functional BCPs **P1** (Figure 4.3, A1 and B1) and **P2** (Figure 4.3, C3). However, under any of the stipulated conditions, **P3** did not form nanoparticles with stacked lamellae structures, and rather formed onion-like structures with the PS phase constituting the outermost layer under all investigated SORP conditions. As previously discussed in Section 2.5.4 and 4.1, BCP blends can be used to alter the phase-separation morphologies, introduce specific functional anchors, and/or modify the physical or chemical

properties of the nanostructured nanoparticles. Therefore, this strategy was implemented to enable the formation of lamellae structured particles using BCP **P3**.

2.8.3.8 Effect on the phase-separation morphology using BCP blends

From previous reports, it is known that mixing BCP blend systems can lead to a variety of phase-separation morphologies.²⁰⁶ We thus assumed that blending **P3** with a well-chosen block copolymer could lead to the desired functional striped nanoparticles. As mentioned above, BCPs **P1-3** synthesized by NMP possess a carboxylic acid group at the end of the PS segment that seemed to drive this block towards the outside of onion-like structure. So, **P5** (non-functional PS-*b*-PI devoid of a carboxylic acid end group) was chosen for blending with **P3** because of its ability to undergo phase separation to form onion-structured nanoparticles where PI constitutes the outermost layer (Figure 4.5), unlike in **P3** where PS preferably forms the outermost layer.

Table 4.2. Composition of block copolymer blends of **P1-3** and non-functional PS-*b*-PI **P5**.

Polymer mixtures	% THF for SORP	Blend number	Mixing ratio (weight)
P5:P1	25	1	3:1
		2	1:1
		3	1:3
P5:P2	50	4	3:1
		5	1:1
		6	1:3
P5:P3	75	7	3:1
		8	1:1
		9	1:3

When two such block copolymers as **P3** and **P5** that form onion-like structures independently with opposite polymer segments at the interface are mixed, they would compete for the nanoparticle–water interface and lead to nanoparticles (equally) presenting both segments at the surface. Utilizing this concept, BCP blends were prepared using **P3** and **P5** (Table 4.2, blends 7-9) in order to obtain nanoparticles exhibiting stacked lamellae internal structures.

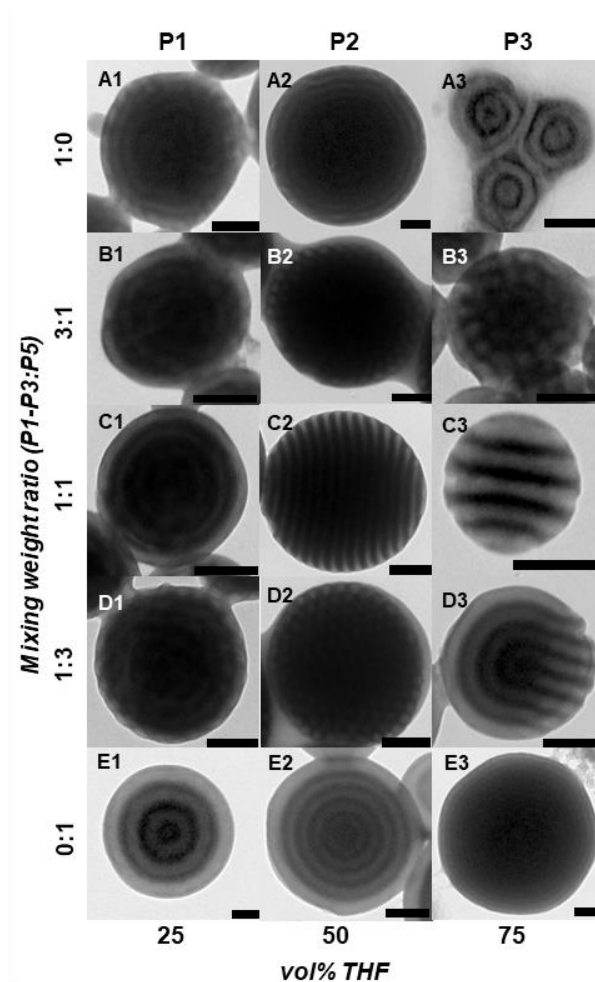


Figure 4.6. Bright field TEM images for nanoparticles obtained by SORP with mixtures of custom-made BCPs **P1–3** and commercial BCP **P5**, at various weight ratios. THF contents of 25, 50, and 75 vol% were employed for blends with **P1**, **P2**, and **P3**, respectively. All scale bars represent 100 nm. Lower magnification TEM images displaying larger population of nanoparticles prepared from blends of **P1–3** with **P5** (here, rows B, C, and D) can be found in Figure B7. Reproduced from reference 239.

This was further extended to BCP blends of **P5** with **P1** and **P2** to better understand the transformation in internal phase-separation structures. As the functional BCPs **P1–3** and **P5** both contain the same polymer segments, they should precipitate together upon evaporation of THF leading to the formation of polymer blended nanoparticles. Since it was observed in the previous section that only lower polymer concentrations lead to striped particles, nanoparticles of BCP blends were prepared by mixing different weight ratios of each **P1–3** and **P5** at 0.1 mg mL^{-1} . The mixing ratio of THF:water for SORP was selected based on the condition that led to formation of nanoparticles with onion-like structures.

But, as **P1** and **P2** did not form nanoparticles with clear onion-like structures, the closest conditions leading to such a structure, *i.e.*, transformation from onion-like towards more ordered structures was chosen (Figure 4.3 C1 and B3, respectively for **P1** and **P2**). The chosen condition in case of **P1** additionally helped validate our hypothesis (discussed later).

As expected, nanoparticles formed from BCP blends showed morphological transformations in the internal structure (Figure 4.6, B1–D1, B2–D2, and C3–D3) in comparison to BCP nanoparticles obtained from single block copolymers (Figure 4.6, A1–A3 and E1–E3). For example, at 0.1 mg mL^{-1} and 75 vol% THF, both **P3** and **P5** independently formed nanoparticles exhibiting onion-like structures with an outermost layer composed of PS or PI (Figure 4.6, A3 or E3), respectively. Yet, when a 1:1 blend of **P3:P5** was prepared (Table 4.2, blend 8), the nanoparticles formed by simultaneous precipitation and self-assembly of both BCPs featured stacked lamellae structures (Figure 4, C3, **NP3**). Similar transformation in the internal structures was obvious on mixing **P2** with **P5** at a 1:1 weight ratio (Table 4.2, blend 4; Figure 4.6, C2). It must be noted that in this case, although **P2** does not independently form highly defined onion-like structures (Figure 4.3, B3), it constitutes the bulk of the nanoparticle, while the surface displayed a mixed PS/PI composition (Figure 4.6, A2 and Figure 4.4). In this case, blending promoted the stacked lamellae structure to form throughout the particles.

It is interesting to note that such transformation in the internal structures only held true for specific mixing ratios. Indeed, other blends of **P2** (3:1 and 1:3; Figure 4.6, B2 and D2) or **P3** (3:1 and 1:3; Figure 4.6, B3 and D3) with **P5** did not lead to pure stacked lamellae structures. Mixing **P1** in conditions where it does not form onion-like structures with PS as the outermost layer (Figure 4.6, A1) together with **P5** (Figure 4.6, E1) did not produce blend nanoparticles with the desired striped morphology (Figure 4.6, B1–D1), validating this hypothesis. Finally, electron tomography was performed to reconstruct a 3D model of the **NP3** nanoparticles to visualize the exact composition of the phases present in the internal structures, confirming the formation of striped particles (Figure 4.7).

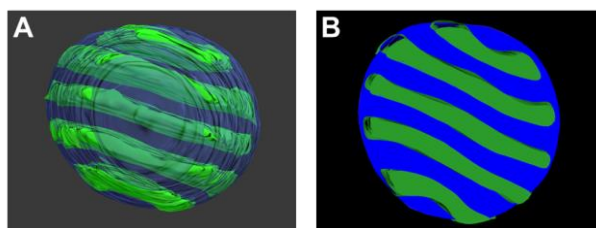


Figure 4.7. Electron tomography images **NP3** nanoparticles showing PS and PI phases, where PS phases are blue and the PI phases are represented in green (A); 3D reconstructed cross-sectional half cut image of the PS and PI phases (B). Reproduced from reference 239.

The current set of blends is the first example of nanoparticles made by AB+A'B type BCP mixtures. These sets of blends showed the influence of functional moieties in driving the transformation of internal structures, since mixing block copolymers based essentially on the same motifs, yet differing by a small fraction of functional moieties, led to a range of well-defined morphologies and their intermediate states. The blends of **P3** and **P5** among others was the best representative of the phenomenon described to obtain striped particles **NP3** (Figure 4.6 C3). Consequently, they were further tested for their surface-reactivity for precise immobilization.

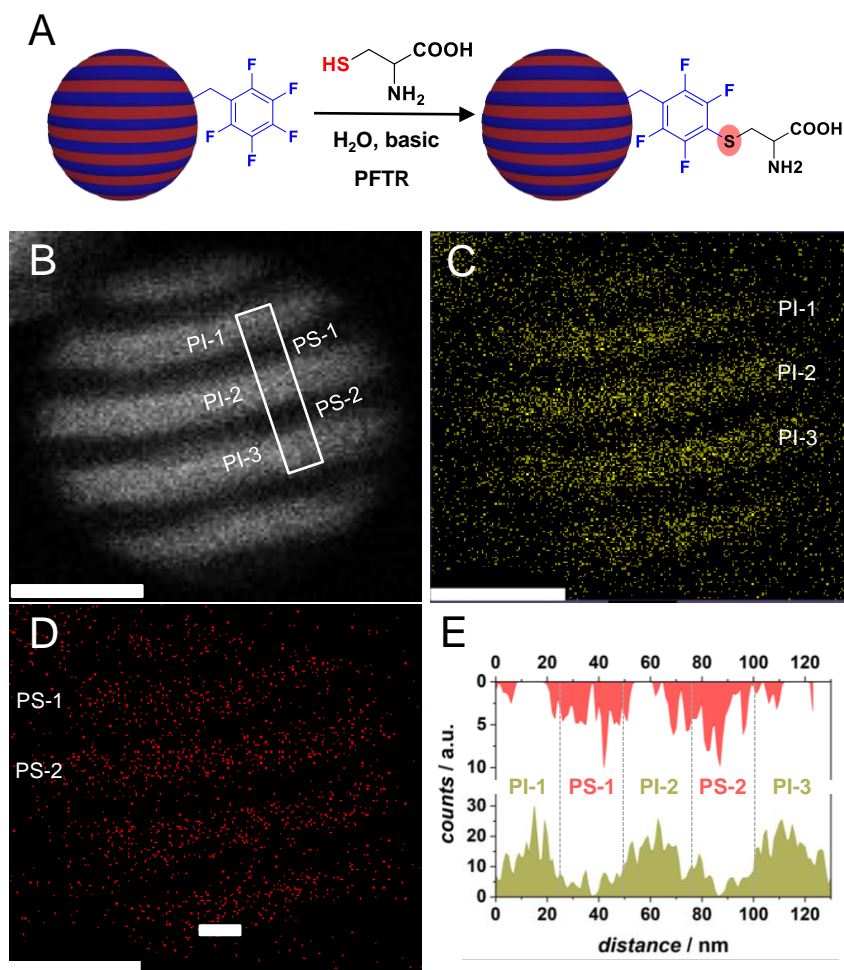


Figure 4.8. (A) Schematic representation of PFTR on the PS segment of the striped nanoparticles **NP3** with cysteine (B) Dark field STEM image of **NP3** nanoparticles where the bright parts (PI 1–3) represent the PI segment while the dark regions that of PS. (C) EDX mapping of Os-L α lines represented by green dots (D) EDX mapping of S-K α lines represented by red dots. (E) Grey value pixel map obtained by integrating the area in the marked region in (B) showing PS segments PS 1–2 and PI segments PI 1–3 showing alternate stacks of S (red) and Os (green) that represent PS and PI segments, respectively. All scale bars represent 50 nm. Reproduced from reference 239.

4.3.2.7 Proof of concept: Patterned immobilization of small molecules on striped particles

Having successfully obtained functional stacked lamellae nanoparticles that have both PI and functional PS segments on the surface for each functional BCP, the availability of the functional groups for further immobilization of molecules was investigated. The modification of pentafluorophenylalkyl nanoparticles **NP3** by *para*-fluoro–thiol substitution reaction (PFTR) using cysteine was demonstrated. (Figure 4.8 A). As the nanoparticles are

stable only in a non-solvent like water, the PFTR was performed on **NP3** in aqueous media at basic pH using cysteine as a model thiol, as Guillaume and co-workers recently demonstrated the feasibility of this reaction condition for PFTR.⁹⁶ Successful patterned immobilization of cysteine on the PS segments of **NP3** was confirmed using energy dispersive X-ray (EDX) spectroscopic mapping (obtained from STEM images) as shown in Figure 4.8 B-D. Here, Figure 4.8 C shows the energy dissipative map of Os-L α line (marked as PI 1-3) corresponding directly to the regions marked PI 1-3 in the representative STEM image (Figure 4.8 B) of the nanoparticle. Likewise, the S-K α lines marked as PS 1-2 in Figure 4.8 D match the same region of the STEM image of the nanoparticle in Figure 4.8 B. As the PI segments are cross-linked by osmium and the PS segments reacted with cysteine, the alternate stripes of Os-L α line and S-K α (Figure 4.8 C and D) were in accordance to the alternating PI and PS segments, respectively in Figure 4.8 B. Additionally, by tracing a line perpendicular to the domains and plotting the intensities obtained from both energy maps (Figure 4.8 B), a clear alternation of osmium- and sulfur-containing domains was visible (Figure 4.8 E). Lastly, a positive zeta potential value of +0.018 mV for **NP3** reacted with cysteine compared to -20.3 and -24.1 for **NP3** and a control sample strongly indicated the grafting of an amphiphilic molecule such as cysteine on the surface of **NP3**. These observations unambiguously proved the success of the PFTR reaction, and additionally validated the precise patterned immobilization of specific molecules.

2.8.3.9 Transformation of the striped particles and its functionalization

As the functional striped particles **NP3** showed great potential as a functional nanostructured material, we further aimed at generating other functional materials by simply transforming the already available nanostructured nanoparticles. Subsequently, nanodiscs **ND3** were fabricated by transforming the striped nanoparticles **NP3** by a previously reported method, called selective immobilization and selective elution (SISE). This technique proceeds by swelling the multicompartments particles with a good solvent which are previously cross-linked in one domain.

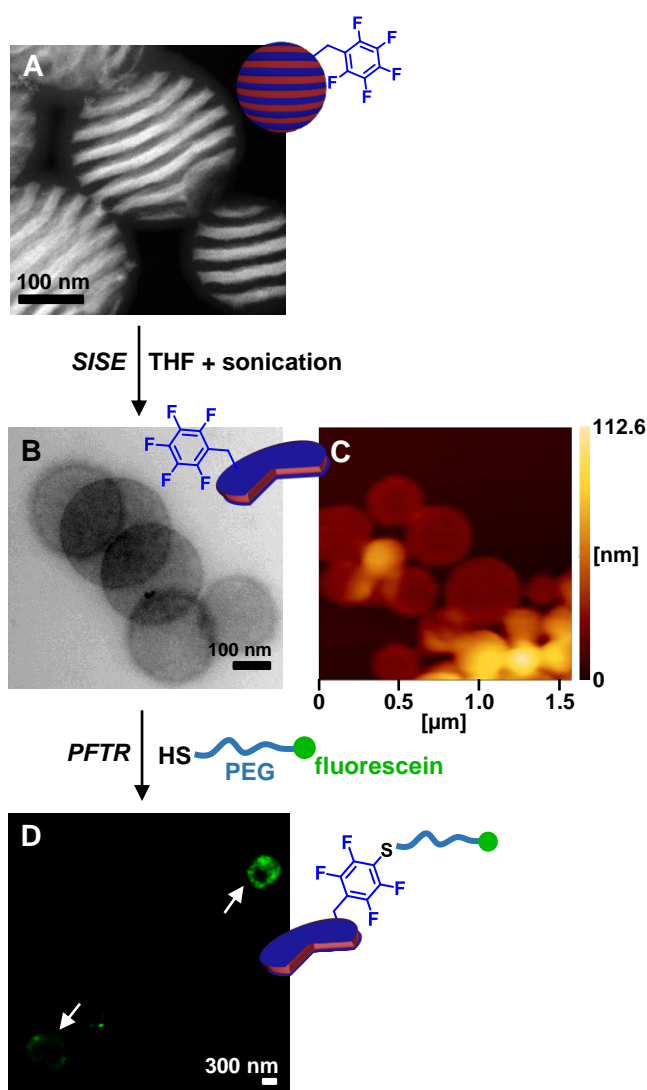


Figure 4.9. Dark field STEM images of nanoparticles **NP3** with stacked lamellae structures (A) and the corresponding nanodiscs **ND3** obtained by SISE (B). (C) AFM topography image of the nanodiscs **ND3**. STED fluorescence microscopy image of **ND3** after PFTR with FITC-PEG-SH (D), the corresponding control sample (F), and the STED BF image of the control sample (E). Reproduced from reference 239.

Using SISE, **NP3** nanoparticles were incubated in THF and sonicated to completely swell and disentangle the PS domains, leading to the delamination of the PI segments (Figure 4.9 A and B). These nanodiscs thus formed consist of an osmium-crosslinked disk-shaped PI core and a pentafluorophenylalkyl-functionalized brush-like PS shell. STEM image of **ND3** showed the presence of flat, circular objects with diameters in the range of those of the original **NP3** nanoparticles and below (Figure 4.9 B). **ND3** nanodiscs were found to be approximately 18 nm in thickness by AFM, corresponding well to the thickness of a stack

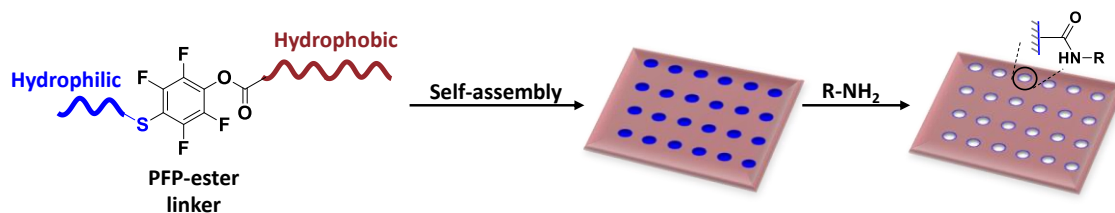
of PS or PI in **NP3** nanoparticles (Figure 4.9 C). As the PS block of **P3** contains the same pentafluorophenyl moieties as **NP3**, it was further reacted with α -fluorescein thioisocyanate- ω -thio-polyethyleneglycol (FITC-PEG-SH) by PFTR to prove the surface functionality of the nanodiscs. This was confirmed by stimulated emission depletion (STED) microscopy image of the nanodiscs after PFTR as seen in Figure 4.9 D. A control reaction was performed by incubating **ND3** with FITC-PEG-SH that did not exhibit fluorescence (Figure 4.9 F), while the presence of particles was unreacted particles was confirmed by the BF image (Figure 4.9 E). Hence, the green fluorescence of the nanodiscs compared to that of the control sample showed that the nanodiscs possess reactive surfaces.

Therefore, using a simple nanoprecipitation method like SORP, surface-reactive patchy nanoparticles and other derived functional materials, like nanodiscs, were obtained using functional PS-*b*-PI BCPs. However, this was not possible using the initially investigated PMMA-*b*-PS and PnBMA-*b*-PS BCPs. Consequently, the next section of this chapter deals with the preparation of porous membranes using one of the findings of Chapter 3 based on the PMMA-*b*-PS BCP system.

4.3.3 Preparation of porous membranes

2.8.3.10 Strategy

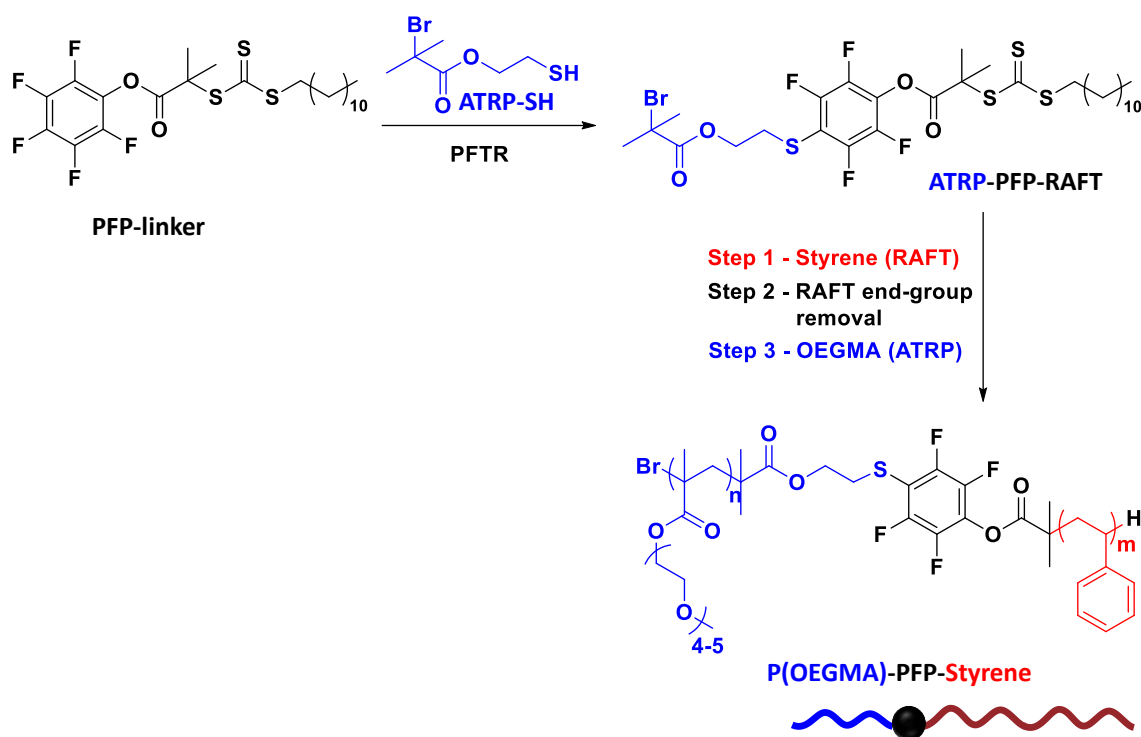
During the optimization of a synthesis of block copolymer libraries using distinct pentafluorophenyl (PFP) units (Chapter 3), we were able to obtain conditions for exclusive *para*-fluoro–thiol substitution reaction (PFTR) on pentafluoropheny methacrylate (PFPMA) motifs. The mono-substituted product remained susceptible towards amidation with amines (see Section 3.3.3 for details). Making use of this newly established reaction, we aimed at using a PFP-ester based methacrylate as a linker for the preparation of a cleavable amphiphilic BCP. Further, membranes consisting of the hydrophobic segment of the BCP as the bulk of the film can be prepared using BCP self-assembly. Finally, pores can be generated by cleaving off the PFP-ester linker (linked to the hydrophilic segment) by simply washing with an amine. A general schematic representation of the idea can be seen in Scheme 4.6. In order to obtain the amphiphilic BCP, three different strategies were attempted as discussed next.



Scheme 4.6. Schematic representation of the preparation of porous membranes using an amphiphilic block copolymer with para-substituted PFP-ester junction point.

2.8.3.11 Preparation of the amphiphilic BCP

As described in Section 3.3.3, PFP-ester is capable of undergoing PFTR under certain reaction conditions without multiple substitutions of the *meta*-fluorine atoms with thiols. Keeping this in mind, we devised a simple synthetic route (**Strategy 1**, Scheme 4.7) to obtain an amphiphilic BCP. Briefly, we aimed at performing PFTR on a pentafluorophenyl-based RAFT agent (**PFP-linker**) using a custom-made ATRP initiator as the thiol (**ATRP-SH**). This should lead to the formation of a bifunctional molecule that consists of an ATRP initiator and RAFT agent on either end of a PFP-linker (**ATRP-PFP-RAFT**). Such a molecule could then be used to grow two polymer chains on either side of the PFP-linker by ATRP and RAFT polymerization to obtain, for instance, **POEGMA-PFP-PS**. Two parameters were considered for the synthesis of the BCP: (i) choice of polymer for the hydrophobic and hydrophilic segments, and (ii) the molar masses of each of the segments in order to obtain phase separation with dot pattern that would lead to the formation of cylindrical pores in the membrane.



Scheme 4.7. Synthetic route towards the synthesis of the amphiphilic BCP according to **Strategy 1**.

Polystyrene (PS) was chosen as the hydrophobic segment of the BCP as styrene can readily be polymerized by RAFT polymerization. Poly(oligoethylene glycol methacrylate) (POEGMA) was chosen as the hydrophilic block as POEGMA is a widely investigated, water soluble polymer that can be obtained by ATRP with precise control. We aimed to obtain PS with molar mass in the range of $20,000 \text{ g mol}^{-1}$, while a shorter block of POEGMA with molar mass of approximately 7000 g mol^{-1} was targeted to be able to obtain the desired phase-separated structures later on.

First, the **PFP-linker** was reacted with **ATRP-SH** in a classical PFTR (Strategy 1, Scheme 4.7, Table 4.3, entry 1). Unfortunately, under these conditions the PFTR did not occur (see Figure 4.10).

Table 4.3. A detailed list of all conditions used for PFTR. PFP-R represents the type of pentafluorophenyl-ester moiety used for PFTR, while the thiol shows the different thiols used. OT:octanethiol.

Entry	PFP-R	Thiol	PFTR conditions		
			PFP-alkyl:Thiol (eq:eq)	Base / eq	Time (h)
1	PFP-linker	ATRP-SH	1:5	TEA / 2	4
2	PFP-linker	OT	1:1	TEA / 5	2
3	PFP-linker	OT	1:1	TEA / 5	4
4	PFP-linker	OT	1:1	TEA / 5	48
5	PS-H	OT	1:10	TEA / 2	24
6	PS-H	OT	1:10	TEA / 2	48
7	PFP-linker	PGMA-thiol	10:1	DBU / 5	0.25

From the ^1H NMR, it can be seen that all the peaks belonging to **ATRP-SH** are intact. The integrals of the peaks belonging to **PFP-linker** (Figure 4.10, top, peaks d, e, e', and f) suggest that only 10% of the RAFT end-group is remaining. Additionally, ^{19}F NMR spectroscopy shows the presence of *ortho*, *meta*, and *para*-F peaks associated with the unreacted **PFP-linker**. These observations suggest that the reaction did not proceed at all, and the PFP-ester underwent 90% hydrolysis under the reactions conditions used. Therefore, to better understand the series of events, the same reaction was performed using octanethiol (OT) as a model thiol for different reaction times (2, 4, and 48 h, Table 4.3, entries 2-5).

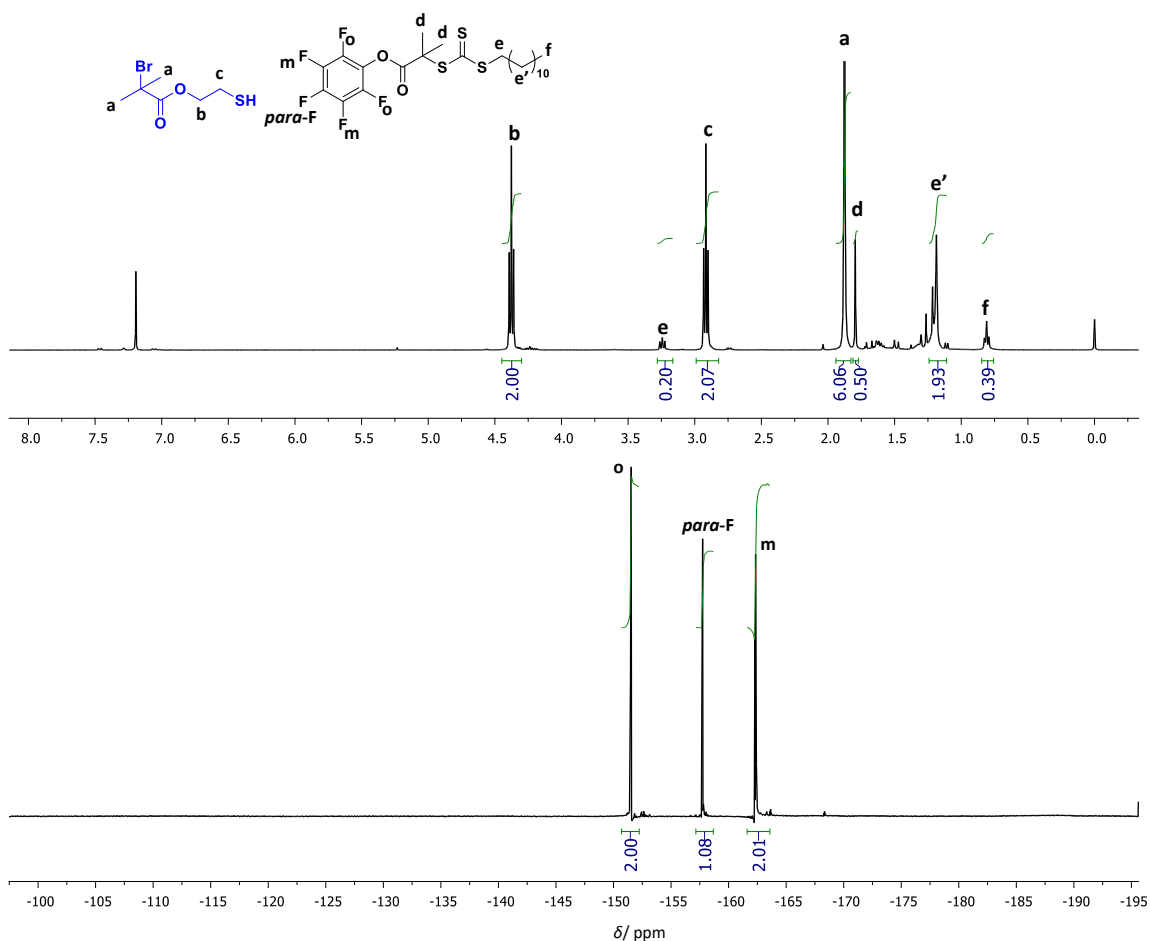
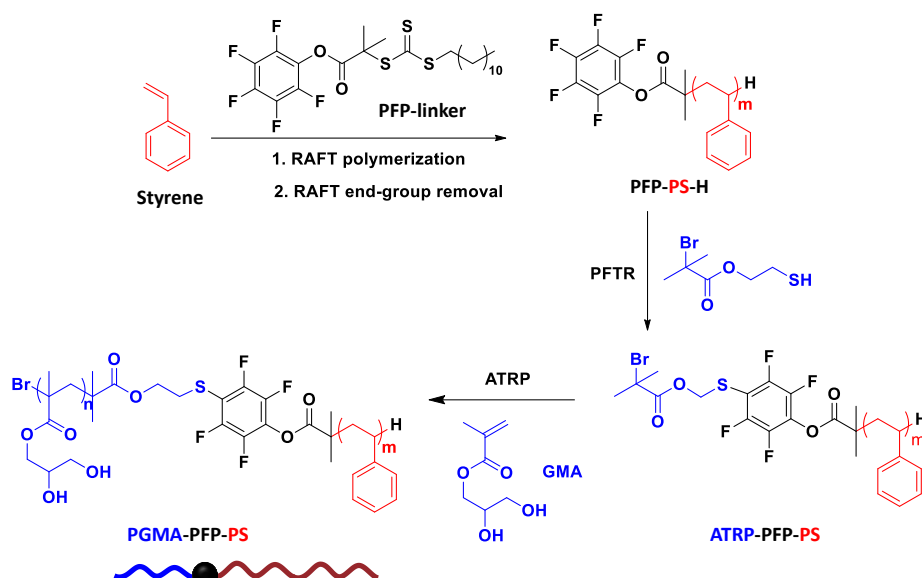


Figure 4.10. ^1H (top) and ^{19}F (bottom) NMR after PFTR of **PFP-linker** with ATRP-SH using **Strategy 1**.

Unfortunately, in this case, the PFP-linker hydrolyzed with time to form pentafluorophenol as seen in the ^{19}F NMR spectrum at each time point (Appendix B, Figure B8). In summary, using a small molecule like **PFP-linker** for PFTR was not feasible due to the instability of the PFP-ester group. Hence, to perform the PFTR on a molecule similar to the PFPMA pendant groups as discussed in Chapter 3, another strategy was devised (**Strategy 2**, Scheme 4.8).



Scheme 4.8. Synthetic route towards the synthesis of the amphiphilic BCP according to **Strategy 2**.

In this strategy, styrene was first polymerized by RAFT polymerization using **PFP-linker** to obtain the polymer **PFP-PS** (see Section 8.2 for synthetic details, for ^1H , ^{19}F , SEC trace, and UV-Vis spectra, refer to Appendix B, Figure B 15 (top), Figure B16 (top), Figure B17 (dotted line), and Figure B18 (dotted line), respectively). The RAFT end group (trithiocarbonate, TTC) was subsequently cleaved by a simple radical mechanism based photo reaction using ethylpiperidine hypophosphite (EHP) to obtain **PFP-PS-H** (see Section 8.2 for synthetic details, for ^1H , ^{19}F , SEC trace, and UV-Vis spectra, refer to Appendix B, Figure B 15 (bottom), Figure B16 (bottom), Figure B17 (solid line), and Figure B18 (solid line), respectively). Although the PFTR was to be performed using the **ATRP-SH** to enable the growth of the hydrophilic polymer segment, OT was first used to optimize the PFTR reaction. The hydrophilic segment used henceforth is poly(glycerol monomethacrylate) (PGMA) due to the synthetic ease of handling (powder) compared to POEGMA which is an oily liquid. Additionally, it is gaining popularity as an efficient biocompatible polymer for several applications.²⁴² Followed by the synthesis of **PFP-PS-H**, PFTR was performed with OT (Table 4.3, entries 5 and 6). After 24 and 48 h, the ^{19}F NMR spectra suggests that 50 and 80 % of the *para*-fluorine was substituted by OT, respectively (Figure 4.11).

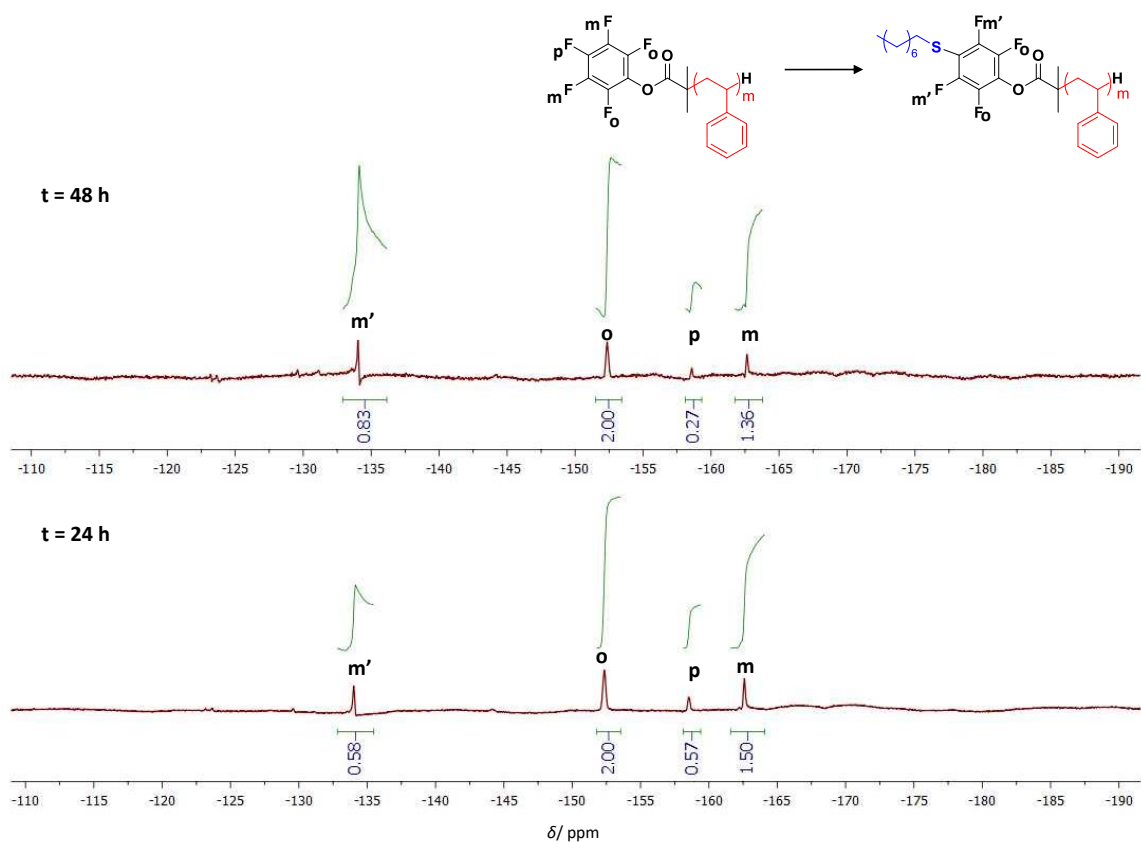
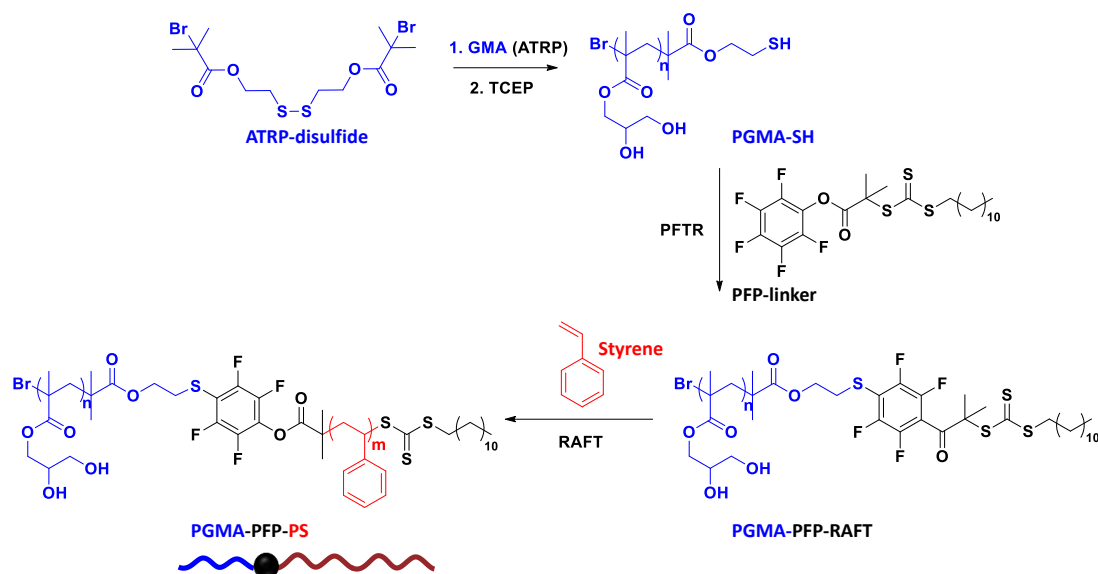


Figure 4.11. ^{19}F NMR spectra after PFTR of **PFP-PS-H** with octanethiol for 24 h (bottom) and 48 h (top).

This is proven by the disappearance of the *para*-F peak (p) at -158 ppm and a simultaneous appearance of the substituted *meta*-F peak (m') at -134 ppm. In addition to that, absence of any peaks between -110 and -130 ppm (at 24 h) shows that no multiple substitutions at the *meta*-F position by the thiol took place (Figure 4.11 bottom), but presence of small peaks at 48h suggests that the *meta*-F substitution begins before the complete *para*-F substitution by the thiol (Figure 4.11 top). The presence of the $\alpha\text{-CH}_2$ peak of OT in the ^1H NMR spectra additionally confirmed the formation of the substitution product (Appendix B, Figure B9). In general, partially *para*-substituted **PFP-PS-H** (with **ATRP-SH**) and further growth of the hydrophilic segment would not affect the formation of the membrane and subsequently the pores, as the PS homopolymer would remain in the bulk of the film/membrane. But, to precisely obtain the desired amphiphilic BCP, we sought to obtain a 100% *para*-substituted **PFP-PS-H** for the preparation of the porous membranes. As this strategy was not completely feasible, yet another strategy (**Strategy 3**) was employed (Scheme 4.9).



Scheme 4.9. Synthetic route towards the synthesis of the amphiphilic BCP according to Strategy 3.

Herein, the hydrophilic segment (**PGMA**) was first synthesized using **ATRP-disulfide** as the initiator to obtain **PGMA-SH** after the cleavage of the disulfide bond in **PGMA-S-S-PGMA** (see Section 4.4.5 for the synthesis of **ATRP-disulfide**, **ATRP-SH**, and **PGMA-SH**). This strategy differs from the previous ones with respect to the PFTR performed further. Here, we use the **PGMA-SH** for the PFTR with an excess of the **PFP-linker** in contrast to the previous cases where the thiol was always used in excess. We expect that this would lead to 100% *para*-F substitution with the corresponding thiol, and therefore further enable the synthesis of the desired amphiphilic BCP as targeted for the preparation of porous membranes. Accordingly, the PFTR was performed using DBU as the base (Table 4.3, entry 7) to obtain 100% conversion of the reaction. Although the ^1H NMR spectrum shows the presence of the *para*-substituted product (**PGMA-PFP-RAFT**) (Figure 4.12 A), ^{19}F NMR spectrum clearly shows that the activated ester in **PFP-linker** was hydrolyzed to form pentafluorophenol (Figure 4.12 B). This cannot be used to further form the hydrophobic PS segment due to the loss of the RAFT moiety which is required for chain extension. The PFTR conditions are yet to be optimized at this point to obtain **PGMA-PFP**. One of the possible alternatives would be to use a milder base, such as trimethylamine (TEA), as suggested in Chapter 3. We expect that this may prevent the hydrolysis of the PFP-ester

allowing for the successful formation of **PGMA-PFP**. Nevertheless, compared to the first two strategies employed, we envisage this route to be the most feasible.

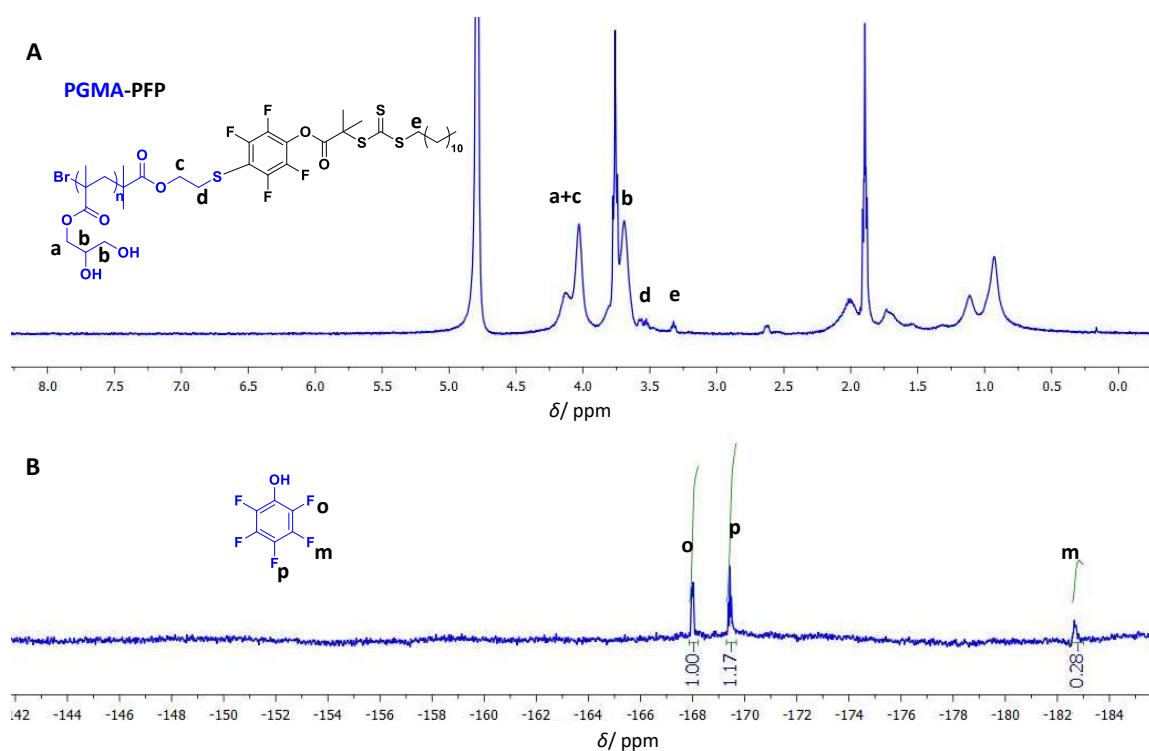


Figure 4.12. ^1H (A) and ^{19}F (B) NMR spectra after the reaction of **PGMA-SH** and **PFP-linker** in a PFTR to obtain **PGMA-PFP-RAFT**.

4.4 Conclusion

Two non-functional block copolymers (**PMMA-*b*-PS** and **PnBMA-*b*-PS**) and three different functional analogues of **PS-*b*-PI** with equal volume fractions of each of the blocks were synthesized by RAFT polymerization and NMP, respectively. The functional moieties incorporated in the latter were halide (chloro, **P1**), azide (**P2**), or pentafluorophenylalkyl (pentafluorostyrene (PFS), **P3**) in small amounts ($\approx 5\%$) in the PS block. The nanoparticles prepared by SORP for the PMMA-*b*-PS did not lead to formation of internal structures with both segments of the BCP at the surface, but rather formed core-shell nanoparticles. Formation of nanoparticles from PnBMA-*b*-PS lead to similar internal structures as that of PMMA-*b*-PS nanoparticles, but they were transformed into onion-like structures after mi-

crowave annealing the core-shell nanoparticles. Nonetheless, due to the solubility parameters of PMMA and PnBMA, their respective BCPs were not suitable to obtain nanoparticles with stacked lamellae internal structures.

In the case of functional PS-*b*-PI, formation of nanoparticles by SORP consistently led to nanoparticles with internal phase separation, whose exact nature depended on the nature of the reactive groups. The encountered morphologies ranged from onion-like to dotted or stacked lamellar patterns. Intermediate transformation structures were also found, in the absence of annealing. The onion-like structures systematically displayed an external PS-based layer due to the presence of a carboxylic acid group at the PS chain end arising from the polymerization initiator. Although striped morphologies could be obtained for the chloro- and azide containing PS-*b*-PI nanoparticles, blending with a non-functional PS-*b*-PI copolymer was applied for the pentafluorophenyl alkyl containing PS-*b*-PI. The A'B + AB type blending strategy to transform the internal structures of BCP nanoparticles was exploited for all the functional PS-*b*-PI BCPs leading to an understanding of the competing interfacial phenomenon. Ultimately, striped morphologies were obtained for all the functional BCPs. As an example to prove the reactivity of the surface functional moiety, site-selective surface functionalization of the pentafluoroalkyl-functionalized striped particles was achieved by aqueous PFTR, as evidenced by SEM/EDX mapping. Furthermore, these same nanoparticles, were used to produce surface-reactive nanodiscs by selective delamination as demonstrated by STED microscopy.

Lastly, the newly discovered capability of pentafluorophenyl ester containing PMMA-*b*-PS to undergo PFTR was utilized to target an amine-cleavable amphiphilic BCP. For this, **Strategy 3** involving the PFTR of PFP-ester RAFT agent with a hydrophilic thiol terminated polymer proved to be the most accessible route. **Strategy 1** wherein PFTR on PFP-PS-H with a thiol containing ATRP initiator also seemed plausible. However, these strategies have to be optimized to obtain the amine-cleavable amphiphilic BCP and finally prepare porous membranes.

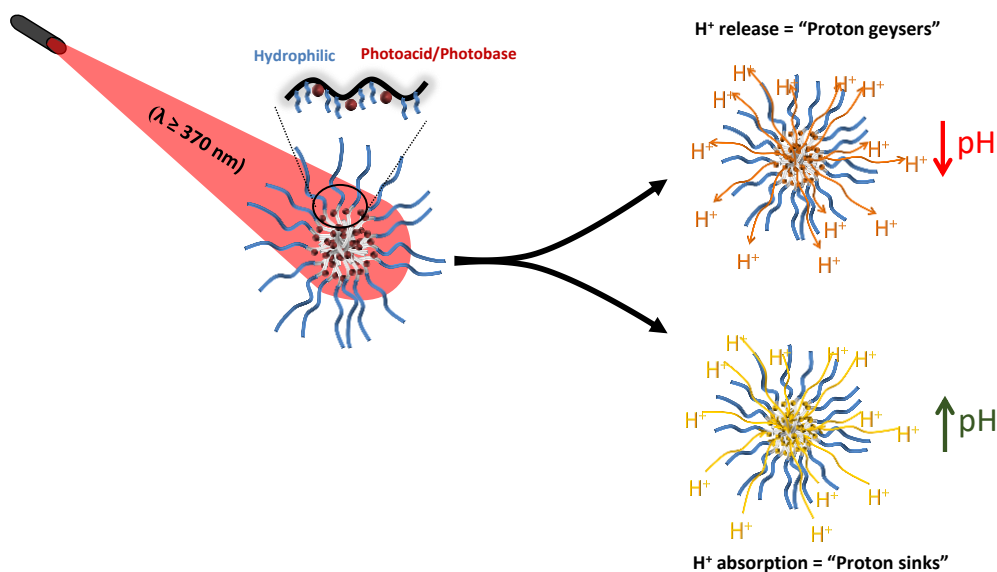
In the future, the well-ordered domains of striped particles could be employed for controlled co-enzyme immobilization to produce biosensors.²⁴³ The flat anisotropic disc-like

nanostructures are rather rare in the synthetic realm,²⁴⁴ yet a famous example in the biological context is that of phospholipid/membrane protein co-assembly.²⁴⁵ Apart from such nanostructured nanoparticles, BCPs are an interesting class of synthetic compounds for applications in the field of membranes, wherein the types of the micro- or nanostructure in the membranes can be altered based on the final purpose.

5. PHOTOREACTIVE POLYMERS AS INFLAMMATION PROBES

5.1 Introduction

Functional polymers are macromolecules that have unique properties. These properties are often determined by the presence of chemical functional groups dissimilar to those in the backbone of the polymer. Chemical heterogeneity on the polymer chains can lead to enhanced reactivity, phase separation, in addition to their ability to self-assemble or form supramolecular structures. Some of the aspects with respect to versatile homo- and block copolymer synthesis, incorporating functionality and their self-assembly have been discussed earlier in Chapters 3 and 4. Furthermore, the formation or dissociation of such functional polymers can also be triggered by an internal or external stimulus such as pH,²⁴⁶ specific enzymes,²⁴⁷ or light²⁴⁸ etc., to create “smart” materials.



Scheme 5.1. Schematic representation of the role of photoacid and photobase generators (PAG and PBG) as inflammation probes.

Parts of the experiments described in this chapter were carried out by Shamini Madhava.

Particularly, light-cleavable functional polymers could be useful in the biological realm to understand several biochemical aspects such as inflammation, among others. During the initial stages of inflammation, pH changes govern the inflammatory response, yet the exact mechanism of pH fluctuation is unknown. In a collaboration with the Institute of Toxicology and Genetics, we therefore aim at uncovering the underlying mechanism of the pH dependence using new polymer based targetable photoacid and photobase generators (**PAG** and **PBG**, respectively) (Scheme 5.1).

In general, **PAGs** are a class of compounds that are capable of generating highly reactive intermediates, such as radicals, ions, or radical-ions and subsequently acids upon irradiation with UV or visible light. Commonly, they have been implemented in various applications like preparation of adhesives, coatings, or inks and in lithography.²⁴⁹ They have also been used to catalyze an esterification reaction²⁵⁰, in polymerizations to catalyze crosslinking²⁵¹, in condensation reactions or depolymerizations.²⁵² **PAGs** can be divided into ionic and non-ionic compounds. Although the former bears certain advantages with respect to their thermal stability and ability to induce bathochromic shift by structural modification,²⁴⁹ their poor solubility in organic solvents remains an issue for practical uses. On the other hand, non-ionic compounds that generate carboxylic, sulfonic, or phosphoric acids upon irradiation are widely known.²⁵⁰ These photoacids have the advantage of being soluble in common organic solvents, which is essential in a wide range of organic and polymer reactions in addition to their low thermal stability that can nonetheless be improved as shown by Reichmanis *et al.*²⁵² In this context, we aimed at synthesizing novel non-ionic **PAG** based monomers and incorporate them into biocompatible polymers, which are then capable of inducing a significant jump in pH upon irradiation with near-UV/Visible light, and possibly by two-proton irradiation in the IR range.

PBGs are a compounds that have the ability to generate bases *in situ* when they are irradiated with light, usually in the UV-Vis region. Although **PAGs** have been studied in greater detail and utilized in polymer synthesis and reactions more often compared to that of **PBGs**, the latter has certain advantages such as tolerance to the presence of oxygen, inertness to metal-corrosion, and their air stability. These justify their growing use in different fields of

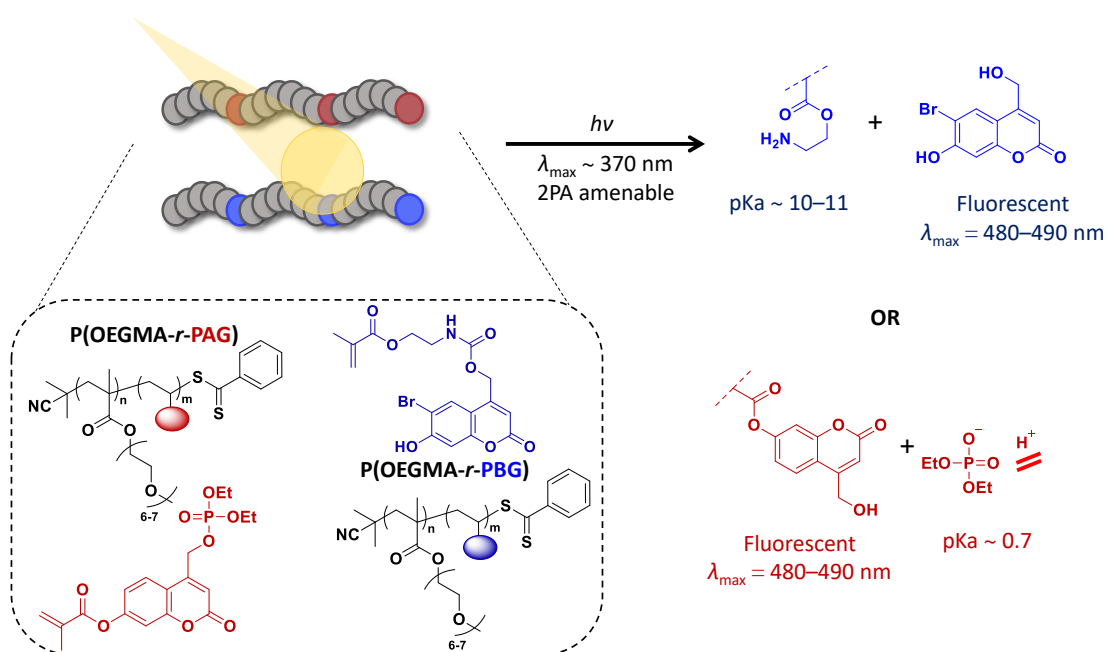
applications such as in the field of resists,²⁵³ electronic industry,²⁵⁴ surface modifications,²⁵⁵ and operations related to metal surfaces such as coatings of steel.²⁵⁶ Besides carbamates^{257,258} and oxime esters²⁵⁹ that have previously been introduced into polymeric scaffolds, a visible light-responsive coumarin moiety was introduced by Zhang *et al* which was coupled with the strong base tetramethyl guanidine. This adduct can be cleaved upon irradiation, and catalyzes the initiation of a thiol-Michael addition-based polymerization.⁴³

In particular, (coumarin-4-yl)methyl based chromophores are popularly used as photolabile groups. For example, Givens *et al.* presented the photorelease of phosphate by the irradiation of diethyl 2-(4-hydroxy-1-naphthyl)-2-oxoethyl phosphate at 350 nm as one of the first examples.²⁶⁰ Akinobu *et al.* investigated the photolysis ($\lambda_{\max} = 350$ nm) properties of coumarin-4-ylmethoxy carbonates as caged compounds for hydroxyl-containing molecules.²⁶¹ Among the compounds tested, (6-brom-7-hydroxycoumarin-4-yl)methoxycarbonyl showed the highest photochemical efficiency to make caged compounds for alcohols. A common property of all the above discussed coumarin-based photocleavable groups are their high photosensitivity and ability to undergo two-photon excitation/absorption (2PA). 2PA is a process where the molecules are excited using pulsed-laser irradiation at approximately twice the wavelength for classic one photon absorption. As lower energy photons are used for excitation, it reduces the damage of the sample being used making it viable for *in-vivo* studies, and three-dimensional resolution.^{262,263}

The aim in the current chapter was therefore to synthesize **PAG** and **PBG** monomers based on (coumarin-4-yl)methyl in order to trigger spatially controlled pH jumps. They were further incorporated into a polymeric scaffold to guarantee their solubility in aqueous media and make the final “agent” biocompatible for targeted delivery.

5.2 Strategy

The central idea revolves around the design and synthesis of a biocompatible functional polymer, where the functionality incorporated is a photolabile **PAG** or **PBG**. When the final compound is irradiated, it will either catch or release protons, depending on the nature of the functional moiety, i.e., **PBG** or **PAG**, respectively. The following aspects were considered to design the functional polymer: (i) exact nature and type of the PAG and PBG molecules that are capable of inducing a pH change upon irradiation, (ii) a method to deliver such a compound *in-vivo*, and lastly (iii) light source to activate the final compound with spatial and temporal control. Firstly, as discussed in the previous section, derivatives of coumarin-4-yl methyl were used as the **PAG** or **PBG**. Secondly, they were copolymerized with poly(oligoethylene glycol methacrylate) (**POEGMA**) (**P(OEGMA-*r*-PAG)** or **P(OEGMA-*r*-PBG)**) to enable the solubilization and impart biocompatibility to the entire system. Finally, on irradiation at ≈ 320 nm, the increase or decrease in pH (**PBG** or **PAG**, respectively) was monitored by measuring the pH of the polymer solution in water. A scheme representing the strategy is shown in Scheme 5.2.

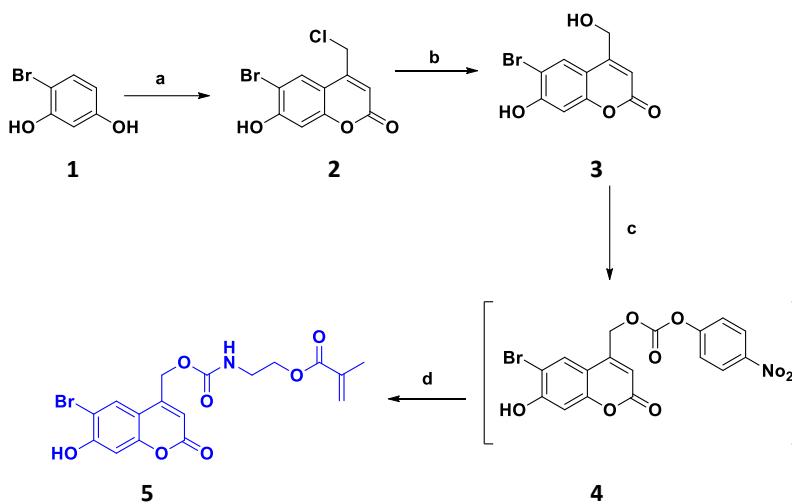


Scheme 5.2. Schematic representation of the irradiation of the coumarin-based P(OEGMA-*r*-PAG) or P(OEGMA-*r*-PBG) copolymers to visualize a decrease or increase in pH, respectively with the release of coumarin-4-yl methylalcohol or phosphate.

Additionally, the use of RDRP would allow future incorporation of targeting ligands to reach the site of inflammation. The next two sections describe the design, synthesis and photolysis studies of the **P(OEGMA-*r*-PBG)** and **P(OEGMA-*r*-PAG)** copolymers.

5.3 Results and Discussion

5.3.1 Synthesis of the photobase generator (PBG)



Scheme 5.3. Synthetic scheme towards the synthesis of PBG **5**. (a) Ethyl 4-chloroacetate, H₂SO₄, RT, 6 d; (b) H₂O, reflux, 2-3 d; (c) DMAP, 4-nitrophenyl chloroformate, ACN, RT, 7 h; (d) DMAP, 2-aminoethyl methacrylate hydrochloride, DMF, rt, 24 h.

The targeted PBG **5** was designed to have 2 important components: (i) a photosensitive moiety, which can undergo photolysis upon irradiation with mild UV (or NIR by 2PA), and (ii) an olefinic double bond that can be polymerized by radical polymerization. The coumarin-4-yl methyl scaffold of the PBG was chosen owing to its recent use in the development of novel phototriggers to make caged compound of phosphates,²⁶⁴ alcohols,²⁶¹ and amines.²⁶⁵ The PBG **5** was successfully synthesized following the route depicted in Scheme 5.3.

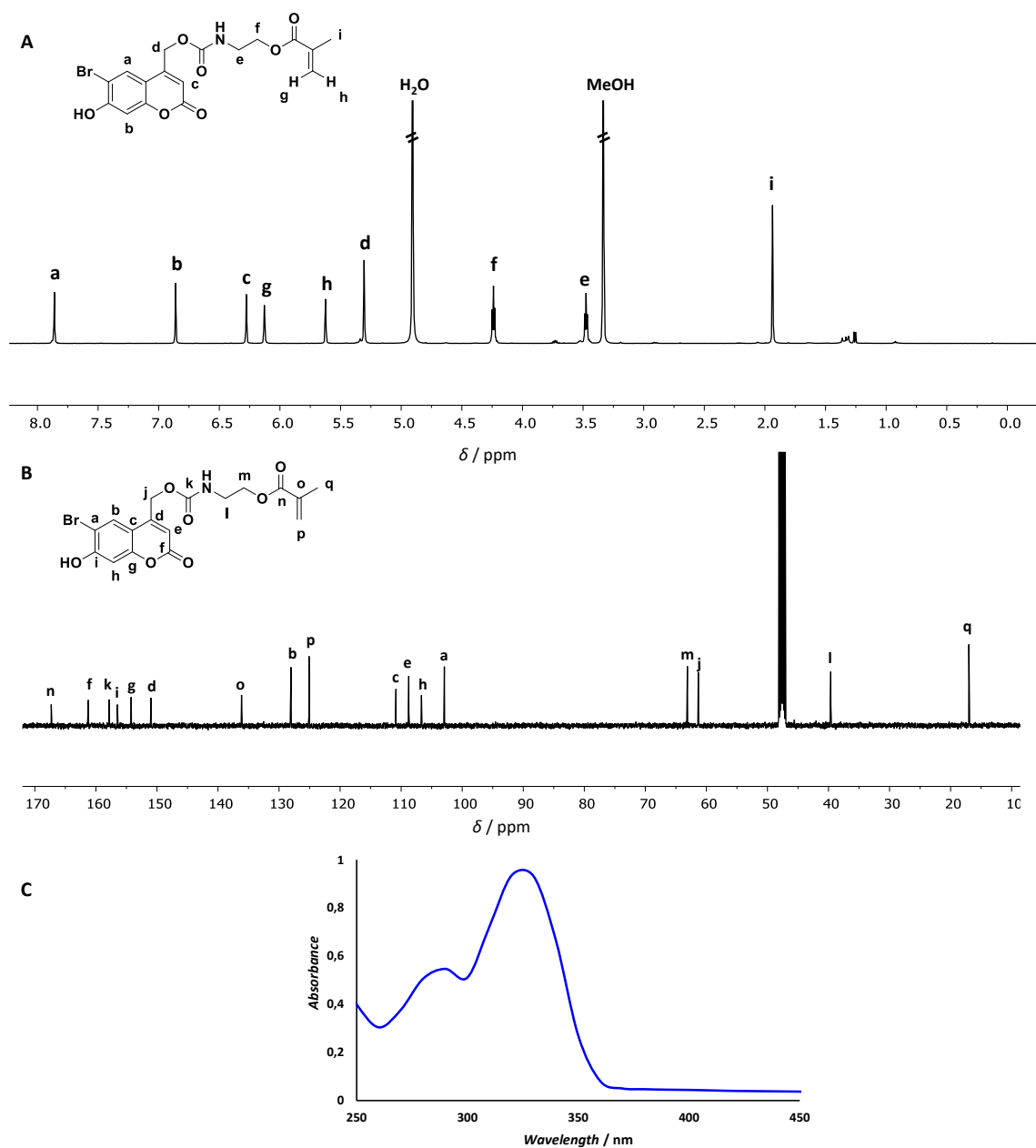
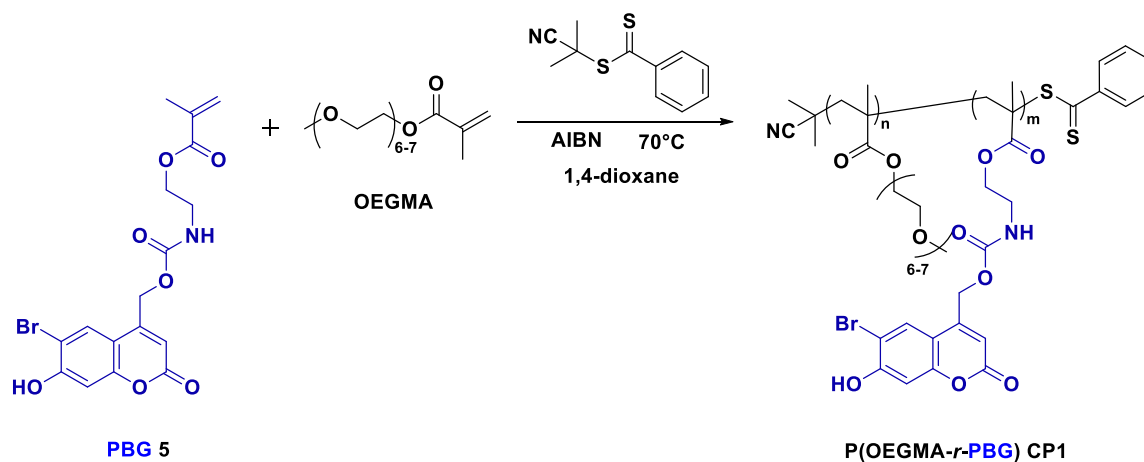


Figure 5.1. ^1H (A) and ^{13}C (B) NMR, UV-Vis (C) spectra of the photobase generator, PBG 5. The ^1H and ^{13}C NMRs are measured in MeOD, while the UV-Vis in acetonitrile at a concentration of 0.025 mg mL^{-1} of PBG 5.

The 6-bromo-7-hydroxycoumarin-4-ylmethyl (BHC 3) was synthesized from 4-bromoresorcinol 1 by a modified Pechmann condensation reaction²⁶⁶ using 4-chloroacetoacetate and methanesulfonic acid as the catalyst as well as the solvent, followed by nucleophilic sub-

stitution of **2** in refluxing water. The hydroxyl group was activated using *p*-nitrophenylchloroformate to obtain **4** *in situ* that was not isolated. **2** and **3** were characterized by ^1H and ^{13}C NMR (Appendix C; **2**: Figure C1 and **3**: Figure C2). Formation of **3** was conclusive based on ^{13}C NMR, where the $\alpha\text{-CH}_2$ carbon shows a shift from 20 ppm in **2** to 60 ppm in **3**, as the ^1H NMRs of **2** and **3** display similar peaks. To further obtain the PBG **5**, polymerizable methacrylate, 2-amino methacrylate, was chosen over its acrylate analogue, as methacrylates are typically more stable. The successful formation of PBG **5** was proven by ^1H and ^{13}C NMR (Figure 5.1 A and B, respectively). This was additionally confirmed by determining the exact mass by electrospray ionization mass-spectrometry (ESI-MS) (Appendix C, Figure C3), where the m/z (448.0025) was in close correlation to the theoretical m/z ($(\text{C}_{17}\text{H}_{16}\text{BrNO}_7 [\text{M} + \text{Na}^+]) = 448.0008$), and by measuring the UV-Vis absorption spectrum (Figure 5.1C).

The UV-Vis spectrum showed several absorption maxima. In order to explain this, the spectrum of the basic unsubstituted coumarin skeleton, as reported by Preat *et al.*,²⁶⁷ has been taken into consideration. The unsubstituted coumarin skeleton has two absorption maxima. The first absorption band λ_{max}^1 at 330 nm represents an excitation from the highest occupied molecular orbital (HOMO) to the lowest unoccupied molecular orbital (LUMO). The second absorption band λ_{max}^2 at about 300 nm is associated with the excitation from HOMO-1 to the LUMO due to the benzenoid absorption.²⁶⁷ In general, the mechanism of excitation in coumarin and its derivatives involve $\pi \rightarrow \pi^*$ transitions from the benzene to the pyranone moiety. Consequently, the UV-Vis spectrum of PBG **5** measured in acetonitrile (ACN) shows an intense band λ_{max}^1 at 325 nm and a smaller short-wavelength shoulder λ_{max}^2 at around 289 nm. The intensity of λ_{max}^2 is lower compared to that of the parent coumarin structure. This behavior can be explained by the increase in intramolecular charge transfer of the new substituted coumarin **5** possibly due to the lower redistribution of charges.

5.3.2 Synthesis of P(OEGMA-*r*-PBG) copolymer CP1

Scheme 5.4. Synthetic scheme for the synthesis of P(OEGMA-*r*-PBG) **CP1** copolymer.

Following the synthesis of the PBG monomer, it was copolymerized with OEGMA by RAFT polymerization to obtain **CP1** copolymer (Scheme 5.4). Firstly, to ensure the stability of the coumarin towards the polymerization conditions (DMF, 70 °C), **3** was incubated in a free radical polymerization (FRP) mixture to track potential changes in the coumarin structure (Appendix C, Figure C4). It was clearly observed that the three peaks (a-c) belonging to the coumarin ring remain intact after FRP. Secondly, the ability of the PBG **5**, containing a methacrylate group, to polymerize was confirmed by subjecting PBG **5** to FRP (Appendix C, Figure C5). The appearance of broad peaks and decrease in the vinyl proton intensities in the ^1H NMR suggested the formation of a polymer by polymerization through C=C double bonds. Having proven the stability of the coumarin ring as well as the ability of the PBG **5** to polymerize, few parameters were considered for the final copolymerization of the PBG **5** and OEGMA. A sufficiently high molar mass of $20,000 \text{ g mol}^{-1}$ was targeted to obtain a water soluble copolymer with reasonable amounts of PBG as the PBG **5** is insoluble in water due to the presence of the hydrophobic coumarin moiety. For the same reason, the copolymerization was performed in DMF to ensure the complete solubility of both the monomer and the comonomer throughout the polymerization. The amount of PBG **5** incorporated in **CP1** was kept at $\approx 10 \text{ mol}\%$ to retain the properties of the backbone polymer and at the same time have a significant amount (0.044M) to obtain the pH jump on irradiation (discussed later).

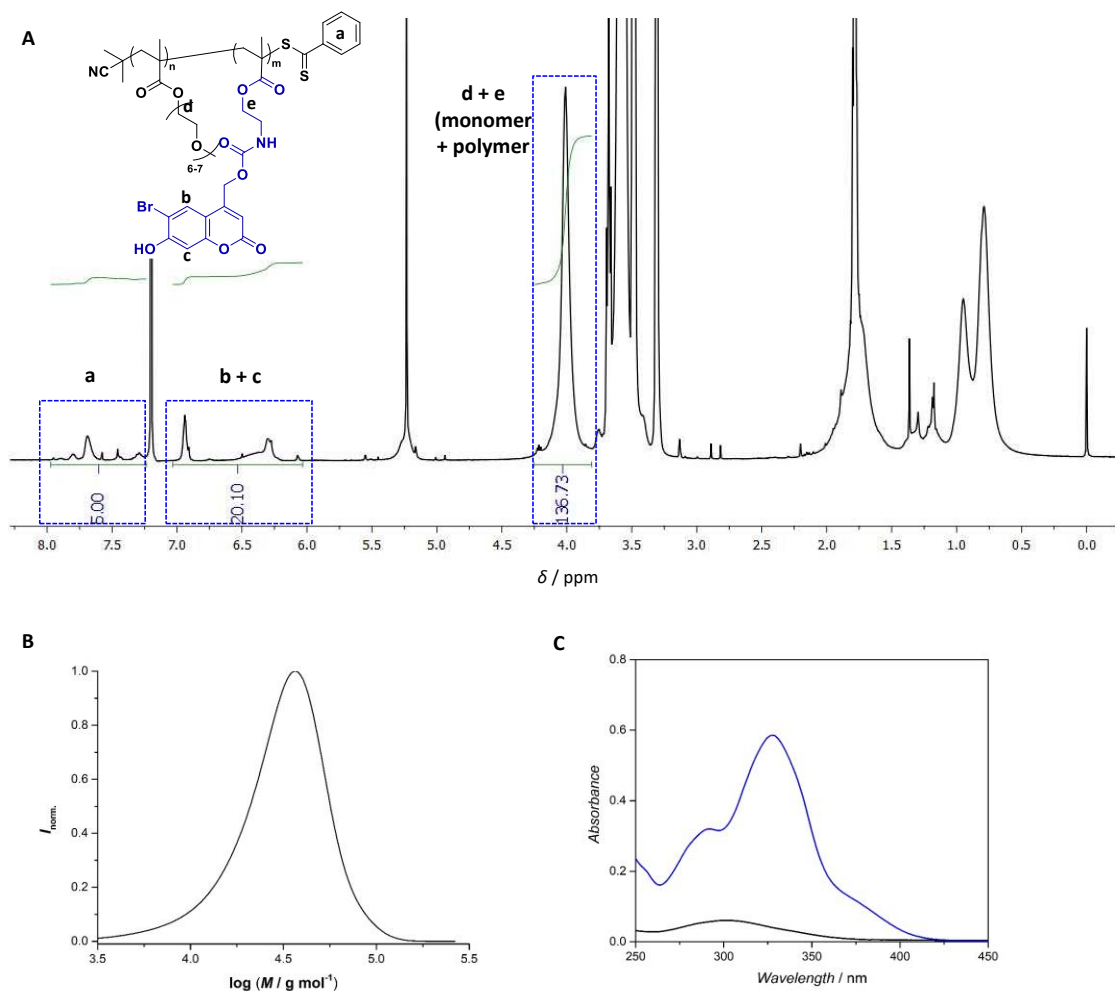


Figure 5.2. (A) ¹H NMR of **CP1** in CDCl₃. (B) Size exclusion chromatogram of **CP1** in dimethylacetamide (DMAc), and (C) UV-Vis of **CP1** (blue) and POEGMA (black) measured in H₂O (1 mg mL⁻¹).

Consequently, PBG **5** and OEGMA were copolymerized in DMF with an initial feed of 10 mol% of the PBG **5** to obtain copolymer **CP1**. The formation of **CP1** was confirmed by ¹H NMR spectroscopy where the molar mass was calculated using the peaks ‘a-e’ as seen in Figure 5.2A and SEC (Figure 5.2B) ($M_{n,NMR} = 28,000 \text{ g mol}^{-1}$, $M_{n,SEC} = 23,000 \text{ g mol}^{-1}$, $D = 1.45$). 9.3 mol% of the PBG comonomer was incorporated in the final **CP1** copolymer in comparison to 10% of the initial feed. Apart from the visible peaks belonging to the PBG comonomer in the ¹H NMR spectrum (Figure 5.2A), its presence was also confirmed by comparing the UV-Vis absorption spectra of a POEGMA homopolymer synthesized by RAFT polymerization to that of **CP1** (Figure 5.2C). Evidently, the copolymer **CP1** shows

an absorption spectrum similar to that of the pure PBG **5** (Appendix C, Figure C3 B) with two absorption maxima at $\lambda_{\max}^2 = 328$ nm and $\lambda_{\max}^2 = 292$ nm (Figure 5.2C, blue), while the homopolymer shows a weak absorption band with a maxima at 310 nm corresponding to the presence of the RAFT end group (Figure 5.2C, black).

5.3.3 Photolysis study of P(OEGMA-*r*-PBG) **CP1**

The copolymer **CP1** was designed such that an increase in the pH of the solution is observed upon irradiation due to the formation of a primary amine and release of compound **3** (Scheme 5.2). Firstly, the photolysis was performed to ensure the effective release of **3** upon irradiation of **CP1**. All photolysis experiments were conducted by irradiating the copolymer solution placed at a distance of 2 cm from the source (Arimed B6 lamp, $\lambda_{\max} = 320$ nm). As the coumarin based **3** possesses strong fluorescence, its release was monitored by fluorescence spectroscopy ($\lambda_{\text{exc}} = 328$ nm). The fluorescence intensity of **CP1** solution in water (10 mg ml^{-1}) after photolysis for 1 hour was measured (Figure 5.3). Contrary to our expectation, the fluorescence intensity of **CP1** was higher before irradiation (Figure 5.3, black line) compared to that of after (Figure 5.3, red).

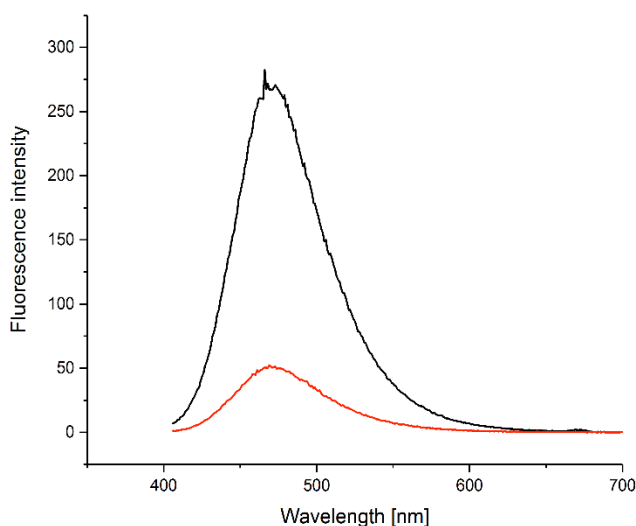


Figure 5.3. Emission spectra of **CP1** in water (10 g L^{-1}) before (black) and after (red) irradiation at 320 nm for 1 h; λ_{exc} : 328 nm, λ_{em} (before): 473 nm and λ_{em} (after): 469 nm.

We hypothesize that this behavior arises from the extremely low solubility of the released **3** in water. A ^1H NMR spectrum of the solution was measured after irradiation (Appendix

C, Figure C6). As assumed, the aromatic peaks belonging to the coumarin moiety **3** disappeared after photolysis owing to its extremely low solubility in water (see Appendix C, Figure C6 A and B, peaks a-c).

Table 5.1. Variation of pH of **CP1** solutions in water after irradiation at 320 nm for 0-60 minutes.

Entry	Polymer conc. (g L ⁻¹)	Irradiation time (min)	pH	Entry	Polymer conc. (g L ⁻¹)	Irradiation time (min)	pH
1		0	5.71	10		0	5.71
2		1	5.37	11		1	5.42
3		2	5.49	12		2	5.37
4		5	5.71	13		5	5.53
5	10	10	5.97	14	20	10	5.78
6		15	6.12	15		15	6.01
7		30	6.25	16		30	6.17
8		45	6.27	17		45	6.19
9		60	6.28	18		60	6.21

Having confirmed the photolysis of **CP1** in water to release **3**, two different photolysis experiments to study the change in pH were conducted: (i) study of change in pH of **CP1** solution (10 and 20 g L⁻¹) at different irradiation times, and (ii) study of change in pH of different concentration of **CP1** with a constant irradiation time of 1 h. For the former study, high concentrations of **CP1** were chosen ensure the easy monitoring of the pH changes, wherein 10 and 20 gL⁻¹ solutions of **CP1** contain 0.041 and 0.082 M of PBG **5**. After irradiation of **CP1** for different times (Table 5.1, Figure 5.4 A), two trends with respect to the change in pH were observed: (i) the increase in pH with increasing irradiation times was not significant after an initial drop in pH by 0.3 units from 0 to 1 min (Table 5.1, entries 1, 2 and 10, 11), and (ii) the pH at every time point is higher for the 10 g L⁻¹ **CP1** solution (Figure 5.4 A, solid symbols and Table 5.1, entries 2-9) than that for 20 g L⁻¹ **CP1** (Figure 5.4 A, hollow symbols and Table 5.1, entries 11-18).

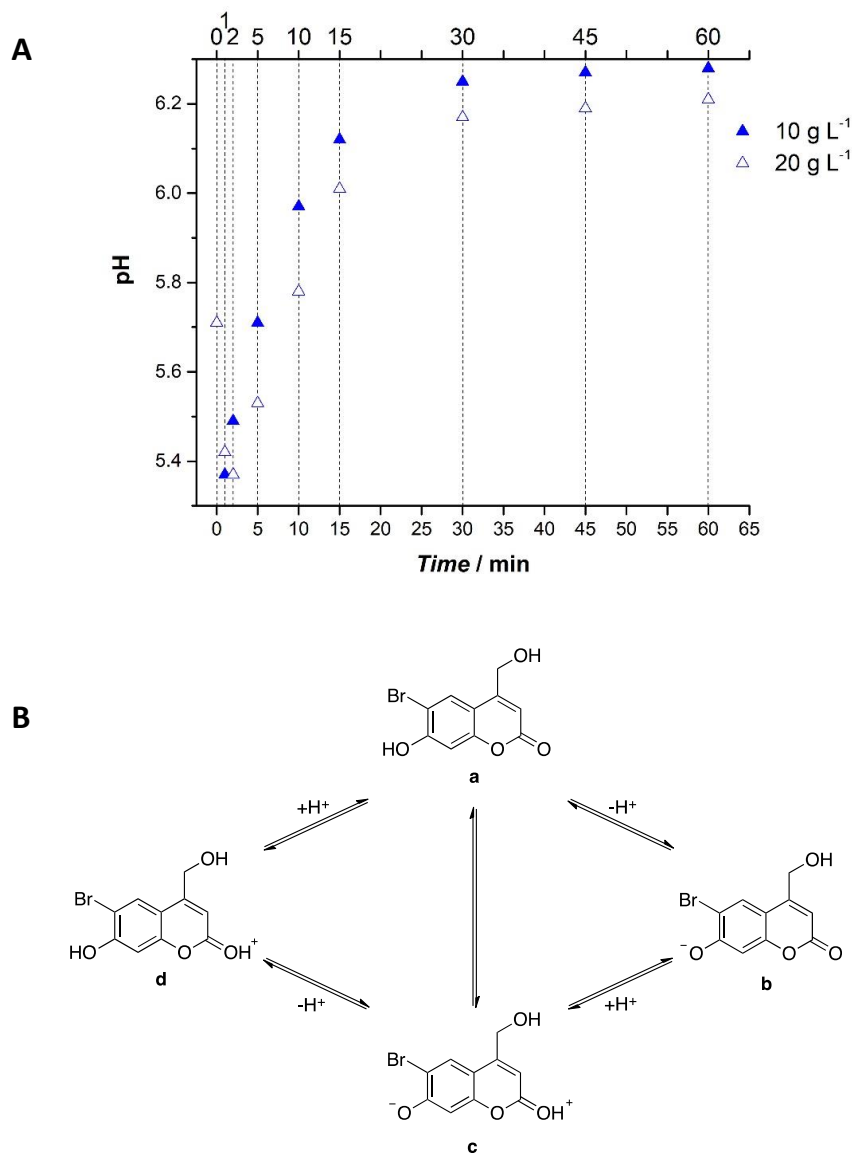


Figure 5.4. (A) pH of 10 g L⁻¹ (solid) and 20 g L⁻¹ (hollow) **CP1** solution (in water) after different irradiation times (0, 1, 2, 5, 10, 15, 30, 45, and 60 min). $\lambda_{\text{max}} = 320$ nm. (B) Possible pH dependent forms of **3** in the ground and excited states.

A plausible explanation of the weak change in pH of **CP1** after photolysis for different times and the inverse dependency of pH with concentration could be the occurrence of several pH-dependent forms of **3** (Figure 5.4 B).

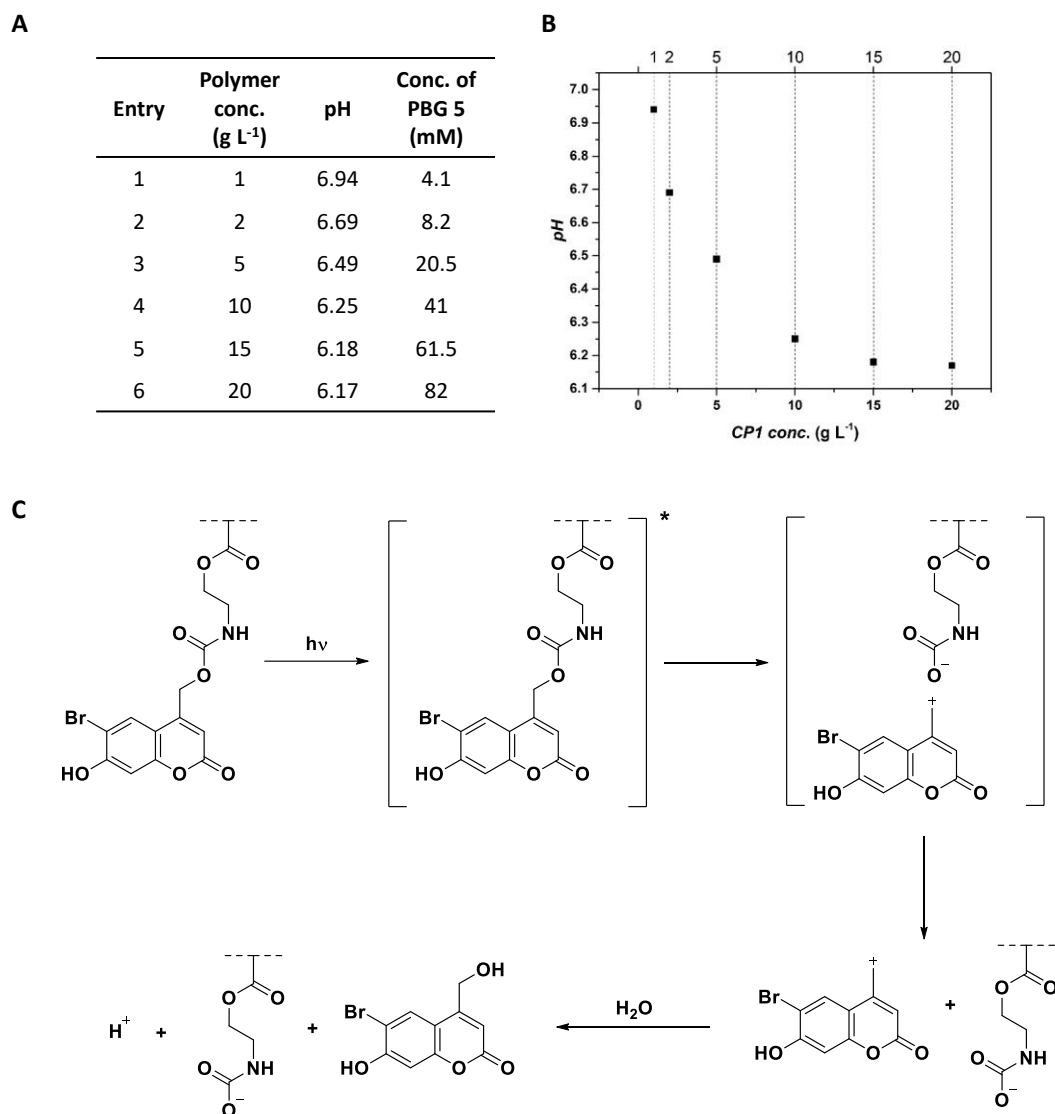


Figure 5.5. (A) Table showing the pH of **CP1** solutions at different concentrations after irradiation for 1 h and the expected concentration of **PBG 5** in each case. (B) Plot of evolution of pH on irradiation of different concentrations of **CP1** for 1 h. $\lambda_{\text{max}} = 320$ nm. (C) Mechanism of photosolvolysis of (coumarin-4-yl) methyl esters that leads to the formation of (coumarin-4-yl) methyl alcohol and the corresponding acid anion A^- and H^+ .

The coumarin compound possesses a carbonyl group that can behave as a strong proton acceptor, and a hydroxyl group which may be deprotonated. The cationic form (Figure 5.4 B, d) is predominant in acidic conditions, while in neutral or alkaline conditions, the hydroxyl group of the excited neutral molecule can be deprotonated, resulting in the anionic form (Figure 5.4 B, b). As the photolysis of **CP1** should lead to the formation of an amine

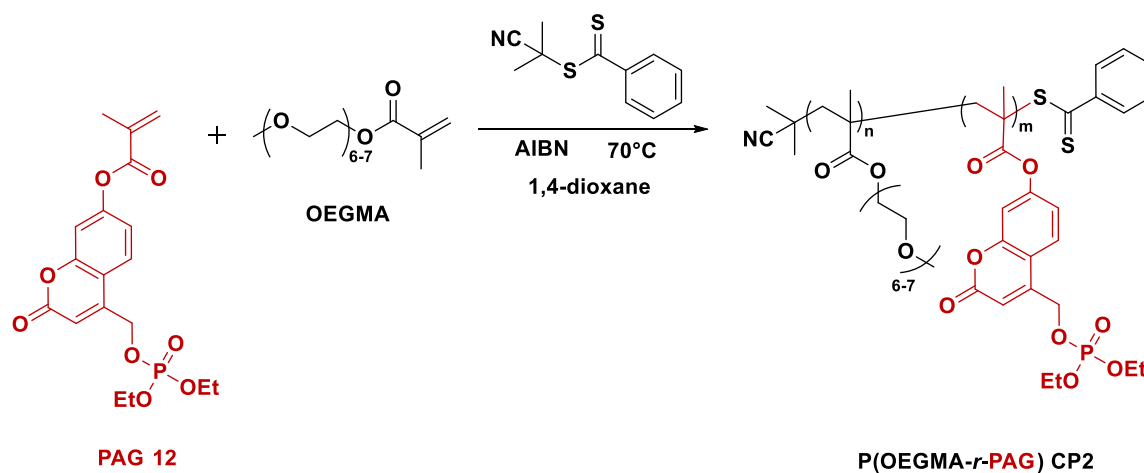
creating a basic environment, the deprotonation of the hydroxyl group in **3** may counteract the increase in pH caused by the photolysis of **CP1**. This could explain the insignificant jump in pH after photolysis of **CP1**. Further, we presume that the low pH (5.71) of **CP1** in water before irradiation, and in general, that of a homopolymer of POEGMA (pH = 3.80) may have contributed to this unexpected behavior.

Next, from the above experiment, an irradiation time of 1 h was chosen to ensure 100% photolysis of **CP1** for different concentrations of **CP1** (1, 2, 5, 10, 15, and 20 g L⁻¹). All samples were irradiated at 320 nm and the pH was measured after 1 h in each case (Figure 5.5 B). Compared to the pH of the **CP1** solution before irradiation (5.71), the largest jump in pH after photolysis was observed for 1 g L⁻¹ (from 5.71 to 6.94, Figure 5.5 A, entry 1). Furthermore, on increasing the concentration of **CP1**, weaker jump in pH was observed with 6.17 for 20 g L⁻¹ (Figure 5.5 A, entries 2-6). This observation was contradictory to similar concentration dependent experiments performed for ethanolamine in different concentrations where an increase in pH was logically observed with increasing amounts of ethanolamine (see Appendix C, Figure C7). A plausible explanation for such a behavior can be realized by the two competing events that take place on irradiating the PBG **5**^{268,269} (see Figure 5.5 C). Herein, the pendant PBG in **CP1** absorbs light and goes to the excited state. This is capable of undergoing heterolytic bond cleavage to form the ion pair. Followed by this, the formation of the product happens in two steps, wherein the solvent-separated ions are formed first, and then the (coumarin-4-yl) methyl cation reacts with water to yield the coumarin alcohol, H⁺ and the acid anion. Therefore, as the concentration of **CP1** was increased, a weaker increase in pH was observed for the same irradiation time. The UV-Vis absorption spectrum of **CP1** (10 g L⁻¹) before and after irradiation show similar profiles, but a lower intensity of the band at \approx 280 nm that corresponds to **3** is observed in the latter (Appendix C, Figure C8). The above results do not provide conclusive proof regarding the efficiency of the photolysis of **CP1** to produce **3**, and thereby, a significant increase in pH.

Therefore, further optimization of the photolysis of **CP1** with respect to the solubility of the released **3**, interference of its acidic behavior, as well as its low solubility is necessary as it makes the analysis ambiguous. Apart from this, the inherent acidic property of

tection (Scheme 5.5, step ‘e’) to avoid the substitution of the 7-OH by diethyl chlorophosphate was carried out to obtain the PAG **12**. Although pure PAG **12** could not be obtained after several purification steps, it could be used as a comonomer for the polymerization (discussed below). The formation of compounds at each synthetic stage (**7**, **8**, **9**, **10**, and **11**) was confirmed by ^1H , ^{13}C NMR and additionally ^{31}P NMR spectroscopy in case of **10** and **11** (see Appendix C, Figure C9 to Figure C13). PAG **12** was characterized by ^1H and ^{13}C NMR (refer to Appendix C, Figure C14), UV-Vis spectroscopy (Appendix C, Figure C15A), and ESI-MS (Appendix C, Figure C15B). The UV-Vis absorption spectrum of the skeletal coumarin moiety has previously been explained in Chapter 5, Section 5.3.1. Accordingly, the UV-Vis absorption spectrum of PBG **12** shows two absorption maxima at $\lambda^1_{\text{max}} = 312 \text{ nm}$ and $\lambda^2_{\text{max}} = 277 \text{ nm}$, where a hypsochromic shift compared to that of PBG **5** is seen. The m/z value obtained from ESI-MS (419.0882) is in close correlation to the theoretical m/z ($\text{C}_{17}\text{H}_{16}\text{BrNO}_7 [\text{M} + \text{Na}^+] = 419.0872$).

5.3.5 Synthesis of P(OEGMA-*r*-PAG) copolymer CP2



Scheme 5.6. Synthetic scheme for the synthesis of P(OEGMA-*r*-PAG) copolymer, **CP2** by RAFT polymerization.

PAG **12** was incorporated as a comonomer in the RAFT polymerization of OEGMA to obtain P(OEGMA-*r*-PAG) **CP2**. Similar molar mass and amount of the PAG **12** incorporation was targeted as for **CP1**. The overall molar mass of **CP2** was calculated by NMR to be 27000 g mol^{-1} (Figure 5.6 A, peaks used for calculation: ‘a-d’). The successful synthesis was confirmed by SEC which showed acceptable dispersities and comparable molar

mass to that obtained by NMR (Figure 5.6 B, $M_{n,SEC} = 23500 \text{ g mol}^{-1}$, and $\bar{D} = 1.23$). 9.6 mol% () of the PAG **12** was incorporated in **CP1** (calculated from ^1H NMR, see Figure 5.6A). In addition, the incorporation of PAG **12** was confirmed by UV-Vis spectroscopy, where two absorption bands corresponding to the coumarin moiety ($\lambda_{\text{max}}^2 = 328 \text{ nm}$ and $\lambda_{\text{max}}^2 = 292$) are seen (Figure 5.6 C).

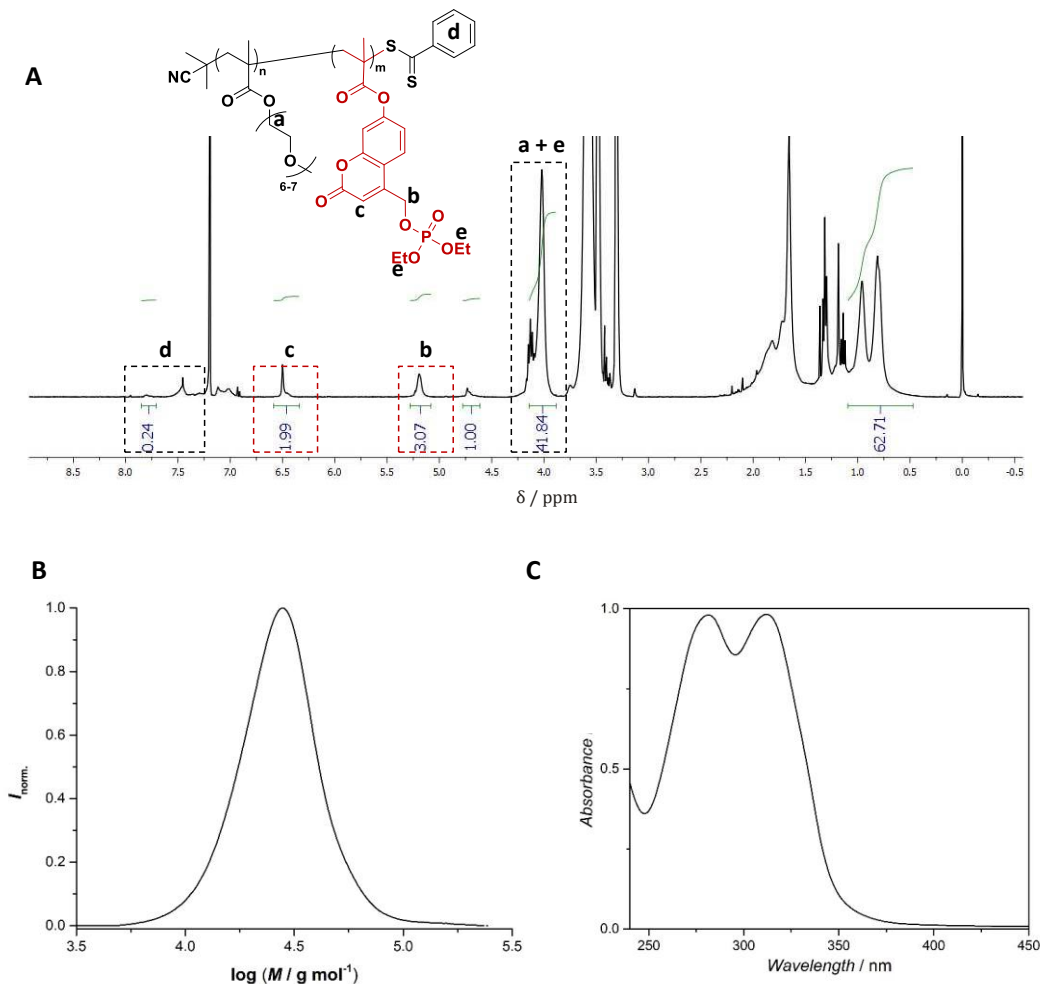


Figure 5.6. ^1H NMR spectrum in CDCl_3 (A), size-exclusion chromatogram in DMAc (B), and UV-Vis absorption spectrum in water (C) of **CP2**.

5.3.6 Photolysis study of P(OEGMA-*r*-PAG) **CP2**

As the efficient photolysis of **CP1** containing a coumarin based PBG was previously proved, similar experiments were conducted for **CP2**. Herein, we expect to observe a drop in the pH of the solution after irradiation due to the release of the phosphoric acid moiety

(see Scheme 5.2). Unlike in the case of **CP1**, the coumarin moiety of the PAG remains as a pendant group on the polymer backbone after photolysis. To study the change in pH after photolysis of **CP2**, two different studies were conducted: (i) change in pH of 10 and 20 g L⁻¹ **CP2** in water after irradiating for different times, and (ii) change in pH of different concentrations of **CP2** in water after irradiation for a constant time (1 h).

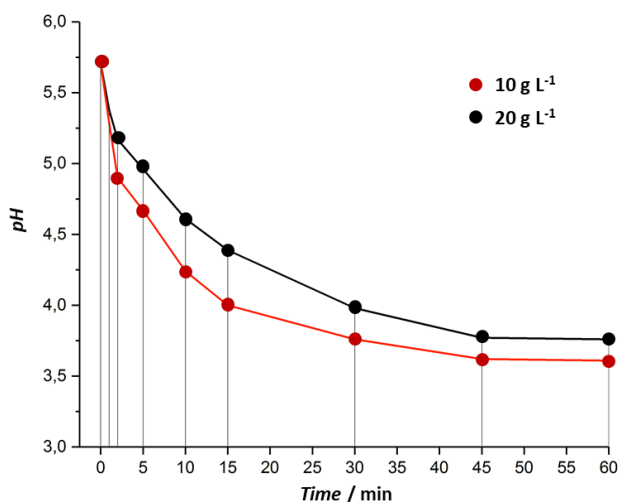


Figure 5.7. Evolution of pH of 10 g L⁻¹ (red) and 20 g L⁻¹ (black) **CP2** solutions in water after different irradiation times. Irradiation for every sample was performed at 320 nm.

On irradiation of **CP2** solution from 1 up to 60 min, a clear decrease in the pH of the solution was observed owing to the release of the phosphoric acid group, as expected (Figure 5.7). From a pH of 5.70 of **CP2** before irradiation, a drop of 2.07 units for 10 g L⁻¹ (pH = 3.63) (Figure 5.7, red), while 1.94 units for that of 20 g L⁻¹ (pH = 3.76) (Figure 5.7, black) after irradiation for 60 min was observed. A change in the intensity of absorption in the UV-Vis spectrum qualitatively confirmed the photolysis of **CP2** (see Appendix C, Figure C16). But, contrary to our expectation, a higher concentration of **CP2** induced a weaker drop in pH upon photolysis (Figure 5.7).

Further, the maximum irradiation time of 60 min from the previous experiment was chosen to irradiate various concentrations of **CP2** in water (1, 2, 5, 10, 15 and 20 g L⁻¹) to study the concentration dependence of **CP2** on the photolysis. As expected, the pH drop increases with increasing concentration due to larger amounts H⁺ ions in solution resulting from the

ionization of the produced phosphoric acid after photolysis (Figure 5.8). Unfortunately, the dip in pH at high concentrations (20 g L^{-1}) is still limited to approximately 2 units after 60 min of irradiation. Consequently, at this stage, a more detailed study of the photolysis of **CP2** is required. Lastly, **CP2** as **PAG** seemed to be more promising compared to that of **CP1** as **PBG**. Nevertheless, optimization of the system is required to observe a pH drop of 3 or more units for use in the intended application.

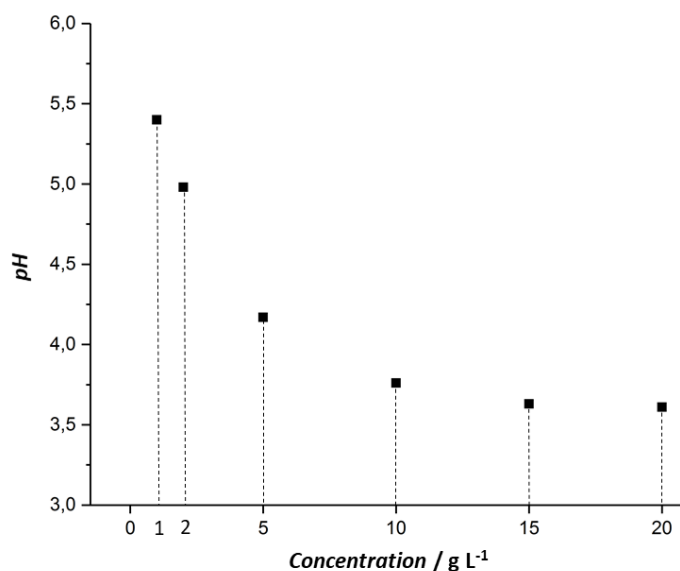


Figure 5.8. pH of of **CP2** solutions in water at various concentrations after a constant irradiation time of 60 min. $\lambda_{\text{max}} = 320 \text{ nm}$.

5.4 Conclusion

Photobase and photoacid generator monomers were designed to catch or release protons, respectively, on photolysis to induce pH jumps in aqueous media. Subsequently, novel **PBG 5** and **PAG 12** were synthesized and successfully incorporated as comonomers into a well-defined POEGMA polymer to obtain **CP1** and **CP2**, respectively. 9.3 and 9.6 mol% of **PBG** and **PAG** were incorporated into **CP1** and **CP2**, respectively. Further photolysis studies ($\lambda_{\text{max}} = 320 \text{ nm}$) were performed both on **CP1** and **CP2** to observe the change in pH upon irradiation considering two aspects: (i) change in pH of the copolymer solutions with irradiation time, and (ii) effect of concentration of **CP1** and **CP2** on the change in pH.

In the case of **CP1**, upon irradiation of the copolymer solution in water for 60 min at 320 nm, an increase in pH of 0.57 and 0.50 units for 10 and 20 g L⁻¹, respectively, were observed. A gradual increase in pH was observed with irradiation time with a maximum of 6.28 and 6.21 for 10 and 20 g L⁻¹ of **CP1**, respectively. Contrary to expectation, a higher pH jump was observed for 10 g L⁻¹ than 20 g L⁻¹ of **CP1** on irradiating for the same time. Furthermore, an increase in concentration of **CP1** at a constant irradiation time (60 min) induced weaker pH increases. The maximum jump in pH was 1.23 units for 1 g L⁻¹ of **CP1**, while a minimum jump of 0.46 units was seen for that of 20 g L⁻¹. Collectively, we hypothesize that there are two important factors contributing to such a behavior: (i) the inherent property of the coumarin skeleton of the PBG to undergo deprotonation after photolysis and thereby imparting counteracting acidic property, and (ii) the initially low pH of **CP1** in Millipore water (5.7). To counteract this, the secondary alcohol in the coumarin moiety can be protected before incorporation into POEGMA and the primary water soluble biocompatible polymer POEGMA can be replaced with similar alternatives such as PGMA or PNAM.

Similarly, **CP2** (in Millipore water, pH = 5.70) was subjected to photolysis for different irradiation times and herein a maximum drop in pH of 2.07 and 1.94 units was observed for 10 and 20 g L⁻¹. Further, a more important pH drop was observed with increasing concentration of **CP2** from 1-20 g L⁻¹ with a maximum of 2 units for 20 g L⁻¹. Although the expected trend of a decrease in pH upon photolysis of **CP2** was observed, the drop in pH (2 units) may not be sufficient for the final application. In conclusion, the investigated systems **CP1** and **CP2** are promising candidates as **PBG** or **PAG**, but require optimization with respect to the design of the macromolecular carrier.

6. SUMMARY AND OUTLOOK

In this thesis, a modular approach for the synthesis of various well-defined functional homo- and block copolymers (BCPs) has been successfully demonstrated. Furthermore, an elegant strategy to obtain nanostructured nanoparticles with reactive surface-exposed patches by controlling the internal phase separation has been elaborated. The design and synthesis of photoreactive homopolymers, and amine-cleavable BCPs have also been dealt with, targeted for applications as inflammation probes, or for the preparation of functional separation membranes, respectively.

Chapter 2 provides a detailed theoretical background of the aspects dealt with in the following chapters. The basic differences in the mechanism of ATRP, NMP, and RAFT polymerization has been explained. The state of the art of two post polymerization modification methods, *para*-fluoro-thiol reaction and activated ester-amine reaction, has been reported. A detailed understanding of the underlying concept behind phase separation of BCPs and their self-assembly in bulk and in solution has been discussed. Additionally, examples of BCP self-assembly into thin films and multicompartmental nanoparticles has been highlighted. Finally, the optics and the working principles behind TEM, STEM, and STED used to analyze the functional nanostructured nanoparticles has also been explained.

Chapter 3 deals with the synthesis of functional BCP libraries. The synthesis of a precursor BCP PMMA-*b*-PS containing two distinct pentafluorophenyl (PFP) moieties PFPMA and PFS in the PMMA and PS block, respectively was achieved ($M_{n,NMR} \approx 50000 \text{ g mol}^{-1}$, $f_{PMMA}:f_{PS} \approx 0.50:0.50$, % functionality < 10 mol%). Further, by post-polymerization modification using amidation and *para*-fluoro-thiol reaction, several bifunctional BCPs containing allyl, norbornyl, furanyl, azide, and thiol as secondary reactive handles were produced. A previously non-reported reaction of the *para*- and *meta*-fluorine atoms of PFPMA towards nucleophilic thiol-substitution reaction has been uncovered. Furthermore, the same concept was extended to produce functional BCPs based on P(nBMA-*r*-PFPMA)-*b*-P(S-*r*-PFS). Hence, the complementary and simple reactions of distinct PFP moieties in defined polymer architectures makes them powerful orthogonal groups to synthesize libraries of multifunctional BCPs.

Chapter 4 focuses on the fabrication of functional nanostructured materials using BCP self-assembly. The targeted patchy nanoparticles could not be obtained using the self-assembly of PMMA-*b*-PS and PnBMA-*b*-PS BCP systems. But, it was successfully prepared by self-organized precipitation (SORP) of chloro, azido and PFP containing PS-*b*-PI BCPs. Several morphologies of phase separation leading to onion-like, dots, and stacked lamellae (stripes) structured nanoparticles were obtained. In the case of functional PS-*b*-PI that did not form striped nanoparticles, SORP of A'B+AB type blends were used. These new types of BCP blends led to internal phase transformation, e.g., from onion-like to stacked lamellae. The immobilization of model thiols on the PFP rich domains of these striped particles proved the domain-specific surface reactivity of the nanoparticles. Furthermore, the striped nanoparticles were also transformed into surface-reactive nanodiscs, and their surface-reactivity was achieved. In a different approach, an amphiphilic BCP containing a central PFP linkage was designed and synthesized for the preparation of porous membranes by BCP self-assembly and amine wash in tandem. The BCP was constructed using a PFP ester-functionalized RAFT agent, which could further be subjected to PFTR to obtain a water-soluble segment at the *para* position. The RAFT functionality on the other hand was used to grow a hydrophobic segment, e.g., PS, which would form the bulk of the membrane. Performing PFTR on PFP-ester based RAFT agent or PFP-PS using a thiol terminated water-soluble polymer (PGMA-SH) or a thiol-functionalized ATRP initiator, respectively were two promising routes to synthesize the amphiphilic BCP. In a nutshell, such reactive nanostructured materials are promising candidates for applications that rely on site-selectivity and specificity.

In Chapter 5, photo reactive functional copolymers containing novel coumarin based photoacid (PAG) and photobase (PBG) generators were designed and synthesized to observe pH changes upon light irradiation. The POEGMA based P(OEGMA-*r*-PBG) and P(OEGMA-*r*-PAG) copolymers however did not produce a significant change in pH on photolysis. A maximum change of ≈ 2 pH units of pH change could be detected, probably arising from the acidic property of coumarins in water. Nevertheless, certain modifications in this system with respect to the substitutions on the coumarin as well as the homopolymer itself can be helpful in achieving the desired changes in pH. The newly developed PAG

and PBG monomers can nonetheless be useful in the synthetic field as photolabile protecting groups.

The ultimate goal of the presented dissertation is to directly utilize bifunctional BCPs to obtain dual-reactive striped nanoparticles. In particular, we are interested in immobilizing a different recombinant enzymes in each of the lamellae patches, i.e., in close proximity to one another to mimic enzyme cascade reactions that are useful for catalysis and purification. Apart from the nanostructured nanoparticles, it is also within our scope to fabricate the membranes by electrospinning, and generate cylindrical pores using the newly established reactivity of substituted PFP-esters.

7. MATERIALS AND METHODS

7.1 Materials

Methyl methacrylate (MMA; 99 %, Acros), styrene (99.5 %, Acros), 4-vinylbenzyl chloride (VBC; 97%, Sigma Aldrich), and pentafluorostyrene (PFS; 98 %, ABCR) were deinhibited prior to use by passing through a column of basic alumina (Roth). Isoprene (99%, ABCR) was distilled at 40 °C before use. Azobisisobutyronitrile (AIBN) was recrystallized from methanol. 1,8-Diazabicyclo[5.4.0]-undec-7-ene (DBU; Merck) was distilled before use. 2-Cyano-2-propyl benzodithioate (CPBD; > 97%, Aldrich), allylamine (98%, Acros organics), furfurylamine ($\geq 99\%$, Aldrich), 5-norbornene-2-methylamine (> 98%, TCI), 2-aminoethanethiol (> 95%, TCI), 2-mercaptoethanol ($\geq 99\%$, Roth), 1-octanethiol (OT; $\geq 98.5\%$, Aldrich), sodium azide (NaN_3 , $\geq 99\%$, Roth), polystyrene-*b*-polyisoprene **P5** (Polymer Source Inc., Ltd., Canada; $M_n = 78 \text{ kg mol}^{-1}$, $D = 1.05$, $f_{\text{PS}} = 0.57$), osmium tetroxide (OsO_4 , 2 vol% solution for electron microscopy), fluorescein-PEG-thiol (FITC-PEG-SH, MW = 2000 Da, NANOCS), *L*-Cysteine (97%, Aldrich), Tween®20 (Sigma), triethylamine (TEA; 99%, Fisher), resorcinol (Roth, > 99%), 4-bromoresorcinol (Sigma Aldrich, 97%), ethyl 4-chloroacetate (97%, Acros), *N,N*-diisopropylethylamine (DIPEA) ($\geq 99.5\%$, Roth), 4-dimethylaminopyridine (DMAP) ($\geq 99\%$, Sigma Aldrich), 4-nitrophenyl chloroformate (97%, Acros), sulfuric acid (96%, Roth), 2-aminoethyl methacrylate hydrochloride (90%, Sigma Aldrich), citric acid ($\geq 99.5\%$, Roth), MgSO_4 ($\geq 99\%$, Roth), chloromethyl methyl ether (MOMCl) (technical grade, Sigma Aldrich), diethylphosphoric acid chloride (> 97%, TCI), TFA ($\geq 99.5\%$, Fisher Chemical), NaOH ($\geq 99\%$, Roth), and methacryloyl chloride (97%, Alfa Aesar). were used as received.

Anhydrous dichloromethane (Anhyd. DCM; $\geq 99.8\%$, Aldrich), anhydrous acetonitrile (99.9% Acros), anhydrous ethanol (99.8%, Acros), anhydrous pyridine ($\geq 99\%$, Roth), dichloromethane (DCM; 99.7%, VWR), 1,4-dioxane ($\geq 99.5\%$, Roth), tetrahydrofuran (THF; 99.9%, VWR), *N,N*-dimethylformamide (DMF; 99.9%, VWR), acetonitrile (99.99%, Fisher), and methanol (99.99%, VWR), Chloroform ($\geq 99.8\%$, VWR), acetone ($\geq 99.5\%$, Fischer), diethyl ether ($\geq 99.5\%$, Roth) were used as received.

2-methoxy-6-methylbenzaldehyde²⁷⁰, pentafluorophenyl methacrylate²⁷¹, *N*-tert-butyl-*N*-[1-diethylphosphono-(2,2-dimethylpropyl)] nitroxide (SG1), and 2-methyl-2-[*N*-tert-butyl-*N*-(1-diethoxyphosphoryl)-2, 2-dimethylpropyl]aminoxy]propionic acid (MAMA-SG1) were synthesized according to the previously reported procedures.²⁷²

The pH 13 buffer solution was prepared by mixing 0.4 M NaOH (90 mL), a 7.52 g L⁻¹ solution of glycine (140 mL) and a 5.86 g L⁻¹ NaCl solution (140 mL).⁹⁶

7.2 Characterization

7.2.1 Characterization of the polymers

Size-exclusion chromatography (SEC) THF SEC measurements were performed on a TO-SOH Eco-SEC HLC-8320 GPC system, which comprised of an autosampler, a SDV 5 μ m bead size guard column (50 \times 8 mm, PSS) followed by three SDV 5 μ m columns (300 \times 7.5 mm, subsequently 100, 1000, and 10⁵ Å pore size, PSS), and a differential refractive index (DRI) detector with THF as the eluent at 30°C with a flow rate of 1 mL min⁻¹. The SEC system was calibrated by using linear polystyrene standards ranging from 266 to 2.52 \times 10⁶ g mol⁻¹, with linear PMMA standards ranging from 800 to 1.82 \times 10⁶ g mol⁻¹. Calculation of the molar mass proceeded by using the Mark-Houwink-Sakurada (MHS) parameters for PMMA in THF at 30 °C, that is, $K = 129.8 \times 10^{-3}$ mL g⁻¹ and $\alpha = 0.688$.

DMAc SEC measurements were performed on a Polymer Laboratories (Varian) PL-GPC 50 Plus Integrated System, comprising of an autosampler, a PLgel 5 μ m beads size guard column (50 \times 7.5 mm) followed by three PLgel 5 μ m Mixed-C columns (300 \times 7.5 mm). The spectrometer was attached to a differential refractive index detector and a DMAc eluent system containing 0.3 wt% LiBr. The temperature was set to 50 °C with a flow rate of 1 mL min⁻¹. The SEC system is calibrated using linear polystyrene standards ranging from 160 to 6 \times 10⁶ g mol⁻¹ and linear poly(methyl methacrylate) standards ranging from 700 to 2 \times 10⁶ g mol⁻¹. Mark-Houwink-Kuhn-Sakurada (MHKS) parameters for polystyrene ($K = 14.1 \times 10^{-5}$ dL g⁻¹ and $\alpha = 0.7$) were used to calculate molar masses of the polymers.

NMR spectroscopy Measurements were performed on a Bruker AM 500 spectrometer at 500 MHz. The analytes were dissolved in CDCl_3 and the residual solvent signals were employed for shift correction. For the ^{19}F -CPD NMR spectra, at least one of the following corrections was made by using MestReNova 9.0 software: baseline correction with the method Bernstein polynomial fit (with polynomial order of 14), manual correction, or multipoint baseline correction.

Attenuated total reflectance (ATR) FT-IR spectroscopy Solid-state Fourier transform IR spectra were measured using a Bruker Vertex 70 spectrometer, equipped with a tungsten halogen lamp, a KBr beam splitter, and a DTGS detector.

UV-Vis spectroscopy Measurements were carried out on a Biotek Epoch 2 spectrophotometer using a quartz cuvette with a path length of 10 mm (Quartz SUPRASIL®, Hellma Analytics).

Fluorescence spectroscopy Fluorescence spectra were recorded in a Cary Eclipse spectrometer with a Single Cell Peltier System at ambient temperature in water from 300 to 700 nm.

Electrospray ionization mass-spectrometry ESI-MS spectra were recorded on a Q Exactive (Orbitrap) mass spectrometer (ThermoFisher Scientific, San Jose, CA, USA) equipped with an HESI II probe. The instrument was calibrated in the m/z range of 74-1822 using a premixed standard comprising of caffeine, Met-Arg-Phe-Ala acetate (MRFA), and a mixture of fluorinated phosphazenes (Ultramark 1621). A constant spray voltage of 4.6 kV and a dimensionless sweep gas flow rate of 5 were applied. The capillary temperature and the Slens RF level were set to 320 °C. The samples were prepared at a concentration of 0.03 mg mL^{-1} in a mixture of THF and MeOH (3:2) containing 100 μmol sodium trifluoroacetate (NaTFA). The samples were injected with a flow rate of 5 $\mu\text{L min}^{-1}$.

pH measurements pH measurements were conducted using a Mettler Toledo SevenCompact™ pH/Ion S220 pH-meter, calibrated using standard solutions of pH 4.0, 7.0, 9.0 and 12.0 purchased from Roth.

7.2.2 Characterization of the nanoparticles and nanodiscs

Dynamic Light Scattering (DLS) Measurements were performed on a Malvern Zetasizer Nano ZS that uses NIBS (non-invasive back scattering) to measure the hydrodynamic diameter of the nanoparticles. The zeta potential was also measured using the same instrument in deionized water.

(Scanning) Transmission Electron Microscopy (S)TEM The nanodiscs were measured on a JEOL-2100F high resolution STEM with Cs-corrector instrument at 200 KeV accelerating voltage attached to a high angle annular dark field (HAADF) detector. A JS single tilt holder was used to mount the grid. The instrument had attached an energy dispersive X-ray detector (EDX) for elemental analysis: The nanoparticles were either measured using the above STEM or a transmission electron microscope (TEM, H-7650, Hitachi, Japan) set to an accelerating voltage of 100 KeV attached to a bright field detector.

Electron Tomography (ET) Three-dimensional (3D) structures of striped particle were reconstructed by using the series of TEM images observed with an acceleration voltage of 100 kV. The series of TEM images were acquired at tilt angles from -60° to $+60^\circ$ in 1° steps. The TEM images were aligned and reconstructed using an imaging software (Image J, NIH) with a “Tomo-J” plug-in.²⁷³ The reconstruction was performed by using the weighted back-projection algorithm. The reconstructed images were refined and colored with an imaging software (Cinema 4D, MAXON, Inc.).

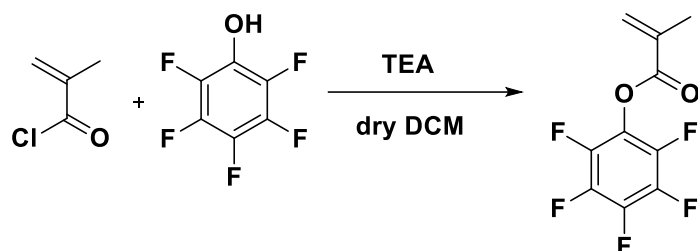
Atomic Force Microscopy (AFM) One drop of THF dispersion of nanodiscs were cast on a Si substrate and dried at room temperature. Surface structures of the nanodiscs were then measured by AFM, SPI400, SII using the DFM (tapping) mode.

Stimulated Emission Depletion (STED) Microscopy The fluorescent nanodiscs were characterized with a Leica TCS SP8 Laser Scanning Confocal Microscope. Excitation was with a white light laser set to 488 nm. The Hybrid Detector window was set to capture 500–550 nm, gated at 1.5–6.5 ns. The stimulated emission depletion super resolution imaging was carried out with a 592 nm depletion laser. Post image acquisition deconvolution was performed with Huygens Professional.

8. SYNTHETIC PROTOCOLS

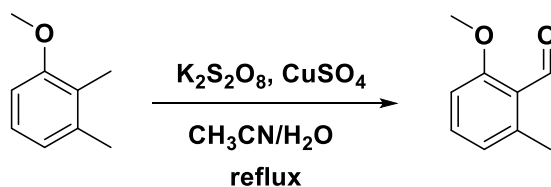
8.1 Synthetic protocols pertaining to Chapter 3

Synthesis of PFPMA



In a two neck round bottom flask, pentafluorophenol (0.91 eq, 10.86 mmol, 2 g) was dissolved in dry DCM (20 mL) under nitrogen. Triethylamine (TEA, 1 eq, 11.94 mmol, 1.21 g) was added via a syringe through the septum. A dropping funnel filled with methacryloyl chloride (1 eq, 11.94 mmol, 1.25 g) was placed above the other neck and methacryloyl chloride was added into the flask dropwise under nitrogen while vigorously stirring the reaction mixture placed in an ice bath. After complete addition, the reaction mixture was cooled down for 15 min and slowly warmed up to room temperature over 12 h. The reaction mixture was extracted with water (3 × 50 mL), brine (2 × 50 mL) and the organic phase dried over magnesium sulfate. Excess DCM was evaporated under vacuum and the brown oily liquid was vacuum distilled at 49 °C and 5×10^{-2} mbar to obtain the pure product as a colorless oily liquid. Yield = 32.5 %.

Synthesis of 2-methoxy-6-methylbenzaldehyde



A vigorously stirred mixture of 2,3-dimethylanisole (36.6 mmol, 4.99 g), copper(II)sulfate (0.99 eq, 36.2 mmol, 5.78 g) and potassium peroxodisulfate (3.01 eq, 110 mmol, 29.74 g) in acetonitrile/water (1:1, 250 mL) was heated to reflux (100 °C). After 30 min, the mixture

changes color from green to brown and thin layer chromatography (TLC) shows the presence of product, some side products and a small amount of the starting material (cyclohexane/ethylacetate = 8.2, $R_f(\text{product}) = 0.8$, $R_f(\text{reactant}) = 0.6$). The mixture was then cooled down to room temperature and dichloromethane (DCM, 75 mL) was added. The aqueous phase was extracted with additional DCM (2×35 mL). The combined organic phases were dried over Na_2SO_4 ; the filtrate evaporated at reduced pressure to give the crude product, which was purified by column chromatography (silica gel, cyclohexane/ethylacetate). Yield = 39.7%.

Synthesis of PFP ester-functionalized macroRAFT agent 1

In a 50 mL round bottom flask, CPBD (55.3 mg, 0.25 mmol) was dissolved in 1,4-dioxane (4.87 mL). To this, MMA (9.5 g, 94.9 mmol) and PFPMA (1.26 g, 0.5 mmol) were added. A 1 mg/mL stock solution of AIBN was prepared in 1,4-dioxane and 5.13 mL from this (5.13 mg, 0.03 mmol) were added into the round bottom flask. A t_0 sample was withdrawn for indirect determination of PFPMA content in the final polymer and the flask was sealed with a septa. The content was deoxygenated by bubbling nitrogen for 1 h and the flask was subsequently placed in a pre-heated oil bath at 90 °C for 3 h. After this, the mixture was cooled down to room temperature and exposed to air. ^1H NMR was used to determine the conversion of both comonomers. The resulting polymer was purified by precipitating twice in an excess of cold methanol and dried under vacuum at 40 °C overnight. The macroRAFT agent **1** was recovered as a pink powder. The incorporation of PFPMA was confirmed both by ^{19}F NMR and FTIR spectroscopy (Figure A1 C and A, respectively). $M_{n,\text{SEC}} = 26000 \text{ g mol}^{-1}$, $D = 1.15$; $M_{n,\text{NMR}} = 25000 \text{ g mol}^{-1}$. The amount of PFPMA incorporated was estimated by NMR and IR spectroscopies, as described below:

Calculation of PFPMA content in the macroRAFT agent P(MMA-*stat*-PFPMA) **1**

The amount of PFPMA incorporated in macroRAFT agent **1** was obtained as an average of the values calculated from NMR and IR data as previously reported by Zhang *et al.* ²⁷⁴

From IR spectroscopy: The amount of PFPMA incorporated was estimated to be 7 mol% obtained by integrating the areas of PFPMA (0.164) and PMMA (2.346) absorption bands in green and pink, respectively (Figure A1 A).

From NMR: Two methods of calculation based on NMR spectroscopy were employed: (i) by calculating the conversion of PFPMA and MMA from the crude polymerization (Figure A1 D) and (ii) from the NMR spectrum of the purified macroRAFT **1** comparing the integral values of the $-\text{OCH}_3$ peak of MMA to those of the backbone (Figure A1 B), respectively.

Method (i)

$$\text{Conversion of PFPMA} = (1.86 - 0.63) / 1.87 = 66\%$$

$$\text{Conversion of PMMA} = (34.40 - 20.18) / 34.40 = 41.3$$

Ratio of PFPMA to MMA introduced into the reaction mixture = 5:95

$$\text{Therefore, mol\% PFPMA incorporated} = (0.66 \times 0.05) / [(0.66 \times 0.05) + (0.413 \times 0.95)] = 7.8 \text{ mol\%}$$

Method (ii)

$$\text{Mol\% PFPMA} = 1 - \left[\frac{2.72}{3.0} \right] \times 100 = 9.3 \text{ mol\%}$$

As stated by Zhang et al., IR spectroscopy provides an overestimated value while NMR gives an underestimated value coming from their noise reductions and baseline corrections. Therefore an average of 8 mol% was calculated as optimum fraction of PFPMA in the macroRAFT agent.

Synthesis of block copolymer P(MMA-stat-PFPMA)-b-P(S-stat-PFS) 2

In a 100 mL round bottom flask, macro-RAFT agent **1** (1.3 g, 0.05 mmol) was dissolved in 1,4-dioxane (19.84 mL). To this, styrene (19.4 g, 186 mmol) and PFS (1.118 g, 5.76 mmol) were added. A 1 mg/mL stock solution of AIBN was prepared in 1,4-dioxane and 1.64 mL from this stock solution (1.64 mg, 0.001 mmol) were added into the round bottom flask. The flask was sealed with a septa and the contents were deoxygenated by bubbling with nitrogen for 1 h. The flask was then placed in a pre-heated oil bath at 90 °C for 80 min. After this, the mixture was cooled down to room temperature and exposed to air. The resulting polymer was purified by precipitating twice in an excess of cold methanol and dried under vacuum at 40 °C overnight. The block copolymer **2** was recovered as a pink

powder. The exact amount of PFS in the final polymer was calculated as described in an earlier report.⁹⁵ $M_{n,SEC} = 46000 \text{ g mol}^{-1}$, $\mathcal{D} = 1.25$; $M_{n,NMR} = 52000 \text{ g mol}^{-1}$.

Calculation of the number-average molar mass of **2** using NMR ($M_{n,NMR}$)

From Figure 3.1 A: For 1 MMA unit, block copolymer **2** contains 0.954 styrene units.

$$\text{Molar mass of the PS block} = \left(\frac{M_{n,SEC}(\text{PMMA } \mathbf{1}) - MW(\text{end groups})}{MW(\text{MMA})} \times \frac{\text{styrene}}{\text{MMA}} \text{ratio} \times MW(\text{styrene}) \right.$$

$$= \left(\frac{(26000 - 221.34)}{100.12} \right) \times 0.954 \times 104.15 = 25800 \text{ g/mol};$$

Hence, $M_{n,NMR}(\mathbf{2}) = 25800 + 26000 = 51800 \text{ g mol}^{-1} = \sim 52,000 \text{ g mol}^{-1}$

Synthesis of block copolymer P(nBMA-stat-PFPMA)-b-P(S-stat-PFS) **5**

In a 100 mL round bottom flask, macro-RAFT agent P(nBMA-*stat*-PFPMA) (195 mg, 0.007 mmol) was dissolved in 1,4-dioxane (3 mL). To this, styrene (3.0 g, 27.94 mmol) and PFS (167.7 mg, 0.86 mmol) were added. A 1 mg/mL stock solution of AIBN was prepared in 1,4-dioxane and 0.25 mL from this stock solution (0.25 mg, 0.0014 mmol) were added into the round bottom flask. The flask was sealed with a septa and the contents were deoxygenated by bubbling with nitrogen for 1 h. The flask was then placed in a preheated oil bath at 90 °C for 90 min. After this, the mixture was cooled down to room temperature and exposed to air. The resulting polymer was purified by precipitating twice in an excess of cold methanol and dried under vacuum at room temperature (due to the low glass-transition temperature (T_g) of butyl-methacrylate) overnight. The block copolymer **2** was recovered as a pink powder. The exact amount of PFS in the final polymer was calculated as for BCP **2**. $M_{n,SEC} = 54000 \text{ g mol}^{-1}$, $\mathcal{D} = 1.18$; $M_{n,NMR} = 53300 \text{ g mol}^{-1}$.

RAFT end group capping

A polymer solution of **1** or **2** was prepared in acetonitrile or **5** in DCM (10 mg mL⁻¹). To this, 2-methoxy-6-methylbenzaldehyde (2 eq.) was added and the solution was deoxygen-

ated by bubbling N_2 for 30 minutes. The flask was then placed in a custom made photoreactor and irradiated at RT with two Arimed B6 lamps ($\lambda_{\max} = 320$ nm, power density = 14.7 $mW\ m^{-2}$). After 1 h, acetonitrile or DCM was removed under vacuum and the residue was re-dissolved in a minimum amount of dichloromethane. The polymer was recovered by precipitation in excess cold methanol. Polymer **1a**, **2a**, and **5a** were obtained as white powders. End group capping was confirmed by UV-Vis spectroscopy from the disappearance of absorbance at 310 nm, typical of the RAFT end group. **1a**: $M_{n,SEC} = 27000$ $g\ mol^{-1}$, $\mathcal{D} = 1.15$; $M_{n,NMR} = 25000$ $g\ mol^{-1}$. **2a**: $M_{n,SEC} = 47000$ $g\ mol^{-1}$, $\mathcal{D} = 1.23$; $M_{n,NMR} = 52000$ $g\ mol^{-1}$. **5a**: $M_{n,SEC} = 53500$ $g\ mol^{-1}$, $\mathcal{D} = 1.18$; $M_{n,NMR} = 53000$ $g\ mol^{-1}$

General procedure for amidation reaction

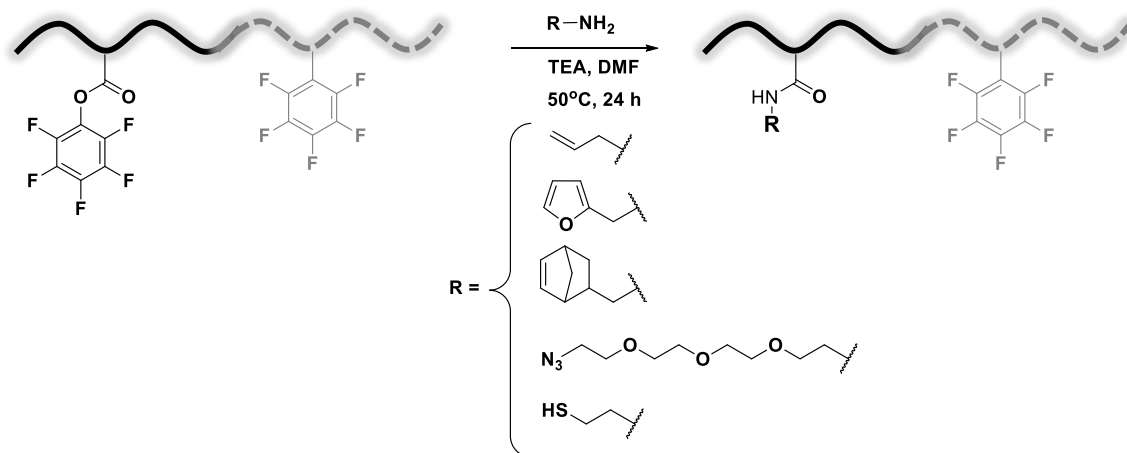


Figure 8.1. General reaction scheme for the reaction of **2a** with various amines.

In a 5 mL round bottom flask, a polymer (100 mg) was dissolved in DMF (0.9 mL, 1 eq.) and placed in a pre-heated oil bath at $50^\circ C$. In another flask, an amine (50 eq.) and triethylamine (5 eq.) were mixed together in DMF (100 μL) and added to the polymer solution. After stirring for 24 h, the reaction mixture was cooled down to room temperature and excess DCM was added. The organic layer was extracted with distilled water (20 mL) followed by brine (2×20 mL) and concentrated under vacuum. The polymer was precipitated in excess cold methanol and washed extensively with cold methanol. The polymer was then dried under vacuum at $40^\circ C$ overnight to obtain the modified polymer as a white

powder. A general scheme of the reaction is shown in Figure 8.1 and characteristics of the obtained polymers are collated in Table 3.1.

General procedure for PFTR

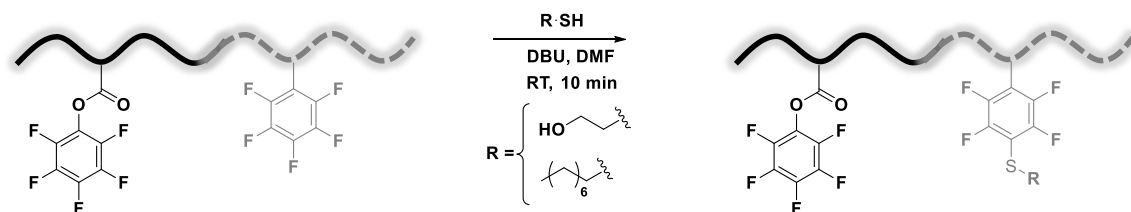


Figure 8.2. General reaction scheme for PFTR using OT and mercaptoethanol as model thiols.

Unless specified, PFTR experiments were conducted as follows. In a 5 mL round bottom flask, a polymer solution was prepared in DMF (100 mg in mL, 1 eq.). To this, DBU (1 eq.) and thiol (5 eq.) were sequentially added. The reaction was stirred at room temperature for ten minutes. An aliquot was then quenched by introducing it into an NMR tube containing CDCl₃ for direct measurement. The polymer was purified by precipitating in cold excess methanol and washing extensively to remove any excess thiol. The polymer was dried under vacuum overnight at 40 °C and recovered as a white powder. The general reaction scheme is shown in Figure 8.2.

One-pot dual functionalization using aminoethanethiol

In a 10 mL round bottom flask, the polymer (100 mg, 1 eq.) was dissolved in DMF (1 mL) and placed in a pre-heated oil bath at 50 °C. In another round bottom flask, aminoethanethiol (148.36 mg, 50 eq.) was dissolved in DMF (2 mL) and TEA (5 eq.) was added. The solution was sonicated for 10 minutes to ensure complete solubility of aminoethanethiol and was then added to the polymer solution. The reaction mixture was stirred at 50 °C for 24 h, after which it was cooled down to room temperature and diluted with excess DCM. In this case, DBU was not added as the base to catalyze PFTR on PFS because TEA catalyzes both reactions under the specified conditions. The organic layer was extracted with distilled water (20 mL) followed by brine (2 × 20 mL) and concentrated under vacuum.

The polymer was precipitated in excess cold pentane, dried under vacuum overnight at 40 °C, and obtained as a white powder.

8.2 Synthetic protocols pertaining to Chapter 4

Synthesis of PMMA-*b*-PS by RAFT polymerization

Synthesis of PMMA macro-RAFT agent

In a 50 mL round bottom flask, CPBD (55.3 mg, 0.25 mmol) was dissolved in 1,4-dioxane (4.87 mL). To this, MMA (10 g, 99.9 mmol) was added. A 1 mg/mL stock solution of AIBN was prepared in 1,4-dioxane and 5.13 mL from this (5.13 mg, 0.03 mmol) were added into the round bottom flask. A t_0 sample was withdrawn for calculating the conversion of MMA and the flask was sealed with a septa. The content was deoxygenated by bubbling nitrogen for 1 h and the flask was subsequently placed in a pre-heated oil bath at 90 °C for 2h 30 min. After this, the mixture was cooled down to room temperature and exposed to air. ^1H NMR was used to determine the conversion of MMA. The resulting polymer was purified by precipitating twice in an excess of cold methanol and dried under vacuum at 40 °C overnight. The macro-RAFT agent was recovered as a pink powder and the exact molar mass was determined by SEC (Figure B11 A'). $M_{n,SEC} = 21300 \text{ g mol}^{-1}$, $\mathcal{D} = 1.10$; $M_{n,NMR} = 16000 \text{ g mol}^{-1}$.

*Synthesis of PMMA-*b*-PS BCP by RAFT polymerization*

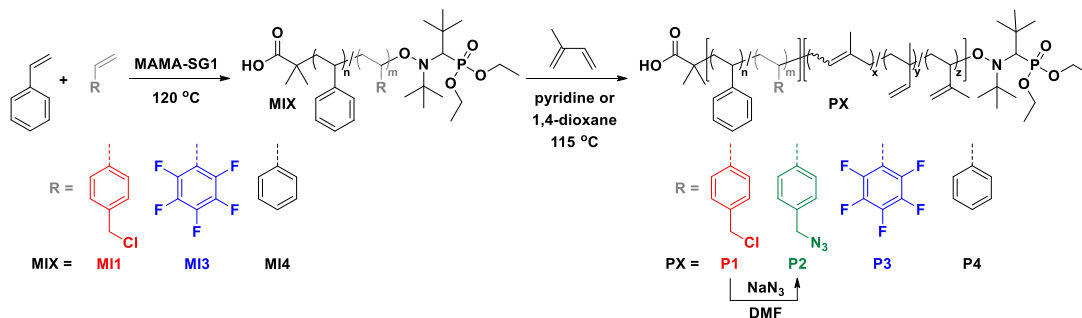
In a 100 mL round bottom flask, PMMA macro-RAFT agent (525 mg, 0.025 mmol) was dissolved in 1,4-dioxane (10 mL). To this, styrene (10 g, 96 mmol) and AIBN (0.85 mg, 0.005 mmol) were added. The flask was sealed with a septa and the contents were deoxygenated by bubbling with nitrogen for 1 h. The flask was then placed in a pre-heated oil bath at 90 °C for 2 h 30 min. After this, the mixture was cooled down to room temperature and exposed to air. The resulting polymer was purified by precipitating twice in an excess of cold pentane and dried under vacuum at 40 °C overnight. The block copolymer was

recovered as a pink powder. The exact molar mass was determined by ^1H NMR and confirmed by SEC (Figure B11 A and A', respectively). $M_{n,\text{SEC}} = 40500 \text{ g mol}^{-1}$, $\mathcal{D} = 1.25$; $M_{n,\text{NMR}} = 44500 \text{ g mol}^{-1}$, $f_{\text{PS}}:f_{\text{PMMA}} = 0.55:0.45$.

Synthesis of PnBMA-*b*-PS by RAFT polymerization

The exact procedure as for the synthesis for PMMA macro-RAFT agent (as described above) was used for the synthesis of PnBMA macro-RAFT agent for a reaction run time of 2 h. $M_{n,\text{SEC}} = 22800 \text{ g mol}^{-1}$, $\mathcal{D} = 1.08$; $M_{n,\text{NMR}} = 21000 \text{ g mol}^{-1}$. Followed by this, using PnBMA as the macro-RAFT agent, similar procedure as for the synthesis of PMMA-*b*-PS was utilized to obtain PnBMA-*b*-PS as a pink powder. The exact molar mass of the macro-RAFT agent was first obtained from SEC, followed by the calculation of the molar mass of the BCP ^1H NMR (Figure B11 B' and B, respectively). $M_{n,\text{SEC}} = 45000 \text{ g mol}^{-1}$, $\mathcal{D} = 1.19$; $M_{n,\text{NMR}} = 47000 \text{ g mol}^{-1}$, $f_{\text{PS}}:f_{\text{PnBMA}} = 0.52:0.48$.

Synthesis of functional PS-*b*-PI BCPs by NMP



Scheme 8.1. Synthetic route towards the synthesis of macroinitiators **M1**, **M2**, **M4** and **P1–4** by NMP.

Table 8.1. Characteristics of the functional PS macroinitiators MI1, MI3, and MI4. %F: percentage of functional monomer introduced in the PS block.

Macro initiator	Comonomer in PS block	%F	$M_{n,SEC}$ g mol ⁻¹	\bar{D}
MI1	VBC	6.0	26,500	1.17
MI3	PFS	4.0	25,300	1.10
MI4	-	-	22,300	1.09

Table 8.2. Characteristics of the PS-*b*-PI block copolymers P1–4. % F: percentage of functional monomer introduced in the PS block.

Functional BCP	%F	$M_{n,NMR}$ g mol ⁻¹	$M_{n,SEC}$ g mol ⁻¹	\bar{D}	$f_{PS}:f_{PI}$
P1	6.0	48,900	62,800	1.32	0.47:0.53
P2	6.0	48,800	64,300	1.35	0.47:0.53
P3	4.0	47,300	61,900	1.32	0.50:0.50
P4	-	43,000	56,400	1.35	0.48:0.52

Chloromethylbenzyl-functionalized PS macroinitiator MI1

Styrene (3.67 g, 35.1 mmol), 4-vinylbenzyl chloride (282 mg, 1.84 mmol), and MAMA-SG1 (35.5 mg, 0.09 mmol) were mixed in a 10 mL round bottom flask. The flask was placed in a preheated oil bath at 120 °C after being purged with N₂ for 30 min. The reaction mixture was cooled to ambient temperature after 130 min. The resulting polymer was precipitated twice in cold methanol and **MI1** was recovered as a white powder. (Scheme 8.1, Table 8.1).

Chloromethylbenzyl-functionalized PS-*b*-PI P1

MI1 (200.4 mg) was dissolved in 1,4-dioxane (2560 μL) in a pressure tube. The tube was sealed with a rubber septum and the content was purged with N₂ for 30 min. A large amount of isoprene was placed in a flask which was then sealed with a rubber septum and purged with nitrogen while being in an ice bath. The isoprene flask and the pressure tube were taken into a glovebox and isoprene (2560 μL, 1740.8 mg, 25.56 mmol) was added into the pressure tube before the latter was quickly sealed with a fitted screw cap. Outside of the glovebox, the pressure tube was placed in a preheated oil bath at 115 °C. After 15 h, the

reaction was stopped by cooling the flask to ambient temperature. 1,4-dioxane was removed under vacuum. The residue was dissolved in a minimal amount of THF and precipitated in a methanol/isopropanol mixture (3:1 v/v) including a small amount of BHT as stabilizer. **P1** was recovered as a white powder (Scheme 8.1, Table 8.2, Figure B12 P1 and Figure B 13 A).

Azidomethylbenzyl-functionalized PS-b-PI P2

P1 (100.8 mg) was dissolved in THF (3 mL). DMF (50 mL) was added. NaN₃ (10 mg, 0.15 mmol) was dissolved in this solution. The content was stirred at RT for 4 days. Solvents were removed in vacuum. Subsequently, the product was dissolved in DCM (20 mL) and extracted with water (3 × 80 mL). The organic layer was dried over MgSO₄, filtered, and concentrated in vacuum. **P2** was precipitated in a methanol/isopropanol mixture (3:1 v/v) including a small amount of BHT as stabilizer and obtained as a white powder (Scheme 8.1, Table 8.2, Figure B12 P2 and Figure B 13 A).

Pentafluorophenyl-functionalized PS macroinitiator MI3

Styrene (4.63 g, 44.5 mmol), PFS (449 mg, 2.3 mmol), and MAMA-SG1 (46.1 mg, 0.12 mmol) were mixed in a 10 mL round bottom flask. Same procedure as for the synthesis of **MI1** was followed for a reaction time of 135 min, followed by similar purification procedures as for **MI1** to obtain **MI3** as a white powder (Scheme 8.1, Table 8.1).

Pentafluorophenyl-functionalized PS-b-PI P3

MI3 (200.6 mg) was dissolved in pyridine (2560 μL) in a pressure tube. The same procedure was applied as for the synthesis of **P1** with isoprene (2560 μL) for a total reaction time of 13 h 55min. The same purification steps were applied and yielded **P3** as a white powder (Scheme 8.1, Table 8.2, Figure B12 P3 and Figure B 13 B).

Polystyrene macroinitiator MI4

In a 25 mL round bottom flask, styrene (10.36 g, 99.4 mmol) was mixed with MAMA-SG1 (98.1 mg, 0.26 mmol) and the flask was sealed with a rubber septum. Similar reaction procedure (reaction time = 2 h) and purification as for **MI1** and **MI3** was applied, and **MI4** was recovered as a white powder (Scheme 8.1, Table 8.1).

Polystyrene-block-polyisoprene (PS-*b*-PI) P4

MI1 (100.6 mg) was dissolved in pyridine (1280 μL) in a pressure tube. The same procedure was applied as for the synthesis of **P1** with isoprene (1280 μL) for a total reaction time of 13 h 40min. The same purification steps were applied and yielded **P1**, **P2** and **P3** to obtain **P4** as a white powder (Scheme 8.1, Table 8.2, Figure B12 P4 and Figure B 13 C).

Synthetic protocols for preparation of nanoparticles and nanodiscs***Preparation of nanoparticles***

The BCPs were dissolved in THF at a concentration of 1.0 and 0.1 mg mL^{-1} . The nanoparticles were prepared using a nanoprecipitation method (Scheme 4.2), as previously reported by Yabu *et al.*,¹⁸⁰ using various THF:water ratios (1:3, 1:1 and 3:1). More precisely, 1.5, 1, or 0.5 mL of millipore water was added dropwise at the rate of 1 mL min^{-1} into 0.5, 1, or 1.5 mL of the polymer solution in THF, respectively, with vigorous stirring. THF was then allowed to evaporate at room temperature and atmospheric pressure for 4 days. The sizes of all nanoparticles were measured by DLS. In another set of experiments, to study the transformation of internal structures with BCP blends, the polymers **P1–3** were mixed in various ratios with the commercial, non-functional PS-*b*-PI BCP **P5**. The nanoparticles prepared using these blends are described in Table 4.2.

Observation of the phase-separated structures in the nanoparticles

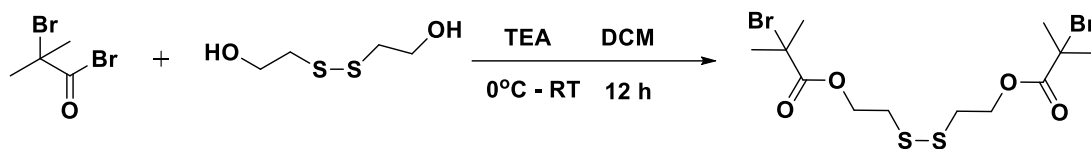
The nanoparticles were stained by mixing with 0.5 mL of a 0.2 vol% solution of OsO_4 for 2 hours. Excess OsO_4 was washed away by ultracentrifugation of the stained nanoparticles (Hitachi, himac CF16RX, 12000 rpm, 15 min, 5 $^\circ\text{C}$). The pellet was collected, redispersed in 700 μL millipore water, and ultrasonicated for 5 minutes to obtain a homogeneously dispersed nanoparticle solution. This washing process was repeated 4 times and the pellet was finally redispersed in water to obtain OsO_4 -stained nanoparticles. A Cu grid with a carbon-coated membrane was subjected to UV/ O_3 treatment (Iwasaki, Japan) for 3 minutes to render its surface hydrophilic and a drop of the stained nanoparticles was then casted onto it. After drying in air, the sample was observed using TEM (bright field, BF) and in some cases STEM (dark field, DF).

Preparation of functional nanodiscs from the striped nanoparticles

Functional BCP nanoparticles **NP3** that exhibited stacked lamellae patterns with pentafluorophenyl-functionalized PS domains (Blend 8, Figure 4.6 C3, Table 4.2) were used in this experiment to prepare functional nanodiscs **ND3**. This was achieved by following a method previously described by Higuchi *et al.* as selective immobilization and selective elution (SISE).¹⁶⁷ For this, firstly a 200 μL dispersion of the nanoprecipitation-made nanoparticles **NP3** was stained with osmium tetroxide as described above. After washing thoroughly, the final pellet was redispersed in 700 μL THF and sonicated at room temperature for 5 h. A 2 μL suspension was casted on a Cu grid coated with carbon for STEM analysis.

Reaction on functional BCP nanoparticles

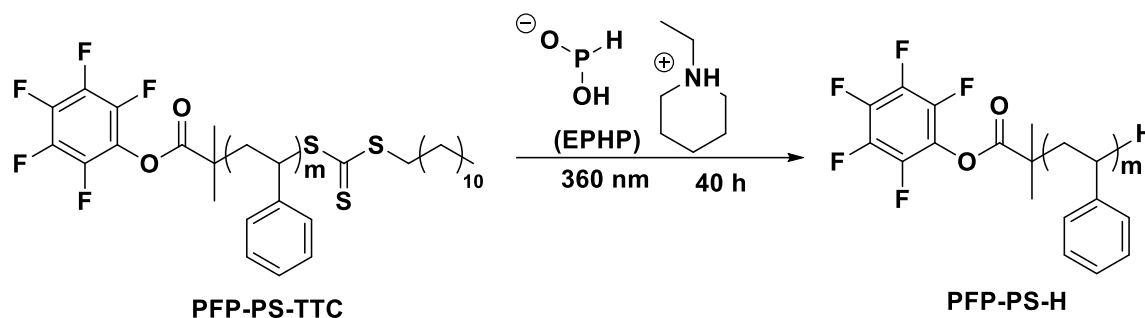
To prove the reactivity of the functional groups on the surface of the functional nanoparticles and nanodiscs, striped particles **NP3** and nanodiscs **ND3** both containing pentafluorophenyl units were chosen to perform *para*-fluoro thiol reaction (PFTR). In the case of **NP3**, a 100 μL homogeneous suspension of **NP3** in water was taken in an Eppendorf tube. To this, 2 mL of 10 mg mL^{-1} cysteine in pH 13 buffer was added and the solution was incubated in a shaker at 50° C for 16 h. On the other hand, for **ND3**, this reaction was performed in THF. To 100 μL of the nanodisc dispersion, first 2 μL of DBU followed by 1 mL of 10 mg mL^{-1} of FITC-PEG-SH was added and the solution was placed in a shaker overnight at room temperature. To prove that the thiols do not non-specifically adsorb on the surface of the nanoparticles or nanodiscs, control experiments were performed. The **NP3** and **ND3** control samples were incubated under the same conditions as the reaction sample, but in the absence of the catalyst, *i.e.*, in neutral water instead of pH 13 buffer solution for **NP3** and in THF in the absence of DBU for **ND3**. After the reactions, in order to remove the buffer solution/DBU and cysteine/FITC-PEG-SH, the solution was centrifuged (15,000 rpm, 30 min, 5 °C), the supernatant carefully decanted and the pellet washed with 1 mL 0.01% Tween@20 solution. This washing step was repeated thrice and finally once with deionized water to remove any excess reactants. The final pellet was re-dispersed in 700 μL of deionized water, tip sonicated and casted on a copper grid coated with carbon for STEM or on a microscopy glass slide for STED analysis.

Preparation of porous membranes***Synthesis of disulfanediylbis(ethane-2,1-diyl) bis(2-bromo-2-methylpropanoate)(ATRP-disulfide)***

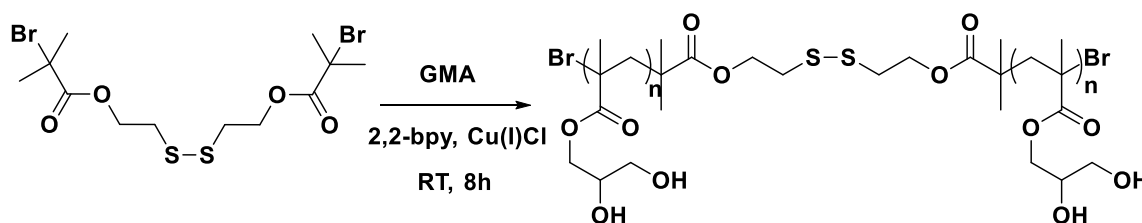
2-bromoisobutyryl bromide (18.6 g, 80.9 mmol, 2.4 eq) was added to a solution of 2-hydroxyethyl disulphide (5.1 g, 0.033 mmol, 1 eq) and trimethylamine (TEA, 8.1 g, 0.080 mmol, 2.4 eq) in dichloromethane (DCM, 67 mL) in a 250 mL round bottom flask placed in an ice bath at 0 °C. After the addition, the reaction was allowed to stir at room temperature for 12h and the ammonium salt formed was removed by filtration. The excess solvent was evaporated under vacuum and the residue was purified by column chromatography in ethyl acetate/pet ether to obtain the pure product as a light yellow liquid. R_f (product) = 0.6, Yield = 30%. The ^1H and ^{13}C NMR of the purified product with the corresponding peaks are represented in Figure B 14.

Synthesis of polystyrene (PS-TTC) by RAFT polymerization

In a 10 mL round bottom flask, perfluorophenyl 2-(((dodecylthio)carbonothioyl)thio)-2-methylpropanoate (**PFP-linker**) (204 mg, 0.38 mmol) was dissolved in styrene (4 g, 38.4 mmol). To this, AIBN (6.24 mg, 0.038 mmol) was added. The flask was sealed with a septa and, the contents deoxygenated by bubbling nitrogen for 20 min, and the flask was subsequently placed in a pre-heated oil bath at 80 °C for 3h 30 min. After this, the mixture was cooled down to room temperature and exposed to air. The resulting polymer was diluted with acetone and purified by precipitating twice in an excess of cold methanol and dried under vacuum at 40 °C overnight. **PS-TTC** was recovered as a yellow powder. ^1H NMR (Figure B 15, bottom) and ^{19}F NMR (Figure B16, bottom) was used to confirm the presence of the **PS-TTC** polymer, while SEC (Figure B17, dotted line) was used to determine the exact molar mass. $M_{n,\text{SEC}} = 3800 \text{ g mol}^{-1}$, $D = 1.07$.

End group cleavage/removal of PFP-PS-TTC

In a 10 mL flask, **PFP-PS-TTC** (150 mg, 0.04 mmol, 1 eq) and ethylpiperidine hypophosphite (EHPH, 106 mg, 0.60 mmol, 15 eq) were dissolved in DCM (2 mL). The flask was capped with a septa and the solution was degassed for 20 min. The flask was then placed at a distance of 2.5 cm from the PLL lamp ($\lambda_{\text{max}} = 360 \text{ nm}$) and irradiated for 40 h. After this, the solution turned colorless and the polymer was purified by precipitating in excess cold methanol to obtain **PFP-PS-H** as a white powder. ^1H NMR (Figure B 15, top) and ^{19}F NMR (Figure B16, top) was used to confirm the presence of the **PS-H** polymer, while SEC (Figure B17, solid line) was used to determine the exact molar mass. $M_{n,\text{SEC}} = 4000 \text{ g mol}^{-1}$, $D = 1.14$. Additionally, UV-Vis spectra of the polymer solution (1 mg/mL in THF) before (Figure B18, **PFP-PS-TTC**, dotted line) and after (Figure B18, **PFP-PS-H**, solid line) confirm the removal of the RAFT trithiocarbonate (TTC) end group by the disappearance of the absorption of the TTC group at 320 nm.

Synthesis of poly(glycerol monomethacrylate) PGMA-SH

In a 25 mL round bottom flask, 2,2-bipyridyl (2,2-bpy, 203 mg, 1.25 mmol, 0.04 eq), glycerol monomethacrylate (GMA, 5 g, 39.25 mmol, 1 eq), and **ATRP-disulphide** (147 mg, 0.3125 mmol, 0.01 eq) were dissolved in methanol (10 mL) and bubbled with nitrogen for

30 min. Cu (I) Cl (65.5 mg, 0.625 mmol, 0.02 eq) was weighed into a separate 25 mL schlenk flask and was deoxygenated for 10 min. The contents of the first flask were transferred into the schlenk flask containing Cu(I) Cl using a cannula. The reaction was stirred at room temperature for 8h and the polymer was precipitated in cold THF to obtain **PGMA-S-S-PGMA** as a bluish-green powder. The crude polymer was then dissolved in methanol and passed through an alumina column (3 cm) and the excess methanol was evaporated under vacuum. Formation of the polymer was confirmed by $^1\text{H NMR}$ (Figure B 19, top) and SEC (Figure B 19, bottom, dotted line). $M_{n,SEC} = 38000 \text{ g mol}^{-1}$, $\mathcal{D} = 1.28$.

Disulfide cleavage of PGMA-S-S-PGMA

In a 5 mL round bottom flask, **PGMA-S-S-PGMA** (100 mg, 0.00625 mmol, 1 eq) and dithiothreitol (DTT, 19.3 mg, 0.125 mmol, 20 eq) were dissolved in methanol (1 mL). The reaction was stirred at room temperature for 3 h and the polymer was purified by precipitation in cold THF. The cleavage of the disulphide bond resulting in the formation of **PGMA-SH** was confirmed by SEC (Figure B 19, bottom, solid line). $M_{n,SEC} = 16000 \text{ g mol}^{-1}$, $\mathcal{D} = 1.53$.

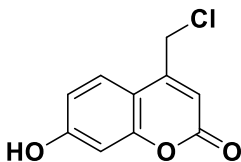
General procedure for PFTR

Similar procedure as described in Chapter 3, Section 3.5 was used for PFTR using the conditions mentioned in Table 4.3.

8.3 Synthetic protocols pertaining to Chapter 5

Photobase generator (PBG)

6-bromo-4-(chloromethyl)-7-hydroxy-2H-chromen-2-one 2

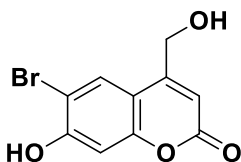


A solution of 4-bromoresorcinol (5.00 g, 26.5 mmol) in sulfuric acid (50 mL) was cooled in an ice bath. Ethyl 4-chloroacetoacetate (3.58 mL, 4.36 g, 26.5 mmol, 1.00 eq.) was added drop wise to the above solution with vigorous stirring and allowed to stir for 6 days at room temperature. This reaction mixture was then poured into ice-water and stirred for an hour. The precipitate was filtered off, washed with water and dried to obtain **2** as a light brown solid (5.33 g, 73% yield).

$^1\text{H-NMR}$: (CD_3OD , 400 MHz) δ /ppm: 4.83 (2H, d, $J = 4.8$ Hz), 6.44 (1H, s), 6.87 (1H, s), 7.97 (1H, s).

$^{13}\text{C-NMR}$: (CD_3OD , 400 MHz) δ /ppm: 40.55, 102.95, 106.58, 111.10, 111.74, 128.78, 150.63, 154.50, 157.89, 161.08.

6-bromo-4-(hydroxymethyl)-7-hydroxy-2H-chromen-2-one 3

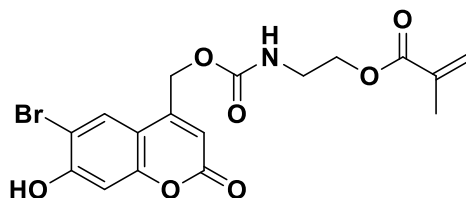


A suspension of **2** (180 mg, 0.65 mmol) in water (200 mL) was refluxed for 3 days. The resulting solution was cooled and excess water was evaporated to obtain **3** as a dark brown powder (104 mg, 74% yield).

$^1\text{H-NMR}$: (CD_3OD , 400 MHz) δ /ppm: 4.79 (2H, d, $J = 0.8$ Hz), 6.40 (1H, t, $J = 1.5$ Hz), 6.87 (1H, s), 7.83 (1H, s).

^{13}C -NMR: (CD_3OD , 400 MHz) δ/ppm : 59.42, 102.82, 106.45, 107.77, 111.33, 127.88, 154.12, 155.83, 157.50, 161.93.

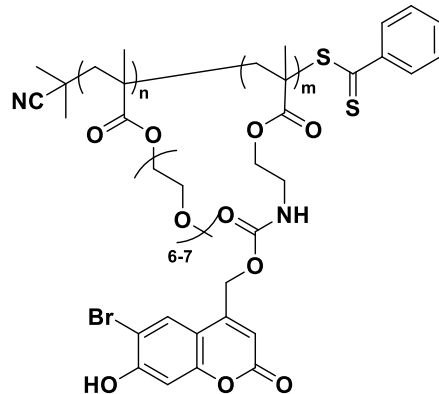
2-((((6-bromo-7-hydroxy-2-oxo-2H-chromen-4-yl)methoxy)carbonyl)amino)ethyl methacrylate **5**



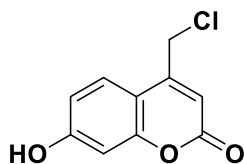
To a solution of **3** (250.00 mg, 0.91 mmol) in dry acetonitrile (10 mL) were added a solution of DMAP (232.83 mg, 1.91 mmol, 2.10 eq) and 4-nitrophenyl chloroformate (219.50 mg, 1.09 mmol, 1.20 eq.) both dissolved in dry acetonitrile (5 mL). All the flasks were individually bubbled with nitrogen for 30 min. The reaction mixture was stirred at room temperature for 7 h, to obtain intermediate **4**, which was not isolated. To this suspension *in situ*, a solution of DMAP (232.83 mg, 1.91 mmol, 2.10 eq.) and 2-aminoethyl methacrylate hydrochloride (165.33 mg, 0.99 mmol, 1.10 eq.) in DMF (5 mL) was added. After the reaction mixture was stirred for 24 h, it was quenched with 0.5 M citric acid solution (5 mL) and diluted with chloroform (10 mL). The organic layer was dried over MgSO_4 and the excess solvent removed under vacuum. The crude product was purified via silica column chromatography using cyclohexane/ethyl acetate as eluents to obtain **5** (82 mg, 21%) as a pale yellow/white solid. TLC: (cyclohexane/ethyl acetate 1:1): $R_f = 0.46$

^1H -NMR: (CD_3OD , 400 MHz) δ/ppm : 1.81 (3H, s), 3.35 (2H, t, $J = 5.4$ Hz), 4.11 (2H, t, $J = 5.4$ Hz), 5.18 (2H, d, $J = 1.13$ Hz), 5.50 (1H, t, $J = 1.6$ Hz), 6.00 (1H, s), 6.16 (1H, s), 6.75 (1H, s), 7.74 (1H, s).

^{13}C -NMR: (CD_3OD , 400 MHz) δ/ppm : 17.01, 39.62, 61.32, 63.11, 102.90, 106.63, 108.77, 110.88, 125.10, 128.05, 136.15, 151.00, 154.22, 156.49, 157.79, 161.24, 167.31.

RAFT copolymerization of OEGMA and PBG: P(OEGMA-*r*-PBG), CP1

A stock solution of CPBD RAFT agent (18.1 mg in 500 μ L DMF) and AIBN (3.2 mg in 500 μ L DMF) were prepared. CPBD-solution (297.4 μ L, 10.77 mg, 0.049 mmol, 5.00 eq.), AIBN-solution (249.53 μ L, 1.59 mg, 0.0097 mmol, 1.00 eq.), OEGMA (1082.8 mg, 3.609 mmol, 371 eq.) and **5** (170.01 mg, 0.398 mmol 41.0 eq.) were dissolved in 3.70 mL of DMF and bubbled with nitrogen for 30 min. A t_0 sample was taken. The solution was placed in a preheated oil bath at 70 °C. The resulting polymer was precipitated twice in diethyl ether.

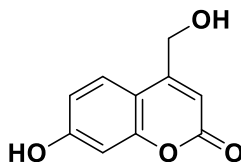
Photoacid generator (PAG)**4-(chloromethyl)-7-hydroxy-2H-chromen-2-one **7****

A solution of resorcinol (5.00 g, 45.4 mmol) in sulfuric acid (50 mL) was cooled in an ice bath, then ethyl 4-chloroacetoacetate (6.14 mL, 7.47 g, 45.4 mmol, 1.00 eq.) was added dropwise. The solution was stirred at room temperature for 6 days. The reaction mixture was then poured into ice-water and stirred for an hour. The precipitate was filtered, washed with water and dried under vacuum to obtain **7** (7.98 g, 84%) as a light brown solid.

$^1\text{H-NMR}$: (CD_3OD , 400 MHz) δ /ppm: 4.84 (2H, d, $J = 0.8$ Hz), 6.39 (1H, s), 6.76 (1H, d, $J = 2.4$ Hz), 6.86 (dd, $J = 6.4$ Hz, 2.4 Hz), 7.69 (1H, d, $J = 8.8$ Hz).

$^{13}\text{C-NMR}$: (CD_3OD , 400 MHz) δ /ppm: 40.71, 102.37, 109.80, 110.50, 113.04, 125.86, 151.69, 155.64, 161.82, 161.87.

6-bromo-4-(hydroxymethyl)-7-hydroxy-2H-chromen-2-one 8

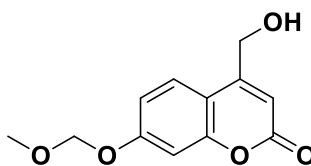


A suspension of **7** (204 mg, 0.97 mmol) in water (210 mL) was refluxed for 3 days. The resulting solution was cooled and evaporated to give **8** (156 mg, 84%) as a grey solid.

$^1\text{H-NMR}$: (CD_3OD , 400 MHz) δ /ppm: 4.76 (2H, d, $J = 1.5$ Hz), 6.31 (1H, t, $J = 1.5$ Hz), 6.68 (1H, t, $J = 2.4$ Hz), 6.75 (1H, dd, $J = 6.3$ Hz, 2.4 Hz), 7.46 (1H, d, $J = 8.7$ Hz).

$^{13}\text{C-NMR}$: (CD_3OD , 400 MHz) δ /ppm: 59.43, 102.21, 106.39, 109.93, 112.93, 124.80, 155.22, 157.04, 161.44, 162.78.

4-(hydroxymethyl)-7-(methoxymethoxy)-2H-chromen-2-one 9



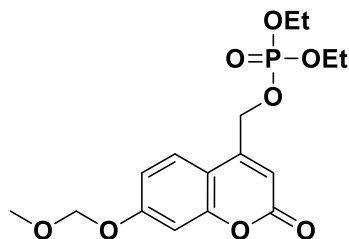
To a suspension of **8** (300 mg, 1.56 mmol) in DCM (3.30 mL), DIPEA (326.29 μL , 242.11 mg, 1.87 mmol, 1.20 eq.) and MOMCl (142.29 μL , 150.82 mg, 1.87 mmol, 1.20 eq.) were added dropwise and stirred at room temperature for 40 min. The reaction mixture was diluted with chloroform (5 mL), washed with 0.5 M citric acid solution, dried over MgSO_4 and excess DCM was evaporated to give **9** (342 mg, 93%) as a yellow solid.

$^1\text{H-NMR}$: (CD_3OD , 400 MHz) δ /ppm: 3.47 (3H, s), 4.83 (2H, d, $J = 1.6$ Hz), 5.28 (2H, s), 6.63 (1H, s), 6.43 (1H, t, $J = 1.52$), 7.03 (2H, m), 7.60 (1H, dd, $J = 5.0, 2.1$).

8. SYNTHETIC PROTOCOLS

^{13}C -NMR: (CD_3OD , 400 MHz) δ/ppm : 55.18, 59.41, 94.15, 103.07, 107.79, 111.72, 113.40, 124.69, 154.82, 156.65, 160.37, 162.29.

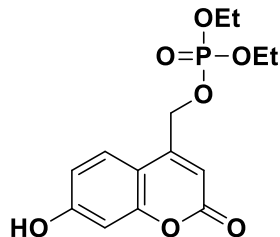
Diethyl ((7-(methoxymethoxy)-2-oxo-2H-chromen-4-yl)methyl) phosphate 10



9 (300 mg, 1.27 mmol) was dissolved in dry pyridine (3.00 mL) and the solution was cooled in an ice bath. To this, diethyl chlorophosphate (233.13 μL , 278.36 mg, 1.61 mmol, 1.27 eq.) was added and stirred at 0°C for 2h and further at room temperature for 2 h. Water (10 mL) was added to dissolve the precipitate. The reaction mixture was extracted with ether (3 x 10 mL) and the organic layer washed with 1 M H_2SO_4 (2 x 10 mL), NaHCO_3 (5%, 1 x 10 mL), water (3 x 10 mL) and brine (1 x10 mL). The combined organic phases were dried over MgSO_4 and excess solvent evaporated under vacuum. This product obtained was used for the next step with no further purification.

^1H -NMR: (CD_3OD , 400 MHz) δ/ppm : 1.36 (6H, td, $J = 7.06$ Hz, 0.86 Hz), 3.31 (3H, t, $J = 1.6$ Hz), 4.19 (4H, m), 5.30 (2H, s), 5.33 (2H, dd, $J = 7.85$ Hz, 1.32 Hz), 6.40 (1H, t, $J = 1.25$ Hz), 7.06 (2H, m), 7.64 (1H, d, $J = 5.1$ Hz)

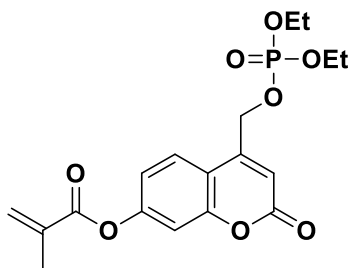
^{13}C -NMR: (CD_3OD , 400 MHz) δ/ppm : 15.00 (d), 55.22, 64.39 (d), 64.60 (d), 94.17, 103.24, 109.63, 110.97, 113.58, 125.03, 150.42, 155.07, 150.72, 161.33.

Diethyl (7-hydroxyl-2-oxo-2H-chromen-4-yl)methyl phosphate 11

A solution of **10** (473,55_{max} mg, 1.27_{max} mmol) in DCM (2 mL) and TFA (2 mL) was stirred at room temperature for 30 min. The solvent was evaporated under vacuum to give the product **11** as a yellow oil.

¹H-NMR: (CD₃OD, 400 MHz) δ /ppm: 1.35 (6H, m), 4.19 (4H, m), 5.29 (2H, dd, J = 7.9 Hz, 1.2 Hz), 6.31 (1H, s), 6.73 (1H, d, J = 2.35 Hz), 6.82 (1H, dd, J = 8.73 Hz, 2.37 Hz), 7.54 (1H, d, J = 7.9 Hz).

¹³C-NMR: (CD₃OD, 400 MHz) δ /ppm: 15.00 (d), 64.44 (d), 64.58 (d), 102.39, 108.19, 109.18, 113.11, 125.13, 150.71 (d), 155.48, 161.77, 161.88.

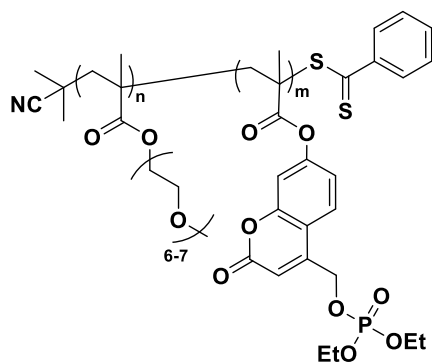
4-(((diethoxyphosphoryl)oxy)methyl)-2-oxo-2H-chromen-7-ylmethacrylate 12

NaOH (85.29 mg, 2.132 mmol, 2.00 eq.) was added to a solution of **11** (350.0 mg, 0.305 mmol) in ethanol (2 mL) and stirred for 5 min. Methacryloyl chloride (207.55 μ L, 222.91 mg, 2.132 mmol, 2.00 eq.) was added dropwise to the reaction mixture with vigorous stirring. The solution was stirred for 2 h, poured into ice water, stirred again for 10 min and centrifuged (4000 rpm, 7min). The final product **12** was obtained as a yellow oil.

$^1\text{H-NMR}$: (CD_3OD , 400 MHz) δ/ppm : 1.38 (6H, t, $J = 1.5$ Hz), 2.09 (3H, s), 4.22 (4H, m), 5.39 (2H, d, $J = 2.10$ Hz), 5.91 (1H, s), 6.40 (1H, s), 6.56 (1H, s), 7.22 (1H, dd, $J = 8.27$ Hz, $J = 2.43$ Hz), 7.31 (1H, d, $J = 2.25$ Hz), 7.80 (1H, d, $J = 8.72$ Hz)

$^{13}\text{C-NMR}$: 15.00 (d), 16.95, 64.61, 64.67, 110.27, 112.06, 114.58, 118.37, 124.97, 127.29, 135.50, 149.82, 153.85, 154.24, 160.54.

RAFT copolymerization of OEGMA and PAG: P(OEGMA-*r*-PAG), CP2



A stock solution of the CPBD RAFT agent (17 mg in 500 μL DMF) and AIBN (2.9 mg in 500 μL DMF) were prepared. CPBD-solution (252.9 μL , 8.85 mg, 0.040 mmol, 5.00 eq.), AIBN (225.86 μL , 1.31 mg, 0.0080 mmol, 1.00 eq.), OEGMA (899.1 mg, 2.997 mmol, 371 eq.) and 11 (131.98 mg, 0.333 mmol 41.0 eq.) were dissolved in 3.02 mL of DMF and bubbled with nitrogen for 30 min. A t_0 sample was taken. The solution was placed in a preheated oil bath at 70 $^\circ\text{C}$ and stirred for 7 h. The resulting polymer was precipitated twice in diethyl ether to obtain **CP2** as a viscous pink oily liquid.

REFERENCES

- 1 B. Bernhard and W. Itamar, *Small*, 2009, **5**, 28–44.
- 2 A. P. Marencic and R. A. Register, *Annu. Rev. Chem. Biomol. Eng.*, 2010, **1**, 277–297.
- 3 F. S. Bates and G. H. Fredrickson, *Phys. Today*, 1999, **52**, 32.
- 4 K. Matyjaszewski and Davis T, *Handbook of Radical POLYMERIZATION*, John Wiley & Sons, New Jersey, 2002.
- 5 M. H. Stenzel and C. Barner-Kowollik, *Mater. Horizons*, 2016, **3**, 471–477.
- 6 O. Takayuki, Y. Masatoshi and T. Toshinori, *Die Makromol. Chemie, Rapid Commun.*, 2003, **3**, 133–140.
- 7 O. Takayuki and Y. Masatoshi, *Die Makromol. Chemie, Rapid Commun.*, 2003, **3**, 127–132.
- 8 A. Goto and T. Fukuda, *Prog. Polym. Sci.*, 2004, **29**, 329–385.
- 9 D. Greszta, D. Mardare and K. Matyjaszewski, *Macromolecules*, 1994, **27**, 638–644.
- 10 J. Nicolas, Y. Guillaneuf, C. Lefay, D. Bertin, D. Gigmes and B. Charleux, *Prog. Polym. Sci.*, 2013, **38**, 63–235.
- 11 H. Fischer, *Chem. Rev.*, 2001, **101**, 3581–3610.
- 12 M. K. Georges, R. P. N. Veregin, P. M. Kazmaier and G. K. Hamer, *Macromolecules*, 1993, **26**, 2987–2988.
- 13 D. H. Solomon, E. Rizzardo, P. Cacioli, US 4581429A, 1986, 429.
- 14 C. J. Hawker, G. G. Barclay, A. Orellana, J. Dao and W. Devonport, *Macromolecules*, 1996, **29**, 5245–5254.
- 15 F. Chauvin, P.-E. Dufils, D. Gigmes, Y. Guillaneuf, S. R. A. Marque, P. Tordo and D. Bertin, *Macromolecules*, 2006, **39**, 5238–5250.
- 16 J.-S. Wang and K. Matyjaszewski, *J. Am. Chem. Soc.*, 1995, **117**, 5614–5615.
- 17 M. Kato, M. Kamigaito, M. Sawamoto and T. Higashimura, *Macromolecules*, 1995, **28**, 1721–1723.
- 18 V. Percec and B. Barboiu, *Macromolecules*, 1995, **28**, 7970–7972.
- 19 D. A. Singleton, D. T. Nowlan, N. Jahed and K. Matyjaszewski, *Macromolecules*, 2003, **36**, 8609–8616.
- 20 W. Tang, N. V Tsarevsky and K. Matyjaszewski, *J. Am. Chem. Soc.*, 2006, **128**, 1598–1604.
- 21 W. Tang, Y. Kwak, W. Braunecker, N. V Tsarevsky, M. L. Coote and K. Matyjaszewski, *J. Am. Chem. Soc.*, 2008, **130**, 10702–10713.
- 22 F. Seeliger and K. Matyjaszewski, *Macromolecules*, 2009, **42**, 6050–6055.

- 23 N. Bortolamei, A. A. Isse, V. B. Di Marco, A. Gennaro and K. Matyjaszewski, *Macromolecules*, 2010, **43**, 9257–9267.
- 24 M. Joachim, B. Michael and M. Krzysztof, *Macromol. Chem. Phys.*, 2011, **212**, 2423–2428.
- 25 L. Mueller, W. Jakubowski, K. Matyjaszewski, J. Pietrasik, P. Kwiatkowski, W. Chaladaj and J. Jurczak, *Eur. Polym. J.*, 2011, **47**, 730–734.
- 26 W. A. Braunecker, N. V Tsarevsky, A. Gennaro and K. Matyjaszewski, *Macromolecules*, 2009, **42**, 6348–6360.
- 27 J. Chiefari, Y. K. Bill Chong, F. Ercole, J. Krstina, J. Jeffery, T. P. T. Le, R. T. A. Mayadunne, G. F. Meijs, C. L. Moad, G. Moad, E. Rizzardo and S. H. Thang, *Macromolecules*, 1998, **31**, 5559–5562.
- 28 T. P. Le, G. Moad, E. Rizzardo, S. H. Thang, US WO1998001478, 1998.
- 29 G. Gody, T. Maschmeyer, P. B. Zetterlund and S. Perrier, *Nat. Commun.*, 2013, **4**, 2505.
- 30 T. Yildirim, A. C. Rinkenauer, C. Weber, A. Traeger, S. Schubert and U. S. Schubert, *J. Polym. Sci. Part A Polym. Chem.*, 2015, **53**, 2711–2721.
- 31 D. J. Keddie, G. Moad, E. Rizzardo and S. H. Thang, *Macromolecules*, 2012, **45**, 5321–5342.
- 32 S. Perrier, *Macromolecules*, 2017, **50**, 7433–7447.
- 33 K. Kinoshita, Y. Mori, T. Takami, Y. Uchida and Y. Murakami, *Polymers*, 2017, **9**, 44.
- 34 G. Moad, E. Rizzardo and S. H. Thang, *Aust. J. Chem.*, 2009, **62**, 1402–1472.
- 35 G. Moad, E. Rizzardo and S. H. Thang, *Aust. J. Chem.*, 2006, **59**, 669.
- 36 D. J. Keddie, *Chem. Soc. Rev.*, 2013, **43**, 496–505.
- 37 H. C. Kolb, M. G. Finn and K. B. Sharpless, *Angew. Chemie Int. Ed.*, 2001, **40**, 2004–2021.
- 38 Z. P. Demko and K. B. Sharpless, *Org. Lett.*, 2001, **3**, 4091–4094.
- 39 J.-M. Noy, M. Koldevitz and P. J. Roth, *Polym. Chem.*, 2015, **6**, 436–447.
- 40 S. Ata, P. Dhara, R. Mukherjee and N. K. Singha, *Eur. Polym. J.*, 2016, **75**, 276–290.
- 41 H. Richard, *Angew. Chemie Int. Ed.*, 2010, **49**, 3415–3417.
- 42 M. H. Stenzel, *ACS Macro Lett.*, 2013, **2**, 14–18.
- 43 X. Zhang, W. Xi, C. Wang, M. Podgórski and C. N. Bowman, *ACS Macro Lett.*, 2016, **5**, 229–233.
- 44 D. P. Nair, M. Podgórski, S. Chatani, T. Gong, W. Xi, C. R. Fenoli and C. N. Bowman, *Chem. Mater.*, 2014, **26**, 724–744.
- 45 C. Nergiz, K. Halil and S. Rana, *J. Polym. Sci. Part A Polym. Chem.*, 2010, **48**, 4737–4746.

- 46 B. Hans-Georg, F. Giselher and R. Helmut, *Angew. Chemie Int. Ed.*, 1972, **11**, 1103–1104.
- 47 P. Ferruti, A. Bettelli and A. Feré, *Polymer*, 1972, **13**, 462–464.
- 48 A. Desai, N. Atkinson, F. Rivera, W. Devonport, I. Rees, S. E. Branz and C. J. Hawker, *J. Polym. Sci. Part A Polym. Chem.*, 2000, **38**, 1033–1044.
- 49 M. Eberhardt, R. Mruk, R. Zentel and P. Théato, *Eur. Polym. J.*, 2005, **41**, 1569–1575.
- 50 K. Nilles and P. Theato, *Eur. Polym. J.*, 2007, **43**, 2901–2912.
- 51 V. Šubr and K. Ulbrich, *React. Funct. Polym.*, 2006, **66**, 1525–1538.
- 52 W. H. Binder and R. Sachsenhofer, *Macromol. Rapid Commun.*, 2008, **29**, 952–981.
- 53 H. Rolf, S. Günter and M. Leander, *Chem. Ber.*, 2006, **100**, 2494–2507.
- 54 H. Rolf, *Pure Appl. Chem.*, 1989, **61**, 613.
- 55 A. Valentina and S. Gottfried, *Angew. Chemie Int. Ed.*, 2007, **46**, 8440–8444.
- 56 C. W. Tornøe, C. Christensen and M. Meldal, *J. Org. Chem.*, 2002, **67**, 3057–3064.
- 57 G. Antony, H. Markus, M. A. H. E. and B. Stephen, *Angew. Chemie Int. Ed.*, 2001, **40**, 594–597.
- 58 E. Pedone, X. Li, N. Koseva, O. Alpar and S. Brocchini, *J. Mater. Chem.*, 2003, **13**, 2825–2837.
- 59 H. Zhicheng, L. Ye, H. Chunyan and P. Caiyuan, *J. Appl. Polym. Sci.*, 2005, **98**, 189–194.
- 60 M. J. Yanjarappa, K. V Gujraty, A. Joshi, A. Saraph and R. S. Kane, *Biomacromolecules*, 2006, **7**, 1665–1670.
- 61 K. A. Aamer and G. N. Tew, *J. Polym. Sci. Part A Polym. Chem.*, 2007, **45**, 5618–5625.
- 62 S. V Orski, K. H. Fries, G. R. Sheppard and J. Locklin, *Langmuir*, 2010, **26**, 2136–2143.
- 63 J. K. Pontrello, M. J. Allen, E. S. Underbakke and L. L. Kiessling, *J. Am. Chem. Soc.*, 2005, **127**, 14536–14537.
- 64 E. B. Coughlin and Y. Simon, *Non-conventional Functional Block Copolymers*, American Chemical Society, vol. 1066., 2011.
- 65 E. M. Kolonko and L. L. Kiessling, *J. Am. Chem. Soc.*, 2008, **130**, 5626–5627.
- 66 E. M. Kolonko, J. K. Pontrello, S. L. Mangold and L. L. Kiessling, *J. Am. Chem. Soc.*, 2009, **131**, 7327–7333.
- 67 L. E. Strong and L. L. Kiessling, *J. Am. Chem. Soc.*, 1999, **121**, 6193–6196.

- 68 Y. Li, B. S. Lokitz, S. P. Armes and C. L. McCormick, *Macromolecules*, 2006, **39**, 2726–2728.
- 69 K. Nilles and P. Theato, *J. Polym. Sci. Part A Polym. Chem.*, 2009, **47**, 1696–1705.
- 70 K. Nilles and P. Theato, *J. Polym. Sci. Part A Polym. Chem.*, 2010, **48**, 3683–3692.
- 71 N. Vogel and P. Théato, *Macromol. Symp.*, 2007, **249-250**, 383–391.
- 72 A. C. Pauly and P. Theato, *J. Polym. Sci. Part A Polym. Chem.*, 2010, **49**, 211–224.
- 73 N. Metz and P. Theato, *Eur. Polym. J.*, 2007, **43**, 1202–1209.
- 74 K. Godula and C. R. Bertozzi, *J. Am. Chem. Soc.*, 2010, **132**, 9963–9965.
- 75 Y. Liu, L. Wang and C. Pan, *Macromolecules*, 1999, **32**, 8301–8305.
- 76 J. Hwang, R. C. Li and H. D. Maynard, *J. Control. Release*, 2007, **122**, 279–286.
- 77 X. S. Li, L. H. Gan and Y. Y. Gan, *Polymer*, 2008, **49**, 1879–1884.
- 78 R. Kakuchi and P. Theato, *Macromolecules*, 2012, **45**, 1331–1338.
- 79 S. R. A. Devenish, J. B. Hill, J. W. Blunt, J. C. Morris and M. H. G. Munro, *Tetrahedron Lett.*, 2006, **47**, 2875–2878.
- 80 A. Das and P. Theato, *Chem. Rev.*, 2016, **116**, 1434–1495.
- 81 T. Akihiro, H. Tomoaki, K. Koutarou, K. Yasuhiro, O. Yoshiyuki, T. Hongxiang and Y. Liang, *J. Appl. Polym. Sci.*, 2007, **106**, 4219–4224.
- 82 N. Lutz, B. Matthias and Z. Rudolf, *Macromol. Biosci.*, 2014, **14**, 607–618.
- 83 M. Barz, R. Luxenhofer, R. Zentel and A. V. Kabanov, *Biomaterials*, 2009, **30**, 5682–5690.
- 84 M. Nicole, B. Matthias, F. Romina and Z. Rudolf, *Macromol. Rapid Commun.*, 2014, **35**, 1522–1527.
- 85 D. Varadharajan and G. Delaittre, *Polym. Chem.*, 2016, **7**, 7488–7499.
- 86 C. E. Hoyle, A. B. Lowe and C. N. Bowman, *Chem. Soc. Rev.*, 2010, **39**, 1355.
- 87 P. J. Roth, C. Boyer, A. B. Lowe and T. P. Davis, *Macromol. Rapid Commun.*, 2011, **32**, 1123–1143.
- 88 L.-T. T. Nguyen, M. T. Gokmen and F. E. Du Prez, *Polym. Chem.*, 2013, **4**, 5527–5536.
- 89 M. T. Gokmen, J. Brassinne, R. A. Prasath and F. E. Du Prez, *Chem. Commun.*, 2011, **47**, 4652–4654.
- 90 A. B. Lowe, *Polym. Chem.*, 2014, **5**, 4820–4870.
- 91 P. Battioni, O. Brigaud, H. Desvaux, D. Mansuy and T. G. Traylor, *Tetrahedron Lett.*, 1991, **32**, 2893–2896.

- 92 R. D. Chambers, D. Close and D. L. H. Williams, *J. Chem. Soc. Perkin Trans. 2*, 1980, 778–780.
- 93 R. Kakuchi and P. Theato, *Functional Polymers by Post-Polymerization Modification*, WILEY-VCH Verlag GmbH, 2012.
- 94 W. A. Pryor and T.-L. Huang, *Macromolecules*, 1969, **2**, 70–77.
- 95 H. Turgut and G. Delaittre, *Chem. Eur. J.*, 2016, **22**, 1511–1521.
- 96 H. Turgut, A. C. Schmidt, P. Wadhvani, A. Welle, R. Müller, G. Delaittre, R. Muller and G. Delaittre, *Polym. Chem.*, 2017, **8**, 1288–1293.
- 97 J. M. Noy, A. K. Friedrich, K. Batten, M. N. Bhebhe, N. Busatto, R. R. Batchelor, A. Kristanti, Y. Pei and P. J. Roth, *Macromolecules*, 2017, **50**, 7028–7040.
- 98 F. Cavalli, H. Mutlu, S. O. Steinmueller and L. Barner, *Polym. Chem.*, 2017, **8**, 3778–3782.
- 99 J. L. Worlinsky, S. Halepas and C. Bruckner, *Org. Biomol. Chem.*, 2014, **12**, 3991–4001.
- 100 T. Cai, W. J. Yang, K.-G. Neoh and E.-T. Kang, *Polym. Chem.*, 2012, **3**, 1061–1068.
- 101 K. Babiuch, C. R. Becer, M. Gottschaldt, J. Delaney, J. Weisser, B. Beer, R. Wyrwa, M. Schnabelrauch and U. S. Schubert, *Macromol. Biosci.*, 2011, **11**, 535–548.
- 102 C. R. Becer, K. Babiuch, D. Pilz, S. Hornig, T. Heinze, M. Gottschaldt and U. S. Schubert, *Macromolecules*, 2009, **42**, 2387–2394.
- 103 A. Wild, K. Babiuch, M. König, A. Winter, M. D. Hager, M. Gottschaldt, A. Prokop and U. S. Schubert, *Chem. Commun.*, 2012, **48**, 6357–6359.
- 104 A. Wild, A. Winter, M. D. Hager, H. Görls and U. S. Schubert, *Macromol. Rapid Commun.*, 2012, **33**, 517–521.
- 105 L. Dumas, E. Fleury and D. Portinha, *Polymer*, 2014, **55**, 2628–2634.
- 106 M. N. Bhebhe, D. Eulate, Eva Alvarez, Y. Pei, D. W. M. Arrigan, P. J. Roth and A. B. Lowe, *Macromol. Rapid Commun.*, 2017, **38**, 1600450.
- 107 C. R. Becer, K. Kenta, W. Christine, C. Aydin, C. Yoshiki and U. S. Schubert, *J. Polym. Sci. Part A Polym. Chem.*, 2010, **48**, 1278–1286.
- 108 J. Chen, D. Vuluga, B. Crousse, J. Legros, J. Duchet-Rumeau, A. Charlot and D. Portinha, *Polymer*, 2013, **54**, 3757–3766.
- 109 J. Chen, J. Duchet, D. Portinha and A. Charlot, *Langmuir*, 2014, **30**, 10740–10750.
- 110 X. Younan and W. G. M., *Angew. Chemie Int. Ed.*, 1998, **37**, 550–575.
- 111 R. Ogaki, M. Alexander and P. Kingshott, *Mater. Today*, 2010, **13**, 22–35.
- 112 A. P. Quist, A. Chand, S. Ramachandran, C. Daraio, S. Jin and R. Lal, *Langmuir*, 2007, **23**, 1375–1380.
- 113 W. Lu and C. M. Lieber, *Nat. Mater.*, 2007, **6**, 841.

- 114 Z. Nie and E. Kumacheva, *Nat. Mater.*, 2008, **7**, 277.
- 115 J. Y. Cheng, A. M. Mayes and C. A. Ross, *Nat. Mater.*, 2004, **3**, 823.
- 116 M. Park, C. Harrison, P. M. Chaikin, R. A. Register and D. H. Adamson, *Science*, 1997, **276**, 1401 – 1404.
- 117 F. Stephan and P. Thomas, *Angew. Chemie Int. Ed.*, 2002, **41**, 688–714.
- 118 L. Leibler, *Macromolecules*, 1980, **13**, 1602–1617.
- 119 F. S. Bates, *Science*, 1991, **251**, 898– 905.
- 120 M. W. Matsen and F. S. Bates, *Macromolecules*, 1996, **29**, 1091–1098.
- 121 Y. Mai and A. Eisenberg, *Chem. Soc. Rev.*, 2012, **41**, 5969.
- 122 H.-C. Kim, S.-M. Park and W. D. Hinsberg, *Chem. Rev.*, 2010, **110**, 146–177.
- 123 Y. Matsushita, K. Mori, R. Saguchi, Y. Nakao, I. Noda and M. Nagasawa, *Macromolecules*, 1990, **23**, 4313–4316.
- 124 G. Hadziioannou and A. Skoulios, *Macromolecules*, 1982, **15**, 258–262.
- 125 A. R. Farrell, G. T. Fitzgerald, D. Borah, D. J. Holmes and A. M. Morris, *Int. J. Mol. Sci.*, 2009, **10**.
- 126 N. A. Lynd and M. A. Hillmyer, *Macromolecules*, 2007, **40**, 8050–8055.
- 127 M. W. Matsen and M. Schick, *Phys. Rev. Lett.*, 1994, **72**, 2660–2663.
- 128 A. N. Semenov, *Macromolecules*, 1993, **26**, 2273–2281.
- 129 M. D. Whitmore and J. Noolandi, *Macromolecules*, 1985, **18**, 2486–2497.
- 130 A. E. Likhtman and A. N. Semenov, *Macromolecules*, 1997, **30**, 7273–7278.
- 131 G. Floudas, N. Hadjichristidis, M. Stamm, A. E. Likhtman and A. N. Semenov, *J. Chem. Phys.*, 1997, **106**, 3318–3328.
- 132 H. Xi and S. T. Milner, *Macromolecules*, 1996, **29**, 2404–2411.
- 133 L. Zhang and A. Eisenberg, *Science*, 1995, **268**, 1728–1731.
- 134 L. Zhang, K. Yu and A. Eisenberg, *Science*, 1996, **272**, 1777–1779.
- 135 G. Zhishen and L. Shiyong, *Macromol. Rapid Commun.*, 2009, **30**, 1523–1532.
- 136 T. P. Lodge, J. Bang, Z. Li, M. A. Hillmyer and Y. Talmon, *Faraday Discuss.*, 2005, **128**, 1–12.
- 137 Z. Lifeng and E. Adi, *Polym. Adv. Technol.*, 1998, **9**, 677–699.
- 138 N. S. Cameron, M. K. Corbierre and A. Eisenberg, *Can. J. Chem.*, 1999, **77**, 1311–1326.
- 139 A. Blanz, N. J. Warren, A. L. Lewis, S. P. Armes and A. J. Ryan, *Soft Matter*, 2011, **7**, 6399–6403.
- 140 O. Casse, A. Shkilnyy, J. Linders, C. Mayer, D. Häussinger, A. Völkel, A. F. Thünemann, R. Dimova, H. Cölfen, W. Meier, H. Schlaad and A. Taubert, *Macromolecules*, 2012, **45**, 4772–4777.

- 141 T. Thurn-Albrecht, R. Steiner, J. DeRouchey, C. M. Stafford, E. Huang, M. Bal, M. Tuominen, C. J. Hawker and T. P. Russell, *Adv. Mater.*, 2000, **12**, 787–791.
- 142 T. P. Russell, *Curr. Opin. Colloid Interface Sci.*, 1996, **1**, 107–115.
- 143 M. W. Matsen and F. S. Bates, *J. Chem. Phys.*, 1997, **106**, 2436–2448.
- 144 T. P. Russell, A. Menelle, S. H. Anastasiadis, S. K. Satija and C. F. Majkrzak, *Macromolecules*, 1991, **24**, 6263–6269.
- 145 A. Knoll, A. Horvat, K. S. Lyakhova, G. Krausch, G. J. A. Sevink, A. V Zvelindovsky and R. Magerle, *Phys. Rev. Lett.*, 2002, **89**, 35501.
- 146 P. Lambooy, T. P. Russell, G. J. Kellogg, A. M. Mayes, P. D. Gallagher and S. K. Satija, *Phys. Rev. Lett.*, 1994, **72**, 2899–2902.
- 147 G. J. A. Sevink, A. V Zvelindovsky, J. G. E. M. Fraaije and H. P. Huinink, *J. Chem. Phys.*, 2001, **115**, 8226–8230.
- 148 J. Feng and E. Ruckenstein, *Macromolecules*, 2006, **39**, 4899–4906.
- 149 W. Li, R. A. Wickham and R. A. Garbary, *Macromolecules*, 2006, **39**, 806–811.
- 150 H. Xiang, K. Shin, T. Kim, S. I. Moon, T. J. McCarthy and T. P. Russell, *Macromolecules*, 2004, **37**, 5660–5664.
- 151 H. Xiang, K. Shin, T. Kim, S. I. Moon, T. J. McCarthy and T. P. Russell, *Macromolecules*, 2005, **38**, 1055–1056.
- 152 M. Ma, V. Krikorian, J. H. Yu, E. L. Thomas and G. C. Rutledge, *Nano Lett.*, 2006, **6**, 2969–2972.
- 153 S.-M. Park, X. Liang, B. D. Harteneck, T. E. Pick, N. Hiroshiba, Y. Wu, B. A. Helms and D. L. Olynick, *ACS Nano*, 2011, **5**, 8523–8531.
- 154 T. Higuchi, *Polym. J.*, 2017, **49**, 467.
- 155 T. Higuchi, A. Tajima, K. Motoyoshi, H. Yabu and M. Shimomura, *Angew. Chemie Int. Ed.*, 2008, **47**, 8044–8046.
- 156 T. Higuchi, K. Motoyoshi, H. Sugimori, H. Jinnai, H. Yabu and M. Shimomura, *Soft Matter*, 2012, **8**, 3791.
- 157 I. Wyman, G. Njikang and G. Liu, *Prog. Polym. Sci.*, 2011, **36**, 1152–1183.
- 158 D. A. Rider, J. I. L. Chen, J.-C. Eloi, A. C. Arsenault, T. P. Russell, G. A. Ozin and I. Manners, *Macromolecules*, 2008, **41**, 2250–2259.
- 159 J. Fu, J. Wang, Q. Li, D. H. Kim and W. Knoll, *Langmuir*, 2010, **26**, 12336–12341.
- 160 D. Bae, G. Jeon, H. Jinnai, J. Huh and J. K. Kim, *Macromolecules*, 2013, **46**, 5301–5307.
- 161 D. Lee, M.-H. Kim, D. Bae, G. Jeon, M. Kim, J. Kwak, S. J. Park, J. U. Kim and J. K. Kim, *Macromolecules*, 2014, **47**, 3997–4003.
- 162 H. Yabu, T. Higuchi, K. Ijiro and M. Shimomura, *Chaos*, 2005, **15**, 047505.

- 163 J. Jennings, M. Beija, a P. Richez, S. D. Cooper, P. E. Mignot, K. J. Thurecht, K. S. Jack and S. M. Howdle, *J. Am. Chem. Soc.*, 2012, **134**, 4772–4781.
- 164 J. Seog-Jin, Y. Gi-Ra, K. M. Chong and Y. Seung-Man, *Macromolecules*, 2007, **40**, 8430–8439.
- 165 J. Seog-Jin, Y. Gi-Ra and Y. Seung-Man, *Adv. Mater.*, 2008, **20**, 4103–4108.
- 166 T. Higuchi, A. Tajima, H. Yabu and M. Shimomura, *Soft Matter*, 2008, **4**, 1302–1305.
- 167 T. Higuchi, A. Tajima, K. Motoyoshi, H. Yabu and M. Shimomura, *Angew. Chemie Int. Ed.*, 2009, **48**, 5125–5128.
- 168 T. Higuchi, K. Motoyoshi, H. Sugimori, H. Jinnai, H. Yabu and M. Shimomura, *Macromol. Rapid Commun.*, 2010, **31**, 1773–1778.
- 169 L. Li, K. Matsunaga, J. Zhu, T. Higuchi, H. Yabu, M. Shimomura, H. Jinnai, R. C. Hayward and T. P. Russell, *Macromolecules*, 2010, **43**, 7807–7812.
- 170 B. Yu, B. Li, Q. Jin, D. Ding and A.-C. Shi, *Macromolecules*, 2007, **40**, 9133–9142.
- 171 I. W. Hamley, *Developments in Block Copolymer Science and Technology*, John Wiley & Sons Ltd, Chichester, 2004, vol. 7.
- 172 A.-C. Shi and B. Li, *Soft Matter*, 2013, **9**, 1398–1413.
- 173 P. Chi, Z. Wang, B. Li and A.-C. Shi, *Langmuir*, 2011, **27**, 11683–11689.
- 174 A. C. Arsenault, D. A. Rider, N. Tétreault, J. I.-L. Chen, N. Coombs, G. A. Ozin and I. Manners, *J. Am. Chem. Soc.*, 2005, **127**, 9954–9955.
- 175 Y. Lu, H. Fan, A. Stump, T. L. Ward, T. Rieker and C. J. Brinker, *Nature*, 1999, **398**, 223.
- 176 K. Landfester, *Adv. Mater.*, 2001, **13**, 765–768.
- 177 K. Matyjaszewski, *Macromolecules*, 2012, **45**, 4015–4039.
- 178 M. Vennes, R. Zentel, M. Rössle, M. Stepputat and U. Kolb, *Adv. Mater.*, 2005, **17**, 2123–2127.
- 179 S. G. Jang, D. J. Audus, D. Klinger, D. V Krogstad, B. J. Kim, A. Cameron, S.-W. Kim, K. T. Delaney, S.-M. Hur, K. L. Killops, G. H. Fredrickson, E. J. Kramer and C. J. Hawker, *J. Am. Chem. Soc.*, 2013, **135**, 6649–6657.
- 180 H. Yabu, T. Higuchi and M. Shimomura, *Adv. Mater.*, 2005, **17**, 2062–2065.
- 181 R. Kevin and C. Bernard, *Angew. Chemie Int. Ed.*, 2012, **51**, 5625–5628.
- 182 K.-H. Roh, D. C. Martin and J. Lahann, *Nat. Mater.*, 2005, **4**, 759.
- 183 S. Rahmani, S. Saha, H. Durmaz, A. Donini, A. C. Misra, J. Yoon and J. Lahann, *Angew. Chemie Int. Ed.*, 2014, **53**, 2332–2338.
- 184 N. Kawase, M. Kato, H. Nishioka and H. Jinnai, *Ultramicroscopy*, 2007, **107**, 8–15.
- 185 H. Sugimori, T. Nishi and H. Jinnai, *Macromolecules*, 2005, **38**, 10226–10233.

- 186 H. Yabu, T. Higuchi and M. Shimomura, *Adv. Mater.*, 2005, **17**, 2062–2065.
- 187 S. P. Nunes, *Macromolecules*, 2016, **49**, 2905–2916.
- 188 I. W. Hamley, *Block Copolymers in Solution: Fundamentals and Applications*, John Wiley & Sons, Ltd, 2012.
- 189 Y. Álvarez-Gallego, B. Ruffmann, V. Silva, H. Silva, A. E. Lozano, J. G. de la Campa, S. P. Nunes and J. de Abajo, *Polymer*, 2008, **49**, 3875–3883.
- 190 Y. Shen, P. O. Saboe, I. T. Sines, M. Erbakan and M. Kumar, *J. Memb. Sci.*, 2014, **454**, 359–381.
- 191 Y. Cho, H. S. Sundaram, C. J. Weinman, M. Y. Paik, M. D. Dimitriou, J. A. Finlay, M. E. Callow, J. A. Callow, E. J. Kramer and C. K. Ober, *Macromolecules*, 2011, **44**, 4783–4792.
- 192 S. P. Nunes, M. L. Sforça and K.-V. Peinemann, *J. Memb. Sci.*, 1995, **106**, 49–56.
- 193 J. S. Lee, A. Hirao and S. Nakahama, *Macromolecules*, 1988, **21**, 274–276.
- 194 J. S. Lee, A. Hirao and S. Nakahama, *Macromolecules*, 1989, **22**, 2602–2606.
- 195 H. Zhao, W. Gu, M. W. Thielke, E. Sterner, T. Tsai, T. P. Russell, E. B. Coughlin and P. Theato, *Macromolecules*, 2013, **46**, 5195–5201.
- 196 S. Y. Yang, J.-A. Yang, E.-S. Kim, G. Jeon, E. J. Oh, K. Y. Choi, S. K. Hahn and J. K. Kim, *ACS Nano*, 2010, **4**, 3817–3822.
- 197 M. J. Robb, L. a. Connal, B. F. Lee, N. a. Lynd and C. J. Hawker, *Polym. Chem.*, 2012, **3**, 1618–1628.
- 198 C. Gao, J. Wu, H. Zhou, Y. Qu, B. Li and W. Zhang, *Macromolecules*, 2016, **49**, 4490–4500.
- 199 A. Cho, Y. La, S. Jeoung, H. R. Moon, J.-H. Ryu, T. J. Shin and K. T. Kim, *Macromolecules*, 2017, **50**, 3234–3243.
- 200 M. J. Greenall, P. Schuetz, S. Fuzeland, D. Atkins, D. M. A. Buzza, M. F. Butler and T. C. B. McLeish, *Macromolecules*, 2011, **44**, 5510–5519.
- 201 H. Yabu, M. Kanahara, M. Shimomura, T. Arita, K. Harano, E. Nakamura, T. Higuchi and H. Jinnai, *ACS Appl. Mater. Interfaces*, 2013, **5**, 3262–3266.
- 202 M. Kanahara, M. Shimomura and H. Yabu, *Soft Matter*, 2014, **10**, 275–280.
- 203 H. Yabu, T. Jinno, K. Koike, T. Higuchi and M. Shimomura, *J. Polym. Sci. Part B Polym. Phys.*, 2011, **49**, 1717–1722.
- 204 H. Yabu, S. Sato, T. Higuchi, H. Jinnai and M. Shimomura, *J. Mater. Chem.*, 2012, **22**, 7672.
- 205 K. Motoyoshi, A. Tajima, T. Higuchi, H. Yabu and M. Shimomura, *Soft Matter*, 2010, **6**, 1253–1257.
- 206 H. Yabu, K. Motoyoshi, T. Higuchi and M. Shimomura, *Phys. Chem. Chem. Phys.*, 2010, **12**, 11944–11947.

- 207 B. V. K. J. Schmidt, C. X. Wang, S. Kraemer, L. A. Connal and D. Klinger, *Polym. Chem.*, 2018, **9**, 1638–1649.
- 208 D. B. Williams and C. B. Carter, *Transmission Electron Microscopy*, Springer, 2009.
- 209 P. D. Nellist, *Scanning Transmission Electron Microscopy*, 2011.
- 210 A. Mendez-Vilas and J. Diaz, Eds., *Microscopy: Science, Technology, Applications and Education*, Formatex Research Center, 4th edn., 2010.
- 211 V. Westphal and S. W. Hell, *Phys. Rev. Lett.*, 2005, **94**, 143903.
- 212 N. Francini, L. Purdie, C. Alexander, G. Mantovani and S. G. Spain, *Macromolecules*, 2015, **48**, 2857–2863.
- 213 C. Barner-Kowollik, F. E. Du Prez, P. Espeel, C. J. Hawker, T. Junkers, H. Schlaad and W. Van Camp, *Angew. Chemie Int. Ed.*, 2011, **50**, 60–62.
- 214 H. Durmaz, A. Sanyal, G. Hizal and U. Tunca, *Polym. Chem.*, 2012, **3**, 825–835.
- 215 S. Chen, D. Ströhl and W. H. Binder, *ACS Macro Lett.*, 2015, **4**, 48–52.
- 216 Y. Zhang, G. Chen, Y. Lin, L. Zhao, W. Z. Yuan, P. Lu, C. K. W. Jim, Y. Zhang and B. Z. Tang, *Polym. Chem.*, 2015, **6**, 97–105.
- 217 B. M. Rosen, G. Lligadas, C. Hahn and V. Percec, *J. Polym. Sci. Part A Polym. Chem.*, 2009, **47**, 3931–3939.
- 218 J. Xu, L. Tao, C. Boyer, A. B. Lowe and T. P. Davis, *Macromolecules*, 2010, **43**, 20–24.
- 219 S. Perrier, P. Takolpuckdee and C. A. Mars, *Macromolecules*, 2005, **38**, 2033–2036.
- 220 H. Willcock and R. K. O'Reilly, *Polym. Chem.*, 2010, **1**, 149–157.
- 221 G. M. Brooke, *J. Fluor. Chem.*, 1997, **86**, 1–76.
- 222 J. Burdon, W. B. Hollyhead and J. C. Tatlow, *J. Chem. Soc.*, 1965, 5152–5156.
- 223 A. H. Gröschel, A. Walther, T. I. Löbbling, F. H. Schacher, H. Schmalz and A. H. E. Müller, *Nature*, 2013, **503**, 247.
- 224 D. Klinger, C. X. Wang, L. A. Connal, D. J. Audus, S. G. Jang, S. Kraemer, K. L. Killops, G. H. Fredrickson, E. J. Kramer and C. J. Hawker, *Angew. Chemie Int. Ed.*, 2014, **53**, 7018–7022.
- 225 C. V. Synatschke, T. Nomoto, H. Cabral, M. Förtsch, K. Toh, Y. Matsumoto, K. Miyazaki, A. Hanisch, F. H. Schacher, A. Kishimura, N. Nishiyama, A. H. E. Müller and K. Kataoka, *ACS Nano*, 2014, **8**, 1161–1172.
- 226 T. Higuchi, A. Tajima, H. Yabu and M. Shimomura, *Soft Matter*, 2008, **4**, 1302.
- 227 J. M. Shin, Y. Kim, H. Yun, G.-R. Yi and B. J. Kim, *ACS Nano*, 2017, **11**, 2133–2142.
- 228 W. Zhang, Z. Kochovski, Y. Lu, B. V. K. J. Schmidt, M. Antonietti and J. Yuan, *ACS Nano*, 2016, **10**, 7731–7737.

- 229 D. Klinger, M. J. Robb, J. M. Spruell, N. A. Lynd, C. J. Hawker and L. A. Connal, *Polym. Chem.*, 2013, **4**, 5038–5042.
- 230 M. Okubo, N. Saito, R. Takekoh and H. Kobayashi, *Polymer*, 2005, **46**, 1151–1156.
- 231 S. Schoffelen and J. C. M. van Hest, *Soft Matter*, 2012, **8**, 1736–1746.
- 232 R. Deng, F. Liang, W. Li, S. Liu, R. Liang, M. Cai, Z. Yang and J. Zhu, *Small*, 2013, **9**, 4099–4103.
- 233 Y. Hirai, T. Wakiya and H. Yabu, *Polym. Chem.*, 2017, **8**, 1754–1759.
- 234 H. Turgut, N. Dingenouts, V. Trouillet, P. Krolla-Sidenstein, H. Gliemann and G. Delaittre, *submitted*.
- 235 H. Turgut, D. Varadharajan, N. Dingenouts and G. Delaittre, *Macromol. Rapid Commun.*, 2018, accepted.
- 236 P. Mansky, Y. Liu, E. Huang, T. P. Russell and C. Hawker, *Science*, 1997, **275**, 1458–1460.
- 237 J. Y. Cheng, C. A. Ross, E. L. Thomas, H. I. Smith and G. J. Vancso, *Appl. Phys. Lett.*, 2002, **81**, 3657–3659.
- 238 T. Higuchi, M. Shimomura and H. Yabu, *Macromolecules*, 2013, **46**, 4064–4068.
- 239 D. Varadharajan, H. Turgut, J. Lahann, H. Yabu and G. Delaittre, *Adv. Funct. Mater.*, 2018, accepted.
- 240 M. Pinna, X. Guo and A. V Zvelindovsky, *Polymer*, 2008, **49**, 2797–2800.
- 241 E. Avalos, T. Teramoto, H. Komiyama, H. Yabu and Y. Nishiura, *ACS Omega*, 2018, **3**, 1304–1314.
- 242 N. G. Morsi, S. M. Ali, S. S. Elsonbaty, A. A. Afifi, M. A. Hamad, H. Gao and M. Elsababy, *Pharm. Dev. Technol.*, 2018, **23**, 387–399.
- 243 F. Kazenwadel, M. Franzreb and B. E. Rapp, *Anal. Methods*, 2015, **7**, 4030–4037.
- 244 X. Qu, L. Omar, T. B. H. Le, L. Tetley, K. Bolton, K. W. Chooi, W. Wang and I. F. Uchegbu, *Langmuir*, 2008, **24**, 9997–10004.
- 245 T. H. Bayburt and S. G. Sligar, *FEBS Lett.*, 2010, **584**, 1721–1727.
- 246 H.-M. Lee, D. R. Larson and D. S. Lawrence, *ACS Chem. Biol.*, 2009, **4**, 409–427.
- 247 I. Yasutaka, P. G. Kibat and R. Langer, *J. Control. Release*, 1990, **14**, 263–267.
- 248 C. B. Gong, M. H. -W. Lam and H. X. Yu, *Adv. Funct. Mater.*, 2006, **16**, 1759–1767.
- 249 M. Shirai and M. Tsunooka, *Prog. Polym. Sci.*, 1996, **21**, 1–45.
- 250 Z. Shi, P. Peng, D. Strohecker and Y. Liao, *J. Am. Chem. Soc.*, 2011, **133**, 14699–14703.
- 251 H. Okamura, S. Toda, M. Tsunooka and M. Shirai, *J. Polym. Sci. Part A Polym. Chem.*, 2002, **40**, 3055–3062.

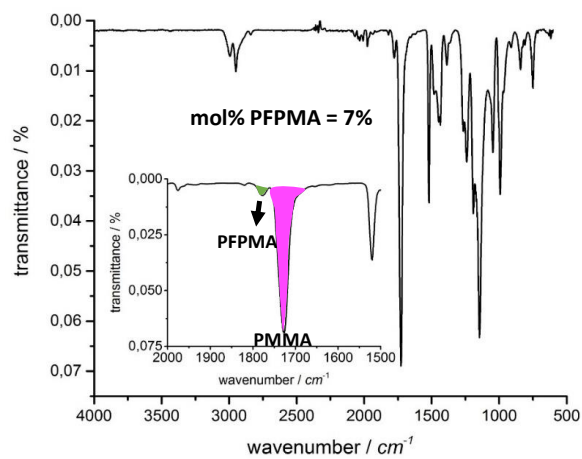
- 252 E. Reichmanis, F. M. Houlihan, O. Nalamasu and T. X. Neenan, *Chem. Mater.*, 1991, **3**, 394–407.
- 253 H. Ito, in *Microlithography · Molecular Imprinting*, Springer Berlin Heidelberg, Berlin, Heidelberg, 2005, vol. 172, pp. 37–245.
- 254 N. J. Turro, Y. Li, S. Jockusch, Y. Hagiwara, M. Okazaki, R. a. Mesch, D. I. Schuster and C. G. Willson, *J. Org. Chem.*, 2013, **78**, 1735–1741.
- 255 M. Shirai, M. Endo, M. Tsunooka and M. Endo, *J. Photopolym. Sci. Technol.*, 1999, **12**, 669–672.
- 256 D. Perrot, C. Croutxe-Barghorn and X. Allonas, *Polym. Chem.*, 2016, **7**, 2635–2638.
- 257 J. F. Cameron, C. G. Willson and J. M. J. Frechet, *J. Chem. Soc. Perkin Trans. 1*, 1997, 2429–2442.
- 258 H. Du and M. K. Boyd, *Tetrahedron Lett.*, 2001, **42**, 6645 – 6647.
- 259 K. Suyama, D. Nakai, T. Ohba and M. Shirai, *J. Photopolym. Sci. Technol.*, 2005, **18**, 707–710.
- 260 S. N. Senadheera, A. L. Yousef and R. S. Givens, *Beilstein J. Org. Chem.*, 2014, **10**, 2038–2054.
- 261 A. Z. Suzuki, T. Watanabe, M. Kawamoto, K. Nishiyama, H. Yamashita, M. Ishii, M. Iwamura and T. Furuta, *Org. Lett.*, 2003, **5**, 4867–4870.
- 262 R. K. P. Benninger and D. W. Piston, *Curr. Protoc. Cell Biol.*, 2013, **59**, 1–24.
- 263 J. Fischer and M. Wegener, *Laser Photon. Rev.*, 2012, **7**, 22–44.
- 264 V. Hagen, J. Bendig, S. Frings, T. Eckardt, S. Helm, D. Reuter and U. B. Kaupp, *Angew. Chemie Int. Ed.*, 2001, **40**, 1045–1048.
- 265 T. Furuta, S. S. Wang, J. L. Dantzker, T. M. Dore, W. J. Bybee, E. M. Callaway, W. Denk and R. Y. Tsien, *Proc. Natl. Acad. Sci.*, 1999, **96**, 1193–1200.
- 266 B. Karimi and D. Zareyee, *Org. Lett.*, 2008, **10**, 3989–3992.
- 267 J. Preat, D. Jacquemin, V. Wathélet, J.-M. André and E. A. Perpète, *J. Phys. Chem. A*, 2006, **110**, 8144–8150.
- 268 R. Schmidt, D. Geissler, V. Hagen and J. Bendig, *J. Phys. Chem. A*, 2005, **109**, 5000–5004.
- 269 B. Schade, V. Hagen, R. Schmidt, R. Herbrich, E. Krause, T. Eckardt and J. Bendig, *J. Org. Chem.*, 1999, **64**, 9109–9117.
- 270 A. Senthilmurugan and I. S. Aidhen, *Eur. J. Org. Chem.*, 2010, **2010**, 555–564.
- 271 R. H. Utama, M. Drechsler, S. Förster, P. B. Zetterlund and M. H. Stenzel, *ACS Macro Lett.*, 2014, **3**, 935–939.
- 272 S. Harrisson, P. Couvreur and J. Nicolas, *Polym. Chem.*, 2011, **2**, 1859–1865.
- 273 C. Messaoudi, T. Boudier, C. O. S. Sorzano and S. Marco, *BMC Bioinformatics*, 2007, **8**, 288.

- 274 Q. Zhang, P. Schattling, P. Theato and R. Hoogenboom, *Polym. Chem.*, 2012, **3**, 1418–1426.

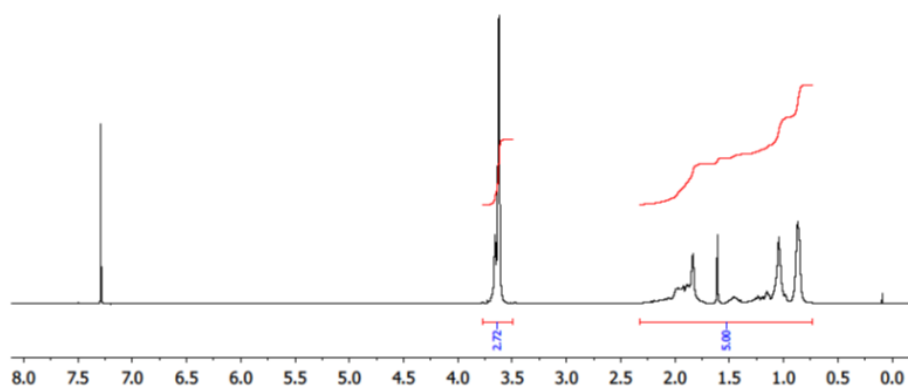
APPENDIX

Appendix A: Additional Figures for Chapter 3

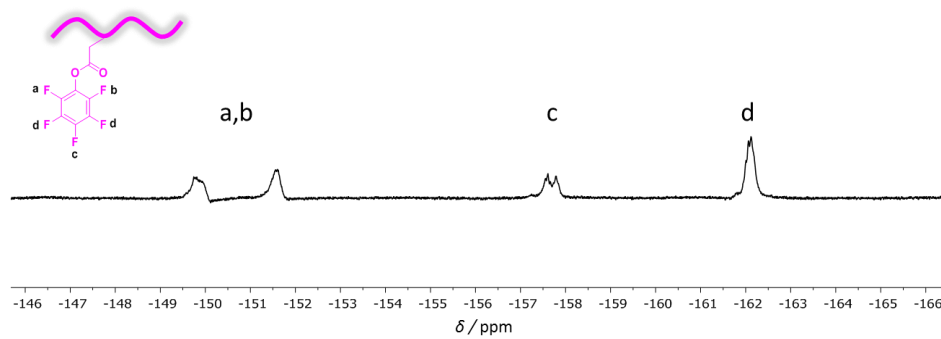
A



B



C



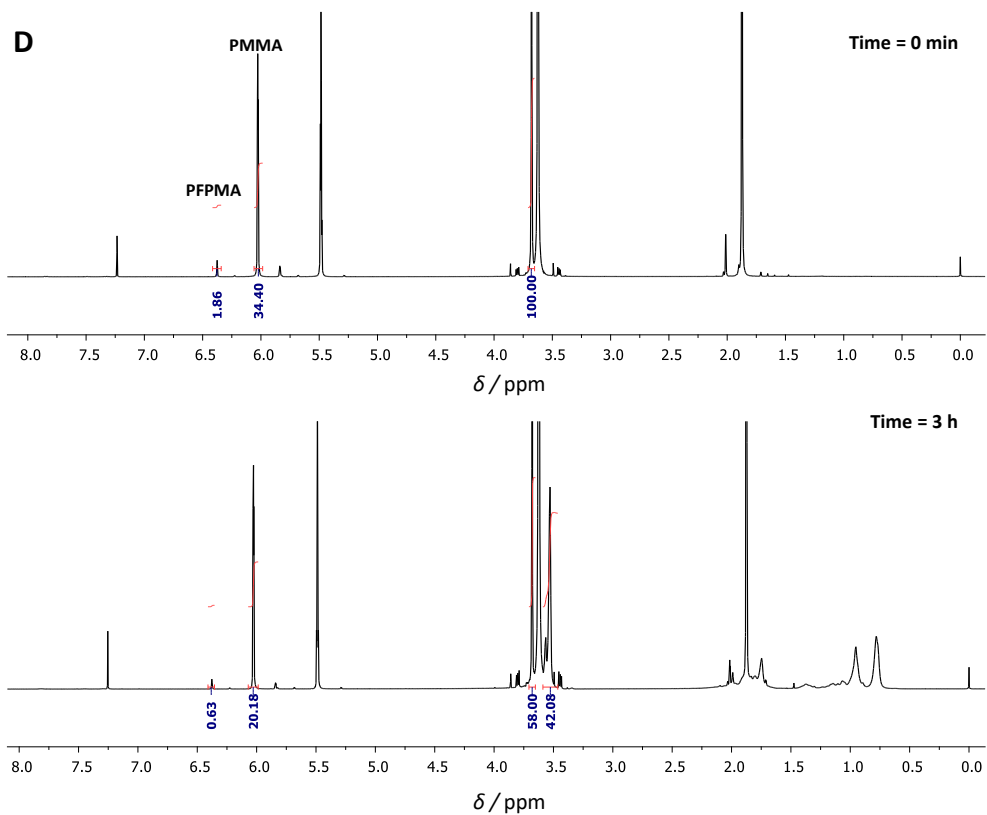
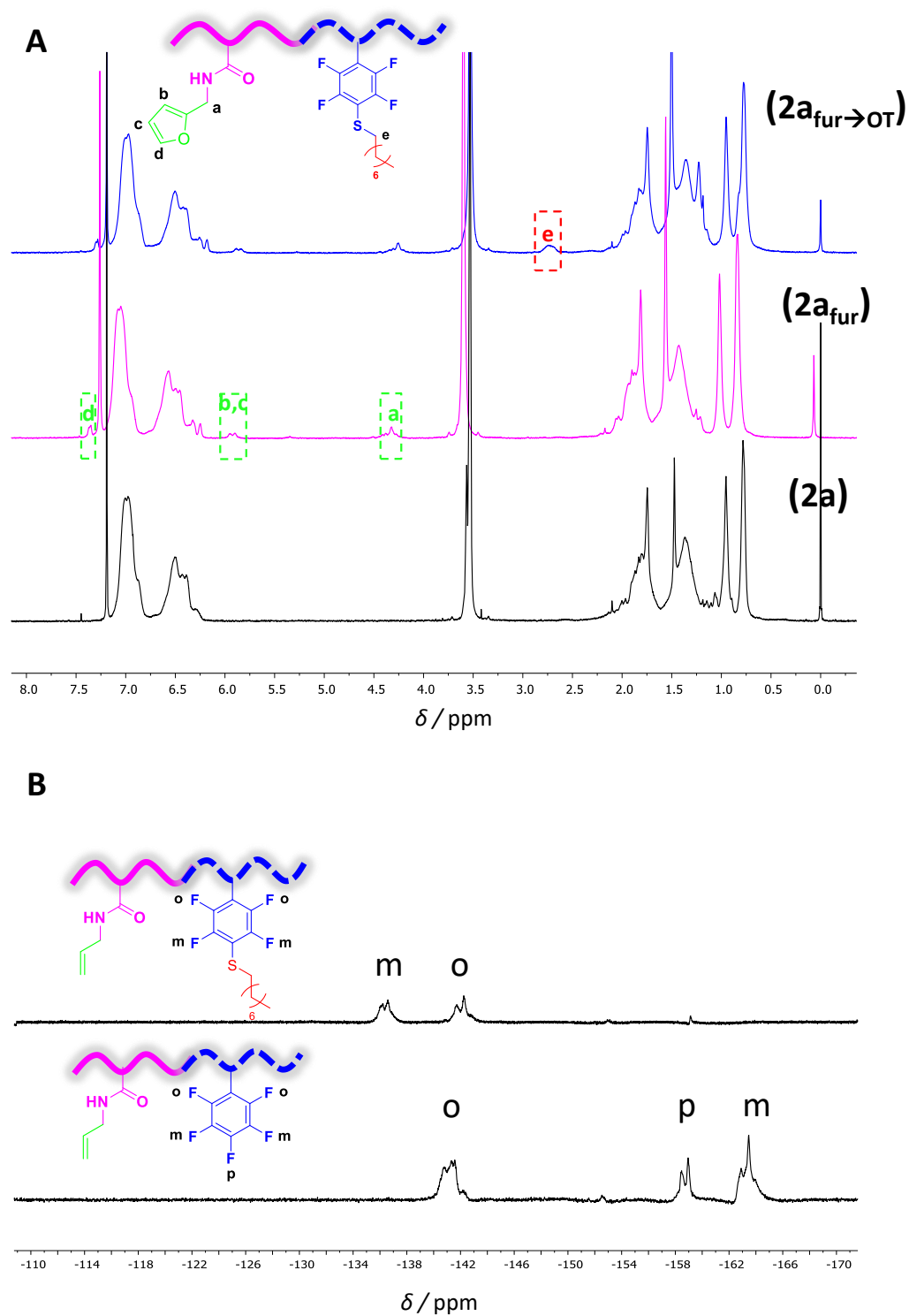


Figure A1. (A) IR spectrum of **1** showing the characteristic absorption bands of -C=O stretches of PMMA (pink) and PFPMA (green). (B) ^1H NMR and (C) ^{19}F NMR spectra of **1**. (D) ^1H NMR spectrum of the crude polymerization mixture at 0 minutes (top) and at the end of polymerization (bottom).



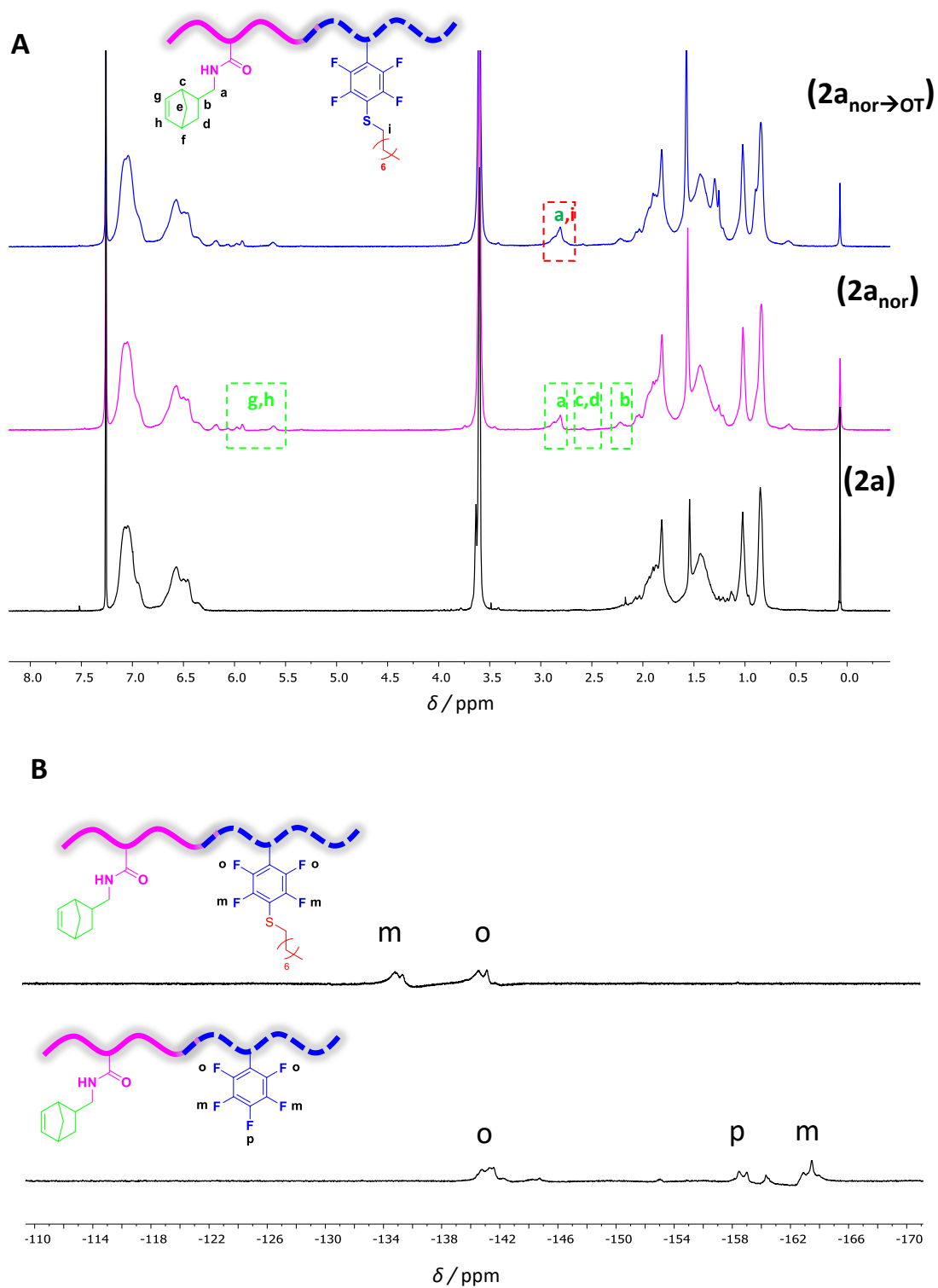
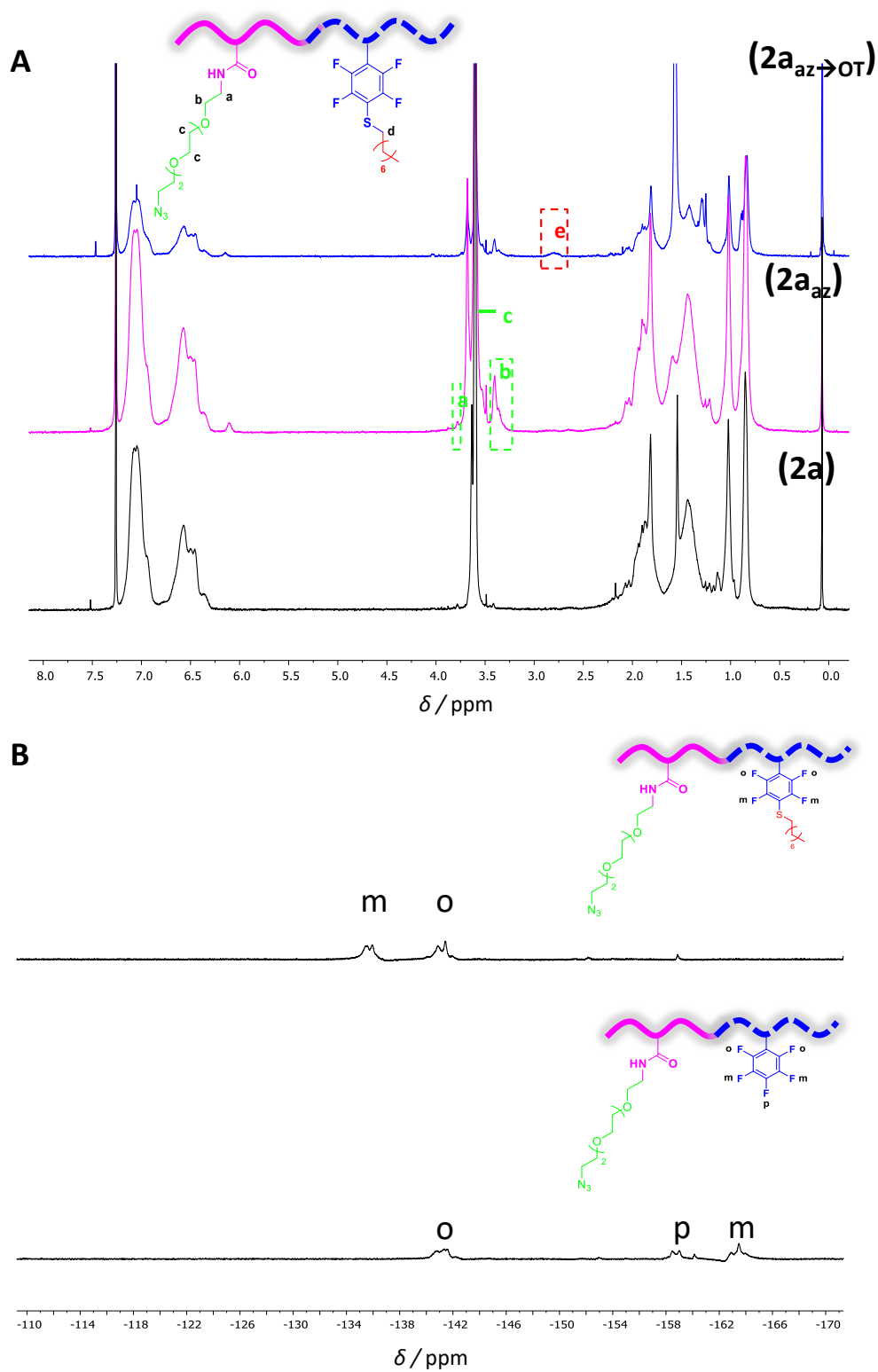


Figure A3. (A) ^1H NMR spectra of block copolymers **2a** (black), **2a_{nor}** (pink), and **2a_{nor}→OT** (blue). (B) ^{19}F NMR spectra of block copolymers **2a_{nor}** (bottom) and **2a_{nor}→OT** (top).



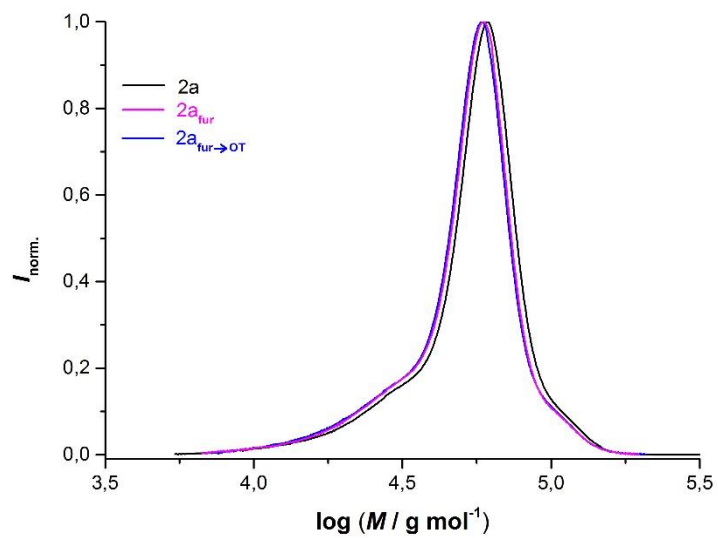


Figure A5. SEC traces of block copolymers **2a** (black), **2a_{fur}** (pink), and **2a_{fur}→OT** (blue).

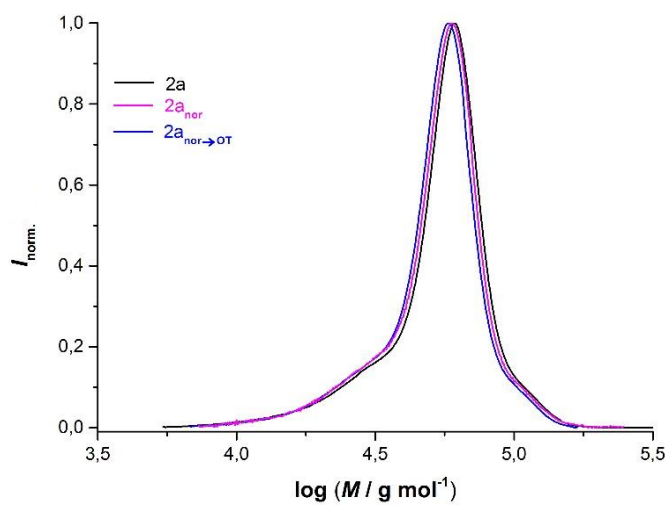


Figure A6. SEC traces of block copolymers **2a** (black), **2a_{nor}** (pink), and **2a_{nor}→OT** (blue).

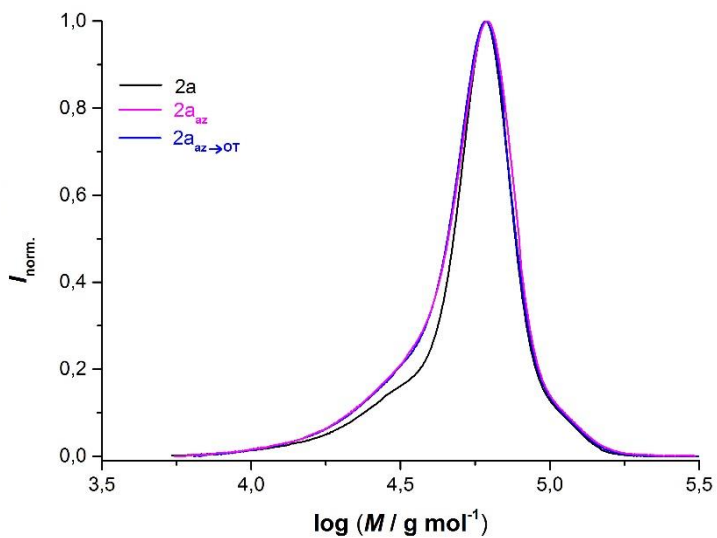


Figure A7. SEC traces of block copolymers **2a** (black), **2a_{az}** (pink), and **2a_{az}→OT** (blue).

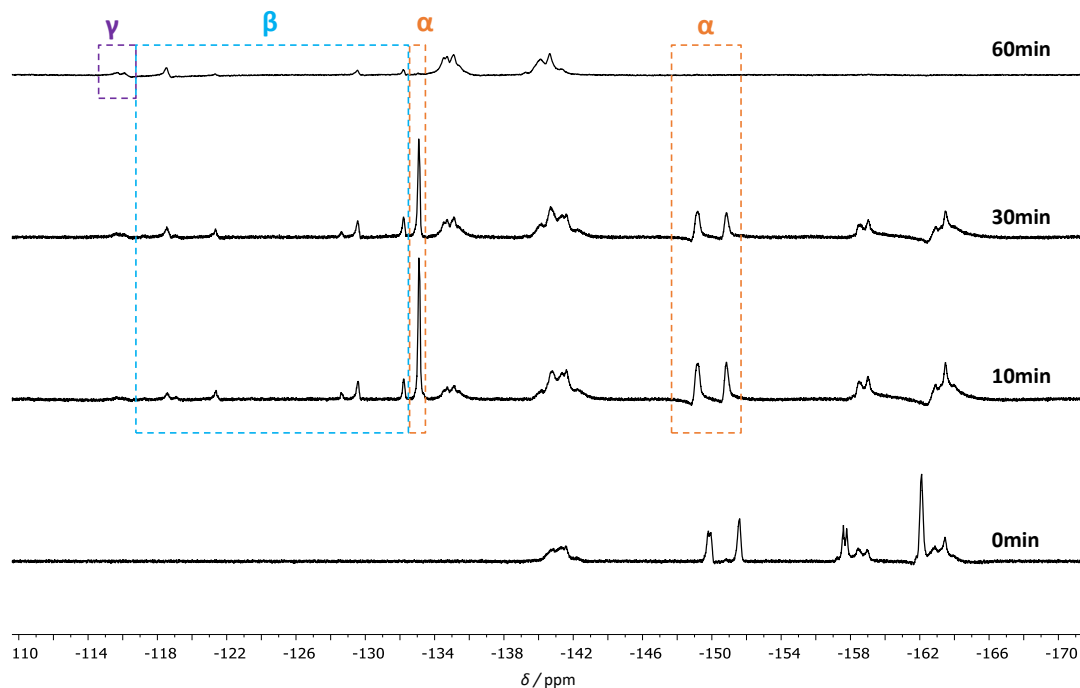


Figure A8. ¹⁹F NMR of **2a** at various time intervals in the presence of 5 eq. mercaptoethanol and 1 eq. DBU at RT. α represents the PFPMA *para*-substituted species while β represents that of mono *meta*-substituted and γ that of *meta* disubstituted.

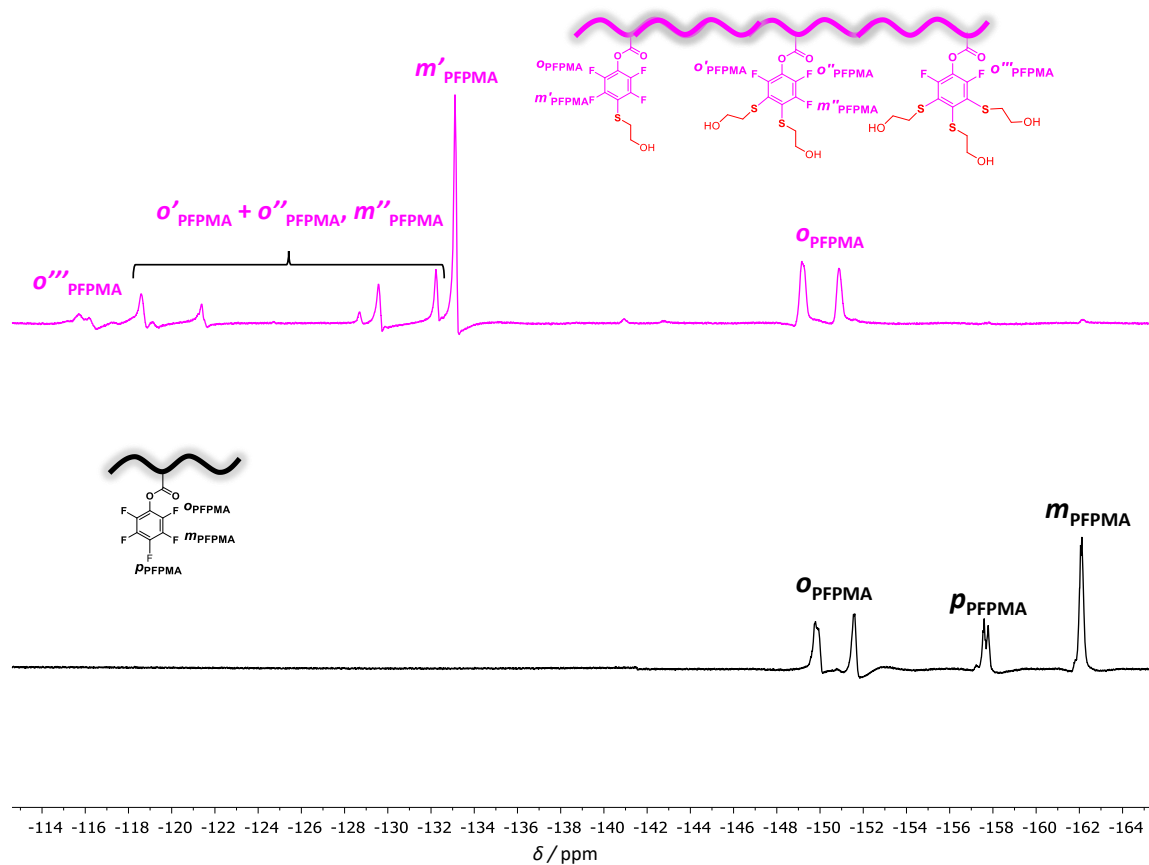


Figure A9. ^{19}F NMR of **1a** before (bottom) and after (top) reaction with 5 eq. mercaptoethanol under PFTR standard conditions.

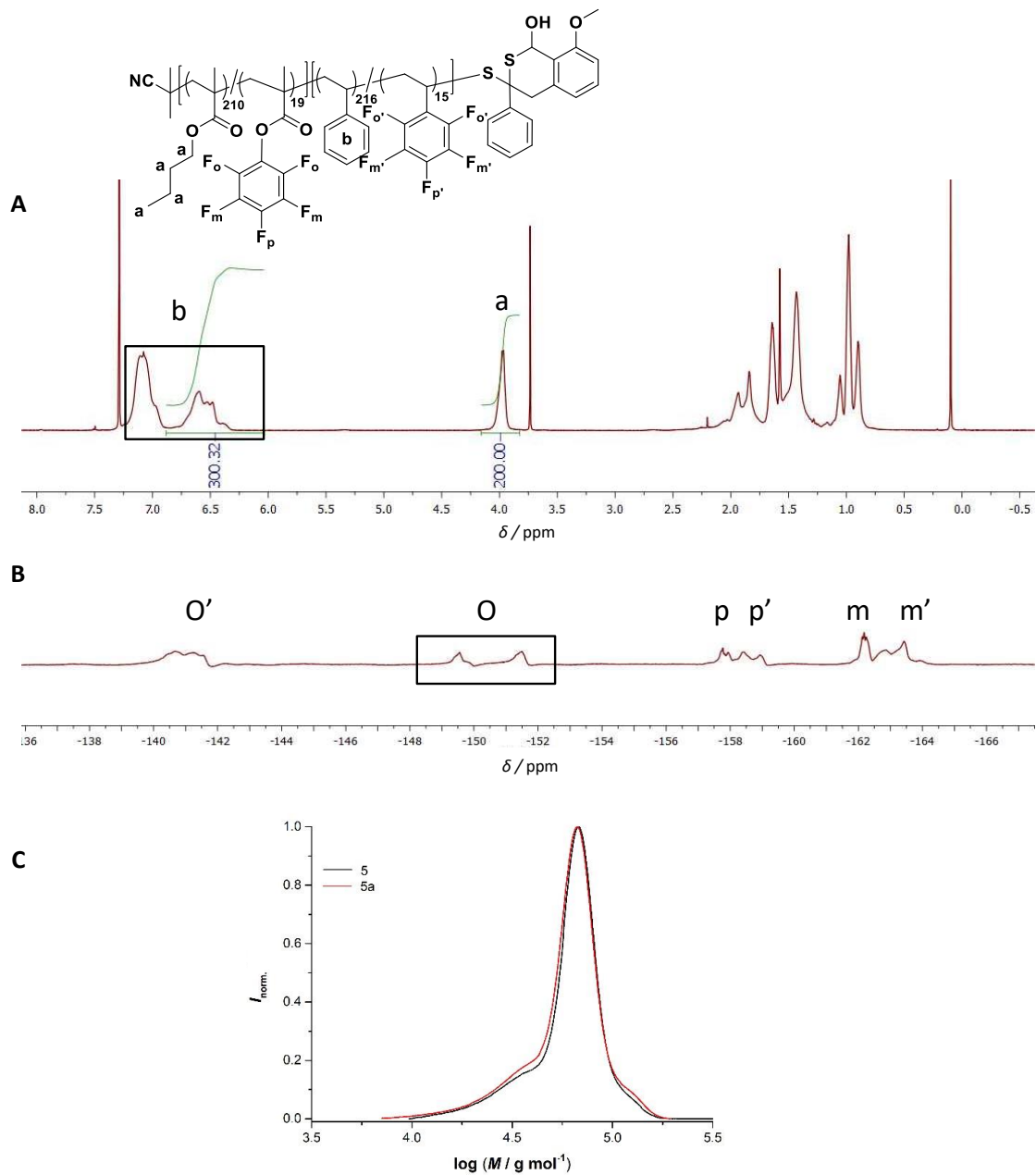


Figure A10. (A) ^1H NMR of **5a** with the integrals used for calculating the overall molar mass. (B) ^{19}F NMR and of **5a**. (C) near-integral overlapping SEC traces of **5** and **5a**.

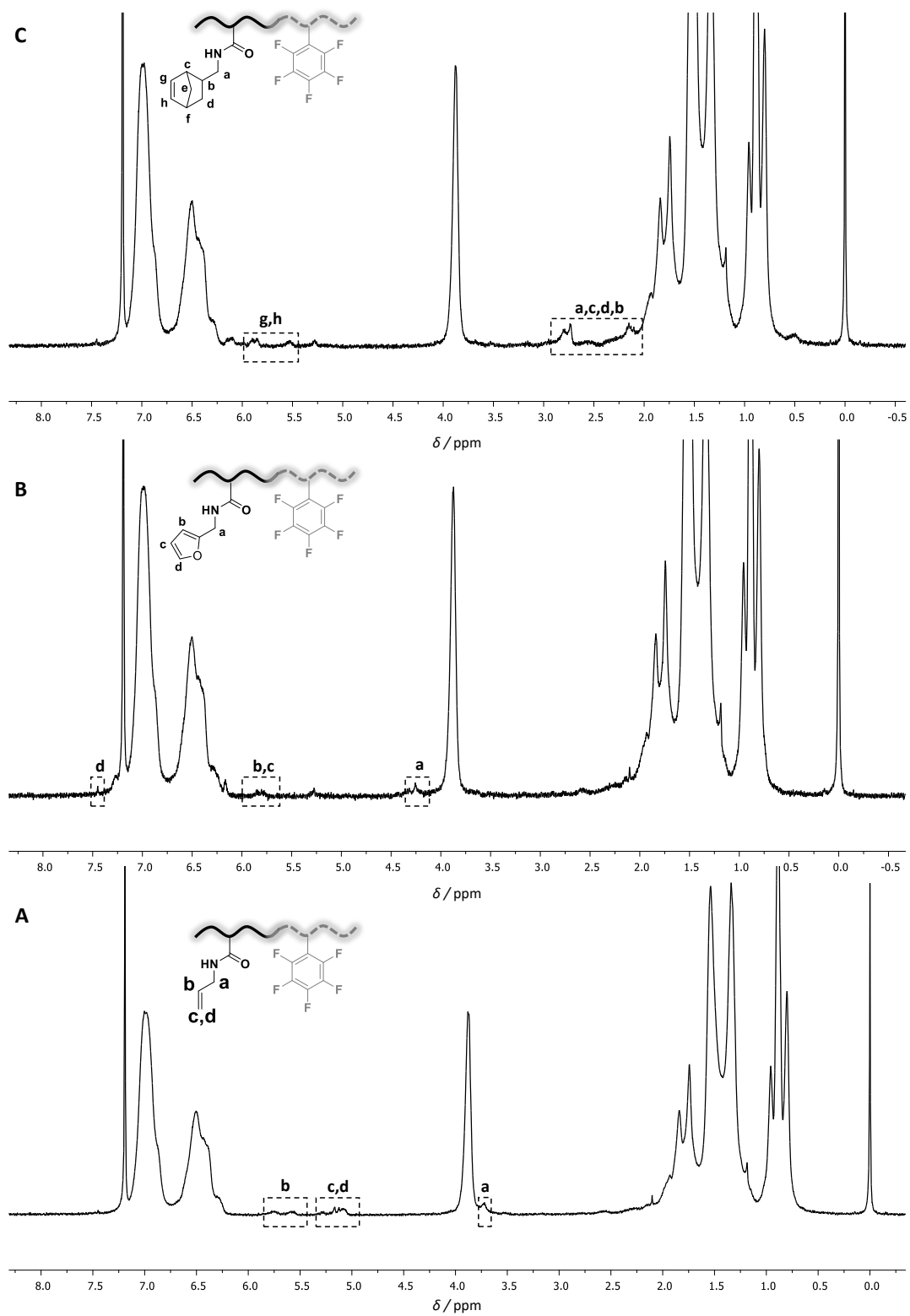


Figure A11. ^1H NMR spectra of **5a** after reaction with allylamine (A), furfurylamine (B), and norbornene methylation (C) using *Pathway 1*.

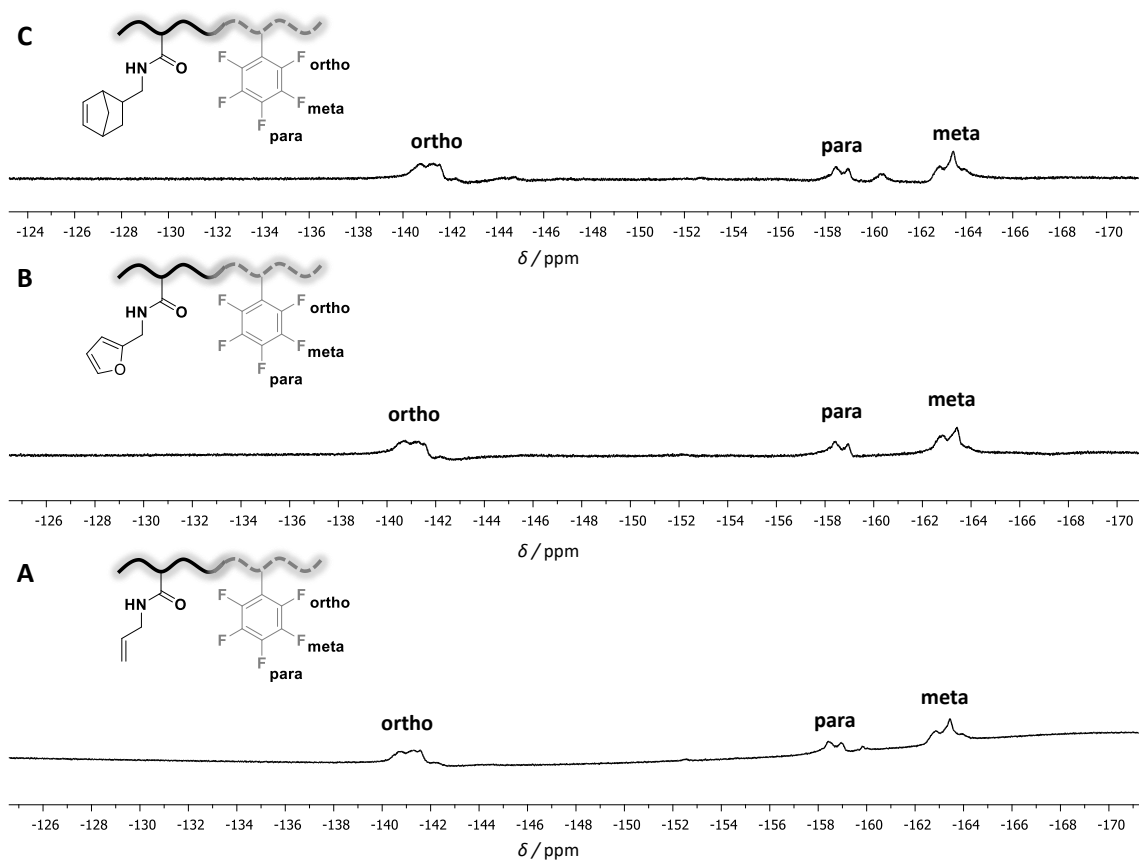


Figure A12. ^{19}F NMR spectra of **5a** after reaction with allylamine (A), furfurylamine (B), and norbornene methylamine (C) using *Pathway 1*.

Appendix B: Additional Figures for Chapter 4

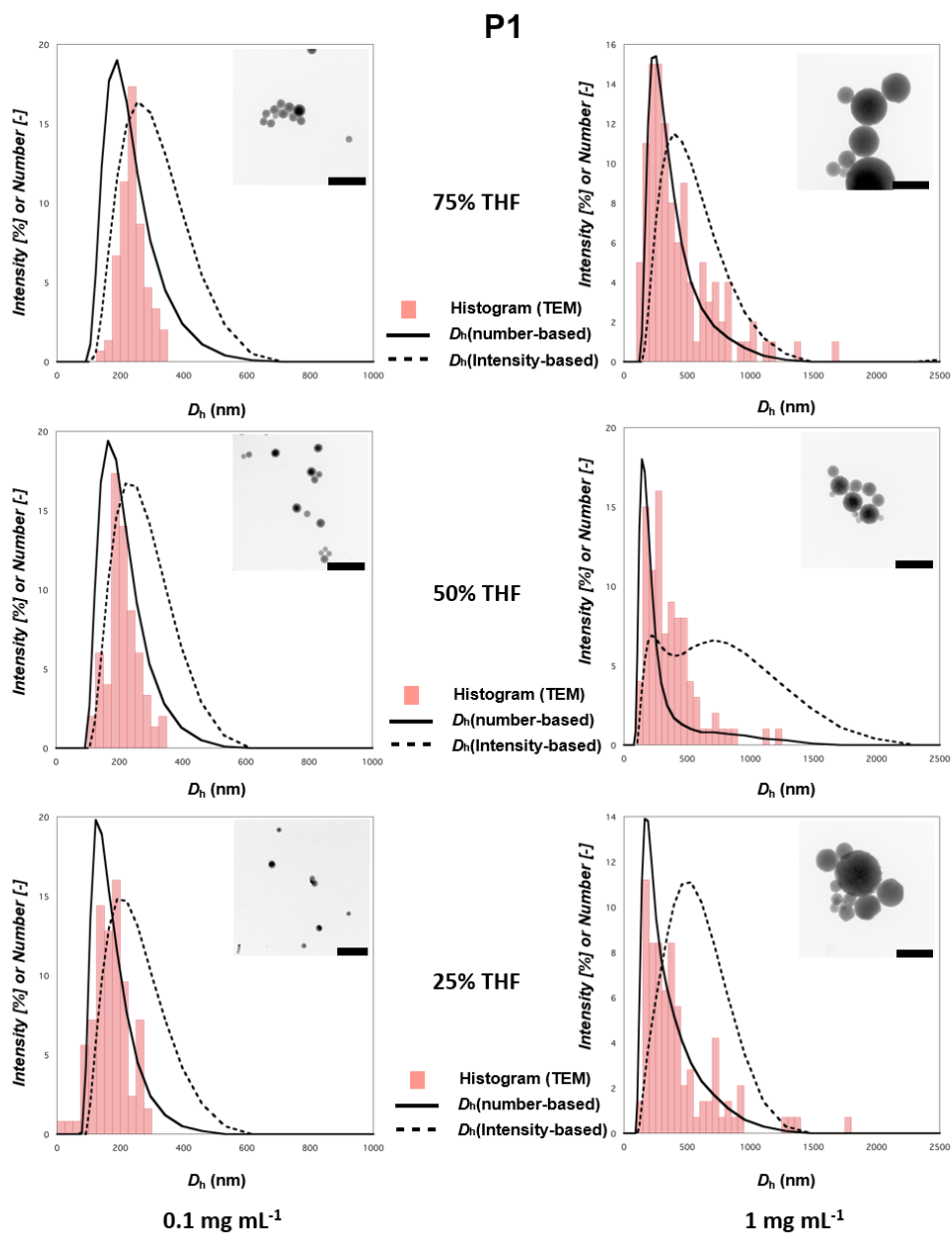


Figure B1. Particle size distribution of particles prepared from BCP **P1** using different conditions (mixing ratio of THF/water and polymer concentration, see Table S3) obtained from statistical analysis of TEM images (histogram), DLS (number-based, black solid line) and DLS (intensity-based, black dotted line). Insets represent an exemplary TEM overview image used for statistical analysis. All scale bars represent 1 μm .

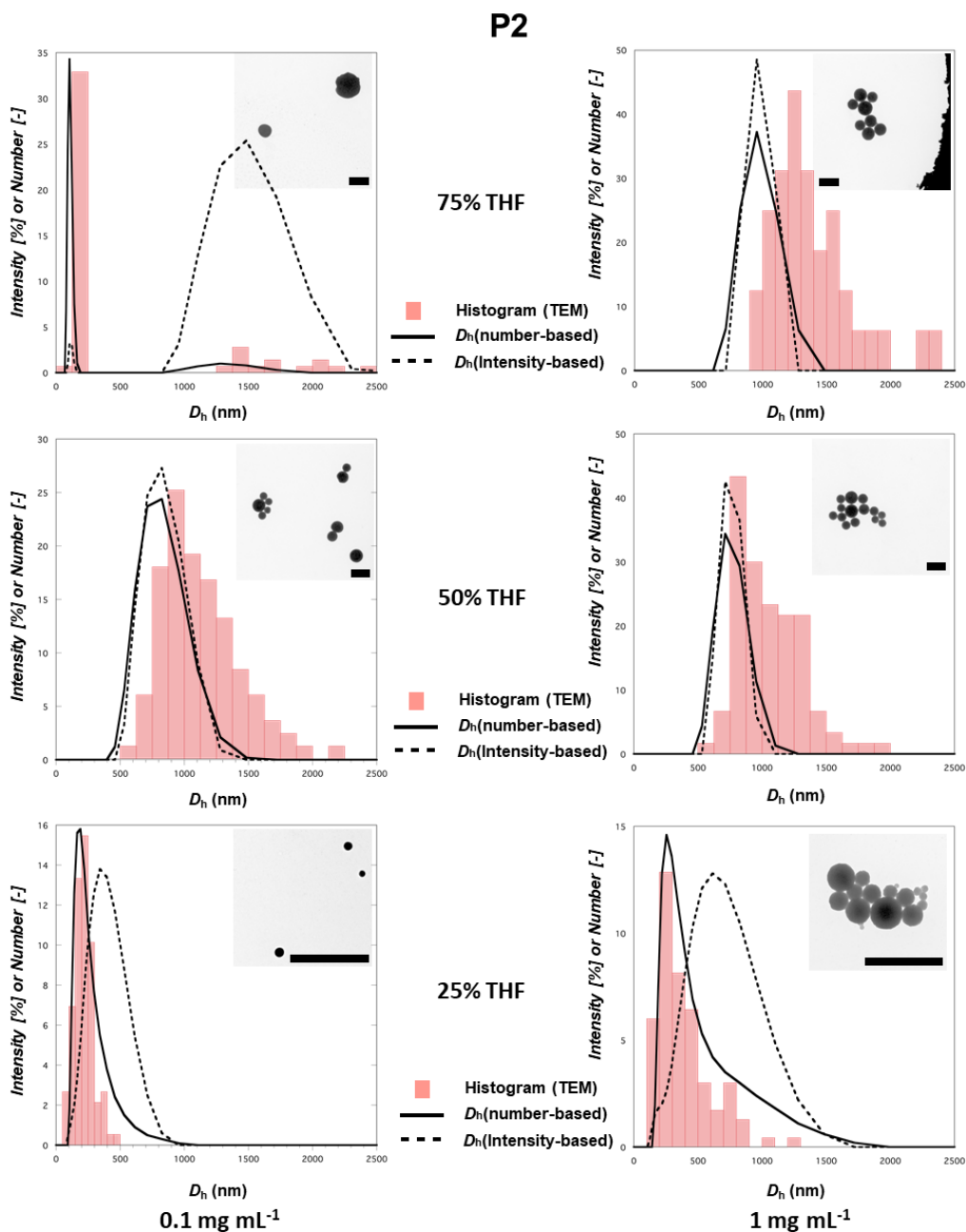


Figure B2. Particle size distribution of particles prepared from BCP **P2** using different conditions (mixing ratio of THF/water and polymer concentration, see Table S3) obtained from statistical analysis of TEM images (histogram), DLS (number-based, black solid line) and DLS (intensity-based, black dotted line). Insets represent an exemplary TEM overview image used for statistical analysis. All scale bars represent 2 μm .

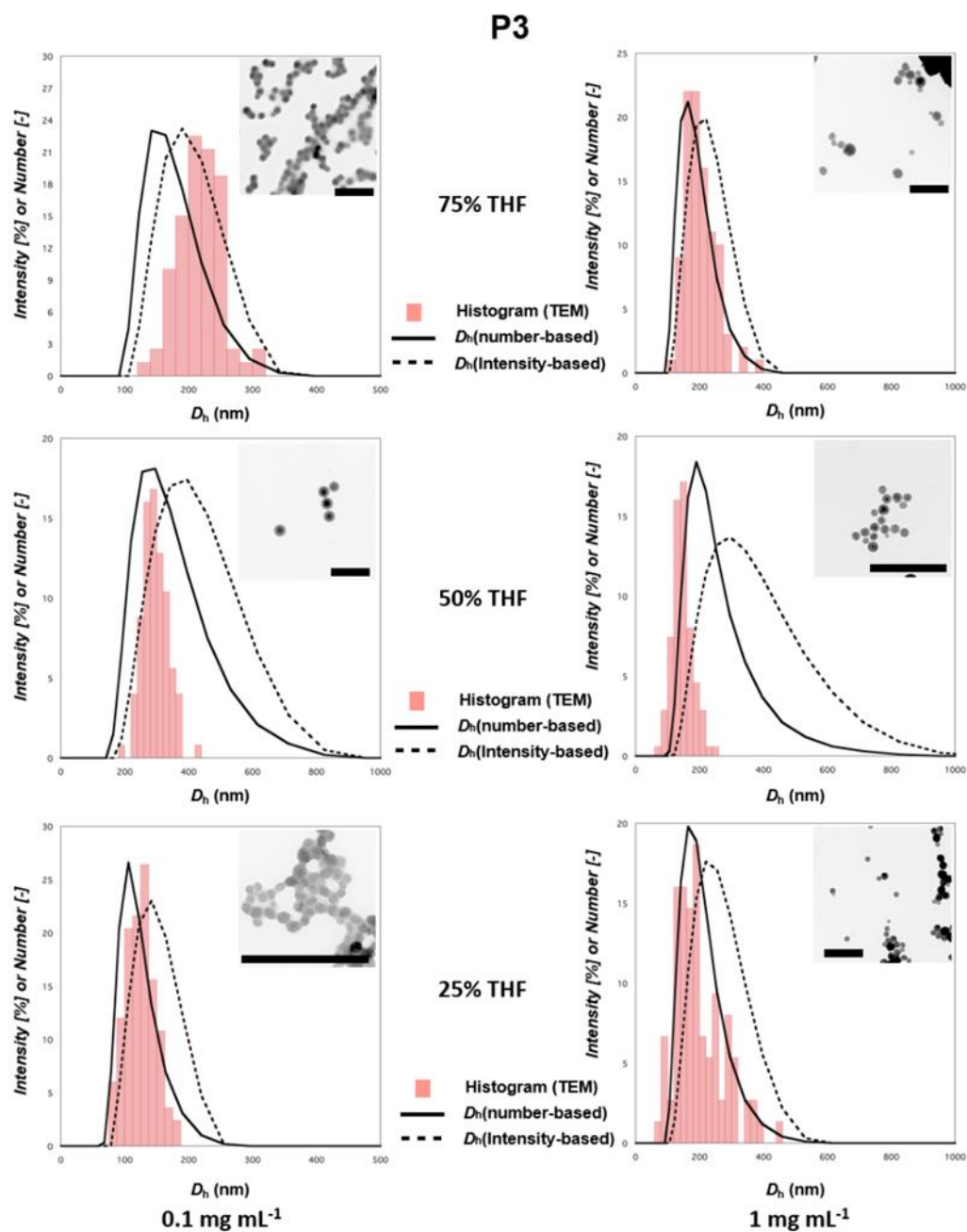


Figure B3. Particle size distribution of particles prepared from BCP **P3** using different conditions (mixing ratio of THF/water and polymer concentration, see Table S3) obtained from statistical analysis of TEM images (histogram), DLS (number-based, black solid line) and DLS (intensity-based, black dotted line). Insets represent an exemplary TEM overview image used for statistical analysis. All scale bars represent 1 μm .

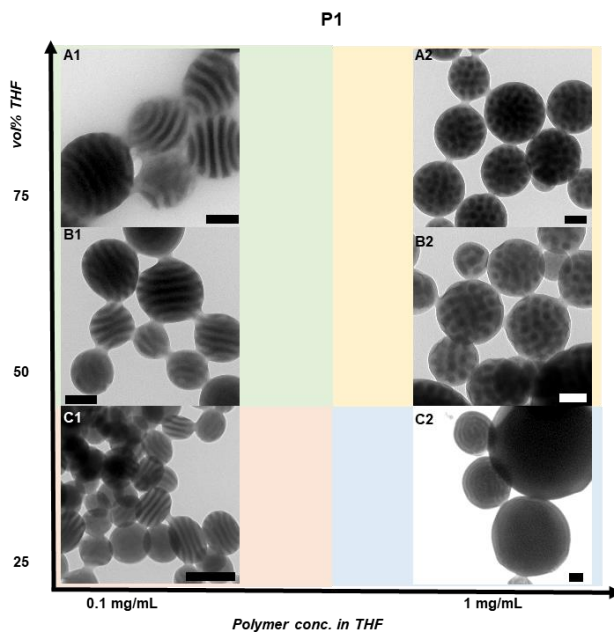


Figure B4. BF-TEM images for nanoparticles obtained by SORP with **P1** in various conditions, presented here at a lower magnification than in Figure 4.3 (codes correspond to those of Figure 4.3 in Chapter 4). All scale bars represent 100 nm.

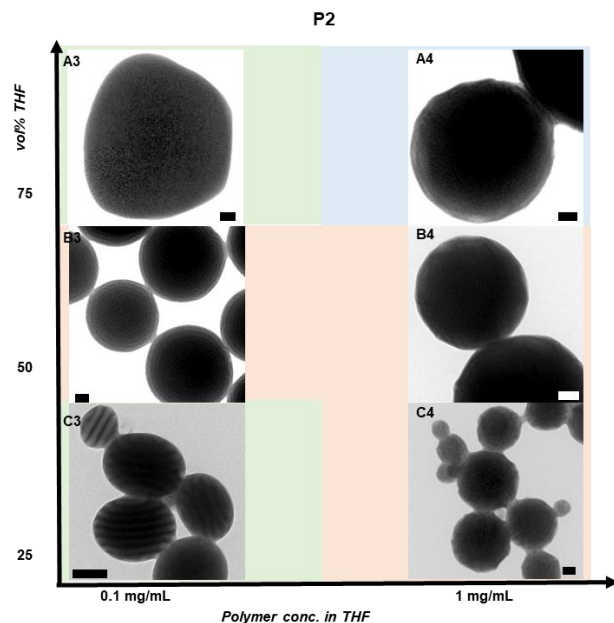


Figure B5. BF-TEM images for nanoparticles obtained by SORP with **P2** in various conditions, presented here at a lower magnification than in Figure 4.3 (codes correspond to those of Figure 4.3 in Chapter 4). All scale bars represent 100 nm.

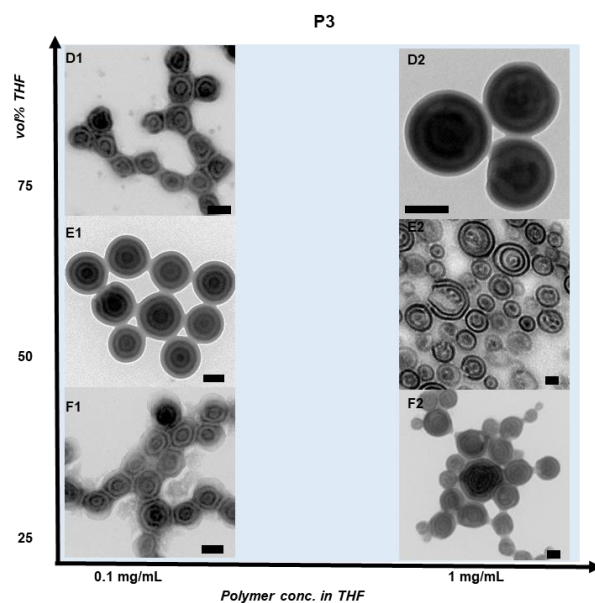


Figure B6. BF-TEM images for nanoparticles obtained by SORP with **P3** in various conditions, presented here at a lower magnification than in Figure 4.3 (codes correspond to those of Figure 4.3 in Chapter 4). All scale bars represent 100 nm. E2: TEM image of the nanoparticles sliced into 50 nm slices using an ultramicrotome.

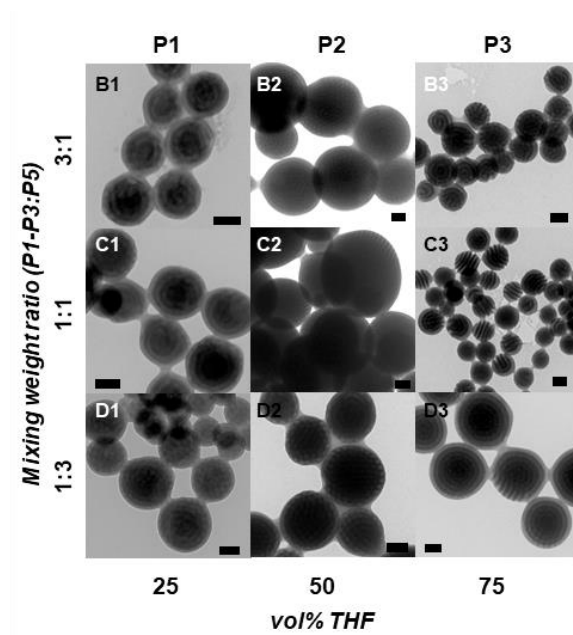


Figure B7. BF-TEM images for nanoparticles obtained by SORP with mixtures of BCPs **P1–3** and commercial BCP **P5** at various weight ratios, presented here at a lower magnification than in Figure 4.6 (codes correspond to those in Figure 4.6). All scale bars represent 100 nm.

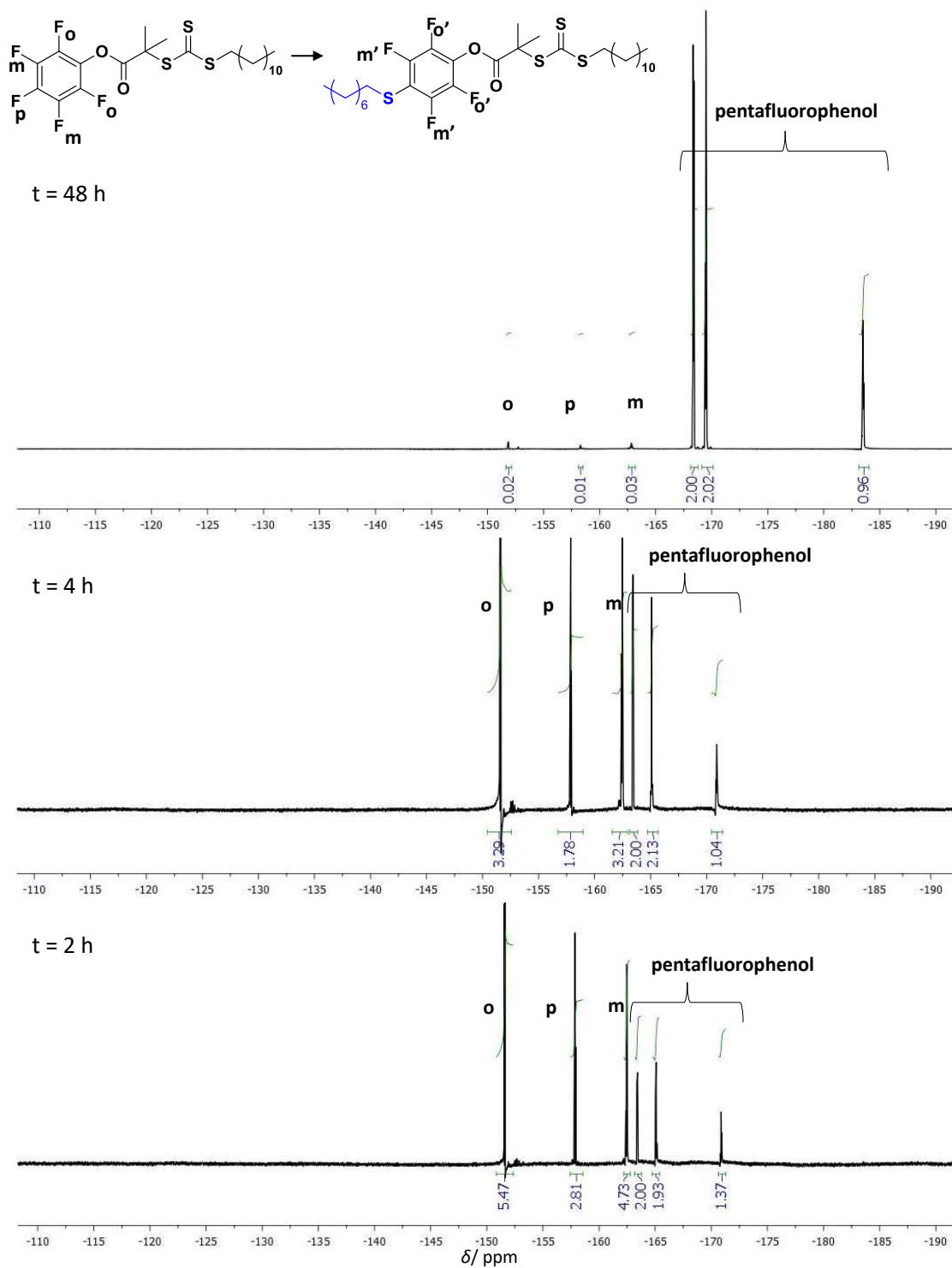


Figure B8. ^{19}F NMR spectrum after the reaction of PFP-linker with octanethiol for 2 h (bottom), 4 h (middle), and 48 h (top).

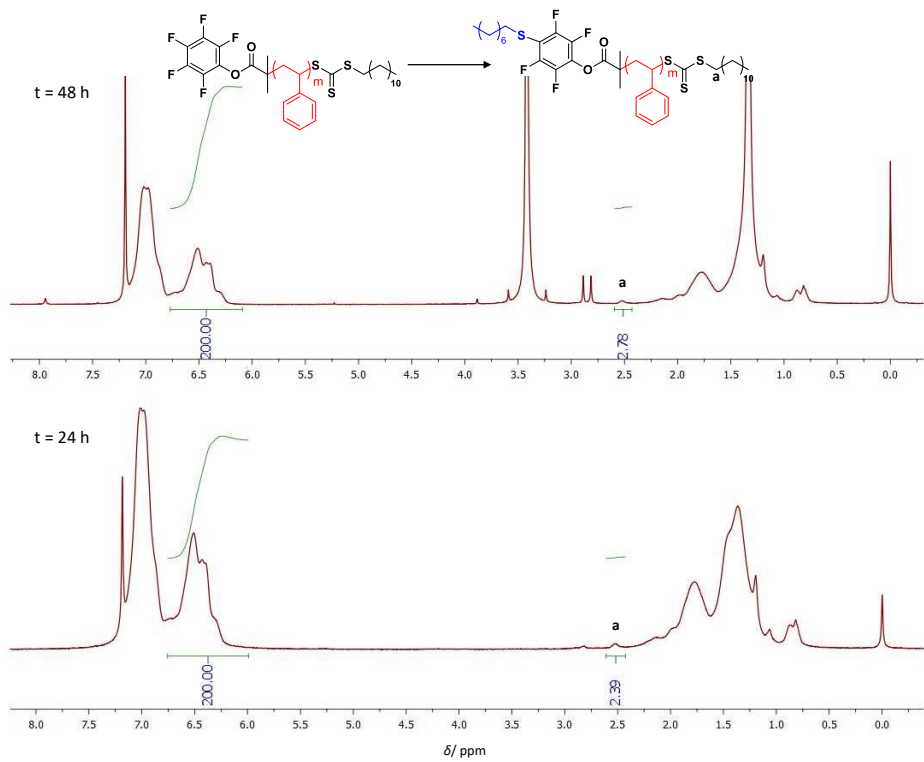


Figure B9. ^1H NMR spectra after PFTR of PFP-PS with octanethiol as a model thiol for 24 h (bottom) and 48 h (top).

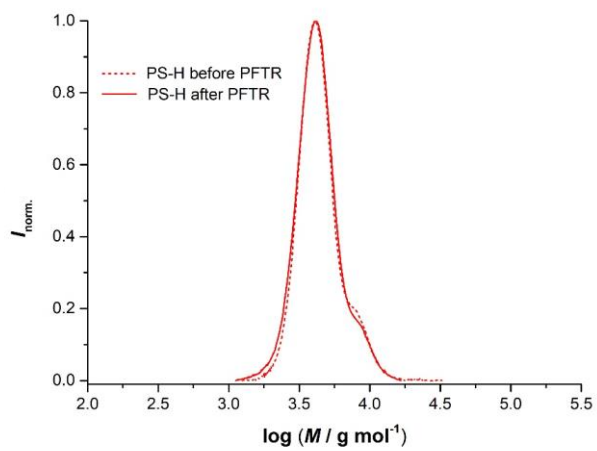


Figure B10. SEC traces of PS-H before (dotted line) and after (dotted line) PFTR with octanethiol for 48h.

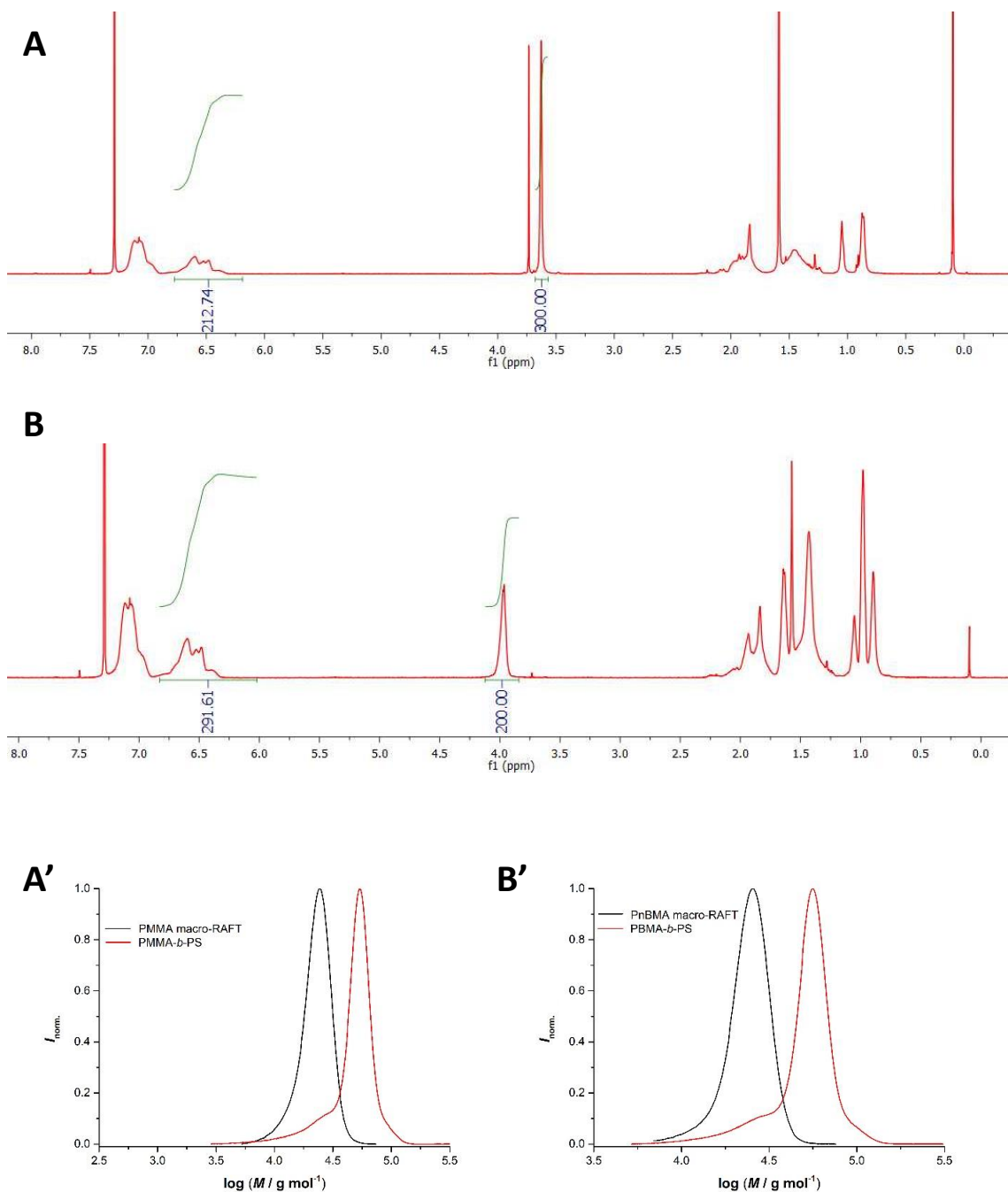


Figure B11. A and B: ^1H NMR spectra of PMMA-*b*-PS and PnBMA-*b*-PS BCPs, respectively. A': SEC traces of PMMA (black) macro-RAFT agent and the corresponding BCP PMMA-*b*-PS (red). B': SEC traces of PnBMA (black) macro-RAFT agent and the corresponding BCP PnBMA-*b*-PS (red).

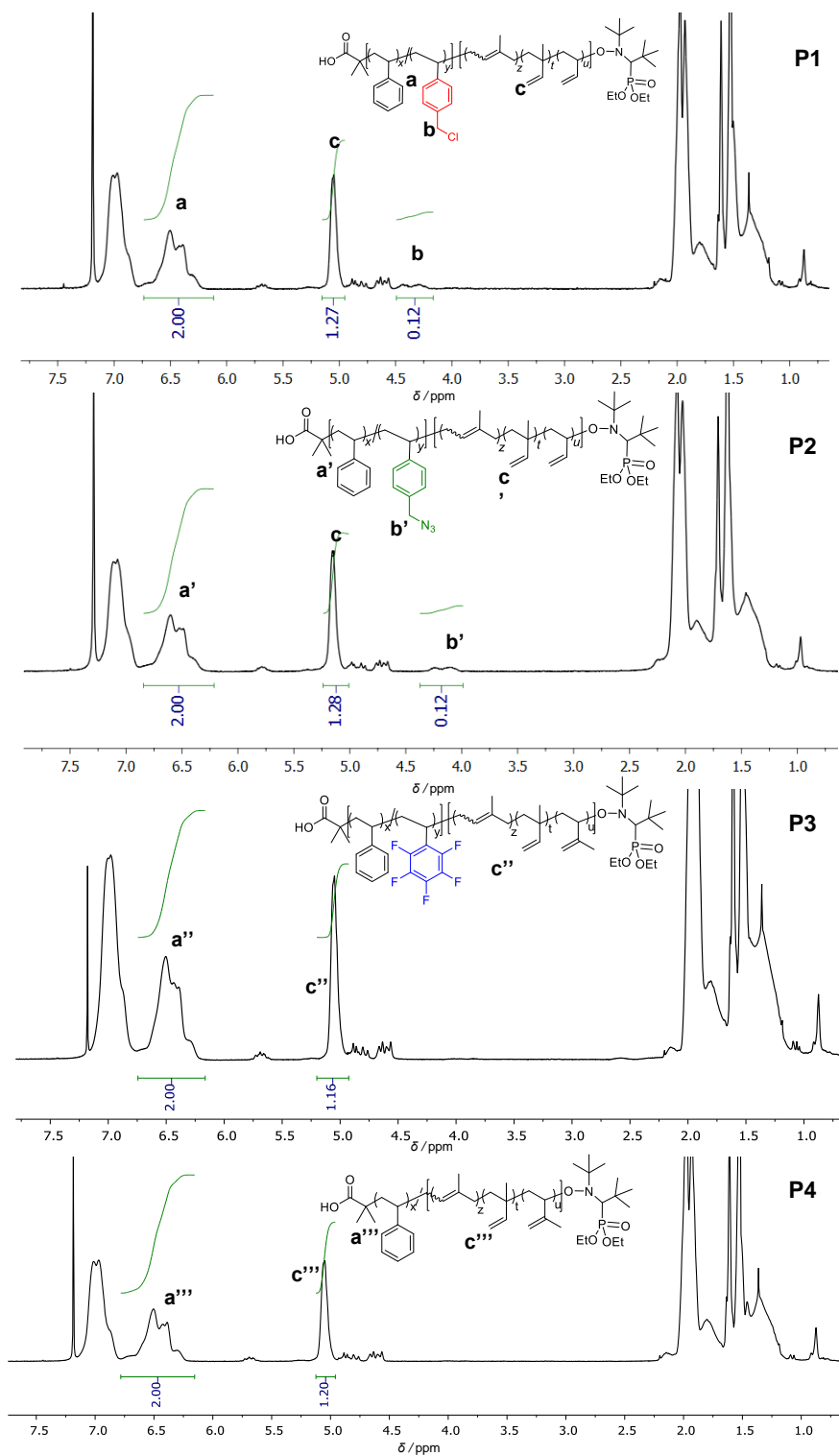


Figure B12. ¹H NMR spectra of polymers **P1-P4**.

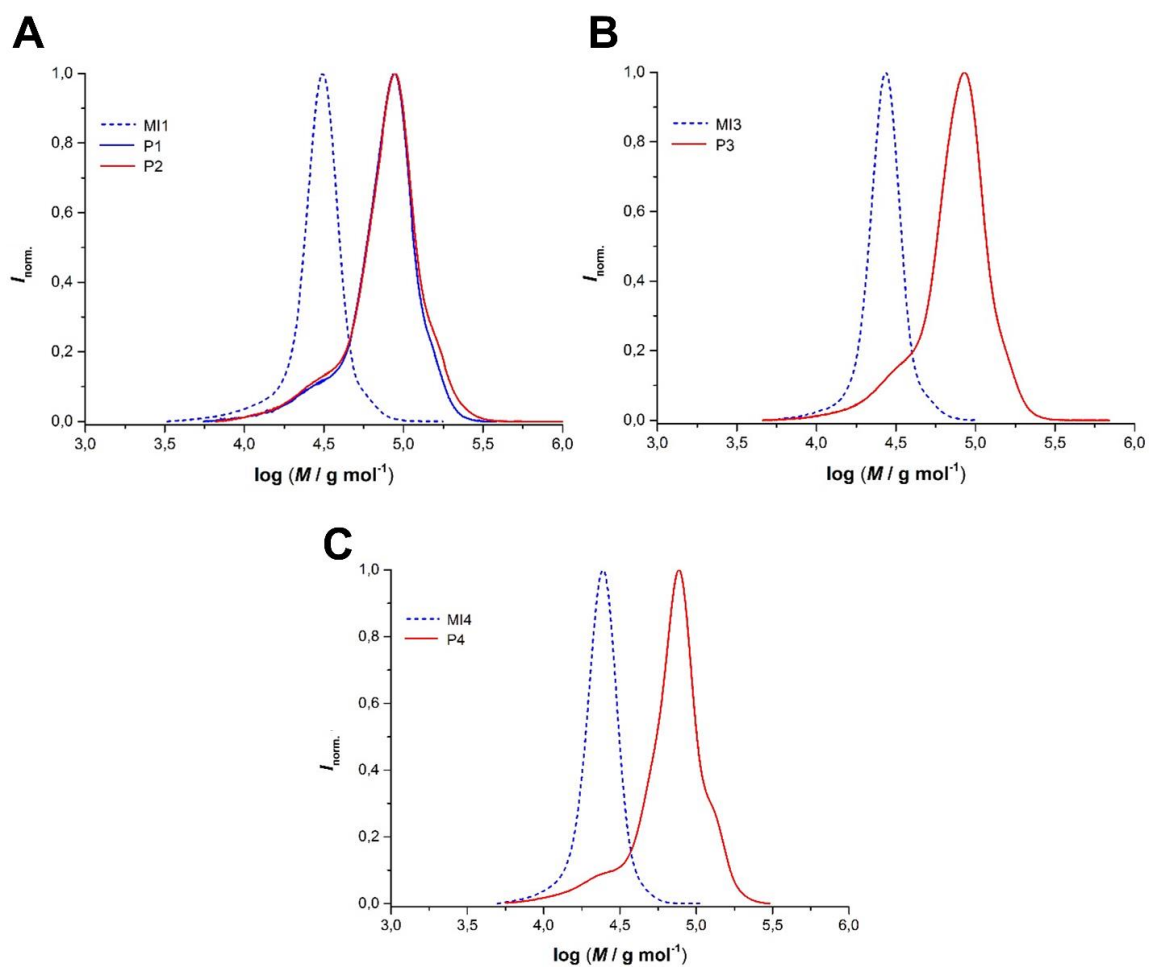


Figure B 13. SEC traces of macroinitiator **MI1** (A), **MI3** (B), **MI4** (C) (blue dotted lines) and BCPs **P1** and **P2** (A), **P3** (B), and **P4** (C) (red solid lines).

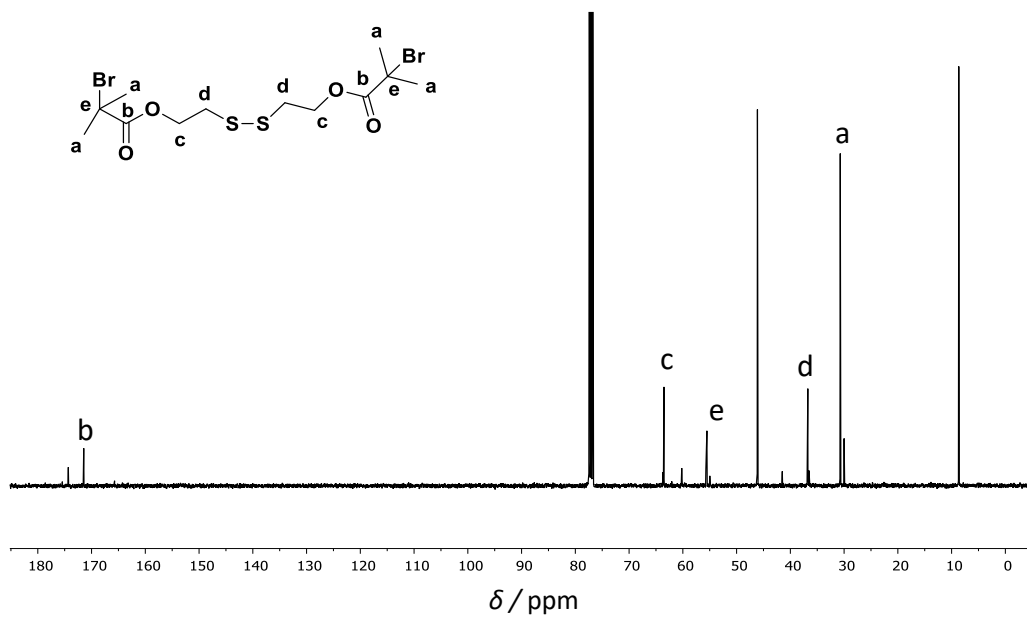
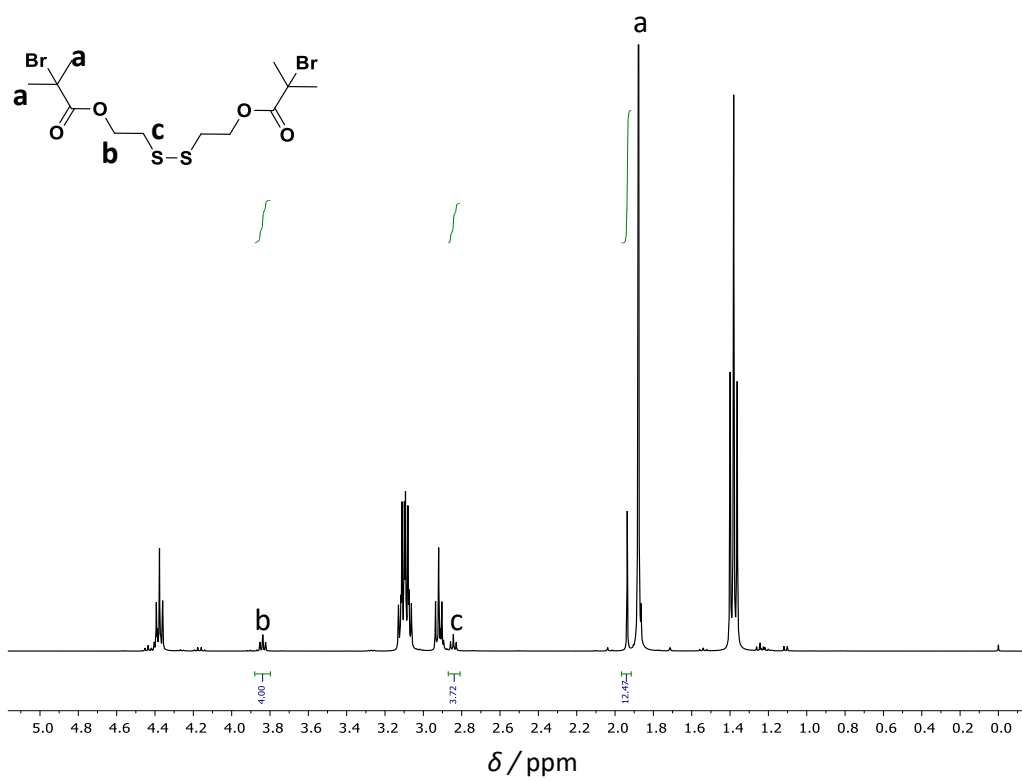


Figure B 14. ¹H (top) and ¹³C (bottom) NMR of ATRP-disulfide.

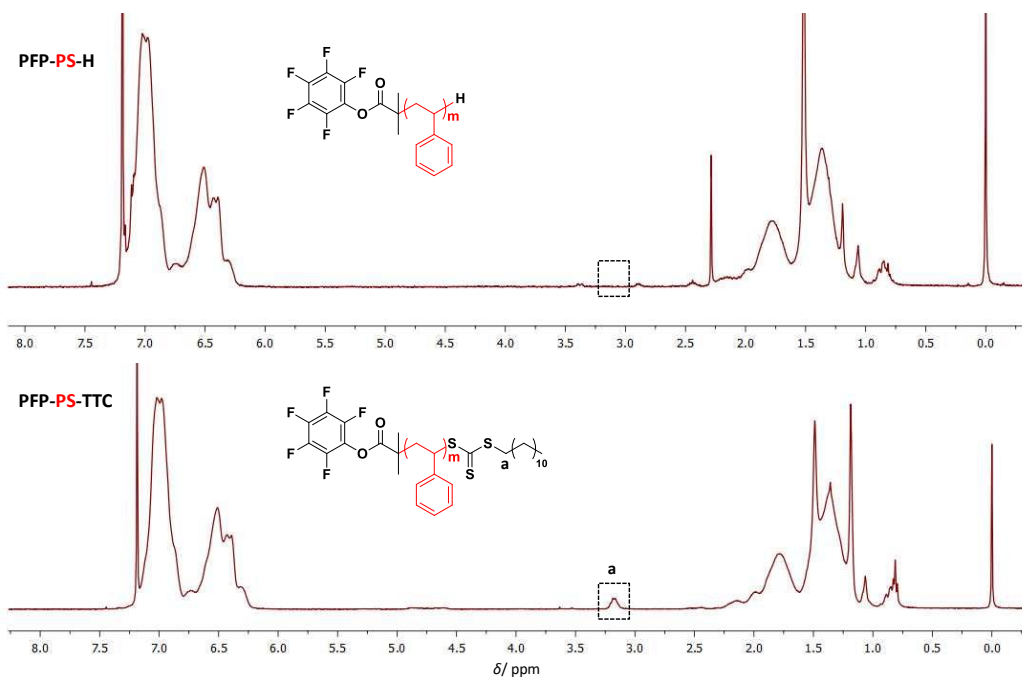


Figure B 15. ^1H NMR of PFP-PS-TTC synthesized by RAFT polymerization (bottom) and after end group removal (PFP-PS-H) (top).

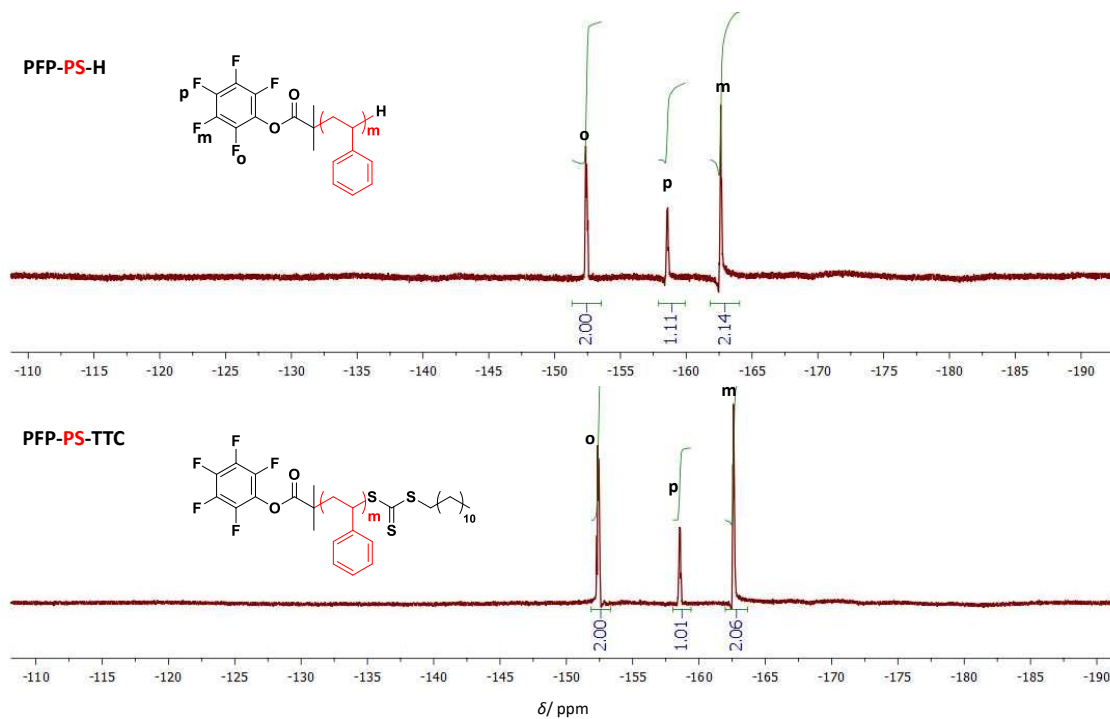


Figure B 16. ^{19}F NMR of PFP-PS-TTC synthesized by RAFT polymerization (bottom) and after end group removal (PFP-PS-H) (top).

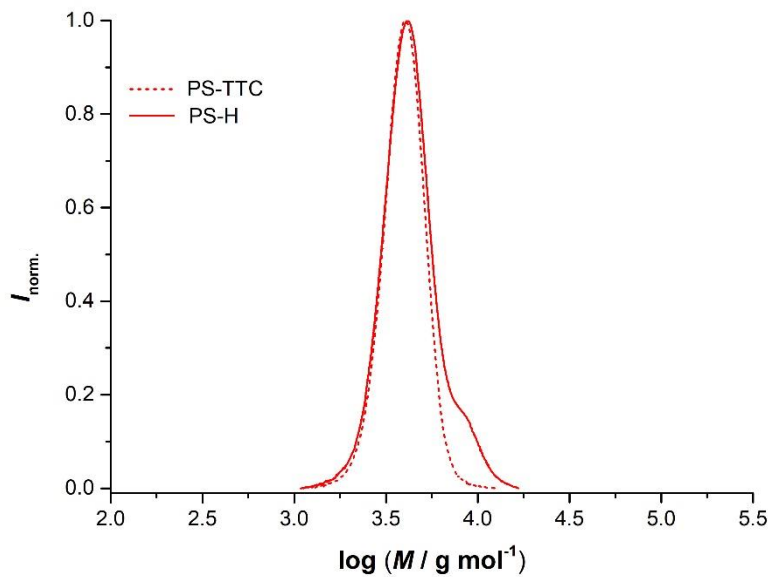


Figure B17. SEC traces of polystyrene before (**PFP-PS-TTC**, dotted line) and after (**PFP-PS-H**, solid line) the RAFT end group removal.

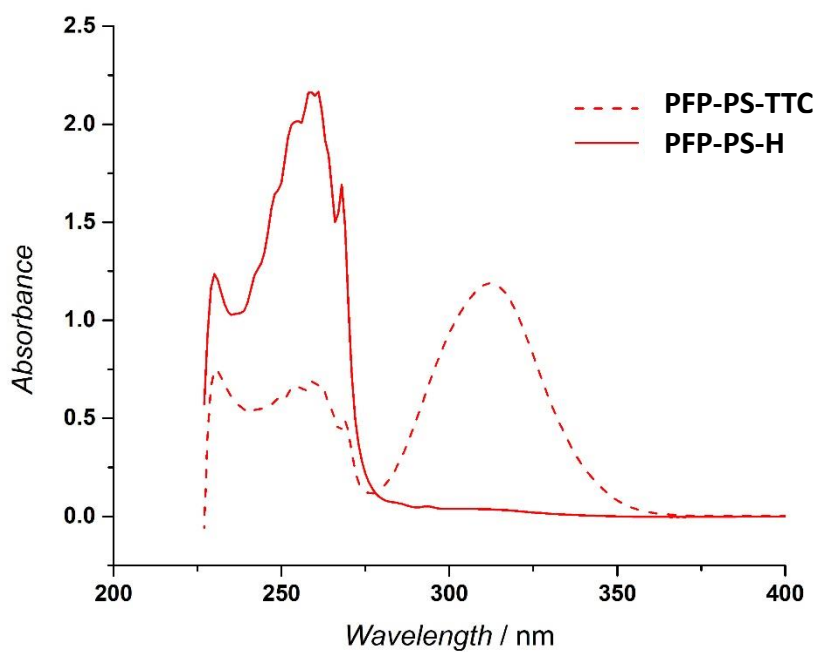


Figure B18. UV-Vis spectra of polystyrene before (**PFP-PS-TTC**, dotted line) and after (**PFP-PS-H**, solid line) the RAFT end group removal.

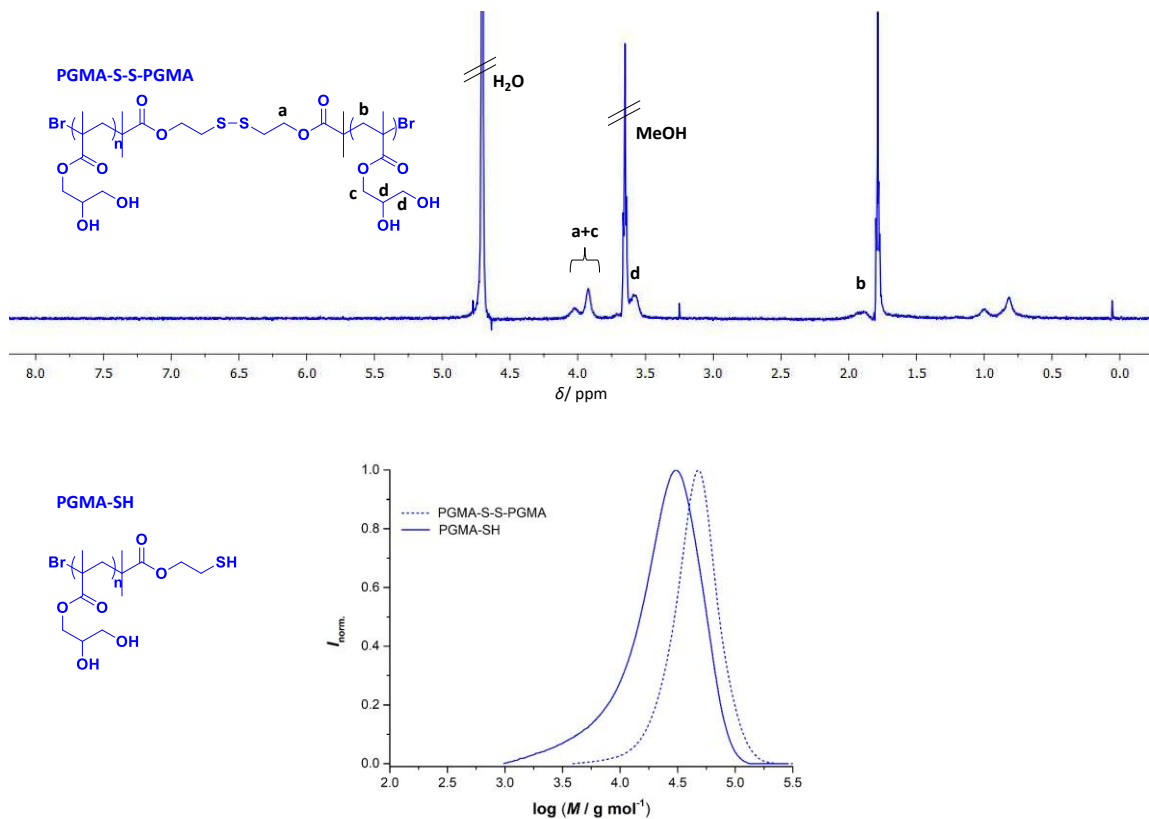
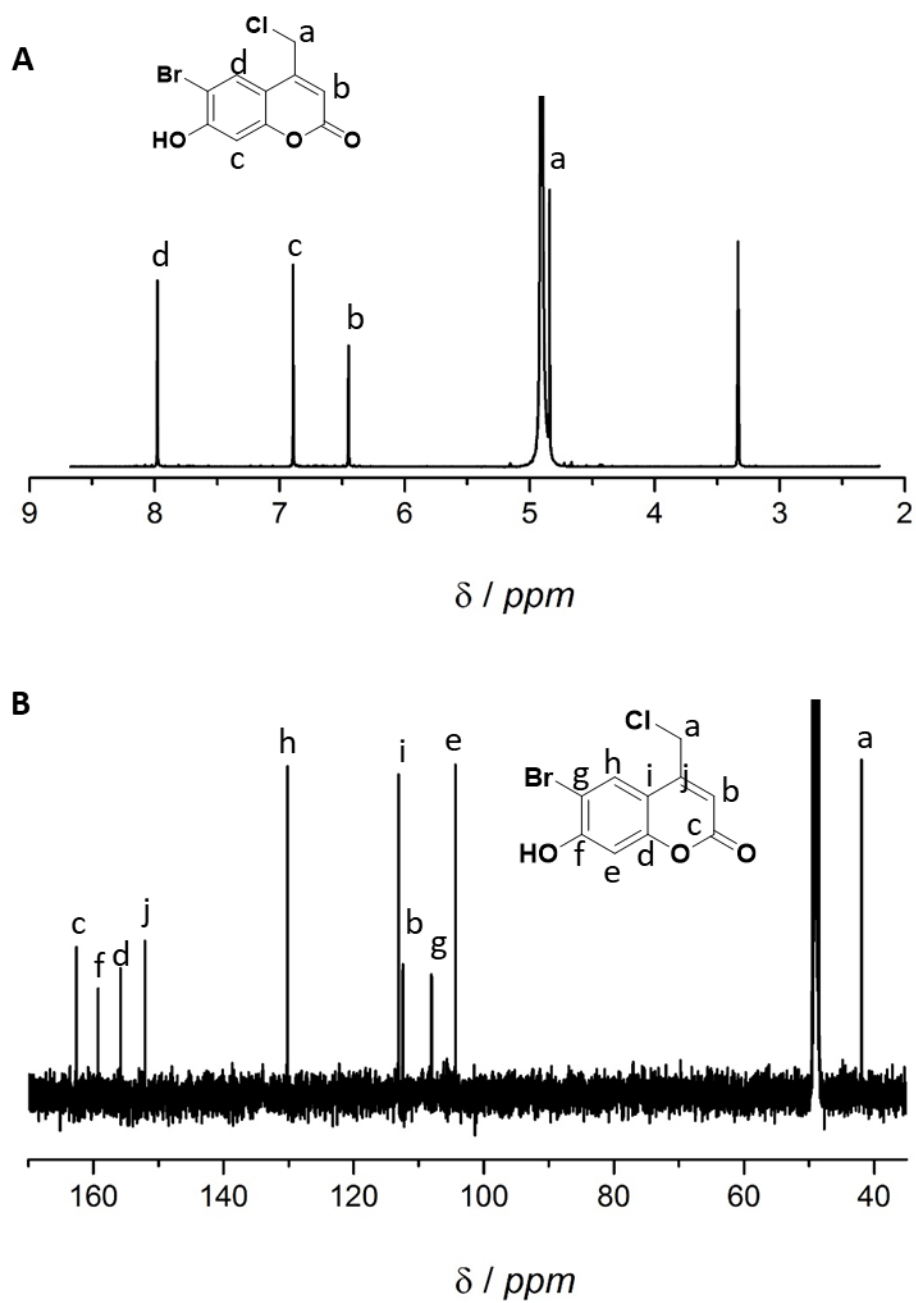
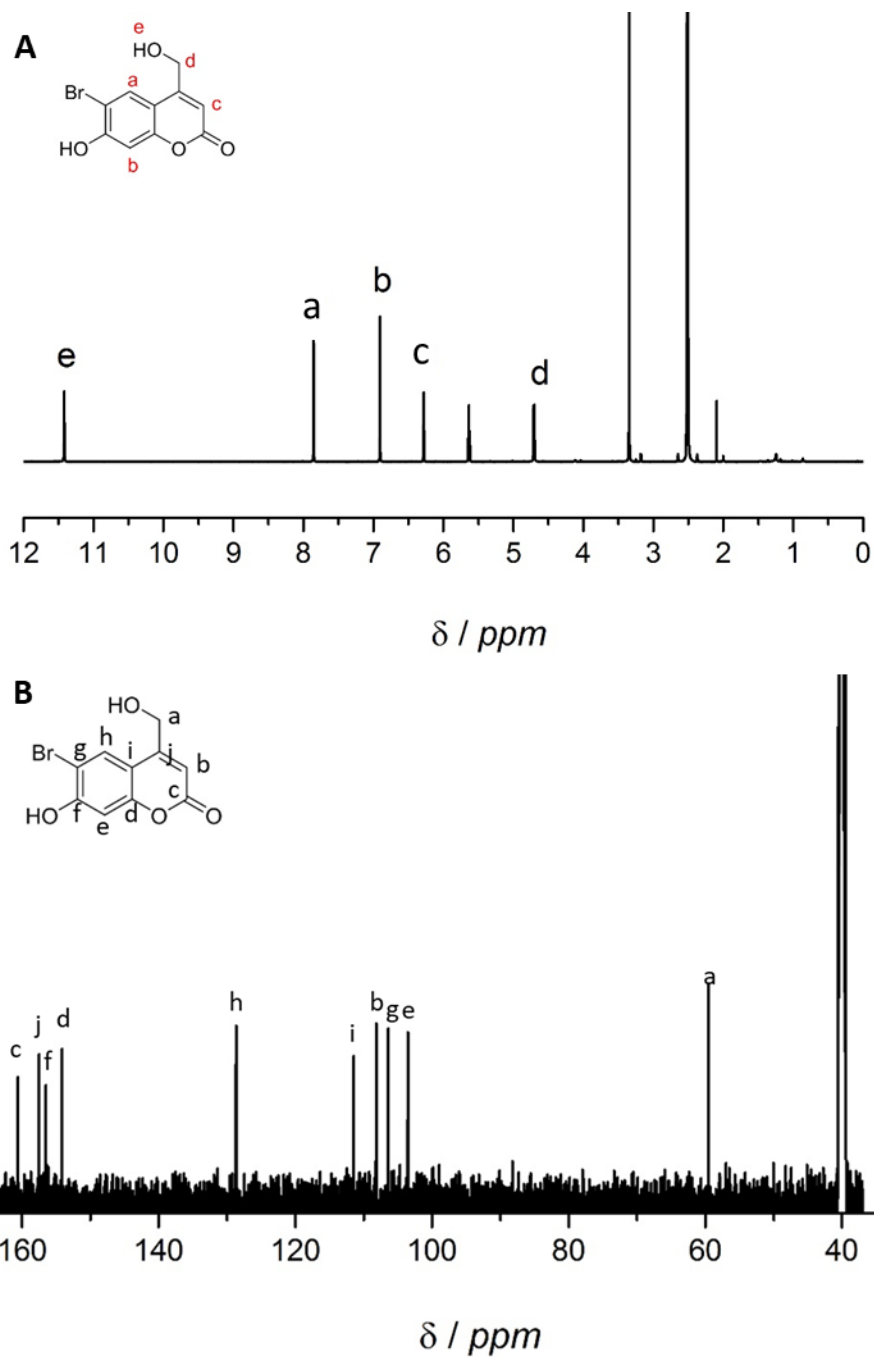


Figure B 19. ^1H NMR of **PGMA-S-S-PGMA** (top) and SEC traces of **PGMA-S-S-PGMA** (bottom, dotted line) and **PGMA-SH** (bottom, solid line).

Appendix C: Additional Figures for Chapter 5





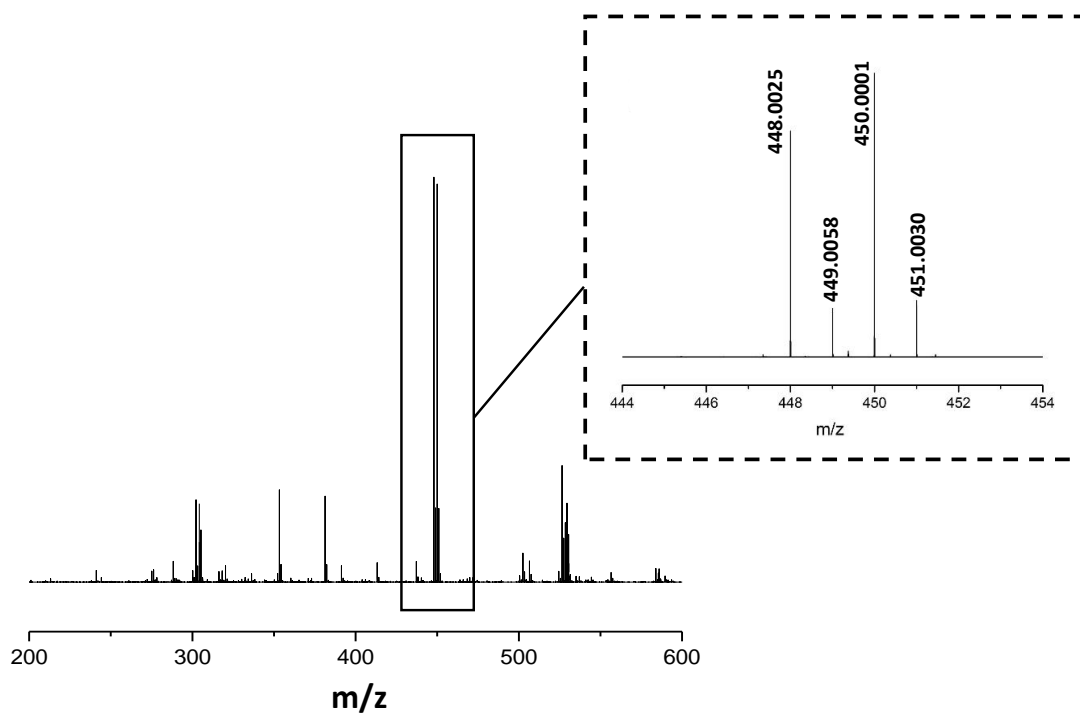


Figure C3. ESI-MS spectrum of the PBG 5 in THF:MeoH = 3:2 mixture.

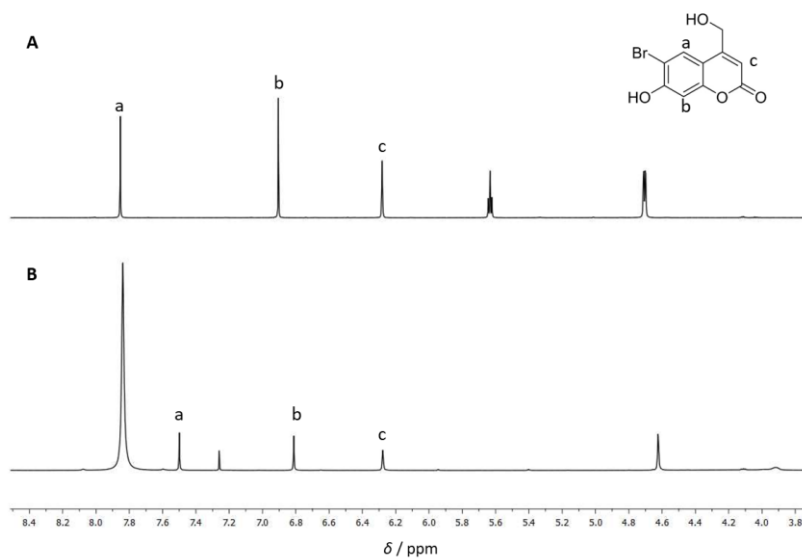


Figure C4. ¹H NMR spectra of 3 before (A) and after (B) free-radical polymerization measured in MeOD and DMSO-d₆, respectively.

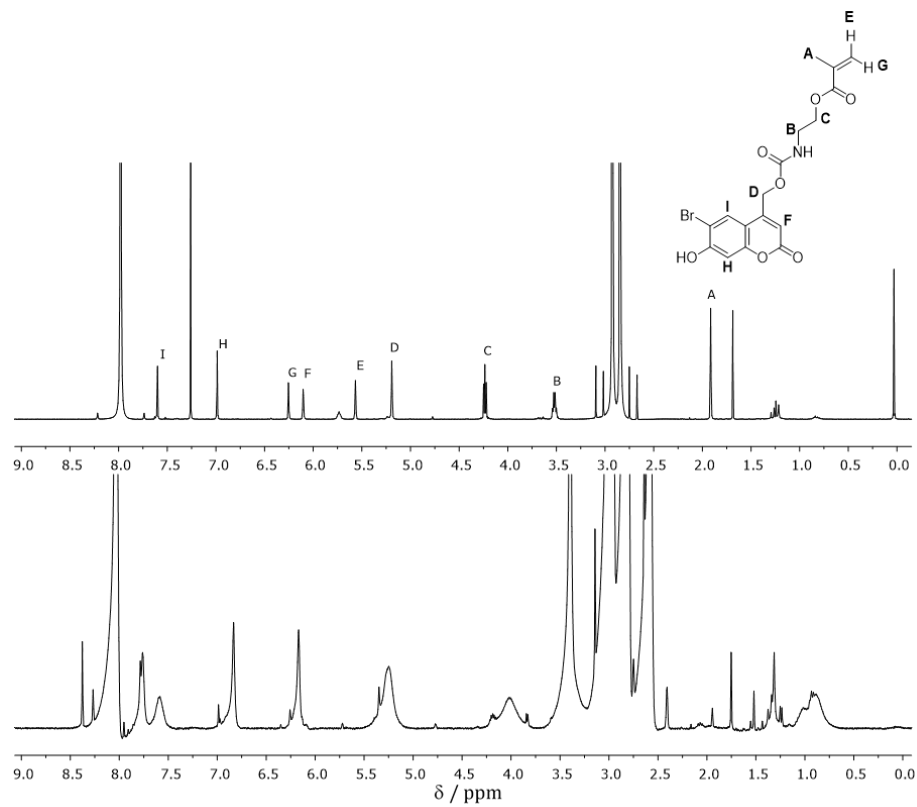


Figure C5. ¹H NMR spectra of PBG 5 before (top) and after FRP at 7 h (bottom) measured in CDCl₃ and DMSO-d₆, respectively.

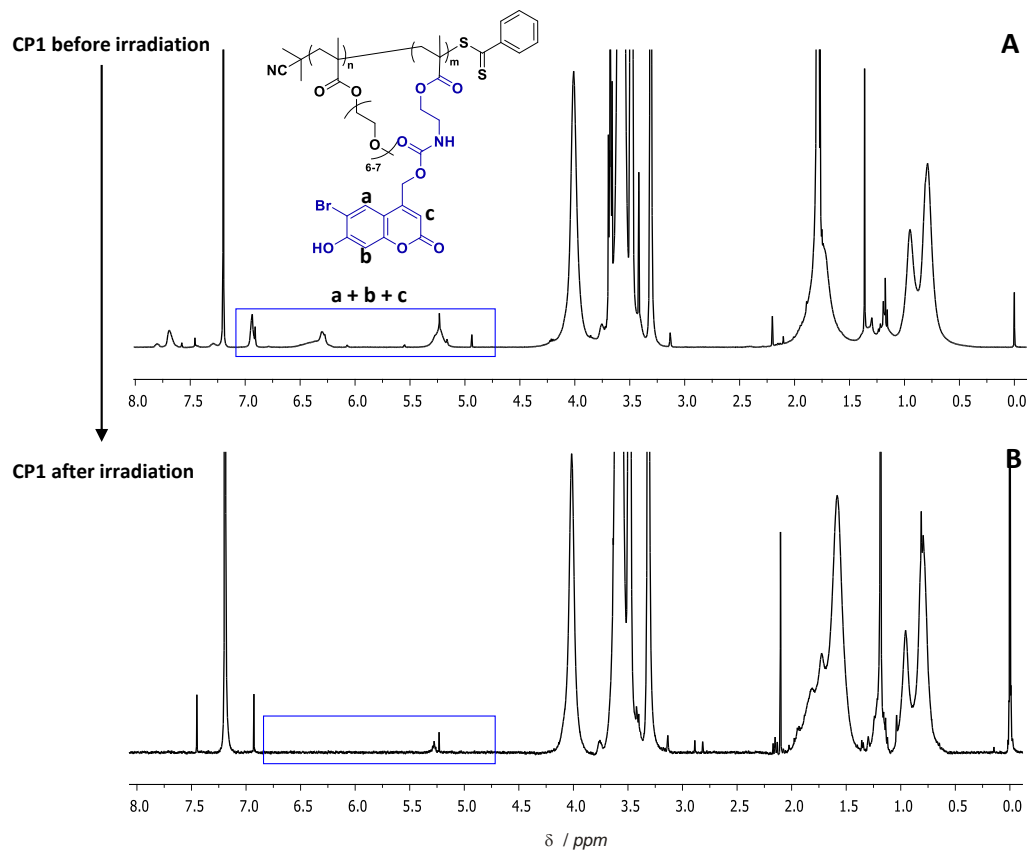


Figure C6. ^1H NMR spectra of 10 g L^{-1} CP1 in water before (A) and after (B) irradiation at 320 nm.

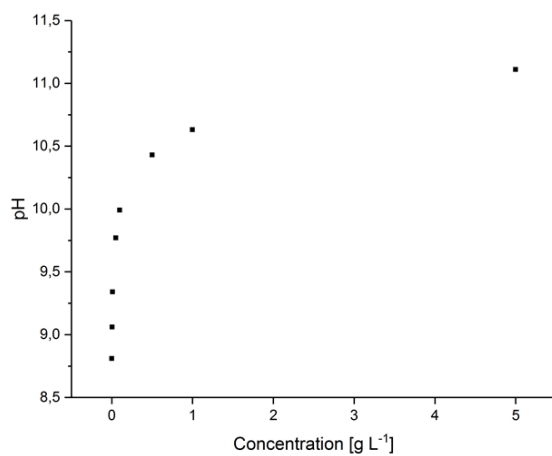


Figure C7. Plot of concentration vs pH for ethanolamine in water.

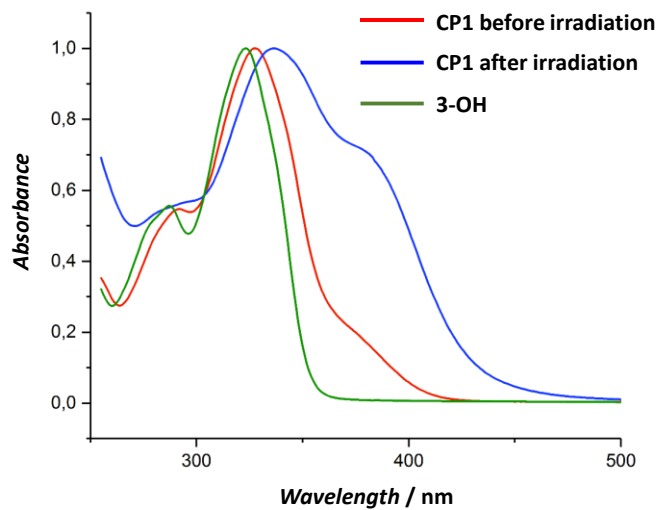


Figure C8. UV-Vis spectra of 3 (green), CP1 before (red) and after (blue) irradiation at 320 nm for 1 h.

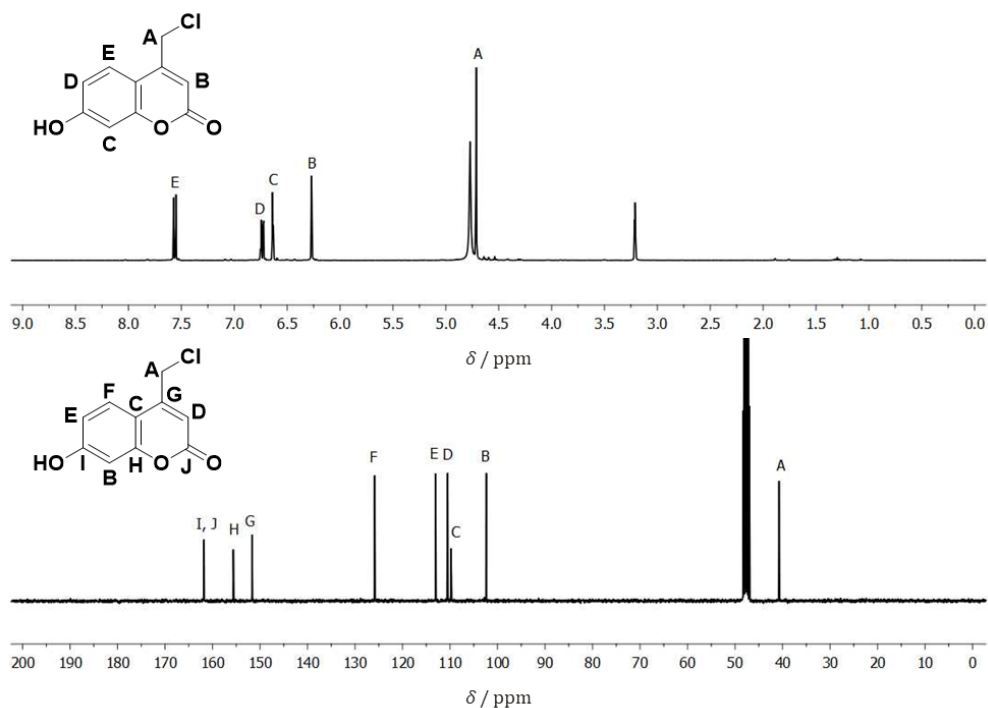


Figure C9. ¹H (top) and ¹³C (bottom) NMR spectra of compound 7.

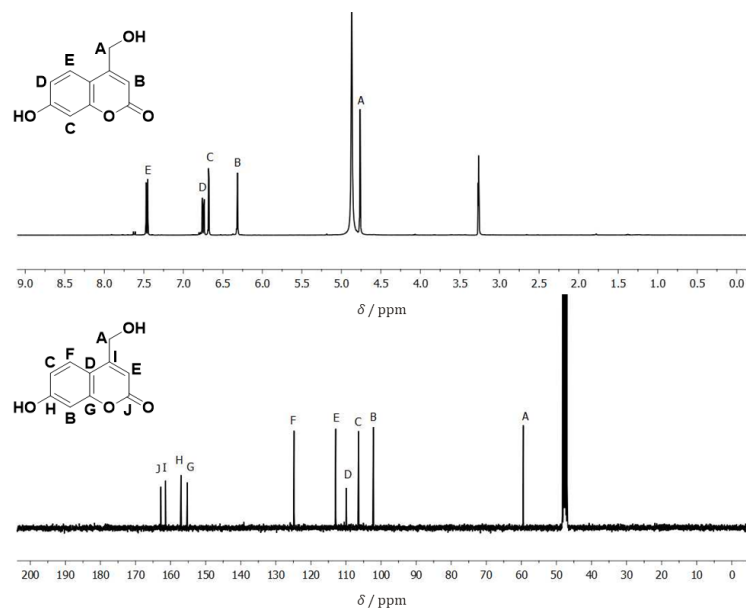


Figure C10. ^1H (top) and ^{13}C (bottom) NMR spectra of compound **8**.

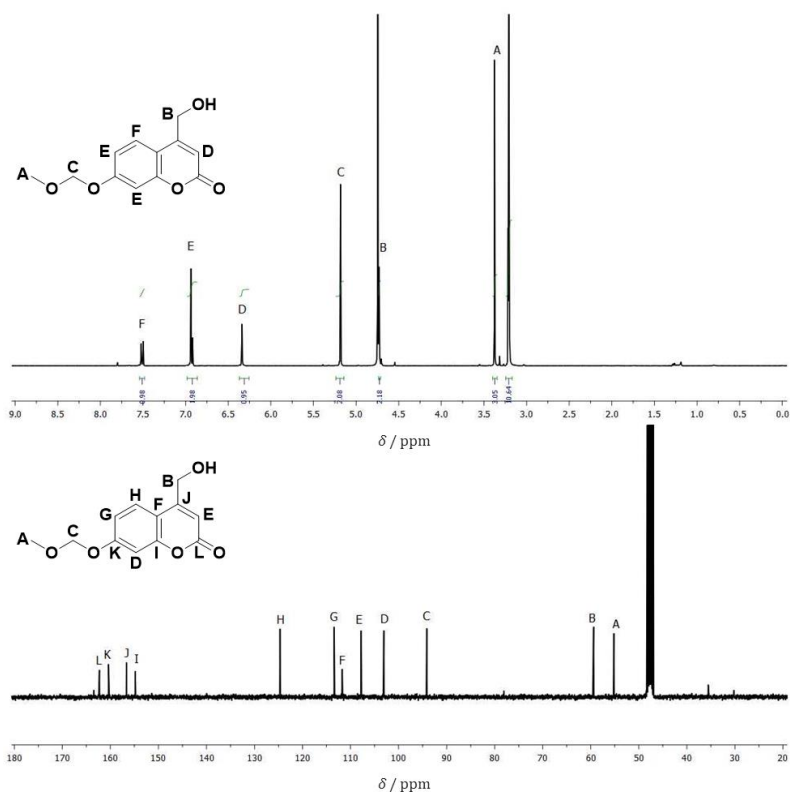


Figure C11. ^1H (top) and ^{13}C (bottom) NMR of compound **9**.

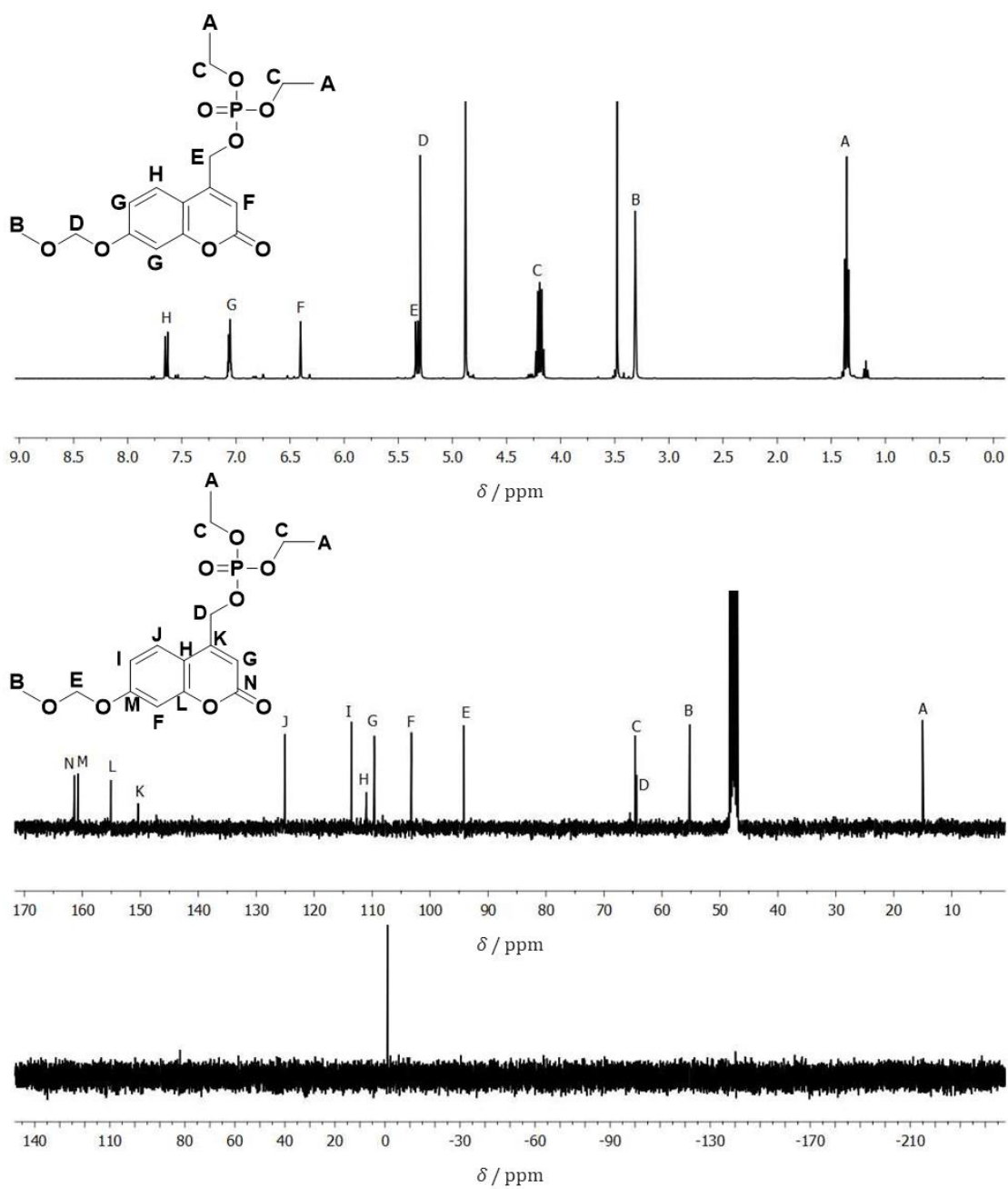


Figure C12. ^1H (top), ^{13}C (middle), and ^{31}P (bottom) NMR of compound 10.

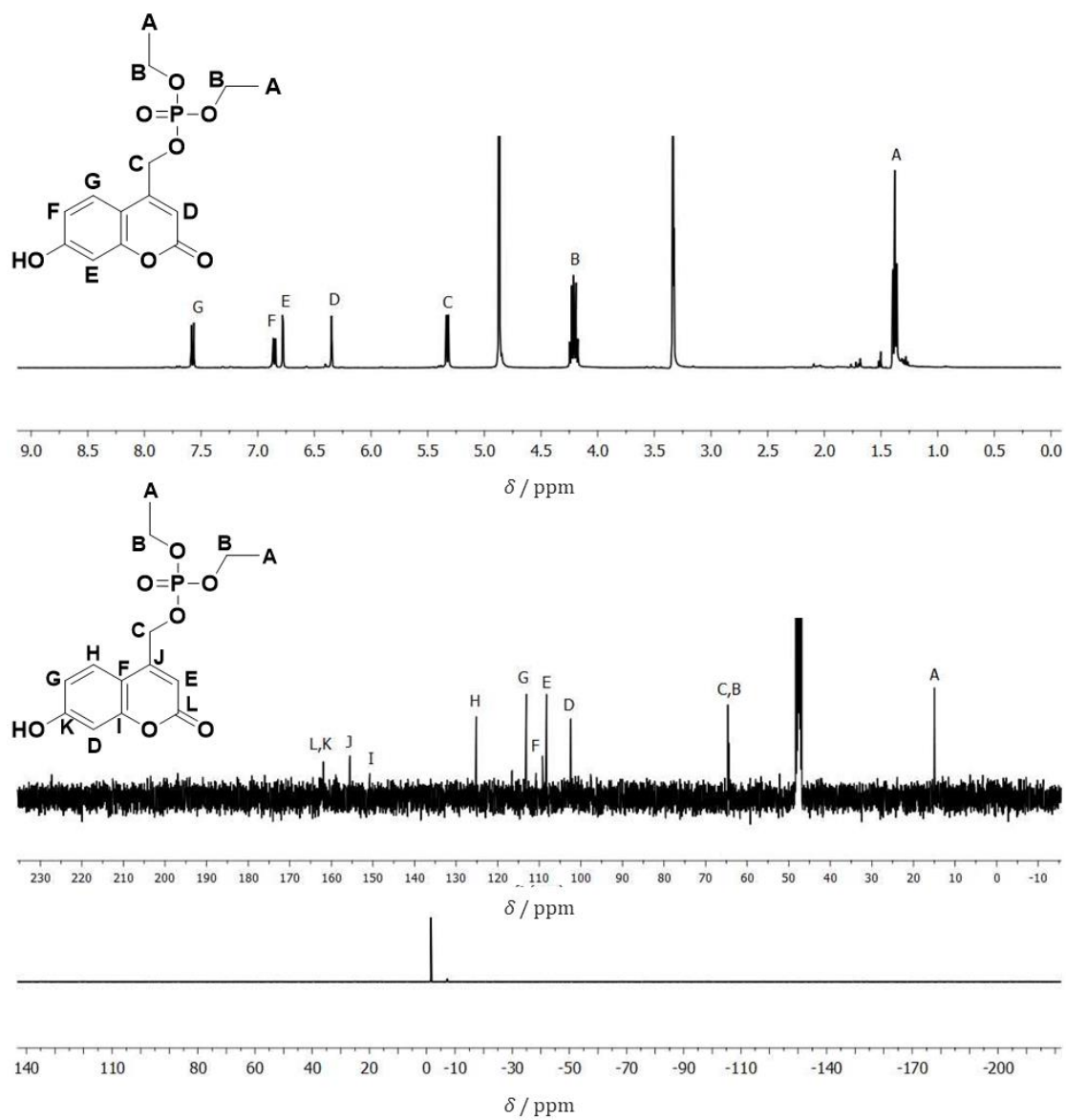


Figure C13. ^1H (top), ^{13}C (middle), and ^{31}P (bottom) NMR of compound 11.

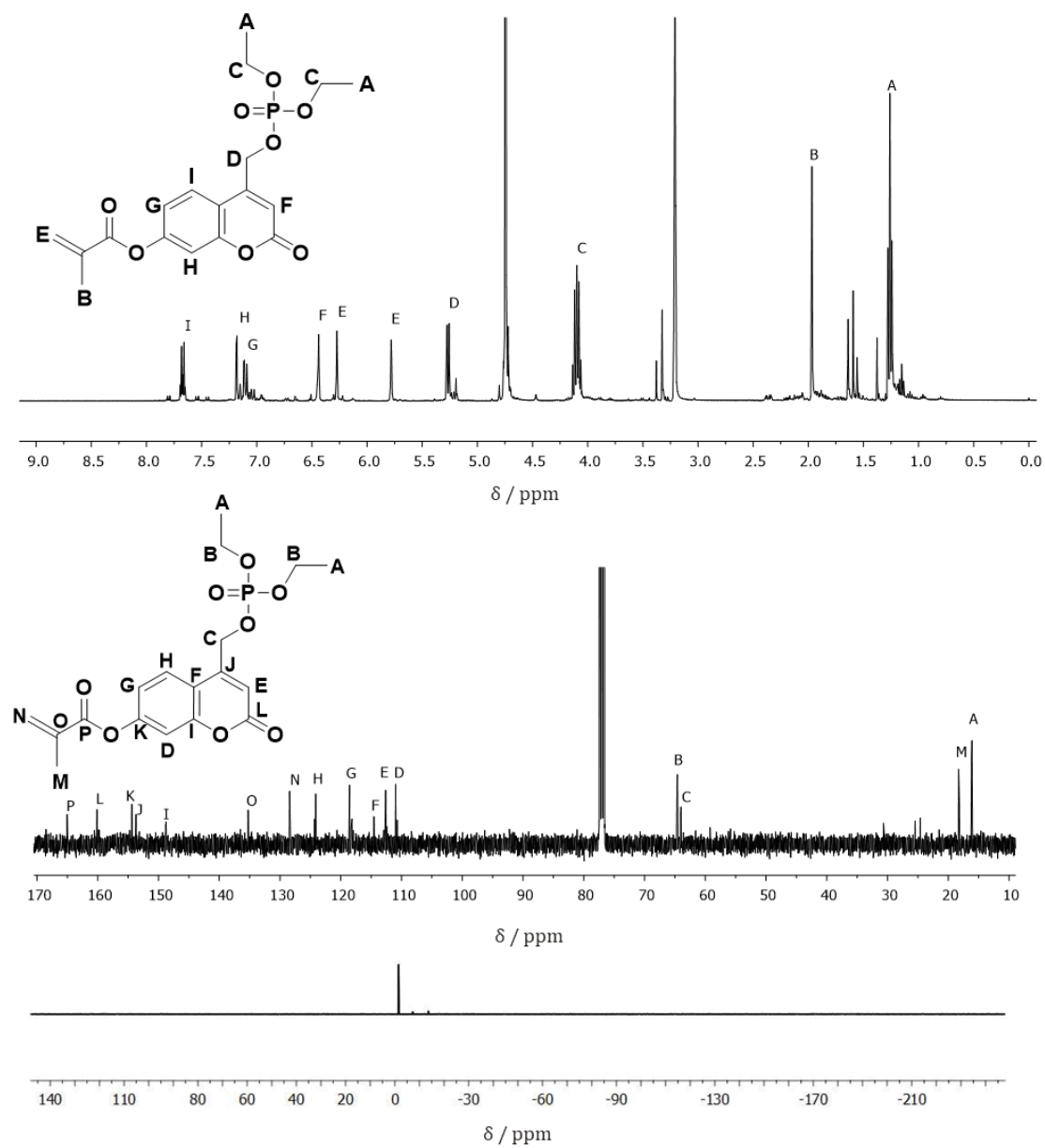


Figure C14. ^1H (top), ^{13}C (middle), and ^{31}P (bottom) NMR of the photoacid generator (PAG, 12).

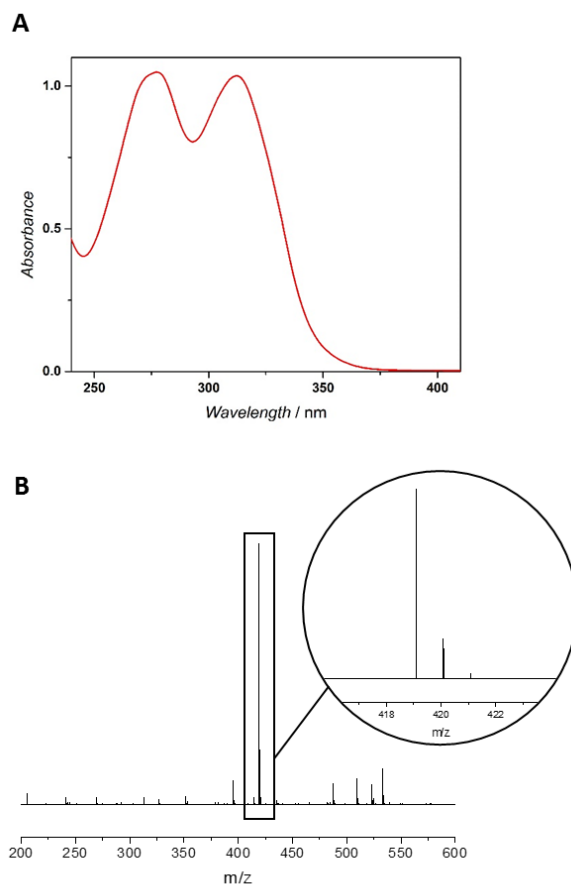


Figure C15. UV-Vis absorption spectrum (A) and ESI-MS (B) of PAG **12** in acetonitrile (1 mg mL^{-1}) and THF:MeOH = 3:2, respectively.

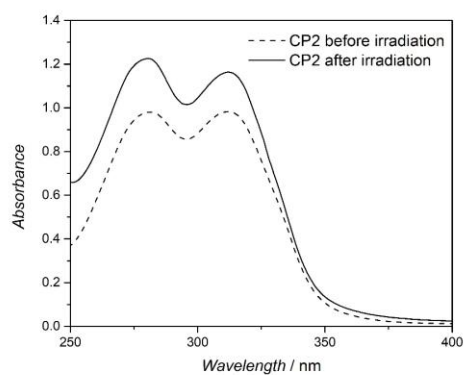


Figure C16. UV-Vis spectra of **CP2** before (dotted) and after (solid) photolysis. Irradiation was performed at 320 nm for 60 min.

LIST OF ABBREVIATIONS

χ	Flory-Huggins interaction parameter
D	dispersity
(P(<i>n</i> BMA- <i>r</i> -PFPMA)- <i>b</i> -P(S- <i>r</i> -PFS))	poly(<i>n</i> -butyl methacrylate- <i>stat</i> -pentafluorophenyl methacrylate)- <i>block</i> -poly(styrene- <i>stat</i> -pentafluorostyrene)
(P(MMA- <i>r</i> -PFPMA)- <i>b</i> -P(S- <i>r</i> -PFS))	poly(methyl methacrylate- <i>stat</i> -pentafluorophenyl methacrylate)- <i>block</i> -poly(styrene- <i>stat</i> -pentafluorostyrene)
1D	1 dimension
2D	2 dimension
2PA	2-photon absorption
3D	3 dimension
AAC	azide /alkyne cycloaddition
ACN	acetonitrile
ADF	annular dark field
AFM	atomic force microscopy
AIBN	2,2'-azobisisobutyronitrile
ATRP	atom-transfer radical polymerization
BCP	block copolymers
BF	bright field
CPBD	2-cyano-2-propyl benzodithioate
CRP	controlled radical polymerization
CTA	chain-transfer agent
DBU	1,8-Diazabicyclo[5.4.0]-undec-7-ene
DF	dark field
diBCP	diblock copolymer
DLS	dynamic light scattering
DPN	dip-pen lithography
EDX	energy dispersive X-ray spectroscopy

EHD.	electro hydrodynamic
ESI-MS.	electrospray ionization mass-spectrometry
ET.	electron tomography
<i>f</i>	block volume fraction
FITC-PEG-SH.	fluorescein-PEG-thiol
GMA.	glycerol methacrylate
HOMO.	highest occupied molecular orbital
L_0	periodicity or domain sizes
LAM.	less activated monomers
LUMO.	lowest unoccupied molecular orbital
MAM.	more activated monomers
MAMA-SG1.	<i>N</i> -(2-methylpropyl)- <i>N</i> -(1-diethylphosphono-2,2-dimethylpropyl)- <i>O</i> -(2-carboxyprop-2-yl)hydroxylamine
MMA.	methyl methacrylate
M_n	number-average molar mass
MS.	microphase separation
<i>N</i>	degree of polymerization
NAM.	<i>N</i> -acryloyl morpholine
NIR.	near- infra red
NMP.	nitroxide mediated polymerization
ODT.	order-disorder transition
OOT.	order-order transitions
OsO ₄	osmium tetroxide
OT.	1-octanethiol
PAG.	photoacid generator
PBG.	photobase generator
PFP.	pentafluorophenyl
PFPMA.	pentafluorophenyl methacrylate
PFS.	2,3,4,5,6 pentafluorostyrene
PFTR.	para-fluoro-thiol substitution reaction
PGMA.	polyglycerol monomethacrylate

PMMA- <i>b</i> -PS.	poly(methyl methacrylate)- <i>block</i> -polystyrene
PnBMA- <i>b</i> -PS.	poly(<i>n</i> -butyl methacrylate)- <i>block</i> -polystyrene
POEGMA.	poly(oligoethyleneglycol methacrylate)
PPM.	post-polymerization modification
PRE.	persistent radical effect
PS- <i>b</i> -PI.	polystyrene- <i>block</i> -polyisoprene
RAFT.	reversible addition-fragmentation chain-transfer polymerization
RDRP.	reversible-deactivation radical polymerization
RP.	radical polymerization
SCFT.	self-consistent mean field theory
SEC.	size-exclusion chromatography
SG1.	<i>N</i> -tert-Butyl- <i>N</i> -[1-diethylphosphono-(2,2-dimethylpropyl)] nitroxide
SISE.	selective immobilization and selective elimination
SORP.	self-organized precipitation
SP.	solubility parameter
SSL.	strong segregation limit
STED.	Stimulated Emission Depletion Microscopy
STEM.	Scanning Transmission Electron Microscopy
T.	temperature
TEA.	triethylamine
TEM.	Transmission Electron Microscopy
TEMPO.	2,2,6,6- tetramethylpiperidinyl-1-oxyl
THF.	tetrahydrofuran
T_{ODT}	order-to-disorder temperature
UV.	ultra-violet
WSL.	weak segregation limit

LIST OF FIGURES

Figure 2.1. Classification of different BCP architectures	6
Figure 2.2. Structure of various nitroxides for a bimolecular system and of an alkoxyamine for a unimolecular system used as controlling agents in NMP.	10
Figure 2.3. Guidelines for the selection of R and Z groups of the RAFT agent for various monomers.....	13
Figure 2.4. Various structure hierarchies from BCP systems.	21
Figure 2.5. (a) Equilibrium morphologies of AB diBCP in bulk (b) Theoretical phase diagram predicted by self-consistent field theory (SCFT), (c) Experimental phase diagram of polystyrene- <i>block</i> -polyisoprene (PS- <i>b</i> -PI).	23
Figure 2.6. Schematic representation of chain conformations at the microphase-separated state.	26
Figure 2.7. a) BCP self-assembly under 1D, 2D (fibers), and 3D confinement (particles) and their symmetry and interface stiffness. b) Comparing the definition of periodicity (L_0) of a phase separated structure (e.g., lamellar) in the bulk state and size D corresponding to the confinement space.....	31
Figure 2.8. Selection of possible shapes for 3D confinement of BCPs.	32
Figure 2.9. Interaction between the polymer chains A and B of a diBCP A- <i>b</i> -B and the matrix in a 3D confinement space.	33
Figure 2.10. BCPs in 3D confinement. a) Schematic representation of preparation of PS- <i>b</i> -P4VP BCP colloidal particles. b) Transmission electron microscopy (TEM) image of BCP nanoparticles containing axially stacked PS and P4VP domains.....	34
Figure 2.11. Self-assembled morphologies for symmetric diblock copolymers confined in spherical pores as functions of the ratio D/L_0 and α	36
Figure 2.12. TEM images of PS- <i>b</i> -PI BCP nanoparticles.....	37
Figure 2.13. STEM images of various phase separation morphologies in PS- <i>b</i> -PI BCP nanoparticles as a function of molar mass and D/L_0 ratio	39
Figure 2.14. AFM phase images of PEO- <i>b</i> -PPFPMA BCP with <i>ortho</i> -nitrobenzyl (ONB) photocleavable junction	41
Figure 2.15. (a) Schematics for the preparation of block copolymer membrane with cylindrical nanochannels.....	42

Figure 2.16. Three-patch particle decorated with alkyne, carboxylic acid and benzophenone functional groups and their utilization for attachment of biomolecules...	43
Figure 2.17. STEM images (dark field) of PS- <i>b</i> -PI ₃₀ nanoparticles prepared at different temperatures showing spheres, stacked-lamellae and onion-like internal structures, respectively	44
Figure 2.18. Multifunctional ellipsoidal striped nanoparticles via <i>non-covalent post-assembly</i> modification	45
Figure 2.19. The STED concept: Schematic representation of a STED microscope.....	52
Figure 3.1. ¹ H, ¹⁹ F NMR spectrum of BCP 2 and 2a , SEC traces of macroRAFT agent 1 , polymer 1a , and BCPs 2 and 2a	59
Figure 3.2. UV-Vis spectra of 1 and 2 before and after end group capping with 2-methoxy-6-methylbenzaldehyde.....	60
Figure 3.3. ¹ H and ¹⁹ F NMR spectra of BCPs 2a , 2a_{allyl} , and 2a_{allyl}→OT	62
Figure 3.4. SEC traces of BCPs 2a , 2a_{allyl} , and 2a_{allyl}→OT	63
Figure 3.5. ¹⁹ F NMR of BCP 2a at various time intervals using standard PFTR conditions at RT.....	65
Figure 3.6. ¹⁹ F NMR spectra of the BCPs obtained after PFTR of BCP 2a with OT under different conditions of base, temperature, and reaction times	67
Figure 3.7. Underlying reaction scheme for the amidation of 3 . ¹⁹ F and ¹ H spectra of 3 and 4	68
Figure 3.8. ¹ H and ¹⁹ F spectra after one-pot orthogonal dual functionalization of 2a with aminoethanethiol.....	69
Figure 3.9. ¹⁹ F NMR spectra of 1a before and after reaction with OT under standard PFTR conditions	70
Figure 3.10. ¹⁹ F and ¹ H NMR spectra after the reaction of polymer 1a with 1 eq. of OT leading only to <i>para</i> -F substitution during nucleophilic thiol substitution reaction.....	71
Figure 4.1. Transmission electron microscope (TEM) images of PMMA- <i>b</i> -PS and PnBMA- <i>b</i> -PS nanoparticles prepared by SORP	81
Figure 4.2. Evolution of the intensity-average hydrodynamic diameters obtained by DLS and diameters from TEM statistical analysis (TEM) of functional PS- <i>b</i> -PI nanoparticles during SORP	86

Figure 4.3. Bright field TEM images for nanoparticles obtained by SORP with BCPs P1–4 in various conditions.....	88
Figure 4.4. An enlarged view showing the outermost layer of the nanoparticles obtained from P2 at 0.1 mg mL ⁻¹ and 50 vol% of THF	90
Figure 4.5. Bright field TEM images for nanoparticles obtained by SORP with commercial BCP P5	91
Figure 4.6. Bright field TEM images for nanoparticles obtained by SORP with mixtures of custom-made BCPs P1–3 and commercial BCP P5 , at various weight ratios.....	93
Figure 4.7. Electron tomography images of NP3 nanoparticles showing PS and PI phases	95
Figure 4.8. Schematic representation of PFTR on the PS segment of the striped nanoparticles NP3 with cysteine, their dark field STEM image, and EDX mapping of Os-L α lines and S-K α lines.....	96
Figure 4.9. Dark field STEM images of nanoparticles NP3 with stacked lamellae structures and the corresponding nanodiscs ND3 obtained by SISE. AFM and STED images of the nanodiscs after functionalization with FITC-PEG-SH.....	98
Figure 4.10. ¹ H and ¹⁹ F NMR spectra after PFTR of PFP-linker with ATRP-SH using Strategy 1	103
Figure 4.11. ¹⁹ F NMR spectra after PFTR of PFP-PS-H with octanethiol for 24 h and 48 h.....	105
Figure 4.12. ¹ H and ¹⁹ F NMR spectra after the reaction of PGMA-SH and PFP-linker in a PFTR to obtain PGMA-PFP-RAFT	107
Figure 5.1. ¹ H and ¹³ C NMR, UV-Vis spectra of the photobase generator, PBG 5	116
Figure 5.2. ¹ H NMR spectra, size-exclusion chromatogram of CP1	119
Figure 5.3. Emission spectra of CP1 in water before and after irradiation at 320 nm ..	120
Figure 5.4. pH of CP1 solution (in water) after different irradiation times.....	122
Figure 5.5. pH of CP1 solutions at different concentrations after irradiation for 1 h....	123
Figure 5.6. ¹ H NMR spectrum, size-exclusion chromatogram, and UV-Vis absorption spectrum of CP2	127
Figure 5.7. Evolution of pH of CP2 solutions in water after different irradiation times	128

Figure 5.8. pH of of CP2 solutions in water at various concentrations after a constant irradiation time of 60 min	129
Figure 8.1. General reaction scheme for the reaction of 2a with various amines.....	143
Figure 8.2. General reaction scheme for PFTR using OT and mercaptoethanol as model thiols.....	144

LIST OF SCHEMES

Scheme 1.1. Strategy employed in this thesis for the fabrication of functional nanomaterials for patterned immobilization using BCPs.	1
Scheme 1.2. Orthogonality problem addressed to obtain functional BCPs	2
Scheme 2.1. Activation-deactivation equilibrium in NMP.	9
Scheme 2.2. ATRP equilibrium showing transition metal activation (k_{act}) of a dormant species with a radically transferable atom.	11
Scheme 2.3. General structure of a RAFT agent and equilibrium between the active and dormant species in a RAFT process.....	12
Scheme 2.4. Synthesis of functional polymer libraries by post-polymerization modification.	15
Scheme 2.5. Collection of a few activated-ester monomers	16
Scheme 2.6. PPM by activated ester-amine chemistry.....	17
Scheme 2.7. Schematic representation of PFTR on PFP-based moieties.....	18
Scheme 2.8. General overview of the <i>para</i> -fluoro substitution reactions of PFP based homo- or copolymers with various nucleophiles.	19
Scheme 2.9. Probable interactions between the primary electron beam and a specimen.	46
Scheme 2.10. Schematic representation of the three components (electron gun, condenser system and image production system) in a TEM.....	47
Scheme 2.11. Ray diagram illustrating the image formation in the BF and DF mode. ...	48
Scheme 2.12. A general schematic representation of the optical configuration of a STEM	50
Scheme 2.13. A schematic diagram showing the equivalence between bright-field STEM and conventional TEM (CTEM) using the principle of reciprocity.	51
Scheme 3.1. Schematic representation of the strategy used (amidation + PFTR) to create dual reactive PMMA- <i>b</i> -PS and PnBMA- <i>b</i> -PS BCP precursors.	56
Scheme 3.2. Synthetic route towards the synthesis of P(MMA- <i>r</i> -PFPMA)- <i>b</i> -P(S- <i>r</i> -PFS) and the capping of the RAFT end group.....	58
Scheme 4.1. Self-assembly of block copolymers into thin films, fibers, and nanoparticles, i.e., 1D, 2D, and 3D confinement, respectively.	75

Scheme 4.2. Schematic representation of self-organized precipitation (SORP) utilized for the preparation of patchy nanoparticles.	77
Scheme 4.3. Overall scheme representing the preparation of patchy nanoparticles from functional block copolymers (BCPs), the supramolecular transformation of the striped particles into nanodiscs, and their surface functionalization.	78
Scheme 4.4. Structure and characteristics of the PMMA- <i>b</i> -PS and PnBMA- <i>b</i> -PS block copolymers synthesized and utilized for the the preparation of nanostructured nanoparticles	80
Scheme 4.5. Structure and characteristics of the PS- <i>b</i> -PI BCPs synthesized for the preparation of nanoparticles.....	83
Scheme 4.6. Schematic representation of the preparation of porous membranes using an amphiphilic block copolymer with para-substituted PFP-ester junction point.	100
Scheme 4.7. Synthetic route towards the synthesis of the amphiphilic BCP according to Strategy 1	101
Scheme 4.8. Synthetic route towards the synthesis of the amphiphilic BCP according to Strategy 2	104
Scheme 4.9. Synthetic route towards the synthesis of the amphiphilic BCP according to Strategy 3	106
Scheme 5.1. Schematic representation of the role of photoacid and photobase generators (PAG and PBG) as inflammation probes.....	111
Scheme 5.2. Schematic representation of the irradiation of the coumarin-based P(OEGMA- <i>r</i> -PAG) or P(OEGMA- <i>r</i> -PBG) copolymers to visualize a decrease or increase in pH.....	114
Scheme 5.3. Synthetic scheme towards the synthesis of PBG 5	115
Scheme 5.4. Synthetic scheme for the synthesis of P(OEGMA- <i>r</i> -PBG) copolymer.	118
Scheme 5.5. Synthetic route towards the synthesis of the photoacid generator 12	125
Scheme 5.6. Synthetic scheme for the synthesis of P(OEGMA- <i>r</i> -PBG) copolymer CP2	126
Scheme 8.1. Synthetic route towards the synthesis of macroinitiators M1 , M2 , M4 and P1–4 by NMP.	146

LIST OF TABLES

Table 3.1. Characteristics of the BCPs obtained through modification of 2a using <i>Pathway 1</i> with different amines and octanethiol.....	61
Table 3.2. Activity of the fluorine atoms of PFPMA and PFS towards thiols at different reaction times.....	64
Table 3.3. Activity of PFPMA and PFS fluorine atoms towards thiols varying certain parameters: base, temperature and reaction times.....	66
Table 4.1. Summary of different conditions used to prepare the functional nanoparticles and their Z-average hydrodynamic diameter as measured by DLS and particle sizes obtained from TEM by statistical analysis.....	85
Table 4.2. Composition of block copolymer blends of P1–3 and non-functional PS- <i>b</i> -PI P5	92
Table 4.3. A detailed list of all conditions used for PFTR.....	102
Table 5.1. Variation of pH of CP1 solutions in water after irradiation at 320 nm for 0-60 minutes.....	121
Table 8.1. Characteristics of the functional PS macroinitiators MI1 , MI3 , and MI4 ...	147
Table 8.2. Characteristics of the PS- <i>b</i> -PI block copolymers P1–P4	147

ACKNOWLEDGEMENTS

First and foremost, I would like to thank Dr. Guillaume Delaittre for allowing me to pursue my PhD in his working group – lead to me making some fancy looking particles many seem to remember! I am extremely grateful for his constant supervision and great support this entire time. In addition, I would like to extend my gratitude to Prof. Christopher Barner Kowolik for giving me a chance to be a part of the macroarc team.

I have my family back in India and my brother, Ajay next to thank for being strong pillars of support all the way.

Thanks to all the people from CN: the Gryffindor lab and its members, now Dr. Gaby and Dr. Ana as we like to call her! Dao for the timely valuable inputs, other members of the AKGD group and members of the Levkin lab (Anna, Kony, Akshita, Ivana, Tina).

My sincere thank you to all the collaboration partners: Prof. Hiroshi Yabu, Suzuki San and Sasaki San for the help and support during my stay in Japan. Prof. Lahann, Nahal for the fruitful work and time at Michigan, USA. Additionally, to my flat mates Tessa and Maria. Special thanks to my master student Shamini Madhava and my vertiefer student Stefan Frech for all the hard work.

Deepest thanks to all my friends back in India (Jubran, Alagu, Subikshaa, and many others all around the world for always being there.

Lastly, I would like extend my heartfelt thank you to some important people who have been there throughout this journey: Matze for the innumerable favors and help I have gotten from you, Fede for all the nice and timely breaks and talks, and Matti, Alan, Stan, Jenny for making home a wonderful place to be at.

LIST OF PUBLICATIONS

From this thesis

- **Divya Varadharajan**, Hatice Turgut, Joerg Lahann, Hiroshi Yabu,* Guillaume Delaittre*
Surface-Reactive Patchy Nanoparticles and Nanodiscs Prepared by Tandem Nanoprecipitation and Internal Phase Separation, *Adv. Funct. Mater.* **2018**, 1800846
- Hatice Turgut, **Divya Varadharajan**, Nico Dingenouts, Guillaume Delaittre*
Nanostructured Thin Films of Moderately Functionalized PMMA-*b*-PS, *Macromol. Rapid Comm.* **2018**, 39, 1800231
- **Divya Varadharajan**, Guillaume Delaittre*
Accessing Libraries of Bifunctional Diblock Copolymers Using Two Distinct Pentafluorophenyl Moieties, *Polym. Chem.* **2016**, 7, 7488–7499

Additional

- Lauri Mäkinen, **Divya Varadharajan**, Heikki Tenhu, and Sami Hietala*
Triple hydrophilic UCST-LCST block copolymers, *Macromolecules*, **2016**, 49, 986–993

Conference Contributions

- 21st – 25th May, 2017, Ghent, Belgium
Conference – “Advanced Polymers via Macromolecular Engineering”, **Poster**
Title: Functional Multicompartmental Polymeric Microparticles
- 15th – 17th February, 2017, Freiburg, Germany
Conference – Macromolecular Colloquium
- 24th – 26th June, 2016, Freiburg, Germany
Conference – Macromolecular Colloquium
- 16th June, 2015, Teltow, Germany
Conference – “Molecular interactions engineering”, **Talk**
Title: Biohybrid nanoarrays for catalysis

